

Probing Interfacial Charge Dynamics in Dye-sensitized Solar Cells using Copper Electrolytes for Indoor Photovoltaics

by

Sourava Chandra Pradhan

20EE18A39022

A Thesis Submitted to the
Academy of Scientific & Innovative Research
for the Award of the Degree of
DOCTOR OF PHILOSOPHY
in
Engineering

Under the supervision of

Dr. Suraj Soman



**CSIR-National Institute for Interdisciplinary
Science and Technology (CSIR-NIIST)
Thiruvananthapuram – 695 019**



Academy of Scientific and Innovative Research
AcSIR Headquarters, CSIR-HRDC campus
Sector 19, Kamla Nehru Nagar,
Ghaziabad, U.P. – 201 002, India

January – 2023



राष्ट्रीय अंतर्विषयी विज्ञान तथा प्रौद्योगिकी संस्थान
NATIONAL INSTITUTE FOR INTERDISCIPLINARY SCIENCE AND TECHNOLOGY

वैज्ञानिक तथा औद्योगिक अनुसंधान परिषद्
इंडस्ट्रियल एस्टेट पी ओ, पाप्पनमकोड, तिरुवनंतपुरम, भारत - 695 019

Council of Scientific and Industrial Research
Industrial Estate P O, Pappanamcode, Thiruvananthapuram, India - 695 019

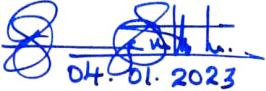
डॉ. सूरज सोमन
वैज्ञानिक
फोटो विज्ञान और फोटोनिक्स अनुभाग

Dr. Suraj Soman
Scientist
Photosciences and Photonics Section

CERTIFICATE

This is to certify that the work incorporated in this Ph.D. thesis entitled, “**Probing Interfacial Charge Dynamics in Dye-sensitized Solar Cells using Copper Electrolytes for Indoor Photovoltaics**”, submitted by *Mr. Sourava Chandra Pradhan* to the Academy of Scientific and Innovative Research (AcSIR), in partial fulfilment of the requirements for the award of the Degree of *Doctor of Philosophy in Engineering*, embodies original research work carried out by the student. We, further certify that this work has not been submitted to any other University or Institution in part or full for the award of any degree or diploma. Research materials obtained from other sources and used in this research work have been duly acknowledged in the thesis. Images, illustrations, figures, tables etc., used in the thesis from other sources, have also been duly cited and acknowledged.


04.01.2023
Sourava Chandra Pradhan


04.01.2023

Dr. Suraj Soman
(Supervisor)

STATEMENTS OF ACADEMIC INTEGRITY

I, Sourava Chandra Pradhan, a Ph.D. student of the Academy of Scientific and Innovative Research (AcSIR) with Registration No. 20EE18A39022 hereby undertake that, the thesis entitled “**Probing Interfacial Charge Dynamics in Dye-sensitized Solar Cells using Copper Electrolytes for Indoor**” has been prepared by me and that the document reports original work carried out by me and is free of any plagiarism in compliance with the UGC Regulations on “*Promotion of Academic Integrity and Prevention of Plagiarism in Higher Educational Institutions (2018)*” and the CSIR Guidelines for “*Ethics in Research and in Governance (2020)*”.



Sourava Chandra Pradhan

Date: 04.01.2023

Place: Thiruvananthapuram

It is hereby certified that the work done by the student, under our supervision, is plagiarism free in accordance with the UGC Regulations on “*Promotion of Academic Integrity and Prevention of Plagiarism in Higher Educational Institutions (2018)*” and the CSIR Guidelines for “*Ethics in Research and in Governance (2020)*”.



Dr. Suraj Soman

(Supervisor)

Date: 04.01.2023

Place: Thiruvananthapuram

DECLARATION

I, Sourava Chandra Pradhan, bearing AcSIR Registration No. 20EE18A39022 declare: that my thesis entitled, “**Probing Interfacial Charge Dynamics in Dye-sensitized Solar Cells using Copper Electrolytes for Indoor**” is plagiarism free in accordance with the UGC Regulations on “*Promotion of Academic Integrity and Prevention of Plagiarism in Higher Educational Institutions (2018)*” and the CSIR Guidelines for “*Ethics in Research and in Governance (2020)*”.

I would be solely held responsible if any plagiarized content in my thesis is detected, which is violative of the UGC regulations 2018.


Sourava Chandra Pradhan
Date: 04.01.2023
Place: Thiruvananthapuram

ACKNOWLEDGEMENTS

I express my deep sense of gratitude to Dr. Suraj Soman, research supervisor, for his invaluable guidance and optimistic research approach that led to the successful completion of this work.

I sincerely thank Dr. C. Anandharamakrishnan, Dr. Ashish Lele and Dr. A. Ajayaghosh, the present and former Directors of CSIR-National Institute for Interdisciplinary Science and Technology (CSIR-NIIST), Thiruvananthapuram, for providing necessary facilities to carry out research at CSIR-NIIST.

I would like to express my sincere thanks to (late) Prof. M. V. George for his inspirational presence at CSIR-NIIST.

I am thankful to the AcSIR coordinator Dr. V. Karunakaran for his timely advice and support in conducting all the academic procedures. I also thank Dr. C. H. Suresh and Dr. R. Luxmi Varma, former AcSIR coordinator, for her support and guidance.

I express my sincere gratitude to Dr. K. V. Radhakrishnan, Head, Chemical Sciences and Technology Division, and the former HODs, Dr. P. Sujatha Devi and Dr. R. Luxmi Varma for their support.

I am very much grateful to Dr. K. N. Narayanan Unni, Head, Photosciences and Photonics Section for the immense help and support that I received from him.

I sincerely appreciate my Doctoral Advisory Committee Members Dr. Ananthakumar S, Dr. U. S. Hareesh and Dr. Biswapriya Deb for their valuable suggestions and guidance throughout my Ph. D. work.

I would like to express my sincere thanks to Prof. Thomas W. Hamann and Prof. Anders Hagfeldt for the fruitful scientific discussions and suggestions.

I thank present and former scientists of the Photosciences and Photonics Section, Chemical Sciences and Technology Division, for their help and support.

I would like to extend my heartfelt gratitude to all the former and present members of our research group, Dr. Anjaly, Dr. Rajeev, Dr. Manuraj, Dr. Hanna, Dr. Jayadev, Mr. Lingamoorthy, Ms. Anjali, Mr. Vibhu, Mr. Gokul, Mr. Sabu, Ms. Anooja, Ms. Kavya, Ms.

Sruthi, Ms. Jebin, Mr. Vipin, Dr. Anantharaj, Mr. Andrew, Ms. Sreelekshmy, Ms. Kanishga and Mr. Sreenandu for all their support and encouragement throughout my research career at NIIST.

I would like to thank my master students Ms. Drishya, Ms. Abya, Ms. Syamika and my summer interns, Mr. Godwin, Mr. Gokul, Ms. Rashmi and Ms. Reshma for experimental help in the lab.

I gratefully acknowledge my teachers and friends for their inspiration and support.

I am very much thankful my family for supporting me during this time, and for thinking I am doing something good though they don't understand what I am doing.

I thank CSIR and DST, Government of India for the financial support.

Finally, I acknowledge all other individuals who helped along this journey. I am humbled by the support I received during my Ph. D. studies.

Thank you everyone!!!

Sourava Chandra Pradhan

TABLE OF CONTENTS

Certificate	i
Statement of academic integrity	ii
Declaration	iii
Acknowledgements	iv
Table of contents	vi
List of figures	xi
List of tables	xviii
List of abbreviations	xx
Preface	xxv
Chapter 1	
Introduction to Copper Electrolyte based Dye-sensitized Solar Cells and Indoor Photovoltaics	
1.1 Abstract	1
1.2 Introduction	2
1.3 Photovoltaics	2
1.3.1 Solar Photovoltaic Cell	3
1.3.2 Indoor Photovoltaic Cell	3
1.4 Generation of Photovoltaic Cells Generations	4
1.4.1 First Generation Photovoltaic Cells	4
1.4.2 Second Generation Photovoltaic Cells	5
1.4.3 Third Generation Photovoltaic Cells	5
1.5 Dye-Sensitized Solar Cells (DSCs)	6
1.5.1 Device Structure and Working Principle of DSCs	6
1.5.2 Fabrication of DSCs	7
1.6 Device Characterization Techniques	8
1.6.1 Current density–voltage (<i>J-V</i>) Measurement	8
1.6.2 Incident Photon-to-Current Conversion Efficiency (IPCE)	10
1.6.3 Current Transient (CT) Measurement	11
1.6.4 Open Circuit Voltage Decay (OCVD)	12

1.6.5	Charge Extraction (CE)	13
1.6.6	Electrochemical Impedance Spectroscopy (EIS)	13
1.6.7	Intensity Modulated Photovoltage Spectroscopy/Intensity Modulated Photocurrent Spectroscopy (IMPS/IMVS)	16
1.6.8	Transient Photovoltage/Photocurrent Decay	17
1.6.9	Photo-Induced Absorption Spectroscopy (PIA)	18
1.7	Evolution of Dye-Sensitized Solar Cells	19
1.8	Copper Electrolyte Based Liquid State DSCs	25
1.8.1	Semiconductor Modification	25
1.8.2	Compatible Sensitizers for Copper Redox Electrolytes	27
1.8.2.1	Metal Complex Sensitizers	27
1.8.2.2	Metal Free Organic Dyes	28
1.8.2.3	Co-sensitization of Organic Dyes	30
1.8.3	Copper Redox Mediators with Structurally Different Ligands	31
1.8.4	Additive Modification in Copper Electrolytes	36
1.8.5	Counter Electrodes Used with Copper Electrolytes	40
1.8.6	Interfacial Charge Dynamics Using Copper Redox Electrolytes	43
1.8.6.1	TiO ₂ /dye Interface	43
1.8.6.2	Dye/Electrolyte Interface	44
1.8.6.3	Semiconductor/Electrolyte Interface	46
1.8.7	Mass Transport	48
1.8.8	Innovative New Architecture Used in DSCs	51
1.8.8.1	Zombie DSCs	51
1.8.8.2	Direct Contact DSCs	55
1.8.9	Indoor/Ambient Light Harvesting Using Cu Electrolyte DSCs	57
1.9	Statement of the Problem	61
1.10	Objectives of the Thesis	61
1.11	References	62

Chapter 2

Resurgence of DSCs with Copper Electrolyte: A Detailed Investigation of the Interfacial Charge Dynamics in Comparison with Cobalt and Iodine

2.1	Abstract	71
2.2	Introduction	72
2.3	Experimental Section	74
2.3.1	Materials and Methods	74
2.3.2	Solar Cell Fabrication	74
2.3.3	Solar Cell Characterization	75
2.4	Results and Discussions	76
2.4.1	Photovoltaic Performance Analysis	76
2.4.2	Mass Transport Limitations	78
2.4.3	Nonlinearity and surface state recombination	82
2.4.4	Investigation of Interfacial Charge Dynamics with Small Electrical and Light Perturbation Techniques	84
2.5	Conclusion	89
2.6	References	90

Chapter 3

Probing Photovoltaic Performance in Copper Electrolyte Dye-Sensitized Solar Cells of Variable TiO₂ Particle Size Using Comprehensive Interfacial Analysis

3.1	Abstract	93
3.2	Introduction	94
3.3	Experimental Section	96
3.3.1	General Methods	96
3.3.2	Fabrication of DSCs	96
3.3.3	Solar Cell Characterization	97
3.4	Results and Discussions	98
3.4.1	Photovoltaic Performance Analysis	98
3.4.2	Probing light harvesting efficiency	100
3.4.3	Probing recombination	101

3.4.4	Probing injection, Regeneration and Mass Transport	104
3.4.5	Probing Charge Collection	106
3.5	Conclusions	107
3.6	References	108

Chapter 4

Fundamental Understanding of Interfacial Charge Dynamics in Copper Electrolyte Based Dye-Sensitized Solar Cells as a Function of Dye Coverage Under Outdoor/Indoor Illuminations

4.1	Abstract	111
4.2	Introduction	112
4.3	Experimental Section	114
4.3.1	General Methods	114
4.3.2	Fabrication of DSCs	114
4.3.3	Solar Cell Characterization	115
4.4	Results and Discussions	116
4.4.1	Solar Cell Characteristics under Full Sun and Indoor light	116
4.4.2	Interfacial charge transfer study	119
4.5	Conclusions	127
3.6	References	128

Chapter 5

Additive Engineering in Copper Electrolyte Based Dye-sensitized Solar Cells for Indoor Photovoltaics

5.1	Abstract	133
5.2	Introduction	134
5.3	Experimental Section	136
5.3.1	General Methods	136
5.3.2	Fabrication of DSCs	136
5.3.3	Solar Cell Characterization	137
5.4	Results and Discussions	138
5.4.1	Photovoltaic Performance under Full Sun	138
5.4.2	Interfacial charge transfer study	141

5.4.3	Photovoltaic performance under indoor LED illumination	144
5.4.4	LITFSi vs. LiI	146
5.4.5	Co-sensitization strategy for indoor photovoltaic performance enhancement	148
5.5	Conclusions	152
5.6	References	153
	Summary and Future Scope	156
	Abstract	159
	List of Publications	160
	List of Conference Presentations	164
	SCI Publications	165

List of Figures

Figure 1.1.	Spectrum of AM 1.5 G solar spectrum	3
Figure 1.2.	Emission spectra of CFL and LED light at 1000 lux.	4
Figure 1.3.	(a) Structure of DSC (b) Energetics and kinetics of DSC	7
Figure 1.4.	Homemade indoor light simulator.	9
Figure 1.5.	(a) <i>J-V</i> characteristics of typical DSC, Energetics and kinetics of DSC under (b) open circuit (c) short circuit and (d) working condition.	10
Figure 1.6.	Schematic of IPCE measurement unit.	11
Figure 1.7.	Current transient plot showcasing current density vs. time for DSC with mass transport limitation	12
Figure 1.8.	(a) Voltage decay with time and (b) lifetime as a function of V_{oc} .	12
Figure 1.9.	(a) Voltage as function of time and (b) extracted charge as a function of voltage measured using charge extraction technique.	13
Figure 1.10.	(a) Input voltage signal and output current signal and (b) Nyquist plot and inset shows equivalent circuit for fitting	14
Figure 1.11.	(a) Nyquist plot and (b) Bode plot for DSC and (c) equivalent circuit for fitting impedance plots	15
Figure 1.12.	Bode plot from IMPS measurement	17
Figure 1.13.	Voltage response and current response of DSC to square wave perturbation in transient photovoltage decay and transient photocurrent decay.	18
Figure 1.14.	(a) Schematic diagram of PIA setup and (b) PIA spectra of DSC in presence and absence of redox electrolyte	19
Figure 1.15.	Representation of energetics of TiO ₂ semiconductor, LEG4 dye and three different electrolytes (I^-/I_3^- , $[Co(bpy)_3]^{3+/2+}$ and $[Cu(dmp)_2]^{2+/1+}$).	21
Figure 1.16.	(a) Number of publications in last 17 years in DSC (data collected with topic of in DSC from Web of Science) (b) Number of publications in DSC using copper electrolyte in last 17 years.	24
Figure 1.17.	Normalized <i>J-V</i> characteristics of DSC with and without silanization.	26
Figure 1.18.	(a) Incident photon-to-electron conversion efficiency (IPCE) of the DSCs (a) various concentration co-sensitization of D35+XY1b and (b) XY1b and the co-sensitization of MS5+XY1b.	31

Figure 1.19.	Structures of (a) $[\text{Cu}(\text{SP})(\text{mmt})]^{0/-}$, (b) $[\text{Cu}(\text{dmp})_2]^{2+/1+}$, and (c) $[\text{Cu}(\text{phen})_2]^{2+/1+}$ complexes.	32
Figure 1.20.	Structures of $[\text{Cu}(\text{bpye})_2]^{2+/1+}$ complex.	32
Figure 1.21.	Molecular structure of (a) $[\text{Cu}(\text{tmby})_2]^{2+/1+}$ and (b) $[\text{Cu}(\text{dmby})_2]^{2+/1+}$ complexes.	33
Figure 1.22.	Molecular structure of $[\text{Cu}(\text{oxabpy})]^{2+/1+}$ complex.	34
Figure 1.23.	Molecular structure of L1 and L2 tetradentate ligands.	34
Figure 1.24.	Molecular structure of (a) $[(\text{S4})\text{Cu}]^{2+}$ (b) $[(\text{N4})\text{Cu}]^{2+}$ complexes.	35
Figure 1.25.	Molecular structure of (a) 1,4-dialkylpipetazine-2,3-dithione based copper complex and (b) bis(2-pyridylmethyl)-1,2-ethanedithiol ligand.	36
Figure 1.26.	Efficiency (η) vs. the $\text{Cu}^{\text{II}}/\text{Cu}^{\text{I}}$ ratio of DSCs using $[\text{Cu}(\text{SP})(\text{mmt})]^{0/-}$ as redox mediator under 1 sun illumination.	37
Figure 1.27.	(a) PCE, (b) V_{oc} , (c) J_{sc} and FF of the $[\text{Cu}(\text{tmby})_2]^{2+/1+}$ reference electrolyte (left) and $[\text{Cu}(\text{oxabpy})_2]^{2+/1+}$ with respect to the addition of $\text{Cu}^{\text{II}}(\text{oxabpy})$ to the electrolyte (5:0 = Cu(I) only, 5:1 = standard electrolyte 0.2 M Cu(I), 0.04 M Cu(II)).	38
Figure 1.28.	J - V curves for DSCs utilizing $[\text{Cu}(\text{PDTO})]^{2+/1+}$ redox shuttle and TD Pt dark electrode (red), IO Pt dark electrode (blue), and in a three-electrode (blue), and in a three-electrode (as opposed to two electrode) set up (black). Dashed lines represent the maximum power points of the individual J - V curves.	41
Figure 1.29.	(a) PIA spectra and (b) TAS spectra of Y123 dye along with $[\text{Cu}(\text{dmp})_2]^{2+/1+}$, $[\text{Cu}(\text{dmby})_2]^{2+/1+}$, $[\text{Cu}(\text{tmby})_2]^{2+/1+}$ and inert electrolyte.	44
Figure 1.30.	Transient absorption spectra of D35 and XY1 sensitized photoanode at various ratio in presence of $[\text{Cu}(\text{tmby})_2]^{2+/1+}$.	45
Figure 1.31.	Lifetime as a function of electron Fermi level for DSC using Y123 sensitizer along with (a) $[\text{Cu}(\text{dmp})_2]^{2+/1+}$, $[\text{Cu}(\text{dmby})_2]^{2+/1+}$ and $[\text{Cu}(\text{tmby})_2]^{2+/1+}$ (b) $[\text{Cu}(\text{beto})_2]^{2+/1+}$, $[\text{Cu}(\text{beto}_{20\text{x}})_2]^{2+/1+}$ and $[\text{Cu}(\text{tmby})_2]^{2+/1+}$.	47
Figure 1.32.	(a) Charge transfer resistance at $\text{TiO}_2/\text{dye}/\text{electrolyte}$ interfaces for devices fabricated with dye Y123, WS-70 and WS-72 and (b) HY63 and HY64 employing $[\text{Cu}(\text{tmby})_2]^{2+/1+}$ electrolyte.	47
Figure 1.33.	J - V curves for D35, D35/XY1, and XY1 at 1 sun and 0.1 sun illumination and (b) IPCE spectrum, (c,d) current transient at 0.1 sun and 1 sun for DSC with D35, D35/XY1, and XY1 along with $[\text{Cu}(\text{tmby})_2]^{2+/1+}$, (e) J - V curves for D35/XY1 with TiO_2 thickness of 4	48

	μm and $8 \mu\text{m}$ and (f) current transient at 1 for D35/XY1 with TiO_2 thickness of $4 \mu\text{m}$ and $8 \mu\text{m}$.	
Figure 1.34.	Nyquist plot of symmetrical (PEDOT-PEDOT) dummy cells with (a) $[\text{Cu}(\text{dmp})_2]^{2+/1+}$ as electrolyte and (b) $[\text{Cu}(\text{tmby})_2]^{2+/1+}$ along with different bases.	50
Figure 1.35.	Schematic illustration of the three different DSC configurations evaluated in this work (a) surlyn cell, (b) epoxy- TiO_2 cell and (c) epoxy- $\text{TiO}_2/\text{ZrO}_2$ cell.	50
Figure 1.36.	Transient photocurrent measurements for the surlyn, epoxy- TiO_2 and epoxy- $\text{TiO}_2/\text{ZrO}_2$ cells.	50
Figure 1.37.	a) Cross section by SEM of a representative working electrode with copper based HTM after removal of the PEDOT coated FTO counter electrode b) PIA spectra of ssDSCs and DSCs with LEG4 employing $[\text{Cu}(\text{dmp})_2]^{2+/1+}$ based HTM or redox mediator.	51
Figure 1.38.	Molecular structures of a) $[\text{Cu}(\text{beto})_2]^{2+/1+}$, b) $[\text{Cu}(\text{beto}2\text{Ox})_2]^{2+/1+}$.	52
Figure 1.39.	Cross sectional image (left) of TiO_2 film sensitized by dye WS-72 infiltrated with $[\text{Cu}(\text{tmby})_2]^{2+/1+}$ based HTM. Element mapping (right) suggesting the dispersion of Cu (red) and Ti (green) elementary in the mesoporous TiO_2 film (a, globe image; b, top image; c, bottom image).	53
Figure 1.40.	(a) Cyclic voltammograms (b) Nyquist plots of electrochemical impedance spectra measured at 0 V from 100 kHz to 0.1 Hz. Red curve denotes pristine closed cell with liquid electrolyte solution; blue curve shows cell opened and the electrolyte solution freely evaporated for 1 day at room temperature and pressure via two filling holes; black curve shows 2 days of free evaporation and green shows the cell with partly evaporated solution was subjected to vacuum at room temperature.	54
Figure 1.41.	The predicted schemes of electron (hole) transport mechanism differences between the LE and HTM.	54
Figure 1.42.	(a) Device structure of new generation DCD and normal DSC (b) Type II junction alignment of the band edges for the mesoporous TiO_2 film and a p-type semiconductor layer.	55
Figure 1.43.	The absorption spectra of the Cu(II)/Cu(I) redox electrolyte in the cells with the separated and contacted electrodes. The thickness of the cell with the contacted electrodes is same as the thickness of the TiO_2 film ($\sim 7 \mu\text{m}$).	56
Figure 1.44.	J - V characteristics of DSCs with photoactive areas of 2.80 cm^2 and 20.25 cm^2 .	57
Figure 1.45.	J - V characteristics for XY1, L1 and XY1:L1 under 1000 Lux illumination.	59

Figure 1.46.	<i>J-V</i> characteristics for DSCs having photoactive area of 2.80 cm ² under 1000 lux, 500 lux and 200 lux illumination condition.	60
Figure 2.1.	(a) Current density versus potential (<i>J-V</i>) characteristic curves and (b) IPCE of I ⁻ /I ₃ ⁻ , [Co(bpy) ₃] ^{3+/2+} and [Cu(dmp) ₂] ^{2+/1+} electrolytes employed along with LEG4 dye measured under 100 mWcm ⁻² , AM 1.5G illumination	76
Figure 2.2.	Light intensity dependence on the short circuit current density for I ⁻ /I ₃ ⁻ , [Co(bpy) ₃] ^{3+/2+} and [Cu(dmp) ₂] ^{2+/1+} electrolytes.	79
Figure 2.3.	Current transients measured at AM 1.5G simulated light from 0.1 sun to 1 sun for (a) I ⁻ /I ₃ ⁻ (b) [Co(bpy) ₃] ^{3+/2+} and (c) [Cu(dmp) ₂] ^{2+/1+} (d) Regeneration Efficiency from 0.1 sun to 1 sun for I ⁻ /I ₃ ⁻ , [Co(bpy) ₃] ^{3+/2+} and [Cu(dmp) ₂] ^{2+/1+}	80
Figure 2.4.	(a) Nyquist plot (b) diffusion resistance (<i>R_d</i>) as a function of corrected potential and (c) equivalent circuit used to fit Nyquist plot.	82
Figure 2.5.	Light intensity dependence of the open-circuit voltage for I ⁻ /I ₃ ⁻ , [Co(bpy) ₃] ^{3+/2+} and [Cu(dmp) ₂] ^{2+/1+} electrolytes.	83
Figure 2.6.	(a) Chemical capacitance (<i>C_μ</i>) (b) recombination resistance (<i>R_{rec}</i>) and (c) electron lifetime (<i>τ_n</i>) and transport time (<i>τ_d</i>) as a function of corrected potential employing I ⁻ /I ₃ ⁻ , [Co(bpy) ₃] ^{3+/2+} and [Cu(dmp) ₂] ^{2+/1+} electrolytes.	84
Figure 2.7.	((a) Diffusion coefficient (<i>D_n</i>) and (b) diffusion length (<i>L_n</i>) as a function of corrected potential.	87
Figure 2.8.	(a) Lifetime (<i>τ_n</i>) and (b) Transport time (<i>τ_d</i>) as a function of light intensity.	88
Figure 3.1.	(a) Current density - voltage (<i>J-V</i>) and (b) Incident photon current conversion efficiency (IPCE) plot of DSCs fabricated with 20 nm and 30 nm TiO ₂ particles employing D35 sensitizer and [Cu(tmby) ₂] ^{2+/1+} redox mediator.	99
Figure 3.2.	Current density - voltage (<i>J-V</i>) of DSCs fabricated with 20 nm and 30 nm TiO ₂ particles employing D35 sensitizer and [Cu(tmby) ₂] ^{2+/1+} redox mediator under compact fluorescent light (CFL) light.	100
Figure 3.3.	Light-harvesting efficiency (<i>LHE</i>) of dye soaked TiO ₂ electrodes with 20 nm and 30 nm TiO ₂ particles as a function of wavelength. The thickness of TiO ₂ layer is 4 μm.	101
Figure 3.4.	<i>V_{oc}</i> as a function of extracted charge for DSCs with 20 nm and 30 nm TiO ₂ particles.	102

Figure 3.5.	Lifetime (τ_n) measurements using (a) Transient photovoltage decay and (b) Open circuit voltage decay (OCVD) for DSCs with 20 nm and 30 nm TiO ₂ particles.	103
Figure 3.6.	V_{oc} as a function light intensity for DSCs with 20 nm and 30 nm TiO ₂ particles.	103
Figure 3.7.	PIA spectra for DSCs with TiO ₂ electrodes with 20 nm and 30 nm TiO ₂ particles.	104
Figure 3.8.	(a) Light intensity dependence on J_{sc} for DSCs with 20 nm and 30 nm TiO ₂ particles and (b) Current transient plot measured at AM 1.5G simulated light for DSCs fabricated using 20 nm and 30 nm TiO ₂ particles.	105
Figure 3.9.	(a) Diffusion length (L_n) and (b) charge collection efficiency (η_{cc}) as a function of LED current for DSCs using 20 nm and 30 nm TiO ₂ particles.	106
Figure 3.10.	Transport time (τ_d) measurements using transient photocurrent decay for DSCs with 20 nm and 30 nm TiO ₂ particles.	107
Figure 4.1.	(a) Structure of D35 dye and [Cu(tmby) ₂] ^{2+/1+} redox mediator (b) energetics and (c) dye loading as a function of dye concentration on TiO ₂ films.	116
Figure 4.2.	(a) Current density–voltage (J – V) and (b) incident photon current conversion efficiency (IPCE) plot of DSCs fabricated with various D35 dye concentrations along with [Cu(tmby) ₂] ^{2+/1+} redox mediator.	117
Figure 4.3.	Solar cell characteristics of DSCs with D35 sensitizer and [Cu(tmby) ₂] ^{2+/1+} electrolyte (a) V_{oc} , (b) J_{sc} , (c) FF and (d) efficiency from 0.1 sun to 1 sun as a function of dye concentration (0.01 mM, 0.05 mM, 0.1 mM, 0.2 mM, and 0.3 mM).	118
Figure 4.4.	(a) Current density-voltage (J - V) and (b) power curve for DSCs fabricated with different D35 dye concentrations along with [Cu(tmby) ₂] ^{2+/1+} redox mediator under 1000 lux illumination.	119
Figure 4.5.	Current density as a function of light intensity for DSCs fabricated with various D35 dye concentrations using [Cu(tmby) ₂] ^{2+/1+} electrolyte.	120
Figure 4.6.	V_{oc} as a function of (a) Irradiance (mW/cm ²) under 1 sun irradiation(100 mW/cm ²), (b) illuminance (lux) under indoor light illuminations (c) ideality factor calculated as a function of D35 dye	122

concentration under solar and indoor CFL illumination and (d) dark current as a function of of D35 dye concentration.

Figure 4.7.	(a) Nyquist plot, (b) Bode plot and (c) equivalent circuit used for fitting the obtained Nyquist plot for DSCs with different D35 concentration employing $[\text{Cu}(\text{tmby})_2]^{2+/1+}$ electrolyte.	123
Figure 4.8.	(a) Chemical capacitance (C_μ), (b) lifetime (τ_n), (c) transport time (τ_d) and (d) charge collection efficiency (η_{cc}) as a function of V_F for DSCs with different dye concentrations using D35 sensitizer and $[\text{Cu}(\text{tmby})_2]^{2+/1+}$ electrolyte.	125
Figure 4.9.	(a) Injection and (b) regeneration plot measured using photo-induced absorption (PIA) spectroscopy for devices fabricated using D35 sensitizer and $[\text{Cu}(\text{tmby})_2]^{2+/1+}$ electrolyte under various dye concentrations.	127
Figure 5.1.	(a) Structures of D35, XY1 sensitizers (b) $[\text{Cu}(\text{tmby})_2]^{2+/1+}$ electrolyte and (c) energetics of the sensitizers and electrolyte used in the present study.	136
Figure 5.2.	(a) J - V characteristics under AM 1.5G one sun illumination (100 mW/cm^2) and (b) IPCE response with various LiI concentrations using devices fabricated using XY1 sensitizer and $[\text{Cu}(\text{tmby})_2]^{2+/1+}$ electrolyte.	138
Figure 5.3.	Trend in (a) V_{oc} (b) J_{sc} (c) FF and (d) η as a function of LiI concentration under 1 sun and 0.1 sun illumination (100 mW/cm^2 and 10 mW/cm^2) using DSCs fabricated using XY1 sensitizer and $[\text{Cu}(\text{tmby})_2]^{2+/1+}$ electrolyte.	141
Figure 5.4.	(a) J_{sc} as function of light intensity and (b) current transient measurements of DSCs with various concentrations of LiI using XY1 dye and $[\text{Cu}(\text{tmby})_2]^{2+/1+}$ electrolyte.	142
Figure 5.5.	(a) Nyquist plot of CE-CE dummy cells at various LiI concentration, (b) equivalent circuit used for fitting Nyquist plot and (c) Equivalent charge transfer resistance as a function of LiI concentrations.	143
Figure 5.6.	(a) Extracted charge as function Fermi voltage (V_F) measured using charge extraction (b) Lifetime as function of voltage measured using OCVD at various LiI concentration in devices fabricated using XY1 dye and $[\text{Cu}(\text{tmby})_2]^{2+/1+}$ electrolyte.	144
Figure 5.7.	J - V characteristics measured under 1000 lux LED illumination for DSCs fabricated using XY1 dye and $[\text{Cu}(\text{tmby})_2]^{2+/1+}$ electrolyte with different LiI concentrations.	145

Figure 5.8.	(a) J-V characteristics of DSCs under LED illumination using XY1 dye along with $[\text{Cu}(\text{tmby})_2]^{2+/1+}$ containing 0.1 M LiTFSI, (b) extracted charge as a function of V_F and (c) lifetime as a function of voltage for DSCs using $[\text{Cu}(\text{tmby})_2]^{2+/1+}$ containing 0.1 M LiTFSI and 0.1 M LiI.	147
Figure 5.9.	J-V characteristics of DSCs with (a)D35, (b) XY1 and (c) D35+XY1 sensitizers with $[\text{Cu}(\text{tmby})_2]^{2+/1+}$ containing 0.3 M LiI under LED illumination.	148
Figure 5.10.	(a) Error plot for V_{oc} , J_{sc} , FF and η evaluated by measuring 14 DSCs under 1000 lux LED illumination and (b) stability test under 1000 lux LED illumination upto 700 hours for DSCs fabricated using co-sensitized (D35+XY1) dyes and $[\text{Cu}(\text{tmby})_2]^{2+/1+}$ electrolyte.	150
Figure 5.11.	(a) I-V characteristics and (b) P-V plot for DSC masterplates with an active area of 1.92 cm ² under LED illumination using co-sensitized (D35+XY1) dyes and $[\text{Cu}(\text{tmby})_2]^{2+/1+}$ electrolyte.	151

List of Tables

Table 1.1.	<i>PV</i> parameters of DSCs based on TiO ₂ film with particle of 20 nm and 30 nm employing L156 and L224 with [Cu(tmby)] ^{2+/1+} redox couple.	25
Table 1.2.	<i>PV</i> performance of DSC employing [Cu(tmby) ₂] ^{2+/1+} , [Cu(dmby) ₂] ^{2+/1+} and [Cu(dmp) ₂] ^{2+/1+} electrolytes with Y123.	33
Table 1.3.	<i>J-V</i> parameters of the [Cu(mpdt) ₂] ^{2+/1+} at different concentrations.	39
Table 1.4.	<i>PV</i> characteristics studied using Cu-mediated DSCs with different bases and Y123 as sensitizer under 1 sun (AM1.5G) condition.	40
Table 1.5.	EIS parameters of symmetrical PEDOT/PEDOT cell and Pt/Pt cells filled with either 1/2 or 3/4 redox shuttle.	41
Table 1.6.	<i>PV</i> parameter of DSCs using PEDOT and Pt counter electrodes.	42
Table 1.7.	<i>PV</i> parameters of DSC using D35 dye and [Cu(tmby) ₂] ^{2+/1+} electrolyte with different counter electrodes.	42
Table 1.8.	Regeneration times and efficiencies for Y123-sensitized photo-anodes in inert and Cu(oxabpy) electrolyte, by addition of Cu ^{II} into the electrolyte.	45
Table 1.9.	<i>PV</i> parameters derived from <i>J-V</i> measurements of LEG4 sensitized ssDSCs and DSCs using [Cu(dmp) ₂] ^{2+/1+} based HTM or redox mediator.	52
Table 1.10.	The photovoltaic parameters of Y123 cells with the contacted and separated electrodes tested under light projection onto either the front TiO ₂ electrode or the back PEDOT electrode. The cells employ ~200 nm thick PEDOT layer counter electrode and ~4.5 μm thick nanocrystalline mesoscopic TiO ₂ film without light scattering layer. With further optimization of TiO ₂ thickness the efficiency of DCDs with Y123 dye reached up to 11%. Co-sensitization of Y123 with XY1 again pushed the efficiency of DCD to 13.6% under one sun illumination and 32% under indoor light conditions (1000 lux).	56
Table 1.11.	Photovoltaic metrics for DSCs and GaAs solar cells for indoor-light sources at 200 lux and 1,000 lux.	57
Table 1.12.	<i>J-V</i> parameters with photoactive areas of 2.80 cm ² and 20.25 cm ² .	58
Table 1.13.	<i>J-V</i> parameters at different indoor intensity for XY1, L1 and XY1:L1	59
Table 1.14.	<i>PV</i> parameters of the DSC based on MS5+XY1b (active area of 2.80 cm ²) under different illumination intensities (Osram 930 Warm White fluorescent light).	60
Table 2.1.	Tabulated current-voltage characteristics of I ⁻ /I ₃ ⁻ , [Co(bpy) ₃] ^{3+/2+} and [Cu(dmp) ₂] ^{2+/1+} electrolyte with LEG4 dye measured under 100 mWcm ⁻² , AM 1.5G illumination. ^a ΔG ⁰ =E ⁰ _{dye} -E ⁰ _{redox} .	77

Table 3.1.	<i>J-V</i> parameters of DSCs fabricated using 20 nm and 30 nm TiO ₂ particles using D35 sensitizer and [Cu(tmby) ₂] ^{2+/1+} electrolyte.	99
Table 3.2.	Indoor photovoltaic parameter of DSCs fabricated with 20 nm and 30 nm TiO ₂ particles employing D35 sensitizer and [Cu(tmby) ₂] ^{2+/1+} redox mediator under CFL light.	100
Table 4.1.	Photovoltaic parameters of DSCs fabricated with various D35 dye concentrations along with [Cu(tmby) ₂] ^{2+/1+} redox mediator.	117
Table 4.2.	Photovoltaic parameters of DSCs fabricated with different D35 dye concentrations and [Cu(tmby) ₂] ^{2+/1+} electrolyte under 1000 lux illumination.	119
Table 5.1.	Photovoltaic parameters of DSCs fabricated using XY1 sensitizer and [Cu(tmby) ₂] ^{2+/1+} electrolyte having different LiI concentrations.	139
Table 5.2.	Photovoltaic parameters of DSCs fabricated using XY1 dye and [Cu(tmby) ₂] ^{2+/1+} electrolyte under 1000 lux LED illumination using various concentrations of LiI.	145
Table 5.3.	Photovoltaic parameters of DSCs fabricated with XY1 dye along with [Cu(tmby) ₂] ^{2+/1+} containing 0.1 M LiTFSI and 0.1M LiI under 1000 lux LED illumination (303 μW/cm ²).	147
Table 5.4.	Indoor photovoltaic parameters of DSCs with D35, XY1 and co-sensitized D35+XY1 dye combinations with [Cu(tmby) ₂] ^{2+/1+} electrolyte containing 0.3 M LiI under LED illumination of variable intensities (1000 lux, 700 lux, 500 lux, 200 lux)	149
Table 5.5.	Indoor photovoltaic parameters of large area (active area 1.92 cm ²) DSC masterplate with cosensitized D35+XY1 dyes under LED illumination of different intensities using [Cu(tmby) ₂] ^{2+/1+} electrolyte containing 0.3 M LiI.	151

List of Abbreviations

A	Ampere
A	Area (cm ²)
Å	Angstrom
AC	Alternating current
ACN	Acetonitrile
AFM	Atomic force microscopy
Ag	Silver
Al	Aluminium
Al ₂ O ₃	Aluminium oxide
ALD	Atomic layer deposition
AM 1.5G	Air mass 1.5 global
Au	Gold
BIPV	Building integrated photovoltaics
CB	Conduction band
CE	Charge extraction
CdSe	Cadmium selenide
CdTe	Cadmium telluride
Co	Cobalt
[Co(bpy) ₃] ^{3+/2+}	Cobalt (III/II) tris(2,2'-bipyridyl)
CT	Charge transport
Cu	Copper
[Cu(dmp) ₂] ^{2+/1}	bis-(2,9-dimethyl-1,10-phenanthroline) copper
[Cu(tmby) ₂] ^{2+/1}	bis-(4,4',6,6'-tetramethyl-2,2'-bipyridine) copper
CV	Cyclic Voltammetry
CVD	Chemical vapour deposition
D-π-A	Donor-π-acceptor
D35	(E)-3-(5-(4-(bis(2',4'-dibutoxy-[1,1'-biphenyl]-4-yl)amino)phenyl)thiophen-2-yl)-2-cyanoacrylic acid
D _n	Diffusion coefficient

DC	Direct current
DFT	Density functional theory
DLS	Dynamic light scattering
DSC	Dye-sensitized solar cell
e	Electron charge
E_A	Activation energy
E_F	Fermi level
E_g	Energy band gap
EIS	Electrochemical impedance spectroscopy
EQE	External quantum efficiency
FF	Fill factor
FTO	Fluorine doped tin oxide
G	Generation rate
Ga	Gallium
GaAs	Gallium arsenide
h	Plank's constant
H ₂ O	Water
HOMO	Highest occupied molecular orbital
HRTEM	High resolution transmission electron microscope
I	Current
I^-/I_3^-	Iodide/triiodide
I_d	Dark current
IMPS	Intensity modulated photocurrent decay
IMVS	Intensity modulated photovoltage decay
InAlGa _{1-x-y} N	Indium aluminium gallium nitride
InGa _{1-x} N	Indium gallium nitride
InN	Indium nitride
IoT	Internet of things
IPA	Isopropyl alcohol
IPCE	Incident photon to current conversion efficiency

I_{ph}	Photocurrent
IR	Infrared
J_d	Dark current density
J_{sc}	short-circuit current density
J - V	Current density vs. voltage
K_B	Boltzmann constant
LED	Light emitting diode
L	Semiconductor thickness
LEG4	3-{6-{4-[bis(2',4'-dibutyloxybiphenyl-4-yl)amino-]phenyl}-4,4-dihexyl-cyclopenta-[2,1-b:3,4-b']dithiophene-2-yl}-2-cyanoacrylic acid
L_n	Diffusion length
Li	Lithium
LUMO	Lowest unoccupied molecular orbital
MPP	Maximum power point
MS5	N-(2',4'-bis(dodecyloxy)-[1,1'-biphenyl]-4-yl)-2',4'-bis(dodecyloxy)-N-phenyl-[1,1'-biphenyl]-4-amine-4-(benzo[c][1,2,5]thiadiazol-4-yl)benzoic acid
n	Ideality factor
N	Nitrogen
NHE	Normal hydrogen electrode
OCVD	Open circuit voltage decay
PCE	Power conversion efficiency
PEDOT	Poly(3,4-ethylenedioxythiophene)
P_{in}	Input power
Pt	Platinum
PV	Photovoltaic
q	Elemental charge
QDs	Quantum dots
SEM	Scanning electron microscope
SHE	Standard hydrogen electrode
Si	Silicon

SnO ₂	Tin (IV) oxide
ssDSC	Solid-state dye-sensitized solar cell
T	Temperature
t	Time
tbp	Tert-butyl pyridine
TCO	Transparent conducting oxide
TiCl ₄	Titanium (IV) chloride
TiO ₂	Titanium dioxide
UV	Ultraviolet
V	Bias voltage
VB	Valance band
V_{app}	Applied voltage
V_F	Fermi voltage
V_{oc}	open-circuit voltage
XRD	X-ray diffraction
XY1	(E)-3-(4-(6-(7-(4-(bis(2',4'-bis((2-ethylhexyl)oxy)-[1,1'-biphenyl]-4-yl)amino) phenyl)benzo[c][1,2,5]thiadiazol-4-yl)-4,4-bis(2-ethylhexyl)-4H-cyclopenta[2,1-b:3,4-b']dithiophen-2-yl)phenyl)-2-cyanoacrylic acid
XY1b	(E)-3-(4-(6-(7-(4-(bis(2',4'-dibutoxy-[1,1'-biphenyl]-4-yl)amino)phenyl)benzo[c][1,2,5]thiadiazol-4-yl)-4,4-bis(2-ethylhexyl)-4H-cyclopenta[2,1-b:3,4-b']dithiophen-2-yl)phenyl)-2-cyanoacrylic acid
Zn	Zinc
ZnO	Zinc oxide
ε	Molar extinction coefficient
η	Power conversion efficiency
η_{CC}	Charge collection efficiency
η_{INJ}	Injection efficiency
η_{LHE}	Light harvesting efficiency
η_{REG}	Regeneration efficiency
τ_n	Lifetime

τ_t	Transport time
C_μ	Chemical capacitance
R_{rec}	Recombination resistance
α	Absorption coefficient, power constant
λ	Wavelength
ν	Frequency

Preface

The use of earth abundant copper (Cu) metal complexes in dye-sensitized solar cells (DSCs) has recently rejuvenated the area of molecular photovoltaic devices. Due to the small reorganization energy between Cu (I) and Cu (II), even a driving force of merely 0.1 V is sufficient enough for realizing unit dye regeneration employing Cu electrolytes. Cu electrolytes, opening up new avenues and opportunities towards achieving higher power conversion efficiency among the present generation of mesoscopic light harvesters, for indoor/ambient photovoltaic (IPV) application. With minimum voltage loss, Cu electrolyte based DSCs possesses the potential to achieve notable photovoltages above 1 V from single junction devices under both full sun and indoor/artificial lighting conditions. The very positive redox potential of Cu redox mediators promotes charge recombination at semiconductor/electrolyte interface which negatively affects V_{oc} and FF leading to lower power conversion efficiency. Yet again Cu redox mediators possess other issues such as slower ion diffusion, additive co-ordination and charge transfer issues at the counter electrode. Hence our motivation is to understand the interfacial charge transfer dynamics at various interfaces in DSC employing new generation alternative Cu redox mediator and to engineer the devices further to improve the power conversion efficiency particularly for indoor photovoltaic applications.

The thesis is organized into five chapters. Chapter 1 provides a brief introduction of Cu electrolyte-based dye-sensitized solar cells (DSCs) and indoor photovoltaic. Chapter-2 renders a detailed comparison between DSC fabricated using classical iodide/triiodide (I/I_3^-), alternative cobalt $\{[Co(bpy)_3]^{3+/2+}\}$ and new generation copper $\{[Cu(dmp)_2]^{2+/1+}\}$ redox mediators. For a direct comparison we used organic dye LEG4 and PEDOT counter electrode for all the devices with the three different redox mediators. Chapter 3 deals with the comprehensive interfacial analysis of Cu electrolyte based DSCs with TiO_2 working electrodes consisting of different particle size. Organic dye D35 and $Cu[(tmby)_2]^{2+/1+}$ redox mediator was used as the sensitizer and electrolyte for the fabrication of DSCs. Fabrication of efficient Cu-based DSCs requires an entirely new set of innovative materials and optimized device architectures. One such critical device engineering involves the uses of mesoporous titanium dioxide with particle size of 30 nm, however in standard DSC titanium dioxide particle size of 20 nm is used. We investigated DSCs with working electrode consist TiO_2 active layer of particle size of 20 nm and 30 nm respectively. To gain an in-depth understanding of interfacial

charge transfer dynamics of devices, we used various electrical and optical perturbation tools. Chapter 4 deals with the investigation of charge recombination as function of dye concentration in Cu electrolyte-based DSCs. Dyes are used as light harvesters in DSCs which are primarily responsible for current generation. However, the other aspect of dyes to prevent recombination leading to improvement in voltage are not been explored much. Herein, we study the role of dye in preventing recombination at $\text{TiO}_2/\text{dye}/\text{electrolyte}$ interface in Cu electrolyte-based DSC. Chapter 5 deals with the electrolyte additive engineering to improve the power conversion efficiency particularly under indoor light conditions using Cu electrolyte-based DSCs. We introduced a new additive LiI in $[\text{Cu}(\text{tmb})_2]^{2+/1+}$ electrolyte to improve the indoor photovoltaic performance.

Introduction to Copper Electrolyte based Dye-sensitized Solar Cells and Indoor Photovoltaics

1.1. Abstract

Recently, the use of earth abundant copper (Cu) metal complexes as potential electrolytes in dye-sensitized solar cells (DSCs) has rejuvenated this area of molecular photovoltaic devices. Being a metal complex, polypyridyl Cu metal complexes allows fine tuning of the redox potential by judicious substitution of peripheral ligands. The low cost and low toxicity of these earth abundant molecules takes DSCs one step closer to commercialization. Due to the small reorganization energy between Cu (I) and Cu (II), even a driving force of merely 0.1 V is sufficient enough for realizing unit dye regeneration employing Cu electrolytes. With minimum voltage loss, Cu electrolyte based DSCs possesses the potential to achieve notable photovoltages above 1 V from single junction devices under both full sun and indoor/artificial lighting conditions. Being inert to silver and other electrical contacts and with comparatively less mass transport issues, Cu finds a very unique place in spearheading the commercialization of DSCs for indoor photovoltaic (IPV) applications. Copper redox shuttle has emerged as a promising electrolyte for indoor DSCs with a record power conversion efficiency of 34.5% under 1000 lux CFL illumination. With its higher mobility in solid state, Cu electrolyte also offers the possibility to explore new innovative device engineering concepts with DSCs which were not possible so far employing conventional iodide/triiodide and other alternate electrolytes. Zombie DSCs, a new technique to fabricate solid state dye cells contributed to the highest efficiency so far reported among ssDSCs (11.7 %). It's to be noted that Zombie DSCs were only made possible with the introduction of Cu electrolyte. Recently Gratzel and co-workers introduced the ground breaking direct contact devices using copper electrolytes which reduces the technical difficulties in fabrication of DSCs along with reduction in fabrication cost, achieving efficiencies up to 15.2% in one sun illumination and >30% under indoor/artificial light. All these new developments in the area of DSCs were only made possible with the emergence of new generation of copper redox mediators

1.2. Introduction

Clean and affordable energy for all is a prerequisite for achieving global economic development and poverty mitigation. Meeting the energy needs of each and every individual is essential for global development. Presently, this is primarily met from fossil fuels (coal, oil and gas). However, fossil fuels have limited source that will deplete over time. It is estimated that in the next 50 to 60 years the oil and natural gas reserves will severely get exhausted if the extraction rate continues to remain in the same pace as of now.¹² Moreover, burning fossil fuels has serious environmental impacts. It produces carbon dioxide (CO₂) and other greenhouse gas which fundamentally lead to global warming and other climate change related environmental issues. The permanent solution to address the atrocities resulting from the use of fossil fuels is to transform ourselves more to depending on renewable energy sources which is inexorable for our sustainability. Out of all the available renewable energy sources, solar energy occupies the most prominent position. All total of 1.73×10^5 TW of solar energy strikes the earth surface, out of which 600 TW are practically harvestable.³⁻⁵ Even if 5% of this incident solar energy is harvested, the energy crisis can completely be eradicated.

According to the forecasts from analysts, we will be surrounded by around 75 billion IoT devices by 2025 which will reach to almost a trillion devices in the following years.^{6,7} Supplying power to these smart nodes with battery is not a viable option due to the practical difficulty in frequently changing them, where valuable data can be lost in between. Over and above, the serious environmental impact resulting from used batteries is a major concern which needs to be addressed to realize a low carbon economy. Moreover, miniature molecular photovoltaic light harvesters using DSCs proved to be best source, thus making the IoT device self-powered for future.

1.3. Photovoltaics

Photovoltaics is the direct conversion of light into electricity. It relies on photovoltaic effect. Photovoltaic effect can be defined as generation of voltage in a material upon exposure of light. Photovoltaic effect was first demonstrated by a French physicist, Edmund Becquerel, in 1839, who found that certain materials would produce small amounts of electric current when exposed to light.⁸ Photovoltaic cell consists of p-type and n-type semiconductor layers. Semiconductor layer absorbs light and creates electron-hole

pairs which are further separated and collected through electrodes to generate electricity. The photovoltaic cell which efficiently harvest electricity from sun light are called solar cells or solar photovoltaic cells. Similarly, photovoltaic cell that harvest electricity from artificial light are called indoor photovoltaic cell.

1.3.1 Solar Photovoltaic Cell

Solar photovoltaic cells work very efficiently under solar light irradiation. As seen in **Figure 1. 1** solar radiation ranges from 300 nm to 2500 nm. Thus a narrow band semiconductor with band gap of ~ 1 eV is required to absorb such wide spectrum of light. Air Mass 1.5 Global (AM1.5 G) spectrum is considered as standard solar spectrum and has integrated power of 100 mWcm^{-2} . Air mass coefficient defines direct optical path through earth atmosphere. It helps to estimate the spectrum of light available after passing through the earth's atmosphere. Moreover, solar photovoltaic cells are designed to absorb such intense light.

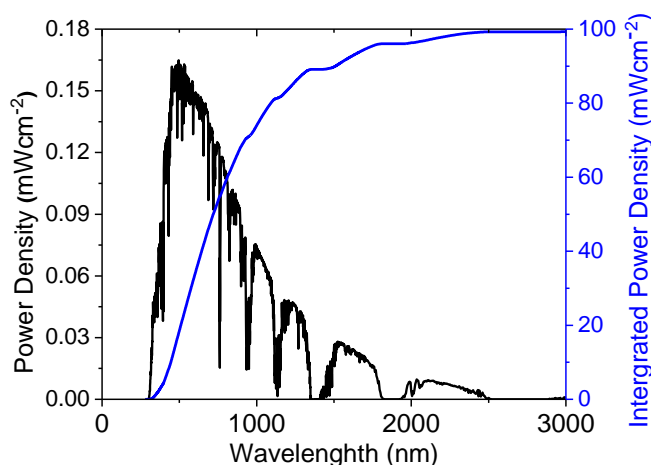


Figure 1. 1 Spectrum of AM 1.5 G solar spectrum

1.3.2 Indoor Photovoltaic Cell

Indoor photovoltaic cells work very efficiently under indoor light. Unlike solar spectrum indoor light spectrums lies only in visible region and is less intense compared to solar spectrum. Inside a room 200 lux to 1000 lux radiation is generally used for clear visibility. Thus, 200 lux to 1000 lux illumination is used for indoor PV measurement, though indoor light spectrum is not yet globally standardized. **Figure 1. 2** shows an emission spectra of commonly used LED and CFL light at standard 1000 lux. The integrated power of 1000 lux illumination from artificial light source is around $300 \mu\text{Wcm}^{-2}$. The absorption profile

of semiconductor material must overlap with the emission spectra of artificial light sources to absorb light efficiently under indoor light conditions.⁹⁻¹¹ The major difference between the solar photovoltaics and indoor photovoltaics owes from the type of semiconductor used.¹² Conceptually narrow band semiconductor is required for solar photovoltaic cell while wide band gap semiconductor works better in indoor photovoltaics cell.

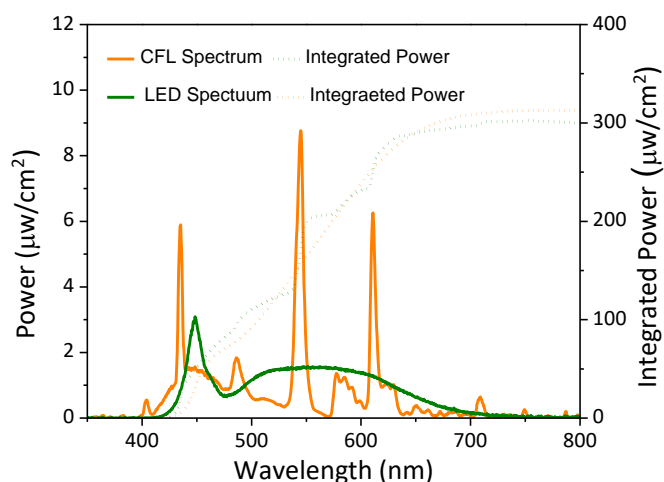


Figure 1. 2 Emission spectra of CFL and LED light at 1000 lux.

1.4.Generation of Photovoltaic Cells

Solar cells are classified into three generations according to the material, method and technology used for the fabrication. The three generations are described below.

1.4.1. First Generation Photovoltaic Cells

First generation of photovoltaic cells are the most common solar cells available in market. It is a wafer based technology and are made up of mono crystalline and poly crystalline silicon. Mono-crystalline and poly-crystalline silicon are indirect bandgap material, thus for efficient light absorption thicker film is essential. Therefore, the thickness of Si wafer is around 200 µm. Moreover, first generation photovoltaics works very efficiently under solar radiation with power conversion efficiency ranging from 25% to 30%.¹³ However, they are not efficient under indoor light illumination.¹⁴ These solar cells are highly stable with a lifetime of up to 25 years. Further, they are less toxic with wide availability of material. The major drawback of these photovoltaic cells are high cost. High cost comes from the use of highly pure Si and expensive methods involves to deposit Si on substrates. These cells are very brittle and hence needs perfect encapsulation which makes

them heavyweight. The heavy weight not only increases its cost but also limits their application.

1.4.2. Second Generation Photovoltaic Cells

Second generation photovoltaic technology rely on thin film technology. The thickness of semiconductor varies from a few nanometers (nm) to tens of micrometers (μm). Unlike, 1st generation photovoltaic cells, 2nd generation solar cells uses direct bandgap semiconductors, which enables them to absorb optimum light even at very thin film. Being a thin film, 2nd generation solar cells are flexible and light weight which opens a variety of new application. Key players in this generation includes Cadmium Telluride (CdTe), Copper Indium Selenide (CIS), Copper Indium Gallium Diselenide (CIGS), etc. Thin-film technology has always been cheaper but less efficient than conventional c-Si technology.¹⁵ The drawback of this technology is the use of rare and toxic materials in device fabrication that possess environmental risks. Moreover, these photovoltaic cells are less efficient under indoor light illumination.

1.4.3. Third Generation Photovoltaic Cells

This mainly includes the emerging molecular photovoltaic technology. These are cost effective alternative photovoltaic cells. The thickness of light absorbing material ranges from nanometer or micrometer scale. Dye Sensitized Solar Cells (DSCs), Perovskite Solar Cells(PSCs), Organic Photovoltaic technology (OPVs), and Quantum Dot solar cells comes under the third generation photovoltaic technology. The materials used here are low-cost and the device fabrication involves simple solution processing which makes the photovoltaic technology very economical. These photovoltaic cells can be made light transparent, color tunable, light weight, and flexible, which offers wide applicability. Most importantly, these cells are highly efficient under indoor/artificial light conditions. Third generation photovoltaic technology has reached to PCE of >25% under sun light and 40% under indoor/artificial light conditions.¹⁶⁻¹⁹ Moreover, outdoor stability is still a matter of concern for these photovoltaic cells.²⁰⁻²²

1.5. Dye-Sensitized Solar Cells (DSCs)

1.5.1. Device Structure and Working Principle of DSCs

The device structure of DSC is very simple. Generally, fluorine doped tin oxide (FTO) coated glass is used as substrate for working electrode and counter electrode. A monolayer of dye over TiO_2 serves as photoanode while a thin catalyst layer deposited over FTO coated glass works as counter electrode. Working electrode and counter electrode are separated by a spacer and the space is filled with a redox mediator. **Figure 1.3** depicts the structure and various forward and backward charge transfer process taking place in conventional DSCs. As apparent in **Figure 1.3**, DSC goes through complicated electron transport and ion transport to convert light to electricity. The forward charge transfer are favorable while backward charge transfer process pulls down the performance. The charge transfer process are sequentially explained in following steps, where step 1 to 5 are forward charge transfer processes and step 6 to 8 are backward charge transfer processes.

- 1) *Light absorption* -Dye molecules absorbs light and electron gets excited from HOMO to LUMO.
- 2) *Electron injection* -Owing to favorable energetics, electrons in LUMO of the dye molecules gets injected to conduction band (CB) of TiO_2
- 3) *Electron diffusion*- The injected electrons diffuses in TiO_2 with multiple trapping and detrapping.
- 4) *Dye regeneration*- The oxidized dye molecules are regenerated by the reduced species present in the redox electrolyte.
- 5) *Ion diffusion*- The oxidized species present in electrolyte diffuses towards the counter electrode to get reduced. Further the reduced redox species diffuse towards oxidized dye to regenerate it and the cycle get completed.
- 6) *Dye relaxation*- Electron from the LUMO of the dye losses energy and moves to the ground state, HOMO.
- 7) *Recombination at TiO_2 /dye interface*-The electrons in CB of TiO_2 recombines with the holes present in HOMO of the dye molecules, after its excitation.
- 8) *Recombination at TiO_2 /electrolyte interface*- The electrons in CB of TiO_2 recombines with the oxidized species present in the redox mediator.

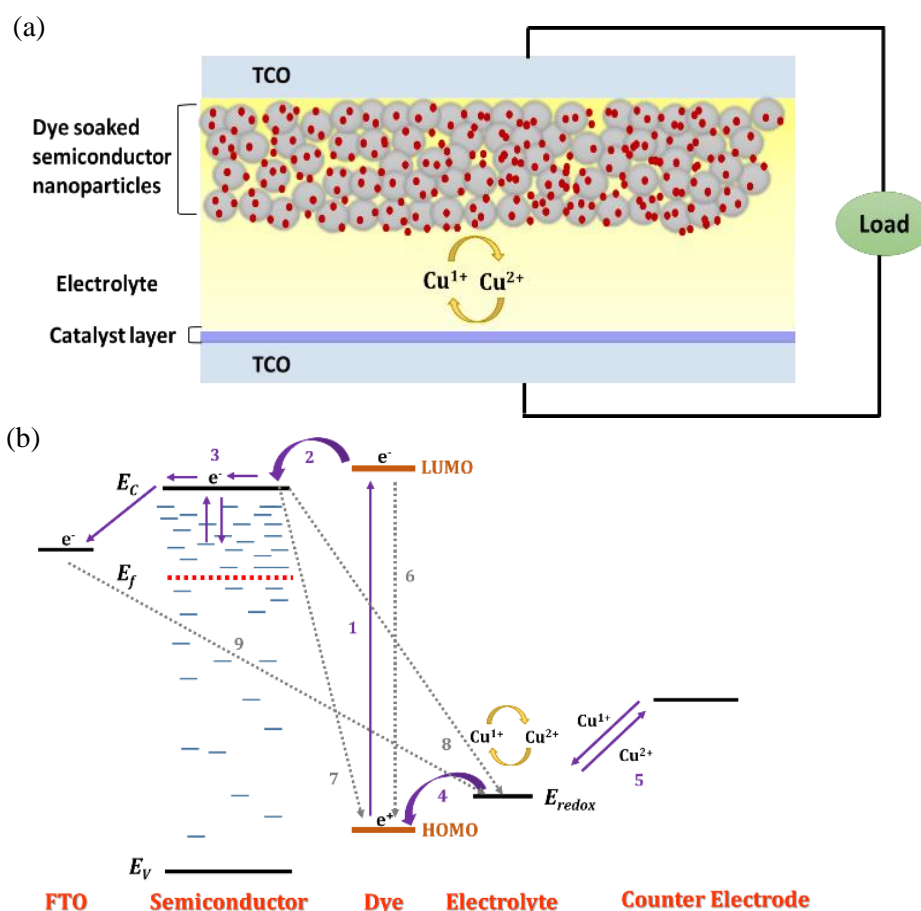


Figure 1.3 (a) Structure of DSC and (b) Energetics and kinetics of DSC

1.5.2. Fabrication of DSCs

The preparation of working electrodes start with cleaning of substrates (FTO coated glass) in detergent, deionized water, acetone and isopropyl alcohol, respectively using an ultrasonic bath. The dried substrates are annealed to 500 °C. A thin blocking layer is coated through dipping of electrodes for 30 min in 40 or 53 mM TiCl_4 solution at 75 °C followed by rinsing with deionized water and ethanol, and further annealed to 500 °C. Mesoporous TiO_2 is coated with doctor-blading or screen-printing technique with TiO_2 paste having different particle size and annealed at ramping temperature of 325 °C for 15 min, 375 °C for 15 min, 450 °C for 15 min and 500 °C for 30 min. Post-blocking layer is deposited over TiO_2 by following the same procedure used for depositing pre-blocking. Finally, the electrodes are soaked in dye solution for efficient dye loading.

The preparation of counter electrodes starts with hole drilling followed by cleaning of substrates (FTO coated glass) in detergent, deionized water, acetone and isopropyl alcohol, respectively using an ultrasonic bath. The dried substrates are annealed to 500 °C. Further, substrates are undergone UV ozone cleaning and suitable catalyst layer is deposited on the substrate.

The working electrodes are assembled with counter electrodes using spacer like polymer and epoxy. Finally, electrolyte is filled through the pre-drilled holes. Further, holes are sealed with cover glasses.

1.6. Device Characterization Techniques

1.6.1. Current Density–Voltage (J - V) Measurement

Current density-voltage (J - V) measurement is the most basic measurement carried out on a photovoltaic cell. For J - V measurement, the photovoltaic cell is kept under light irradiation and voltage is applied across the device using a voltage source and the light generated current is measured with a measuring unit. For solar photovoltaic measurement solar simulator is used while for indoor light measurement artificial light sources like CFL/LED are used. For one sun measurement Newport AAA solar simulator along with Kiethley source meter is used. The intensity of light was measured using certified Si solar cell. For indoor photovoltaic measurements, custom developed indoor light simulator was used (**Figure 1. 4**). The indoor light set up consists of various indoor light sources, Dyanamo potentiostat (DN-AE05), lux meter and a black box. Inside the black box IPV measurements are carried out. Under the roof of the black box, nine holders are placed at equidistance to mount desired indoor light sources. The device under measurement is kept in a movable platform. Between the platform and light mount a diffuser is placed to maintain the uniformity of light with better precision. The platform can be moved with minimum 1 mm per step while it can move at maximum 30 mm per step. The speed of the platform is controlled with HMI (Human-Machine Interface) at the front side of the black box. By moving the platform, the desired intensity is obtained. Illuminance in lux was measured using lux meter and the intensity in μWcm^{-2} was measured using Ocean optics Jaz spectrometer (WW-83500-20) and further cross verified using Dyanamo highly sensitive irradiance measuring unit (DN-AE06).

From current density-voltage measurement the fundamental parameters such as open circuit voltage (V_{oc}), short circuit current density (J_{sc}), maximum voltage (V_{max}) and

maximum current density (J_{max}) are obtained while other parameter such as fill factor and power conversion efficiency are calculated from the fundamental parameters.

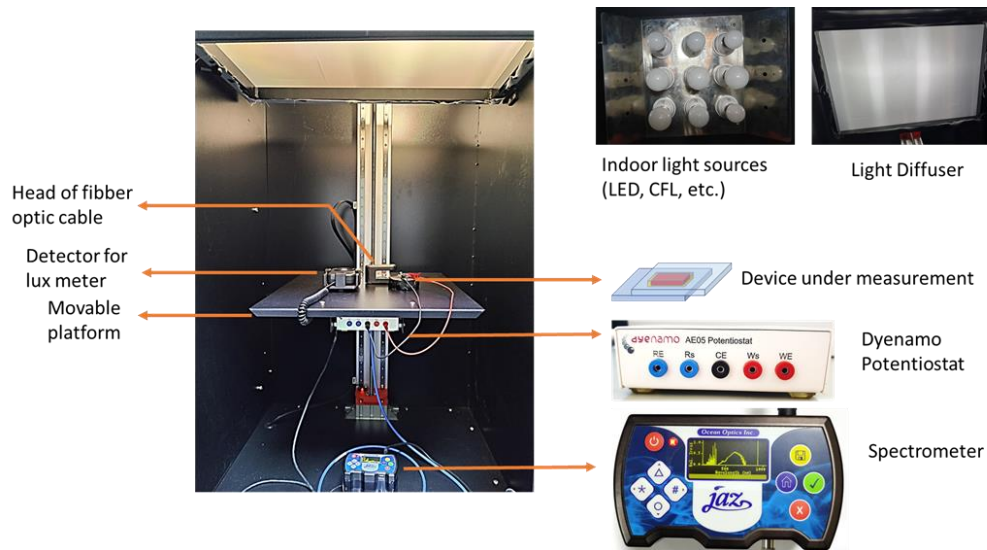


Figure 1. 4 Homemade indoor light simulator

Figure 1. 5 (a) shows typical J - V and P - V characteristics of DSC. As apparent in **Figure 1. 5 (b)** at open circuit, all the injected electrons accumulate at the CB of TiO_2 as there is no path for electron transport while few of them recombine at $\text{TiO}_2/\text{electrolyte}$ interface. At this state, energy difference between the fermi level of TiO_2 and redox potential of electrolyte gives the V_{oc} . As the DSC is short circuited (**Figure 1. 5 (c)**), electrons diffuse in TiO_2 and comes out of the device as it is the minimum resistance path available for electron transport. Here, Fermi level of TiO_2 lies at the similar energy level of redox mediator leading to zero voltage and maximum possible current density (J_{sc}). Under operating condition (i.e. DSC is connected to load, **Figure 1. 5 (d)**) both electron diffusion and recombination simultaneously occurs. Thus at this state both voltage and current density is obtained which is less than V_{oc} and J_{sc} respectively. The obtained voltage is V_{max} and current density is J_{max} . Fill factor (FF) defines the quality of device. It is the maximum power that can be extracted from DSC. It is calculated by the equation,

$$FF = \frac{V_{max} J_{max}}{V_{oc} J_{sc}} \quad (1)$$

Moreover, power conversion efficiency (η) is given by the equation,

$$\eta = \frac{P_{\text{out}}}{P_{\text{in}}} = \frac{FF V_{\text{oc}} J_{\text{sc}}}{P_{\text{in}}} \quad (2)$$

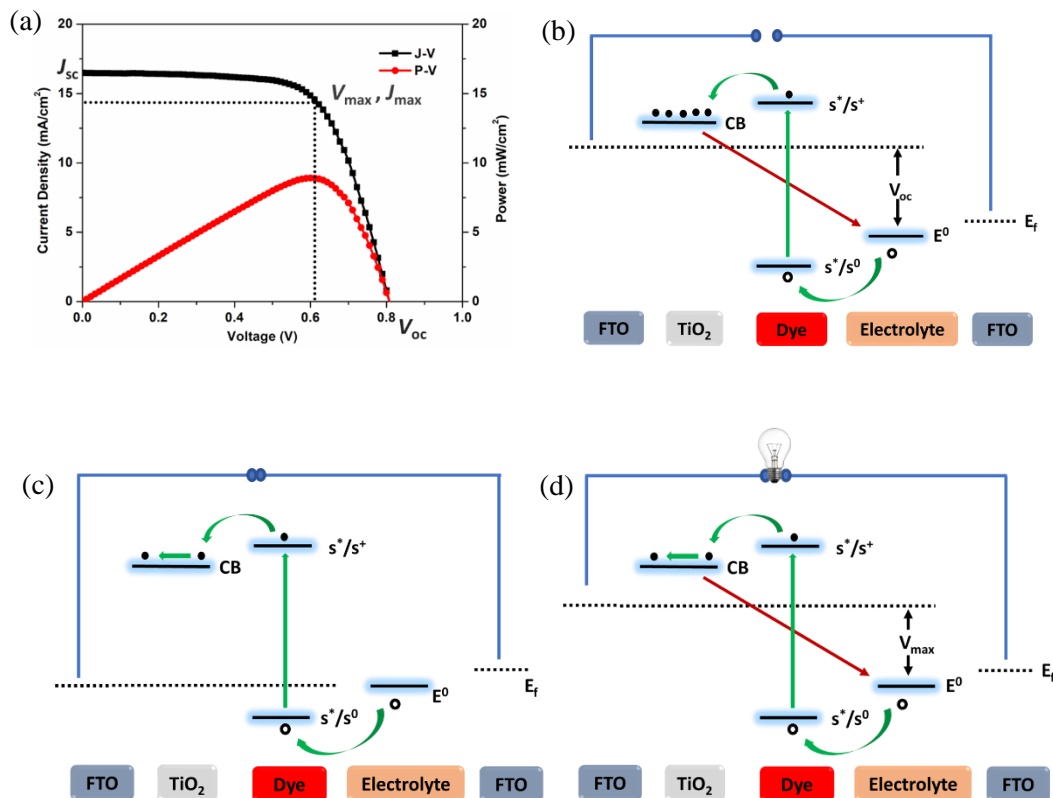


Figure 1. 5 (a) J - V characteristics of typical DSC, Energetics and kinetics of DSC under (b) open circuit (c) short circuit and (d) working condition.

1.6.2. Incident Photon-to-Current Conversion Efficiency (IPCE)

IPCE is the spectral response of a photovoltaic cell. There are two methods of measuring IPCE, in AC and DC modes. For DSCs DC-IPCE is best suitable as the response of device are comparatively slower. IPCE consists of AM 1.5 G light source, monochromator, detector and a measuring unit. Monochromatic light of different wavelength (λ) is allowed to fall on device and detector simultaneously, further the current response (I_{sc}) is obtained and input power (P_{in}) is obtained from the detector. IPCE is calculated as follows,^{23,24}

$$IPCE = \frac{I_{\text{sc}}}{P_{\text{in}}} \times \frac{1239}{\lambda} \quad (3)$$

Generally, J_{sc} obtained from IPCE is the validation of J_{sc} obtained from J - V measurements. However, If DSC is limited by mass transport issues, higher J_{sc} is obtained from IPCE compared to that obtained from the J - V measurements.

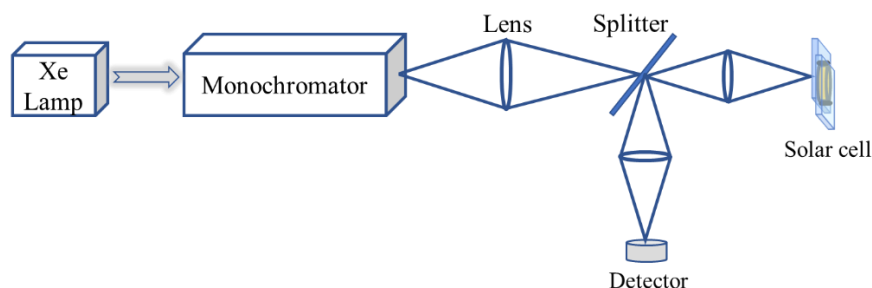


Figure 1. 6 Schematic of IPCE measurement unit.

From IPCE very crucial information of DSC can be obtained, since it is directly proportional to the light harvesting ability (η_{LHE}), injection efficiency (η_{inj}), regeneration efficiency (η_{reg}) and charge collection efficiency (η_{cc}).^{25,26} η_{LHE} is the measure of light harvesting capabilities of the sensitizer, η_{inj} depends on the of LUMO of sensitizer and the conduction band of TiO_2 , η_{reg} depends on the redox potential of the electrolyte and the ground potential of the sensitizer, and η_{cc} depends on electron diffusion in TiO_2 .

1.6.3. Current Transient (CT) Measurement

Current transient provides information about mass transport limitation in DSCs. Slower ion diffusion in electrolyte solution gives rise to mass transport issues. For current transient measurement, light is turned on and off simultaneously and current response of DSC is monitored. **Figure 1. 7** shows current density vs. time obtained from current transient measurement. As apparent in **Figure 1. 7**, as the light is turned on, J_{sc} reaches to its maximum (J_{max}) and then drops and maintains a stable J_{sc} (J_{sat}). If the ratio of J_{max} and J_{sat} is 1 ($J_{sat}/J_{max}=1$), DSC is free from mass transport limitation, likewise if the ratio of J_{max} and J_{sat} is less than 1 ($J_{sat}/J_{max}<1$), then the DSCs is said to have mass transport limitations.^{27,28}

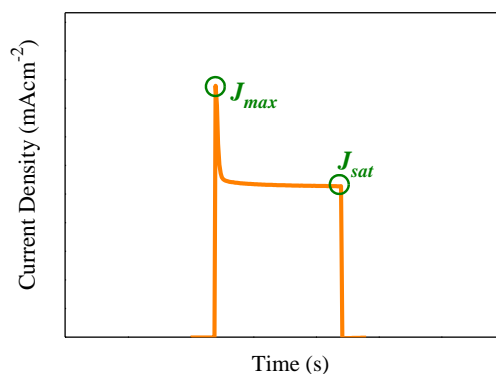


Figure 1.7 Current transient plot showcasing current density vs. time for DSC with mass transport limitation

1.6.4. Open Circuit Voltage Decay (OCVD)

Open Circuit Voltage Decay (OCVD) is a large light perturbation technique to measure lifetime of injected electrons in the conduction band of TiO_2 . In OCVD measurement, DSC in open circuit condition is illuminated using a light source and the illumination is stopped and the voltage decay is monitored on time (**Figure 1. 8**). Under illumination, electrons are injected to the conduction band of TiO_2 and DSC reaches to a stable V_{oc} . As the illumination is stopped electrons in conduction band of TiO_2 recombine with the oxidized species of redox mediator, with subsequent drop in V_{oc} happens. τ_n is calculated from the decay from the equation.^{29,30}

$$\tau_n = -\frac{k_B T}{e} \left(\frac{dV_{oc}}{dt} \right)^{-1} \quad (4)$$

Where e is the elementary charge and $k_B T$ is the thermal energy. **Figure 1. 8 (b)** shows a typical lifetime measured from voltage decay.

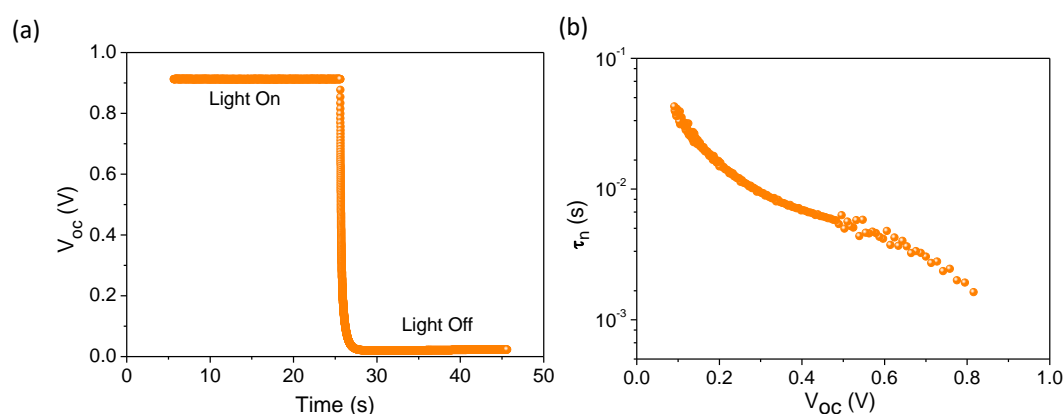


Figure 1. 8 (a) Voltage decay with time and (b) lifetime as a function of V_{oc}

1.6.5. Charge Extraction (CE)

Charge extraction is a large light perturbation technique to measure electron concentration at TiO₂ network, which further provide information about density of states and conduction band of TiO₂. For charge extraction measurement, DSC in open circuit condition is illuminated for a few seconds and the illumination is stopped simultaneously short-circuited to extract the charge. The extracted charge is calculated using the equation,^{31–33}

$$Q_{Ext} = - \int_0^{\infty} i dt \quad (5)$$

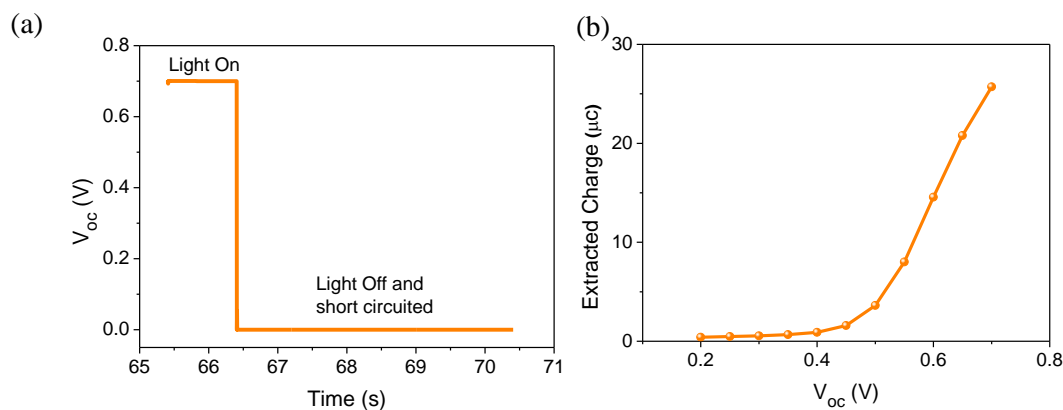


Figure 1. 9 (a) Voltage as function of time and (b) extracted charge as a function of voltage measured using charge extraction technique.

Where, i is the current observed/extracted with time t , and Q_{Ext} is the extracted charge. **Figure 1. 9 (a,b)** shows voltage as function of time during the charge extraction process and calculated extracted charge as a function of voltage. From charge extraction measurement density of states in TiO₂ and position of conduction band in TiO₂ is estimated.

1.6.6. Electrochemical Impedance Spectroscopy (EIS)

Electrochemical Impedance Spectroscopy (EIS) is one of the powerful small perturbation technique used to study interfacial charge transfer of photovoltaic devices. In EIS a sinusoidal electrical voltage signal is applied to the device and the current response is monitored (**Figure 1. 10**). The input sinusoidal signal can be given by the equation,

$$V = V_{dc} + V_o \sin \omega t \quad (6)$$

where, V_{dc} is the steady state voltage, V_o is the amplitude and ω is the angular frequency. The current response has a phase difference ϕ and it is given by the equation,

$$I = I_{dc} + V_o \sin(\omega t + \phi) \quad (7)$$

where, I_{dc} is the steady state current, I_o is the amplitude and ω is the angular frequency and ϕ is the phase of the signal.

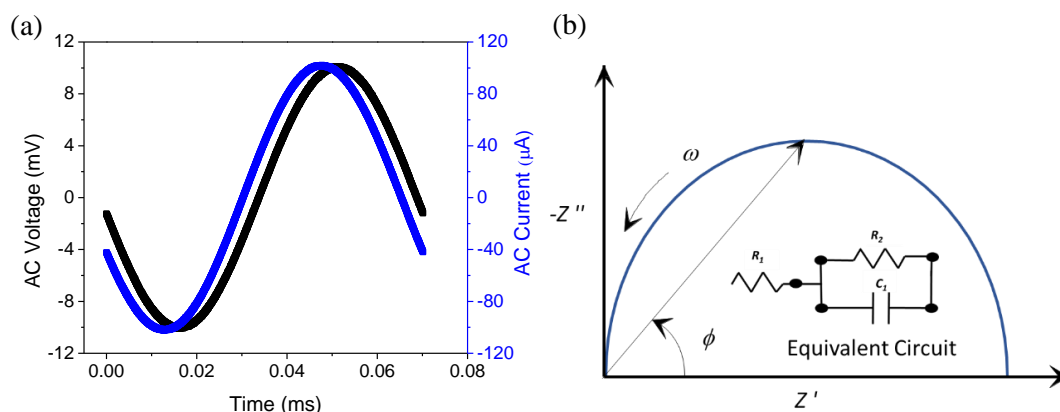


Figure 1.10 (a) Input voltage signal and output current signal and (b) Nyquist plot and inset shows equivalent circuit for fitting

Impedance (Z) of the device is obtained from the equation,

$$Z = \frac{V}{I} = \frac{V_{dc} + V_o \sin \omega t}{I_{dc} + V_o \sin(\omega t + \phi)} = Z' + iZ'' \quad (8)$$

$$\phi = \tan^{-1}(Z''/Z') \quad (9)$$

where Z' and Z'' are the real and imaginary part of impedance. The three dimensional plot between Z' , Z'' and angular frequency (ω) is known as Nyquist plot (**Figure 1.11 (a)**) and it is fitted with equivalent circuit to obtain various electrical parameters which further gives information of the interfacial charge dynamics of the cell. Very often Bode plot (ϕ vs. frequency) is also analyzed to extract critical interfacial charge dynamics.

For DSCs commonly three semicircles are observed in Nyquist plot and Bode plot (**Figure 1.11 (b)**). The semicircle in the high frequency region corresponds to the charge transfer at counter electrode/electrolyte interface, the second semicircle in the middle frequency region corresponds to charge transfer at TiO_2 /dye/electrolyte interface and the third semicircle in the lower frequency region corresponds to the diffusion of ions in the

electrolyte. Yet again, at higher frequency region of the second semicircle a straight line inclined at 45° is observed which corresponds to the diffusion of electron in TiO_2 , but at lower frequency region, clear semicircular characteristics are observed due to the charge recombination at $\text{TiO}_2/\text{dye}/\text{electrolyte}$ interface. The Nyquist plot can be fitted using transmission line model as given in **Figure 1. 11(c)**. The equivalent circuit consists of resistors, capacitors and constant phase element. R_{pedot} and C_{pedot} refers to the resistance and capacitance at the counter electrode/ electrolyte interface. Similarly, R_s is the sheet resistance of the substrates and Z_d is the impedance of ion diffusion in the electrolyte. The transmission line model was used to fit $\text{TiO}_2/\text{dye}/\text{electrolyte}$ interface and it consists of three electrical parameters R_t , R_{rec} and C_μ .^{34–38} R_t corresponds to resistance for the electrons to diffuse in mesoporous TiO_2 , R_{rec} is the resistance for the recombination at $\text{TiO}_2/\text{electrolyte}$ interface and C_μ is the constant phase element that represents the capacitance of $\text{TiO}_2/\text{electrolyte}$ interface.

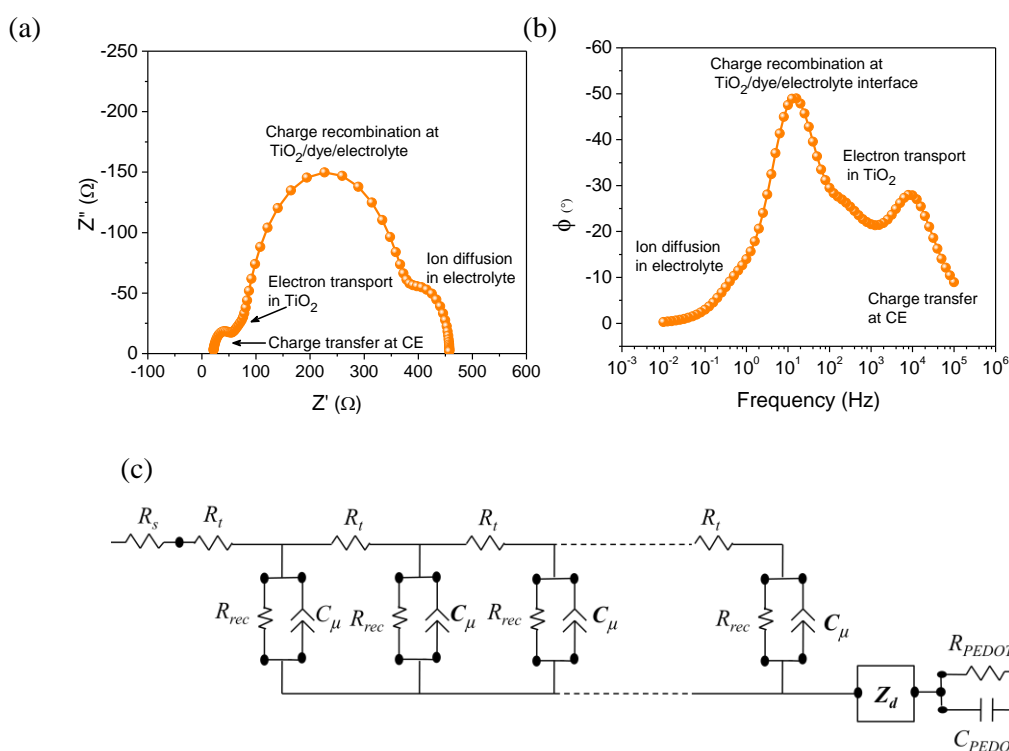


Figure 1. 11 (a) Nyquist plot and (b) Bode plot for DSC and (c) equivalent circuit for fitting impedance plots

From the resistance and capacitance values the time constant also can be calculated. Two important time constants are lifetime and transport time. Lifetime is the time that electrons

stays in TiO₂ before recombination while transport time is the time taken by electrons to diffuse in TiO₂. Both the time constants can be calculated by the relations,^{35,39,40}

$$\text{Lifetime, } \tau_n = R_{\text{rec}} C_{\mu} \quad (10)$$

$$\text{Transport time, } \tau_d = R_t C_{\mu} \quad (11)$$

Other important parameters such as diffusion coefficient of electrons travelling in TiO₂ (D_n), diffusion length of electron in TiO₂ (L_n) and charge collection efficiency (η_{cc}) is calculated from lifetime and transport time using the following equations,^{35,39,40}

$$\text{Diffusion coefficient, } D_n = \frac{d^2}{\tau_d} \quad (12)$$

$$\text{Diffusion length, } L_n = \sqrt{D_n \tau_n} \quad (13)$$

$$\text{Charge collection efficiency, } \eta_{cc} = \left(1 - \frac{\tau_d}{\tau_n}\right) \times 100 \quad (14)$$

1.6.7. Intensity Modulated Photovoltage/Photocurrent Spectroscopy (IMVS/IMPS)

IMVS and IMPS are small perturbation techniques. Unlike EIS, in Intensity Modulated Photovoltage Spectroscopy (IMVS) and Intensity Modulated Photocurrent Spectroscopy (IMPS) the perturbation signal used is light. From IMVS measurement lifetime is obtained while from IMPS measurement transport time is measured. IMVS is carried out under open circuit condition and IMPS is carried out in short-circuit condition. In IMVS measurement, a small light perturbation with different frequency is applied to the solar cell and the voltage response of the solar cell is monitored. The response is further computed to obtain Nyquist and Bode plots. Similar process occurs in IMPS measurement with only difference that the response of the cell is current. An embodiment Bode plot from IMPS is given in **Figure 1. 12**.

Time constant is calculated by the equation,^{41,42}

$$\tau = \frac{1}{2\pi f_{\text{max}}} \quad (15)$$

where, f_{max} is the highest frequency in Bode plot. The time constant obtained from IMVS is lifetime while that obtained from IMPS is transport time.

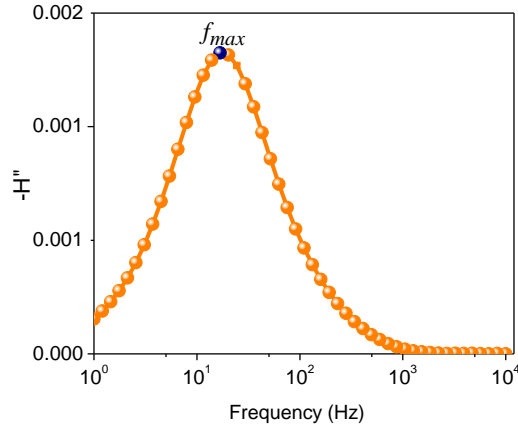


Figure 1. 12 Bode plot from IMPS measurement.

1.6.8. Transient Photovoltage/Photocurrent Decay

Transient photovoltage decay and transient photocurrent decay are simple and user friendly small light perturbation techniques used to determine time constants such as lifetime and transport time in DSCs. From transient photovoltage decay, lifetime of electrons in TiO_2 is measured while from transient photocurrent decay transport time of electrons in TiO_2 is measured. For transient photovoltage decay solar cell is first open circuited and continuously illuminated till it reaches to a steady state V_{oc} . A square wave light perturbation is then superimposed with the steady state illumination and the voltage response of the solar cell is monitored.

Lifetime (τ_n) is obtained by fitting the voltage decay plot using the equation,⁴³

$$\Delta V = V_0 e^{-t/\tau_n} \quad (16)$$

Where, ΔV is voltage decay, V_0 is steady state V_{oc} owing to constant illumination and, t is time. For transient photovoltage decay solar cell is short circuited and continuously illuminated till it reaches to the steady state J_{sc} . A square wave light perturbation is then superimposed with the steady illumination and the current response of the solar cell is further monitored.

Transport time (τ_d) is obtained by fitting the current decay plot using the equation,⁴⁴

$$\Delta I = I_0 e^{-t/\tau_d} \quad (17)$$

Where, ΔI is current decay, I_0 is steady state J_{sc} owing to constant illumination, and t is time. **Figure 1. 13** shows voltage response and current response of DSC to square wave perturbations.

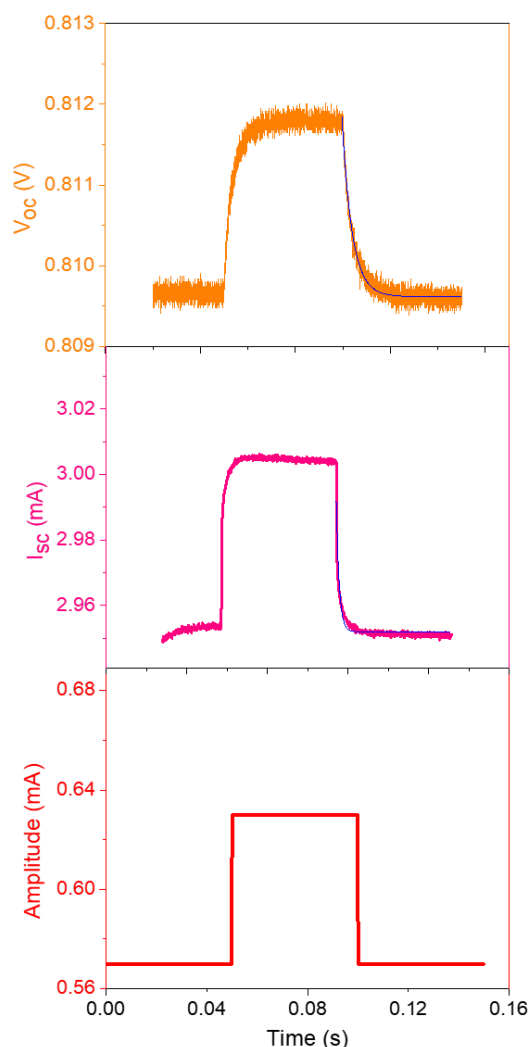


Figure 1. 13 Voltage response and current response of DSC to square wave perturbation in transient photovoltage decay and transient photocurrent decay.

1.6.9. Photo-Induced Absorption Spectroscopy (PIA)

Photo-induced absorption spectroscopy (PIA) is used to study electron injection and dye regeneration kinetics in DSCs.^{47,48} It is a pump-probe technique. A schematic diagram of the PIA setup is shown in **Figure 1. 14 (a)**. It contains a 20 W tungsten-halogen lamp as probe and a 460 nm LED used as a pump for excitation source. The pump light is square-wave modulated with a frequency of 9 Hz. The superimposed probe and pump is passed through the sample and monochromator and finally detected by a UV enhanced silicon photodiode. The detector is connected to a current amplifier and a lock-in amplifier. The

lock-in amplifier measures $\Delta T/T$ in phase component with the modulation frequency $\{\text{Re}(\Delta T/T)\}$ and out of phase component $\Delta T/T$ with the modulation frequency $\{\text{Im}(\Delta T/T)\}$ are measured. Finally, change in absorbance (ΔA) is calculated by the equation,⁴⁹

$$\Delta A \ln(10) = -\text{sgn}\{\text{Re}(\Delta T/T)\} \sqrt{\text{Re}(\Delta T/T)^2 + \text{Im}(\Delta T/T)^2} \quad (18)$$

The set-up therefore allows the measurement of ΔA at different wavelength. **Figure 1. 14 (b)** shows PIA spectrum. It shows negative absorption due to ground state bleaching and positive absorption due to photoinduced absorption of oxidised dye molecule. In presence of inert electrolyte DSCs shows positive absorption indicating electron injection. As the inert electrolyte is replaced with redox electrolyte absorption vanishes which indicates regeneration of oxidised dye. PIA provides a qualitative information on injection and regeneration process in DSCs.

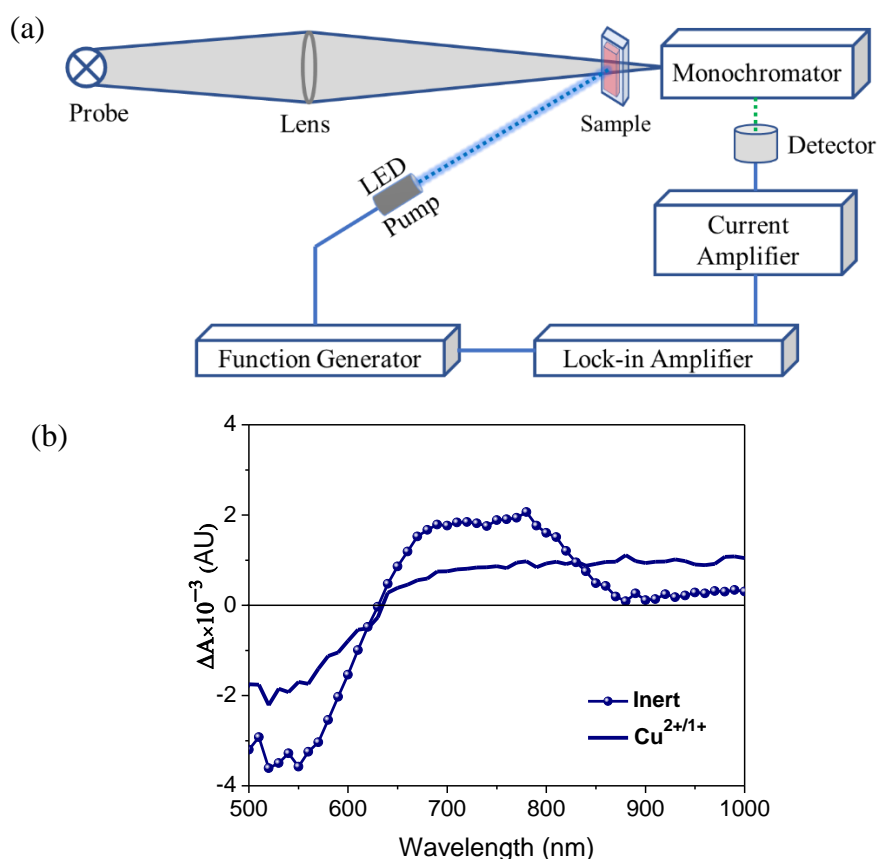


Figure 1. 14 (a) Schematic diagram of PIA setup and (b) PIA spectra of DSC in presence and absence of redox electrolyte

1.7. Evolution of Dye-Sensitized Solar Cells

Brian O'Regan and Michael Gratzel first introduced DSCs in 1991 reporting a power conversion efficiency (PCE) of 7.1% under one sun illumination (100 mW/cm^2)

using nano crystalline mesoporous TiO₂ sensitized with a ruthenium sensitizer RuL₂(μ-(CN) Ru(CN) L₂')₂, where L is 2,2'-bipyridine-4,4'-dicarboxylic acid and L' is 2,2'-bipyridine using iodide/tri-iodide redox mediator.⁵⁰ The simple ruthenium molecule, cis-dithiocyanato bis(2,2'-bipyridine-4,4'-dicarboxylate) ruthenium-(II) (N3) sensitizer with an absorption onset around 800 nm later contributed to 10 % efficiency.⁵¹ Further, terpyridyl complexes of Ru(II) dye (Black dye) exhibited efficient light harvesting over the whole visible range extending into the near-IR region with an absorption onset up to 920 nm, resulting in an overall power conversion efficiency of 10.4%.⁵² The deprotonation of one of the bipyridine carboxylic acid group of the N3 dye, (Bu₄N)₂[Ru(dcbpyH)₂(NCS)₂] (N719), sensitizer raised the efficiency of DSCs later to 11.18% which brings a significant place for ruthenium complexes in DSCs.⁵³ The thiophene moiety in C101 sensitizer and 2-(hexylthio)thiophene in C106 with large molar extinction coefficient further enhanced the light harvesting property of conventional ruthenium sensitizers leading to higher PCE's of 11.0 % and 11.4 % respectively.⁵⁴ Indeed, DSC employing ruthenium sensitizers with modified bipyridine ligands along with I⁻/I₃⁻ redox mediator dominated DSC for the first 20 years since its inception, producing highly efficient devices.

In 2011, the outstanding performance of zinc porphyrin dye breaks the record efficiency of ruthenium dyes. Donor-π-acceptor (D-π-A) sensitizer YD2-o-C8 in conjunction with cobalt(II/III) tris(bipyridyl)-based redox mediator realized a maximum PCE upto 12.3% under one sun illumination.⁵⁵ Later in 2014, Gratzel and co-workers introduced a structurally modified porphyrin sensitizer consisting of proquinoidal benzothiadiazole (BTD) unit exhibiting 13% efficiency with cobalt(II/III) electrolyte.⁵⁶ During this period, cost effective metal free organic sensitizers with higher molar extinction coefficient and structural versatilities received much attention. The D35 sensitizer with bulky alkoxy groups (Anders donor) was able to reach a power conversion efficiency of 6.7% with cobalt (Co) electrolyte.⁵⁷ Yet again thiophene based Y123 dye reported by Tsao et. al., exhibited a PCE of 9.6% with Co electrolyte.⁵⁸ Additionally, solid state DSC (ssDSCs) consisting of Y123 sensitizer and spiro-OMeTAD hole conductor reached a PCE of 7.2%. Co-sensitization with alkoxysilyl anchor based dye ADEKA-1 with LEG4 contributed to the improved power conversion efficiency of 14.3% under one sun illumination using cobalt electrolyte.⁵⁹

Along with the photosensitizers, redox mediators also gained much attention during last two decades. Out of all redox mediators used in DSC, iodide/triiodide (I^-/I_3^-) redox mediator finds much popularity for many reasons such as faster regeneration, slower recombination, good solubility, slower mass transport and faster charge transfer at counter electrode.⁶⁰ Majority of highly efficient reports have employed I^-/I_3^- redox mediator in the initial years. Despite this it has many shortcomings that steered towards finding alternative redox mediators for DSC. Most importantly, I^-/I_3^- redox mediator is limited by V_{oc} due to its fixed redox potential leading to voltage loss. For instance, as apparent in **Figure 1. 15** I^-/I_3^- placed at a more negative potential of 0.4 V vs. NHE DSC fabricated with I^-/I_3^- redox mediator was limited towards achieving open-circuit potential above 0.7 V. I^-/I_3^- redox mediator also possesses complicated charge transfer mechanism which limits fundamental understanding of the charge transfer process taking place in devices employing I^-/I_3^- . It proceeds through multiple steps involving formation of oxidised dye/ I_2 complex followed by I_2 radical ion. Since the mechanism is not so clear the scope for further modification is very limited. These multi step process contribute to larger regeneration driving force of around 400-500 meV. Many of the newly designed and synthesized metal free organic dyes also show poor performance with I^-/I_3^- redox system as they don't allow formation of oxidised dye/ I_2 complex.⁶¹

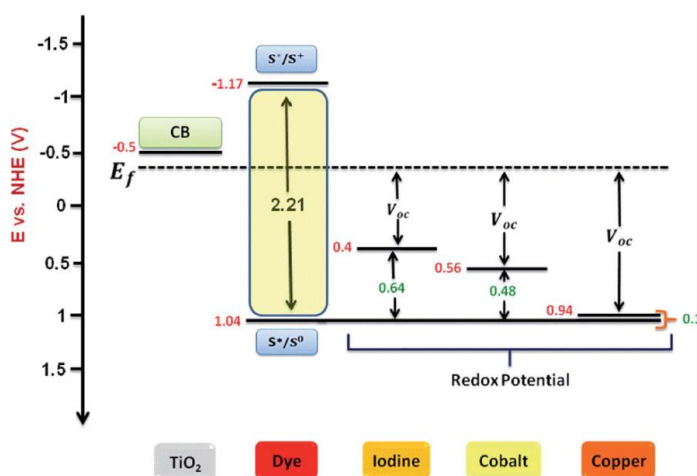


Figure 1. 15 Representation of energetics of TiO_2 semiconductor, LEG4 dye and three different electrolytes (I^-/I_3^- , $[Co(bpy)_3]^{3+/2+}$ and $[Cu(dmp)_2]^{2+/1+}$).⁶²

In a way to address the limitations being placed by the conventional I^-/I_3^- electrolyte, outer sphere redox shuttles were introduced as possible alternatives. It offers simple one

electron charge transfer kinetics that can be systematically investigated using Marcus theory, which leads to designing of a range of new compatible redox mediators for DSCs.⁶³ Furthermore, outer sphere charge transfer process does not involve the intermediate step of dye electrolyte binding. To begin with, Gegg *et al.* introduced the kinetically fast ferrocene (Fc/Fc⁺) based outer sphere mediator redox mediators in DSC, however owing to the fast recombination, the photovoltaic performance was not so promising employing these iron complexes.⁶⁴ Adopting various surface treatments and dye modifications, photovoltaic performance of ferrocene electrolyte based DSCs were improved to some extent, nevertheless the PCE was not promising enough to employ ferrocene based DSCs for practical applications.⁶⁵ Daeneke and co-workers marked the breakthrough employing Fc/Fc⁺ achieving a higher PCE of 7.5% (V_{oc} -842 mV, J_{sc} -12.2 mAcm⁻² and FF -0.73) in conjunction with the novel metal-free organic sensitizer Carbz-PAHTDTT.⁶⁶ The same group synthesized a series of ferrocene derivatives covering a redox potential ranging from 0.09 V all the way up to 0.94 V vs. NHE and achieved a maximum PCE of 5.2%.⁶⁷

Li *et al.* introduced Nickel redox mediators in DSC reaching a PCE up to 1.5%.⁶⁸ Nickel redox mediators (Ni^{III}/Ni^{IV}) possess faster regeneration than I⁻/I₃⁻ redox couple and the recombination is 1000 times slower than Fc/Fc⁺ redox mediator. The slower recombination can be rationalized to the higher activation barrier for reducing Ni (IV) to Ni (III) which requires dicarbollide rotation from a cis-to-trans conformation change. In addition, mass transport in nickel electrolyte is faster than ferrocene electrolyte. Though nickel redox mediators are endowed with many promising properties, substantial PCE is yet to be achieved using these electrolytes.

Cobalt (Co) is one of the most promising alternate outer sphere redox shuttle which was explored extensively as an alternative to I⁻/I₃⁻ redox mediator in DSCs. It has many favourable properties such as minimum visible light absorption, easily tuneable electrochemical potential and physical properties by modifying the peripheral substituents on the ligands being coordinated to the metal center, non-corrosive nature to metal current collectors in modules and its non-volatility nature are a few among the list.^{69,70} The structure of Co complexes strongly influences the photovoltaic properties, the ligands with electron withdrawing groups impart more positive redox potential which in turn improves the photovoltage. On the other hand, being bulkier in nature (six coordinate complexes), the mass transport limitation is prominent for cobalt electrolytes which contributes to

higher viscosity. Furthermore, higher reorganization energy between d^7 (high-spin) and d^6 (low-spin) states of cobalt complexes require additional driving force for dye regeneration. In 2001, Nusbaumer *et al.* introduced cobalt redox mediator in DSCs achieving an initial PCE of 2.2%.⁷¹ Still, for almost a decade the electrolyte remained in dormant stage and cobalt electrolytes started to get noticed with the report from Feldt *et al.* where they achieved a PCE of 6.7% using $[\text{Co}(\text{bpy})_3]^{3+/2+}$ in conjunction with D35 dye.⁵⁷ Later Yella, *et al.* reported a PCE over 12% by employing a $[\text{Co}(\text{bpy})_3]^{3+/2+}$ redox-electrolyte with a donor- π bridge-acceptor zinc porphyrin YD2-o-C8 sensitizer.⁵⁶ The highest efficiency of 14.3% in DSC was reported by Kakiage *et al.* using $[\text{Co}(\text{phen})_3]^{3+/2+}$ along with co-sensitized dyes, LEG4 and ADEKA.⁵⁹ Though cobalt based DSC proved to be efficient, the carcinogenic nature of starting materials used for preparing cobalt complexes along with the mass transport limitation are two major bottlenecks that prevents further commercialization of cobalt electrolytes in DSC.

Recently the introduction of earth abundant copper electrolytes rejuvenated DSC research, addressing and overcoming the issue associated with conventional electrolytes and paving the way toward the commercialization of dye cells. Unlike cobalt redox mediators, copper redox shuttles are cost-effective and environmental friendly. More importantly the new zombie cells, a facile architecture to fabricate ssDSC without compromising power conversion efficiency was exclusively made possible only with the introduction of copper redox mediators.^{72,73} This solves the long term stability issues associated with leakage of liquid electrolyte in DSC. Copper electrolyte requires merely 100 mV of driving force for unit dye regeneration thus minimizing voltage loss.^{74,75} Also copper redox mediators are likely to be less affected by mass transport limitation owing to its less bulkiness in comparison to other transition metal complex electrolytes. Copper redox mediators were first time used by Hartri *et al.* in 2005 achieving a PCE reaching of 1.4% using $[\text{Cu}(\text{dmp})_2]^{2+/1+}$ along with N719 dye.⁷⁶ In 2011 Bai *et al.* achieved a PCE of 7.5% using high absorption coefficient organic dye C128.⁷⁷ Sayagili *et al.* further enhanced the efficiency >10% using $[\text{Cu}(\text{tmpy})_2]^{2+/1+}$ electrolyte along with Y123 sensitizer.⁷⁴ By co-sensitizing Y123 dye with XY1b dye Cao *et al.* realized a higher power conversion efficiency of 13.1% sensitizers along with $[\text{Cu}(\text{tmby})_2]^{2+/1+}$.⁷⁸ Similarly, Zhang *et al.* reached to power conversion efficiency of 13.5% with co-sensitization of MS5 and XY1b along with $[\text{Cu}(\text{tmby})_2]^{2+/1+}$. Recently, Ren *et al.* attained striking power conversion efficiency of 15.2% along with $[\text{Cu}(\text{tmby})_2]^{2+/1+}$ through enriched molecular packing of co-

sensitized dyes SL9 and SL10.⁷⁹ Furthermore, copper electrolyte based DSC attracted immense attention particularly in the domain of artificial light harvesting with the report by Feritag *et al.* where indoor power conversion efficiency of 28.9% was achieved under 1000 lux, even exceeding the PCE of silicon and GaAs solar cells under the same conditions.⁸⁰ Later Michaels *et al.* achieved a power conversion efficiency of 34% under 1000 lux CFL illumination with an embodiment containing multiple fine-tuned organic dyes along with $[\text{Cu}(\text{tmbpy})_2]^{2+/1+}$ electrolyte.⁸¹ With judicious molecular engineering of high V_{oc} co-sensitizers Zhang *et al.* reached to power conversion efficiency of 34.5% with a distinctive V_{oc} of 0.98 V under 1000 lux. Further Chen *et al.* obtained 37% under 6000 lux illumination through molecular engineering of bis-anthracene-based sensitizer.⁸²

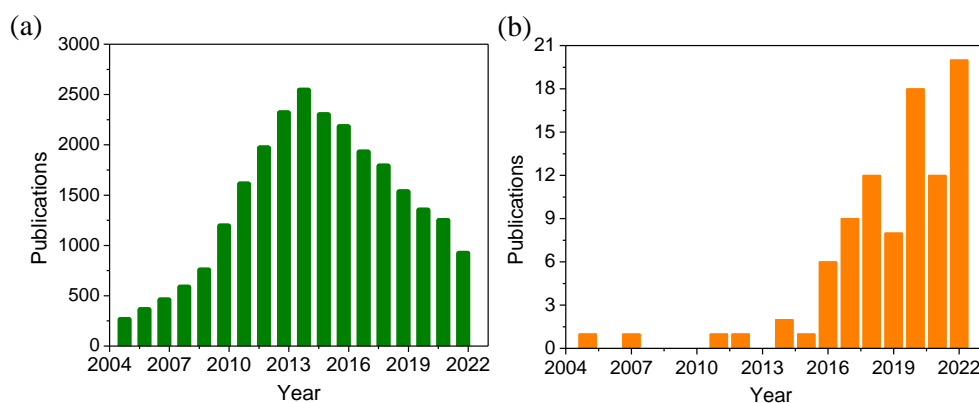


Figure 1. 16 (a) Number of publications in last 17 years in DSC (data collected with topic of in DSC from Web of Science) (b) Number of publications in DSC using copper electrolyte in last 17 years.

Dye sensitized solar cell has been a topic of high interest since it was invented. **Figure 1. 16 (a)** shows research publications published during last 17 years in DSC (data collected by searching Dye sensitized solar cell in Web of Science). Copper complex redox mediators were first reported for DSC application in 2005, till 2015 only seven papers were published using copper electrolytes. In 2016, many high-quality works were published in the area further fuelling copper based DSC research. However, from last few years the number of publications in the area of copper based DSCs are continuously growing showing its relevance in making an impact to the area of dye-sensitized solar cells and indoor photovoltaics. **Figure 1. 16 (b)** shows research publications published in copper electrolyte based DSCs from 2005 to till date (data collected by searching Dye sensitized solar cell and copper electrolyte in Web of Science).

1.8. Copper Electrolyte Based Liquid State DSCs

1.8.1. Semiconductor Modification

The primary role of semiconductor in DSC is to provide a space to accommodate maximum number of dye molecules and to facilitate favorable electron transport path with minimum back electron recombination. So far mesoporous TiO₂ is the best choice as semiconductor material in DSCs. Generally, bilayer TiO₂ (first layer consisting of mesoporous TiO₂ with 20 nm nanoparticles (12 μm) and a second layer with 250 to 400 nm scattering nanoparticles (6 μm)) is used with classical iodide/tri-iodide electrolyte. Unlike I/I₃⁻ electrolyte, copper complexes are comparatively bulky in nature, thus a more porous TiO₂ network is essential for the hassle-free movement of copper ions inside the semiconductor matrix. Perhaps to realize higher porosity in many of the reports employing Cu electrolytes, the 20 nm standard TiO₂ paste is further diluted by adding appropriate quantity of terpinol and ethyl cellulose. Moreover, TiO₂ paste consisting of 30 nm particles are generally preferred in copper electrolyte based DSCs. Nevertheless, the rationale behind using modified mesoporous TiO₂ materials are not studied extensively in literature. Ferdowsi *et. al.* compared the PV performance of DSCs using TiO₂ with particle size of 20 nm and 30 nm along with two different organic dyes L156 and L224 respectively using [Cu(tmby)₂]^{2+/1+} redox mediator.⁸³ Higher J_{sc} leading to better PCE was observed using 30 nm particles employing both the dyes. The PV parameters are summarized in **Table 1. 1**,

Table 1. 1 PV parameters of DSCs based on TiO₂ film with particle of 20 nm and 30 nm employing L156 and L224 with [Cu(tmby)]^{2+/1+} redox couple.

Particle size of TiO ₂ (nm)	Dye	V_{oc} (V)	J_{sc} (mAcm ⁻²)	FF	η (%)
20	L156	1.10	11.64	0.71	9.12
30		1.09	12.20	0.69	9.26
20	L224	1.10	10.84	0.66	8.01
30		1.09	11.32	0.67	8.27

Ruess *et. al.* introduced ZnO photoanode as an alternate semiconductor layer in copper electrolyte based DSCs, reaching an η of 3.85% (J_{sc} -7.5 mAcm⁻², V_{oc} -713 mV and FF -0.72) along with DN216 organic dye and [Cu(tmby)₂]^{2+/1+} redox mediator.⁸⁴ The

photoanode consists of electrochemically deposited 2.5 - 3 μm mesoporous ZnO layer and 600 nm compact blocking layer. The compatibility of ZnO photoanode with Cu redox mediator opens up new possibilities of research to be explored further in future.

Besides the mesoporous semiconductor layer, generally compact blocking layers are used particularly at TiO_2 /electrolyte and FTO/electrolyte interface to prevent back electron transfer (recombination) in DSC. These blocking layers become more essential in DSCs with alternative redox mediators, in particular copper redox shuttles where driving force for recombination is high as a result of its more positive redox potential (>0.9 V vs. NHE). Compact TiO_2 thin layers of few nanometer thickness are commonly used as blocking layers and are deposited by immersing the electrodes in TiCl_4 solution at 70 $^\circ\text{C}$ followed by annealing at 500 $^\circ\text{C}$. In general, for copper electrolyte based DSC, the pre-blocking layer is deposited by dipping the electrodes in 53 mM TiCl_4 for 30 minutes or by immersing the electrodes in 40 mM TiCl_4 for 50 minutes at 70 $^\circ\text{C}$. Yet again deposition of pre-blocking layer by spin coating TiCl_4 solution is also seen in literature.⁸⁵ It is to be noted that majority of the highly efficient DSCs using copper redox mediators employ TiO_2 compact blocking layers deposited by TiCl_4 treatment. Colombo *et al.* used silanization for depositing compact TiO_2 blocking layer. **Figure 1. 17** shows J - V characteristics of DSCs with and without silanization.⁸⁵ Recently Michael *et al.* systematically deposited TiO_2 blocking layer using spray pyrolysis.⁸⁶ They obtained maximum efficiency of 9.2% under one sun illumination with two spray cycles.

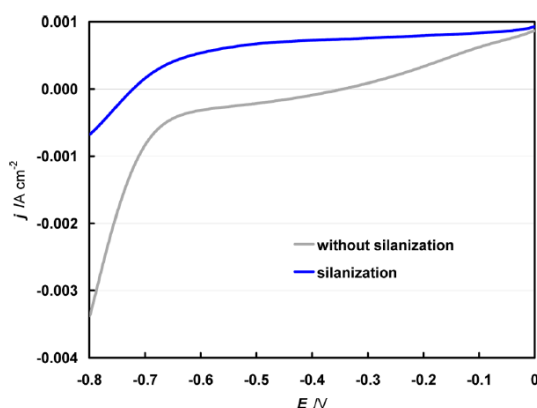


Figure 1. 17 Normalized J - V characteristics of DSC with and without silanization.⁸⁵

In copper electrolyte based DSC the standard method of TiCl_4 treatment is ubiquitously used to create TiO_2 post-blocking layers. Glinka *et al.* adopted a unique approach of molecular multicapping and encapsulation of photoanode layer to prevent recombination at TiO_2 /electrolyte interface.⁸⁷ For molecular multicapping they sequentially immersed the dye sensitized photoanodes under 0.1 mM lignoceric, stearic, heptanoic, and octylophosphonic acids in the ACN/toluene mixture each for 5 seconds. Similarly, for encapsulation they immersed dye sensitized photoanodes in 0.5 mM CB7 in deionized water. Both molecular multicapping and encapsulation were tested for three different organic dyes (D205, D205Si and Y123) along with $[\text{Cu}(\text{tmby})_2]^{2+/1+}$ electrolyte. The effect of molecular multicapping and encapsulation were inconsistent in different dyes; for instance, using D205 dye, recombination resistance increased while recombination resistance remains unaffected with encapsulation. For D205Si recombination resistance increased with both MC and CB7, in contrary multicapping and encapsulation reduced recombination resistance in Y123 based devices. The nature of copper redox mediator changes with its structure, thus semiconductor layer as well as compact blocking layer need to be modified with change in structure of copper redox mediator.

1.8.2. Compatible Sensitizers for Copper Redox Electrolytes

1.8.2.1. Metal Complex Sensitizers

Compatibility of sensitizer with the redox electrolyte used is highly essential to realize efficient DSCs. Inorganic sensitizers are unable to create a mark in copper electrolyte based DSCs. The inherent property of narrow band gap and low absorption coefficient of inorganic sensitizers imposes conceptual dispute that restricts them to deliver better PV performance. The former enables better light harvesting capability but incurs energetic incompatibility between sensitizer and redox mediator whereas lower absorption coefficient necessitates use of thicker semiconductor layer which imposes mass transport issue. In the pioneering contribution, Hartri *et al.* employed N719 dye along with copper redox shuttle and realized a PCE of 1.4%.⁷⁶ One of the major reasons for lower PV performance was the inadequacy in driving force for dye regeneration which limited the J_{sc} and PCE. Likewise, Brugnati *et al.* tested a series of Cu redox shuttles with Z907 dye, the best devices showed IPCE in the range of 30-40% only, many redox shuttles were not even able to regenerate Ru-sensitizer.⁸⁸ Colombo *et al.* screened various Ru dyes which includes Z907, B5, and $[\text{Ru}(\text{dcbpy})_2(\text{dnbpy})](\text{PF}_6)$ along with Cu redox mediator ($[\text{Cu}(2\text{-mesityl-4,7-dimethyl-1,10-phenanthroline})_2]^{2+/1+}$). Among all the dye $[\text{Ru}(\text{dcbpy})_2(\text{dnbpy})](\text{PF}_6)$

was the only one sensitizer that showed a J_{sc} of 2.04 mAcm⁻².⁸⁵ The lower J_{sc} was due to sluggish dye regeneration due to insufficient driving force. Recently, Colombo *et al.* for the first time used zinc porphyrin photosensitizer (D1) along with a series of copper redox mediators.⁸⁹ The dye was modified with decyloxy chains grafted to the porphyrin core that acts as a barrier to prevent back electron transfer at the semiconductor-electrolyte interface. The combination of [Cu(2-mesityl-1,10-phenanthroline)₂]^{2+/1+} and D1 realized devices with a PCE of 3.7% and a J_{sc} of 5.9 mAcm⁻². The lower J_{sc} was attributed to both competitive light absorption by the electrolyte at 460 nm and slower mass transport owing to bulkiness of the redox shuttle. Higashino *et al.* used two push pull zinc porphyrin dyes LG4 and LG5 along with both [Cu(tmby)₂]^{2+/1+} and [Cu(dmp)₂]^{2+/1+} realizing maximum PCE of 5.07% and 4.36% with [Cu(tmby)₂]^{2+/1+}, while with [Cu(dmp)₂]^{2+/1+} it showed a lower PCE of 3.98% and 3.03% respectively.⁹⁰ Most successful ruthenium metal complex dyes did not excel in copper electrolyte based DSC, however compatibility of zinc porphyrin dyes was found to be better with copper electrolytes which need to be explored further to realize higher PCEs.

Dragonetti *et al.* achieved a PCE of 2.0% using heteroleptic copper dye D1, bearing one 2,9- dimesityl-1,10-phenanthroline and a 6,6'-dimethyl-2,2'-bipyridine-4,4'-dibenzoic acid anchoring ligand together with copper electrolyte.⁹¹ Though the PV performance was low, this study confirms the potential of “full copper” DSCs where both copper metal complex dye and electrolyte was used to make DSC. Adopting the approach of full copper DSC the same group introduced two new copper dyes D2 and D3 and achieved an efficiency of 1.2% and 1.0%.⁹² It appears that future work should be devoted to increase the light harvesting properties of the copper based dyes which may be suitable for co-sensitization.

1.8.2.2. Metal Free Organic Dyes

The alliance between organic dyes and copper redox mediators steered towards producing highly efficient DSCs both under full sun and indoor/artificial illuminations. The high absorption coefficient organic dyes deliver maximum J_{sc} using thin semiconductor layers, thus circumventing mass transport which is one of the major issues associated with copper electrolyte DSCs. In addition, structurally engineered organic sensitizers are capable to prevent back electron transfer (recombination) at semiconductor/electrolyte interface.⁹³⁻⁹⁵ Organic sensitizers with triphenylamine (TPA) donor is best suited to be used with copper electrolytes producing DSC with higher PCEs. Indeed, practical feasibility of

DSC with copper redox shuttle was appreciated when Bai *et al.* employed triphenyl organic dye C218 along with $[\text{Cu}(\text{dmp})_2]^{2+/1+}$ and achieved a PCE of 7% with a V_{oc} of 0.9 V under one sun (100 mW/cm^2) illumination.⁷⁷ Favorable energetics and appropriate structure that lowers recombination helped in achieving this initial landmark performance. Using another triphenyl amine based organic dye LEG4 along with $[\text{Cu}(\text{dmp})_2]^{2+/1+}$ Freitag *et al.* pushed efficiency to 8.3% owing to high V_{oc} of 1.02 V under one sun illumination.⁷⁵ Cong *et al.* realized an efficiency of 9.0% using the same LEG4 dye together with $[\text{Cu}(\text{bpye})_2]^{2+/1+}$ redox shuttle under one sun illumination and an improved efficiency of 9.9% under 0.5 sun illumination.⁹⁶ Using Y123 dye Saygili *et al.* crossed the efficiency barrier of 10%. Y123 dye along with $[\text{Cu}(\text{tmby})_2]^{2+/1+}$, $[\text{Cu}(\text{dmby})_2]^{2+/1+}$ and $[\text{Cu}(\text{dmp})_2]^{2+/1+}$ redox shuttles reached PCE of 10.3%, 10% and 10.3%.⁷⁴ Owing to the reliability, reproducibility and high efficiency, Y123 dye has become the standard organic dye to be used in copper electrolyte based DSCs. Further, Freitag *et al.* reported XY1 with a higher efficiency of 10.2% along with $[\text{Cu}(\text{tmby})_2]^{2+/1+}$ electrolyte.⁸⁰ Saygili *et al.* used D5, D35 and D45 dyes having triphenylamine donor unit grafted with alkyl chains of variable lengths providing different degrees of blocking recombination with various copper redox shuttles reaching efficiencies of 7.53%, 8.3% and 9.22% respectively.⁹⁷ Notably, DSC with D35 and D5 was able to realize a higher V_{oc} of 1.13 V and 1.14 V which were among the best V_{oc} obtained using copper based electrolytes. A major advancement in PCE was later obtained by Zhang *et al.* where they achieved PCE up to 11.0% and 11.6 % using WS70 and W72 organic dyes respectively along with $[\text{Cu}(\text{tmby})_2]^{2+/1+}$.⁹⁸ Similarly, Liu *et al.* synthesized a series of indacenodithiophene (IDT)-based D- π -A organic dyes with varying electron-accepting units, the best sensitizer L350 in the series reached to a maximum efficiency of 11.2%.⁹⁹ Further, Jing *et al.* reported a new D-A- π -A featured sensitizer, HY64 with phenanthrene-fused-quinoxaline (PFQ) auxiliary acceptor and achieved highest PCE of 12.5% using $[\text{Cu}(\text{tmby})_2]^{2+/1+}$.¹⁰⁰ Grobelny *et al.* presented two molecularly tailored organic sensitizers, ZS4 and ZS5, through judiciously employing dithieno[3,2-b:2',3'-d]pyrrole (DTP) as the π -linker and hexyloxy-substituted diphenylquinoxaline (HPQ) or naphthalene-fusedquinoxaline (NFQ) as the auxiliary electron-accepting unit, respectively. ZS4 achieved maximum PCE of 13.2% while ZS5 reached to PCE of 10.5%.¹⁰¹ This is the highest efficiency till now reported in copper redox shuttle based DSCs employing single dye. Yet again Ren *et al.* reported maximum efficiency of 10.7% using a newly synthesized blue sensitizer R7.¹⁰² Recently Wu *et al.* synthesized dithienopyrrol derivative

photosensitizer C260A, reaching to a PCE of 10.4% with a high V_{oc} of 1.13 V along with $[\text{Cu}(\text{tmby})_2]^{2+/1+}$.¹⁰³ Through judiciously tailoring the electron acceptor and by introducing Hagfeldt donor, Zhang *et al.* obtained the highest V_{oc} of 1.17 V and 1.24 V with MS4 and MS5 dyes respectively.¹⁰⁴ Notably, it is the highest V_{oc} achieved till date in copper electrolyte based DSCs. Apart from TPA dyes, carbazole based dyes were also used with copper electrolytes in DSC. For the very first time Colombo *et al.* employed widely known carbazole dye MK2 in copper based DSCs.⁸⁵ It showed only dark current under illumination as the device was dominated by recombination. An *et al.* synthesized the novel sensitizers AJ201, AJ202, and AJ206 by the fusion of carbazole rings as the new electron donating group.¹⁰⁵ The AJ206 dye exhibited an excellent PCE of 10.8% along with $[\text{Cu}(\text{tmby})_2]^{2+/1+}$. The same group further explored carbazole donor based dyes by synthesizing two novel sensitizers, AJ301 and AJ303 which reached to a maximum PCE of 8.2% and 5.4% respectively along with $[\text{Cu}(\text{tmby})_2]^{2+/1+}$. TPA dyes has shown excellent compatibility with copper electrolytes, whereas little effort has been given to explore other donor functionalities like carbazoles with copper electrolytes. Moreover, there is a vast range of potential organic dyes which are yet to be tested with copper electrolytes.

1.8.2.3. Co-sensitization of Organic Dyes

Co-sensitization of dyes with complimentary absorption profile is the most appreciated approach to realize panchromatic absorption in DSCs. In addition, co-sensitization improves dye loading, reduces dye aggregation and more importantly provides closely packed dye coverage over semiconductor surface, thus preventing recombination of injected electrons with the oxidized species (Cu^{II}) leading to improved V_{oc} , FF and PCEs. For the first time Freitag *et al.* used co-sensitized photoanodes consisting of XY1 and D35 dye along with $[\text{Cu}(\text{tmby})_2]^{2+/1+}$ and obtained a PCE of 11.3% (V_{oc} -1.03 V, J_{sc} -16.19 mAcm^{-2} and FF -0.68) under one sun illumination, and 13.2% under 0.12 sun illumination.⁸⁰ Co-sensitization of D35 along with XY1 helped in improving J_{sc} as D35 dye absorbs the blue and green light, whereas XY1 covers the yellow and red spectral region. Owing to the achievement of high PV performance XY1 dye is vastly used as a primary dye in co-sensitization employing copper electrolyte. Cao *et al.* employed co-sensitized XY1b and Y123 dyes in direct contact DSC architecture further improving the PCE to 13.1% under one sun illumination.¹⁰⁶ Tanaka *et al.* used co-sensitization approach in an innovative way, reducing the cost of dyes by 30%.¹⁰⁷ They used a mixture of inexpensive dye (5T) with an

expensive dye (XY1) along with $[\text{Cu}(\text{tmb})_2]^{2+/1+}$ and achieved efficiency of 9.53% in one sun illumination, at the same time using costly dye XY1 with $[\text{Cu}(\text{tmb})_2]^{2+/1+}$ an efficiency of 9.56% was obtained. Similarly, Michaels *et al.* co-sensitized XY1 with a small dye L5 realizing an efficiency of 11.5% with a high J_{sc} of 15.9 mAcm^{-2} under one sun illumination.¹⁰⁸ Again Zhang *et al.* used XY1b with the newly synthesized TPA dye MS5 and obtained a PCE of 13.5% under one sun illumination.¹⁰⁴ In another study Ren *et al.* realized a maximum efficiency of 12.7% with a higher J_{sc} of 16.15 mAcm^{-2} by co-sensitizing two dyes R7 and Y123.¹⁰² Recently Wu *et al.* co-sensitized two carbazole based dyes C260A and C272 which reached to an impressive PCE of 11.0%, notably it is the only report where any organic dye other than TPA is used for co-sensitization.¹⁰³ In copper electrolyte based DSC, co-sensitization of dyes is significantly important as it prevents recombination while providing better light harvesting properties. In copper electrolyte based DSC co-sensitization of dyes other than TPA is hardly explored. In all the highly efficient copper electrolyte based DSC, XY1/XY1b or its derivatives are used as the primary dye. Notably IPCE spectra of DSC with co-sensitized dyes is largely similar to the DSC with primary dye leading to very small improvement in J_{sc} and PCE (**Figure 1. 18**). Co-sensitization of dyes with complimentary absorption profile and matching energetics along with copper electrolyte has the potential to further push the efficiencies $> 17\%$.

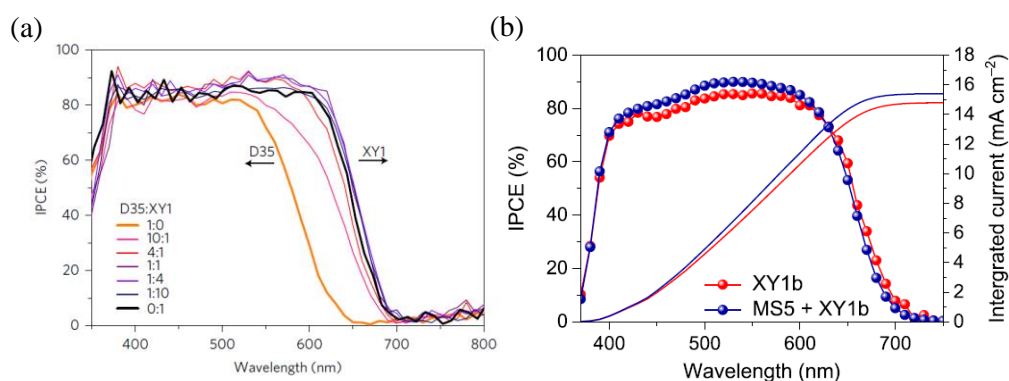


Figure 1. 18 Incident photon-to-electron conversion efficiency (IPCE) of the DSCs (a) various concentration co-sensitization of D35+XY1b and (b) XY1b and the co-sensitization of MS5+XY1b.¹⁰⁴

1.8.3. Copper Redox Mediators with Structurally Different Ligands

Copper complex endowed with faster electron transfer properties were used as mediators in natural transport systems.¹⁰⁹ In 2005 Hattori *et al.* used copper complexes for

the first time as redox mediators in DSC with a target to attain higher V_{oc} .⁷⁶ This pioneering work employing copper complexes opened up a new area of research involving alternate metal complex electrolytes in DSCs. They introduced three new copper complexes [(–)-sparteine- N,N](maleonitriledithiolato-S,S)copper ($[\text{Cu}(\text{SP})(\text{mmt})]^{0/-}$), bis(2,9-dimethyl-1,10-phenanthroline)copper ($[\text{Cu}(\text{dmp})_2]^{2+/1+}$) and bis(1,10-phenanthroline)copper ($[\text{Cu}(\text{phen})_2]^{2+/1+}$) having redox potentials of 0.29 V, 0.66 V and -0.1 V vs. SHE respectively (**Figure 1. 19 (a,b,c)**). Along with N719 sensitizer, $[\text{Cu}(\text{dmp})_2]^{2+/1+}$ showed a maximum efficiency up to 1.4% followed by $[\text{Cu}(\text{SP})(\text{mmt})]^{0/-}$ with an efficiency of 1.2% and 0.2% PCE employing $[\text{Cu}(\text{phen})_2]^{2+/1+}$ under 1 sun (100 mW/cm^2) illumination.

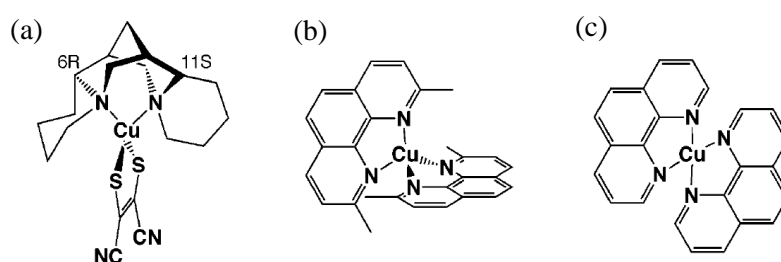


Figure 1. 19 Structures of (a) $[\text{Cu}(\text{SP})(\text{mmt})]^{0/-}$, (b) $[\text{Cu}(\text{dmp})_2]^{2+/1+}$, and (c) $[\text{Cu}(\text{phen})_2]^{2+/1+}$ complexes.⁷⁶

Later Kloo *et al.* introduced a new copper pyridyl complex $[\text{Cu}(\text{bpye})_2]^{2+/1+}$ with 1,1-bis(2-pyridyl)ethane (bpye) ligand, achieving a PCE of 9% (**Figure 1. 20**).⁹⁶ More importantly under similar conditions $[\text{Cu}(\text{bpye})_2]^{2+/1+}$ realized a J_{sc} of 13.8 mAcm^{-2} while $[\text{Co}(\text{bpy})_2]^{3+/2+}$ delivered a J_{sc} of 12.9 mAcm^{-2} . The improved J_{sc} is associated with the reduced mass transport and faster regeneration of dye using $[\text{Cu}(\text{bpye})_2]^{2+/1+}$ electrolyte.

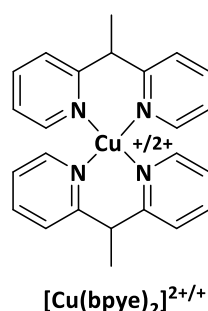


Figure 1. 20 Structures of $[\text{Cu}(\text{bpye})_2]^{2+/1+}$ complex.⁹⁶

A major breakthrough in the area of copper electrolyte was realized by Saygili *et al.* reaching the landmark efficiency of 10% with a V_{oc} of 1 V under one sun illumination using the newly synthesized copper bipyridine complexes, $[\text{Cu}(\text{dmby})_2]^{2+/1+}$ and $[\text{Cu}(\text{tmby})_2]^{2+/1+}$ along with organic Y123 sensitizer.⁷⁴ **Figure 1. 21** shows the molecular structure of $[\text{Cu}(\text{tmby})_2]^{2+/1+}$ and $[\text{Cu}(\text{dmby})_2]^{2+/1+}$. The appropriate geometry around the Cu metal helped in minimizing the reorganization energy between Cu(I) and Cu(II), thus with merely 0.1 V of driving force nearly unit regeneration was realized using these copper complexes. The photovoltaic performance was compared with $[\text{Cu}(\text{dmp})_2]^{2+/1+}$ and the results are summarized in **Table 1. 2**.

Table 1.2 PV performance of DSC employing $[\text{Cu}(\text{tmby})_2]^{2+/1+}$, $[\text{Cu}(\text{dmby})_2]^{2+/1+}$ and $[\text{Cu}(\text{dmp})_2]^{2+/1+}$ electrolytes with Y123.

Redox mediator	Redox potential vs. SHE	Inner sphere reorganization energy (λ_{in} eV)	V_{oc} (V)	J_{sc} (mAcm^{-2})	FF	η (%)
$[\text{Cu}(\text{tmby})_2]^{2+/1+}$	0.87	0.281	1.04	15.53	0.64	10.30
$[\text{Cu}(\text{dmby})_2]^{2+/1+}$	0.97	0.301	1.0	14.15	0.68	10.00
$[\text{Cu}(\text{dmp})_2]^{2+/1+}$	0.93	0.294	1.06	13.61	0.69	10.30

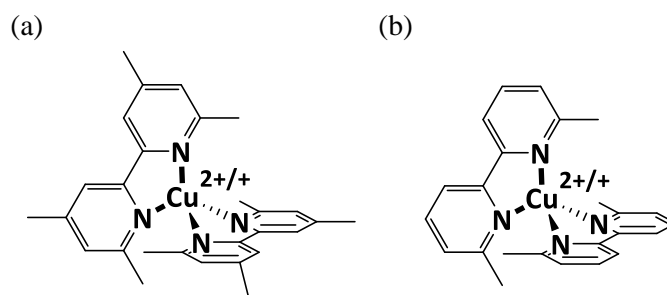


Figure 1. 21 Molecular structure of (a) $[\text{Cu}(\text{tmby})_2]^{2+/1+}$ and (b) $[\text{Cu}(\text{dmby})_2]^{2+/1+}$ complexes.⁷⁴

Copper complexes with tetradentate ligands has garnered much attraction owing to its long-term stability, derived from the chelate effect which impedes the ligand exchange process and ligand loss. Faster self-exchange rate and less visible light absorption are some of the additional features which makes them an attractive alternative to conventional bidentate Cu complex redox couples used in DSCs. In recent years numerous tetradentate

ligands based copper complexes have been tested as redox mediators in DSCs. Michaels *et al.* reported a new copper complex $[\text{Cu}(\text{oxabpy})]^{2+/1+}$ using 6,6'-bis(4-(S)-isopropyl-2-oxazoliny)-2,2'-bipyridine as coordinating tetradentate ligand (**Figure 1. 22**).¹¹⁰ With the coordination of Cu metal center to four N atoms, the molecular geometric rearrangement between Cu^{I} to Cu^{II} was reduced, favouring faster dye regeneration with minimum energy loss. The new redox mediator displayed an efficiency of 6.6% ($J_{\text{sc}}-9.75 \text{ mAcm}^{-2}$, $V_{\text{oc}}-0.92 \text{ V}$ and $FF-0.69$) when used with organic Y123 sensitizer. The remarkably higher V_{oc} of 0.92 V realized using $[\text{Cu}(\text{oxabpy})]^{2+/1+}$ with a more negative redox potential of 0.66 V vs. NHE in comparison to conventional Cu-bipyridine redox mediator is attributed to slower recombination at $\text{TiO}_2/\text{electrolyte}$ interface.

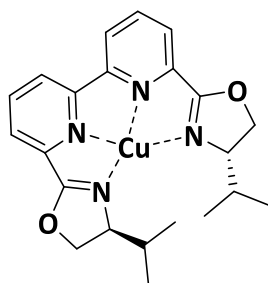


Figure 1. 22 Molecular structure of $[\text{Cu}(\text{oxabpy})]^{2+/1+}$ complex.¹¹⁰

In another study, Hu *et al.* introduced two new diamine-dipyridine tetradentate ligands (L1 = N,N'-dibenzyl-N,N'-bis-(pyridin-2-ylmethyl)ethylenediamine and L2 = N,N'-dibenzyl-N,N'-bis(6-methylpyridin-2-ylmethyl)ethylenediamine) to synthesize corresponding copper metal complexes.¹¹¹ The structure of L1 and L2 (**Figure 1. 23**) are nearly same with L2 having a methyl group attached to the ortho and para position of pyridine unit. The imposition of steric hindrance by L2 due to the presence of two methyl groups pushed the redox potential to 0.61 V vs. NHE for $\text{Cu}(\text{L2})$ which is 300 mV more

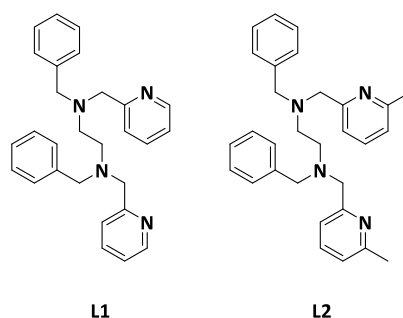


Figure 1. 23 Molecular structure of L1 and L2 tetradentate ligands. ¹¹¹

positive than the redox potential of Cu(L1) (0.31 V vs. NHE). Using $[\text{Cu}(\text{L1})]^{2+/1+}$ and $[\text{Cu}(\text{L2})]^{2+/1+}$ an efficiency of 9.2% and 5.0% was realized when used with Y123 sensitizer. It is to be noted in particular that the introduction copper redox mediators with less positive redox potentials opens up the opportunity to use sensitizers with narrow band gap without compromising regeneration.

Majority of the Cu complexes used as redox mediators in DSCs contains copper attached to nitrogen coordinating ligands. For the first time Zhao *et al.* synthesized copper complex $[(\text{S4})\text{Cu}]^{2+/1+}$ using tetradentate ligand with sulphur coordinate to Cu metal center and compared with $[(\text{N4})\text{Cu}]^{2+/1+}$ with nitrogen coordinate to Cu metal center (**Figure 1. 42 (a,b)**).¹¹² Owing to the longer bond length, redox potential of $[(\text{S4})\text{Cu}]^{2+/1+}$ was 0.91 V vs. NHE, 600 mV more positive than the redox potential of $[(\text{N4})\text{Cu}]^{2+/1+}$ (0.31 V vs. NHE). Both $[(\text{S4})\text{Cu}]^{2+/1+}$ and $[(\text{N4})\text{Cu}]^{2+/1+}$ efficiently regenerate Y123 dye with a regeneration efficiency of 89% and 90% respectively realizing an efficiency of 8.4% and 3.7% with respectively.

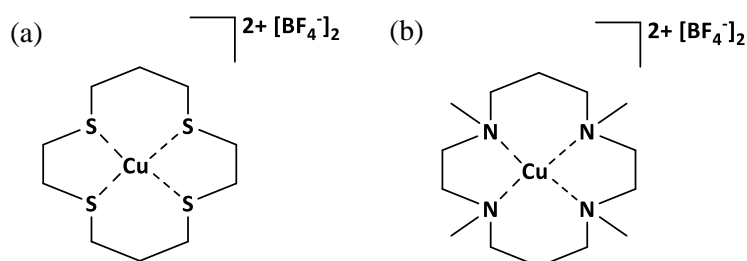


Figure 1. 24 Molecular structure of (a) $[(\text{S4})\text{Cu}]^{2+}$ (b) $[(\text{N4})\text{Cu}]^{2+}$ complexes. ¹¹²

Further, Yang *et al.* synthesised two copper complexes namely $[\text{Cu}(\text{mpdt})_2]\text{TFSI}_{(2/1)}$ (mpdt = 1,4-dimethylpiperazine-2,3-dithione) and $[\text{Cu}(\text{ppdt})_2]\text{TFSI}_{(2/1)}$ (ppdt = 1,4-diisopropylpiperazine-2,3-dithione) with Cu-S coordination. $[\text{Cu}(\text{mpdt})_2]^{2+/1+}$ showcased a PCE of 9.9% while $[\text{Cu}(\text{ppdt})_2]^{2+/1+}$ realized a PCE of 9.1% (**Figure 1. 25 (a)**).¹¹³ Later Li *et al.* synthesised two new sulfur coordinated copper complexes having bis(2-pyridylmethyl)-1,2-ethanedithiol as ligand and tetrafluoroborate- $[\text{BF}_4]$ and hexafluorophosphate- $[\text{PF}_6]$ as counter ions (**Figure 1. 25 (b)**).¹¹⁴ Owing to higher solubility and faster diffusion for PF_6 counter ion based copper redox mediator achieved PCE of 10.3% while BF_4 counter ion based copper redox mediator reached PCE of 7.9%. This is the highest PCE reported for a DSC with sulfur-copper complex as redox mediator.

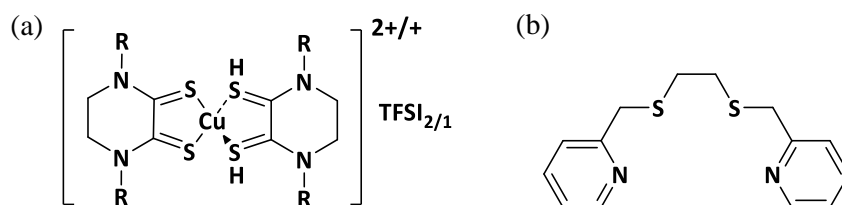


Figure 1. 25 Molecular structure of (a) 1,4-dialkylpiperazine-2,3-dithione based copper complex and (b) bis(2-pyridylmethyl)-1,2-ethanedithiol ligand.^{113,114}

1.8.4. Additive Modification in Copper Electrolytes

Formulation of copper electrolytes with appropriate additives in right proportions play a significant role in realizing higher PV performance while used in DSCs. The critical charge transfer processes such as dye regeneration, charge recombination, regeneration of oxidized species at the counter electrode and mass transport can be well regulated by tuning the ratio of oxidized and reduced species and also by modifying the additives used in electrolyte. In general, for efficient DSCs using copper redox mediators a concentration ratio of 5:1 for reduced and oxidized copper (i.e. 0.2 M Cu(I) and 0.04 M Cu(II)) with 0.1 M LiTFSI or LiClO_4 and 0.5 M/0.6 M tBP is used widely in literature. Indeed, we cannot assume this to be a generalized composition that can be used for all the dye and electrolyte combinations. Since the reduced species in electrolyte regenerates the oxidized dye, the concentration of reduced species (Cu^{I}) is generally taken higher than the oxidized species (Cu^{II}). In principle, additives increase the solubility and conductivity of the electrolyte thus influencing electron injection, charge recombination, reaction at counter electrode and regeneration. Lithium salts (LiTFSI, LiClO_4) and pyridine bases (tBP and NMBI) are two

such prominent additives which are widely used in copper electrolytes for higher photovoltaic performance. Li^+ improves the conductivity and at the same time shifts the conduction band of the semiconductor towards positive potential improving injection yield.^{39,115} On the other hand, the pyridine bases like tBP and NMBI deprotonates the semiconductor and shifts the CB towards more negative potentials thus increasing the chances to realize higher open-circuit potential.^{116,117} It also passivates the exposed semiconductor surface (semiconductor surface which is not covered with the dye) and prevents recombination at semiconductor-electrolyte interface leading to improved lifetime and PCEs. The pyridine bases like tBP and NMBI are non-innocent and coordinates with the Cu metal replacing the ligands leading to changes in both optical and electrochemical properties.

In the very first study carried out by Hattori *et al.* using copper electrolytes, they did an extensive optimization of oxidised and reduced species of $[\text{Cu}(\text{dmp})_2]^{2+/1+}$ in the electrolyte formulation.⁷⁶ The best performance was realized with $\text{Cu}^{\text{II}}/\text{Cu}^{\text{I}}$ ratio of 0.4 (Cu^{I} of 0.12 M and Cu^{II} of 0.08 M). **Figure 1. 26** shows the plot of $\text{Cu}^{\text{II}}/\text{Cu}^{\text{I}}$ ratio as a function of efficiency (η) measured at 100 mWcm^{-2} .

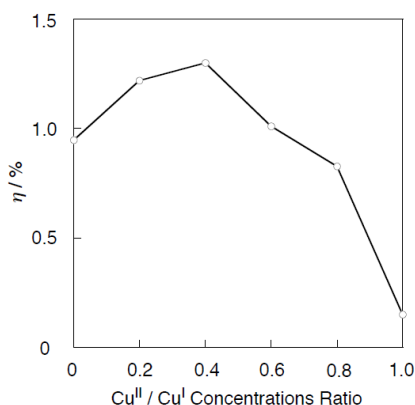
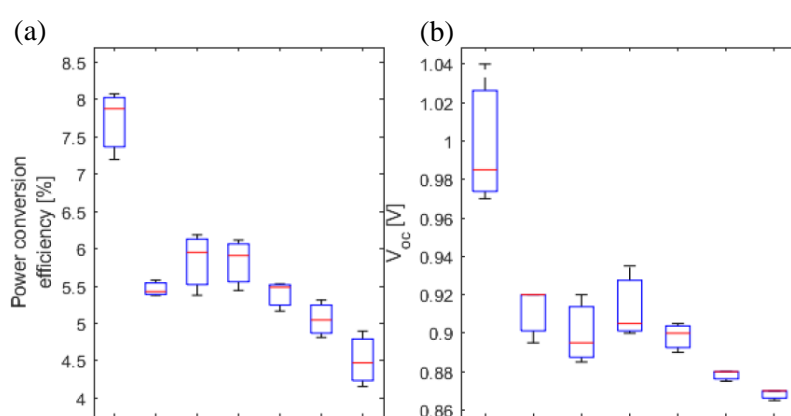


Figure 1. 26 Efficiency (η) vs. the $\text{Cu}^{\text{II}}/\text{Cu}^{\text{I}}$ ratio of DSCs using $[\text{Cu}(\text{SP})(\text{mmt})]^{0/-}$ as redox mediator under 1 sun illumination.⁷⁶

Using $[\text{Cu}(2\text{-mesityl-4,7-dimethyl-1,10-phenanthroline})_2]\text{PF}_6$ redox mediator, Colombo *et al.* used Cu(I) concentration of 0.1 M and 0.15 M by maintaining $\text{Cu}^{\text{II}}/\text{Cu}^{\text{I}}$ ratio of 0.05.⁸⁵ With increase in Cu (I) concentration, the J_{sc} was found to first increase followed by a drop in V_{oc} and FF , ultimately the PCE remained almost unaltered. However, addition of co-mediator ($[\text{Fe}(\text{dmo-bpy})_3]^{2+}$ or $[\text{Fe}(\text{dtb-bpy})_3]^{2+}$) in the electrolyte, further pushed the

redox potentials to more positive value providing more driving force for dye regeneration leading to an increase in J_{sc} of 0.7 mAcm^{-2} and 2 mAcm^{-2} respectively, conversely V_{oc} and FF reduced owing to higher recombination. In way to increase the V_{oc} , 0.1 M tBP was introduced in to the electrolyte formulation. This contributed to an increase in V_{oc} by 7 mV and 16 mV respectively, however J_{sc} decreased as the driving force for injection reduced as a result of negative shift in TiO_2 conduction band. In another study, the same group carried out further modifications to the Cu electrolytes by changing its concentration to achieve higher PCE.⁹¹ Both Cu(I) and Cu(II) complexes were diluted by a factor 2 and 4.5 (initial concentration of Cu(I) and Cu(II) were 0.17 M and 0.017 M respectively) and found that dilution increases V_{oc} , J_{sc} and FF leading to enhanced PCE. Upon dilution, J_{sc} in particular increased significantly due to reduced competitive light absorption by the copper electrolyte.

Similarly, Michaels *et al.* demonstrated the optimization of $[\text{Cu}(\text{oxabpy})_2]^{2+/1+}$ composition where Cu(I)/Cu(II) in the ratio of 5:1 (0.2 M Cu(I), 0.04 M Cu(II)) showed the highest efficiency.¹¹⁰ With increase in Cu(II) content V_{oc} , J_{sc} and PCE got reduced, nonetheless the FF remain mostly unaltered. The reduction in PCE was associated with the inferior electron lifetime and dye regeneration. Notably, DSCs made with Cu electrolyte formulations without using Cu(II) also showcased comparable PCE. The statics of PV parameters with different composition of copper complexes are provided in **Figure 1. 27**.



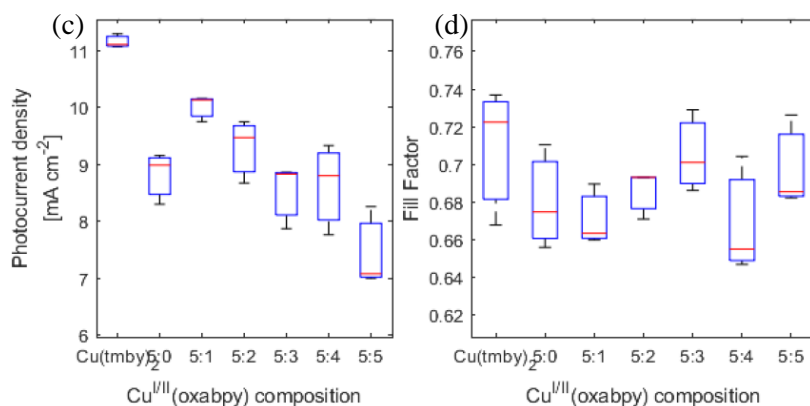


Figure 1.27 (a) PCE, (b) V_{oc} , (c) J_{sc} and FF of the $[\text{Cu}(\text{tmby})_2]^{2+/1+}$ reference electrolyte (left) and $[\text{Cu}(\text{oxabpy})_2]^{2+/1+}$ with respect to the addition of $\text{Cu}^{\text{II}}(\text{oxabpy})$ to the electrolyte (5:0 = Cu(I) only, 5:1 = standard electrolyte 0.2 M Cu(I), 0.04 M Cu(II)).¹¹⁰

To reduce the competitive absorption, Yang *et al.* fabricated devices with varying concentrations of $[\text{Cu}(\text{mpdt})_2]^{2+/1+}$ redox mediator.¹¹³ The statics of PV parameters with different composition of copper complexes are provided in **Table 1.3**. With increase in Cu(I)/Cu(II) concentration, V_{oc} was found to decrease due to more recombination. Maximum J_{sc} was obtained at 0.05 M concentration of Cu(I) owing to optimum balance between dye regeneration and competitive light absorption. Ultimately the best PCE of 9.8% was achieved using 0.05 M concentration of Cu(I) and 0.02 M concentration of Cu(II). It is to be noted that the standard concentration of Cu(I) and Cu(II) are 0.2 M and 0.04 M respectively. Since the diffusion coefficient of $[\text{Cu}(\text{mpdt})_2]^{2+/1+}$ is comparatively higher to that of conventional Cu complexes using bidentate ligands, the authors succeeded in achieving higher efficiency even in such lower concentrations.

Table 1.3 J - V parameters of the $[\text{Cu}(\text{mpdt})_2]^{2+/1+}$ at different concentrations.

$[\text{Cu}(\text{mpdt})]^+$	$[\text{Cu}(\text{mpdt})]^{2+}$	V_{oc} (mV)	J_{sc} (mAcm ⁻²)	FF	η (%)
0.02	0.04	1020	11.4	0.68	7.8
0.05	0.04	956	14.9	0.67	9.6
0.1	0.04	926	10.9	0.72	7.4
0.05	0.1	914	8.0	0.74	5.3
0.05	0.05	950	12.6	0.73	8.9
0.05	0.02	952	14.1	0.73	9.8
0.05	0.01	962	13.7	0.74	9.7

Kavan *et al.* observed that the addition of tBP induces mass transport limitation in Cu electrolyte DSCs and they proposed for the need of introducing other alternative to replace tBP.¹¹⁸ Later Ferdowsi *et al.* introduced three new pyridine complexes 2,6-bis-tert-butylpyridine (BTBP), 4-methoxypyridine (MOP) and 4-(5-nonyl) pyridine (NOP) as potential alternative pyridine bases to tBP.¹¹⁹ Out of these, NOP emerged as a best alternative to tBP with a PCE of 9.4% compared to 9.3% using tBP using Y123 sensitizer. Additionally, NOP based devices also exhibited comparable device stability with respect to tBP. The PV performance are summarised in **Table 1.4.**

Table 1. 4 PV characteristics studied using Cu-mediated DSCs with different bases and Y123 as sensitizer under 1 sun (AM1.5G) condition.

Base	V_{oc} (V)	J_{sc} (mAcm ⁻²)	FF	η (%)
TBP	1.080	11.23	0.76	9.3
BTBP	0.846	8.77	0.67	5.1
MOP	1.079	10.61	0.74	8.6
NOP	1.075	12.01	0.71	9.4

1.8.5. Counter Electrodes Used with Copper Electrolytes

Counter electrode (CE) enables smooth charger transfer from external circuit back to the electrolyte and vice versa. The catalyst layer used in counter electrodes accelerates this charger transfer process. An ideal CE must possesses 80% optical transparency, <20 Ω sq⁻¹ sheet resistance (R_{sq}), and 2–3 Ω cm² charge transfer resistance (R_{ct}).^{120–125} Platinum (Pt) based CEs deposited by printing technique is considered to be the best choice to use with conventional I⁻/I₃⁻ electrolyte even though being expensive and scarce in nature.^{126–128} Nevertheless, Pt based CE are not efficient enough to be used with alternative redox mediators particularly Cu electrolytes where catalytic layers with higher surface area is essential to realize efficient regeneration at CE. Electrochemically deposited PEDOT is used as the best alternative to Pt in Cu electrolyte DSCs.

In the first report of DSC using copper redox mediator, Hatteri *et al.* used sputtered Pt as counter electrode to attain a PCE of 1.4%.⁷⁶ Bai *et al.* later enhanced the PCE to 7% by modifying the device structure, replacing Pt counter electrode with carbon based counter

electrodes.⁷⁷ Hoffeditz *et al.* quantitatively presented the need of high surface area CE material for Cu electrolyte based DSCs.¹²⁹ They compared standard thermally deposited (TD) Pt counter electrodes with 50 fold higher surface area inverse opal (IO) Pt counter electrode deposited via atomic layer deposition. Higher surface area increased the catalytic activity and consequently decreased the dark current enhancing the *FF* from 0.28 to 0.5 leading to 80% augmentation in PCE (1% for TD and 1.8% for IO). The *J-V* curve provided in **Figure 1. 28** shows the impact of high surface area CE on *FF*.

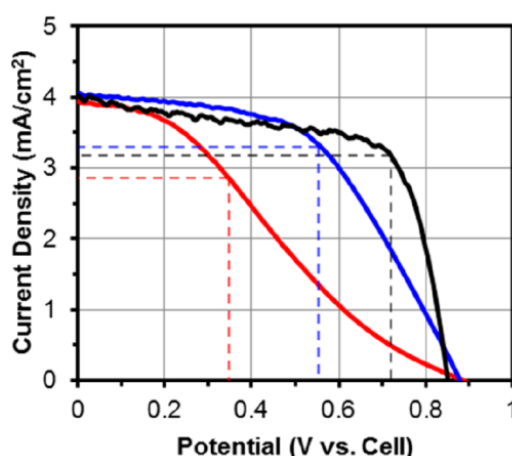


Figure 1. 28 *J-V* curves for DSCs utilizing $[\text{Cu}(\text{PDTO})]^{2+/1+}$ redox shuttle and TD Pt dark electrode (red), IO Pt dark electrode (blue), and in a three-electrode (blue), and in a three-electrode (as opposed to two electrode) set up (black). Dashed lines represent the maximum power points of the individual *J-V* curves.¹²⁹

Magni *et al.* compared PEDOT and Pt CE using two different copper redox electrolytes, tetracoordinated $[\text{Cu}(\text{2-mesityl-4,7-dimethyl-1,10-phenanthroline})_2]$ (1/2) and pentacoordinated $[\text{Cu}(\text{2-mesityl-4,7-dimethyl-1,10-phenanthroline})_2]$ (3/4). They analysed symmetrical PEDOT/PEDOT and Pt/Pt cells filled with either 1/2 or 3/4 redox shuttle using electrochemical impedance spectroscopy (EIS), the obtained parameters are summarised in **Table 1. 5**.¹³⁰ Charge transfer resistance at CE/electrolyte interface (R_{ce}) decreased drastically using PEDOT counter electrode compared to Pt, however Pt counter electrode showed lower sheet resistance (R_{series}) than PEDOT counter electrode.

DSC using 1/2 redox couple and organic sensitizer G3 with Pt counter electrode delivered a PCE of 4.4% (V_{oc} -0.72 V, J_{sc} -9.3 mAcm^{-2} and *FF*-0.66) while DSC with PEDOT counter electrode contribute to a PCE of 4.1% (V_{oc} -0.74 V, J_{sc} -8.2 mAcm^{-2} and

Table 1.5 EIS parameters of symmetrical PEDOT/PEDOT cell and Pt/Pt cells filled with either 1/2 or 3/4 redox shuttle.

Electrolyte	Cathode	R_{series} (Ω)	R_{CE} (Ω)	$C_{CE} \times 10^5$ (F)	R_d (Ω)
1/2	Pt	21	9.8	4.05	12.8
1/2	PEDOT	37	0.82	232	14.2
3/4	Pt	39	61	1.28	164
3/4	PEDOT	53	4.4	500	223

FF-0.67). Notably, sputtered Pt electrodes were highly reflective, while PEDOT counter electrodes were transparent. In contrary, Rodrigues *et al.* found that PEDOT outperformed Pt in DSC fabricated using three different Cu redox mediators. The PV parameters are listed in **Table 1.6**.¹³¹

Table 1.6 PV parameter of DSCs using PEDOT and Pt counter electrodes.

Redox Mediator	Counter Electrode	V_{oc} (mV)	J_{sc} (mAcm ⁻²)	FF	η (%)
[Cu(2)] ^{2+/1+}	PEDOT	693	10.2	0.72	4.7
	Pt	641	14.1	0.45	4.1
[Cu(3)] ^{2+/1+}	PEDOT	792	7.9	0.75	4.3
	Pt	678	10.2	0.45	3.2
[Cu(bpye) ₂] ^{2+/1+}	PEDOT	627	13.2	0.65	5.6
	Pt	651	9.7	0.48	3.1

Though PEDOT is considered as a standard counter electrode to use in copper electrolyte based efficient DSCs, with passage of time, PEDOT CEs releases a large number of undesired anions that alters the composition of the redox mediator, affecting the long term photovoltaic performance. Thus, Marchini *et al.* used polymeric dopants which can block the unwanted anion release by PEDOT CEs.¹³² They doped Nafion (NAF), ClO₄ (PER) and PSS (PSS) with PEDOT. PER outperformed NAF and PSS. The PV parameters are summarized in **Table 1.7**. However, both NAF and PSS displayed better mechanical stability than PER.

Table 1. 7 PV parameters of DSC using D35 dye and $[\text{Cu}(\text{tmby})_2]^{2+/1+}$ electrolyte with different counter electrodes.

Counter electrode	V_{oc} (V)	J_{sc} (mAcm^{-2})	FF	η (%)
PER	1.09	7.4	0.63	5.0
NAF	1.08	6.8	0.59	4.3
PSS	1.07	6.6	0.42	3.0

Recently, Hashmi *et al.* used single walled carbon nanotube (SWCNT) as alternative counter electrode along with copper electrolytes.¹³³ SWCNT was deposited by screen printing followed by annealing at 120 °C for 20 minutes. SWCNT showcased higher surface area with larger porosity than the thermally platinized Pt CEs. SWCNT got a low R_{ct} of 2.1-2.9 Ωcm^2 with $[\text{Cu}(\text{dmp})_2]^{2+/1+}$ redox mediator. DSCs fabricated with SWCNT CE showed a PCE of 7.5% (V_{oc} -0.972 V, J_{sc} -11.60 mAcm^{-2} and FF -0.66), under similar conditions DSCs with Pt CE showed a PCE of 6.5% (V_{oc} -0.976 V, J_{sc} -10.3 mAcm^{-2} and FF -0.65).

Electrochemically deposited PEDOT counter electrodes are extensively used and is proven to be the best counter electrodes for DSC with copper electrolyte to realize higher photovoltaic performance. However, its stability with various copper redox shuttles is yet to be explored. Moreover, there are numerous catalytic materials which can prove to be a better candidate than PEDOT counter electrode when used along with Cu redox shuttles which need to be explored in future to further enhance the PCE of Cu electrolyte based DSCs.

1.8.6. Interfacial Charge Dynamics using Copper Redox Electrolytes

1.8.6.1. TiO_2/dye Interface

Using time-correlated single-photon counting (TCSPC) technique Bai *et al.* estimated an injection efficiency of 89% and 91% using C218 organic dye soaked TiO_2 photoanodes in presence I^-/I_3^- and $[\text{Cu}(\text{dmp})_2]^{2+/1+}$ electrolyte respectively.⁷⁷ They observed that in presence of $[\text{Cu}(\text{dmp})_2]^{2+/1+}$ conduction band of TiO_2 got negatively shifted by 0.04 eV compared to the iodide electrolyte. In another study Glanka *et al.* found that electron injection is accelerated with steady state illumination owing to the decrease in the energy

of TiO₂ CB, and this observation was found applicable in both MK2 and Y123 sensitizers used along with [Cu(tmby)₂]^{2+/1+}, redox mediator.¹³⁴ Further Freitag *et al.* observed that [Cu(dmp)₂]²⁺ species quenches the excited sensitizer LEG4 which further competes with electron injection and diminishes J_{sc} .⁷⁵

1.8.6.2. Dye/Electrolyte Interface

Dye/electrolyte interface play a critical role in determining the performance of DSCs, in particular while using copper electrolytes as dye regeneration occurs at this interface. For efficient dye regeneration enough amount of reduced species must be present in the electrolyte formulation with sufficient driving force for electron transfer. Faster regeneration with minimum driving force is essential to gain higher J_{sc} and V_{oc} . Regeneration efficiency (ϕ_{reg}) is calculated using the equation,

$$\phi_{reg} = \frac{k_{reg}}{k_{reg} + k_{rec}} \approx 1 - \frac{t_{1/2redox}}{t_{1/2inert}} \quad (19)$$

Where, k_{rec} is the first order recombination kinetics, k_{reg} is pseudo first order regeneration kinetics, $t_{1/2redox}$ and $t_{1/2inert}$ are half lifetime in presence of redox mediator, and inert electrolyte. Freitag *et al.* estimated the regeneration of LEG4 dye along with [Cu(dmp)₂]^{2+/1+} and observed regeneration half lifetime is 1.3 μ s leading to a ϕ_{reg} efficiency of ~100%.⁷⁵ It is to be noted that unit regeneration efficiency was realised with merely 0.2 eV of regeneration driving force. Further regeneration kinetics of Y123 dye along with [Cu(dmp)₂]^{2+/1+}, [Cu(dmby)₂]^{2+/1+} and [Cu(tmby)₂]^{2+/1+} electrolytes were analysed in detail by Saygili *et al.* **Figure 1. 29** shows the PIA and TAS spectra of Y123 dye along with [Cu(dmp)₂]^{2+/1+}, [Cu(dmby)₂]^{2+/1+} and [Cu(tmby)₂]^{2+/1+} and inert electrolyte.⁷⁴ Regeneration half life time for [Cu(dmp)₂]^{2+/1+}, [Cu(dmby)₂]^{2+/1+} and [Cu(tmby)₂]^{2+/1+} was found to be 2.8 μ s, 4.8 μ s, and 1.8 μ s respectively. The regeneration lifetime increased with decrease in driving force of regeneration. Here they noted unit regeneration yield even with a mere driving force of 0.1 V vs. NHE. Similarly, Li *et al.* found that [Cu(tmby)₂]^{2+/1+} regenerates oxidized Y123 dye with a half lifetime of 0.6 μ s leading to a regeneration efficiency of 95%.¹³⁵

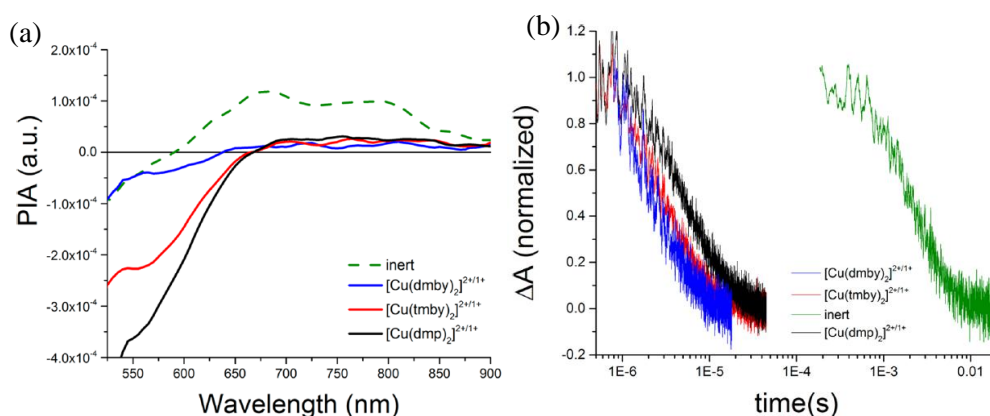


Figure 1.29 (a) PIA spectra and (b) TAS spectra of Y123 dye along with $[\text{Cu}(\text{dmp})_2]^{2+/1+}$, $[\text{Cu}(\text{dmby})_2]^{2+/1+}$, $[\text{Cu}(\text{tmby})_2]^{2+/1+}$ and inert electrolyte.⁷⁴

Freitag *et al.* found immense variation in the rate of dye regeneration with different ratios of primary and secondary dye in a co-sensitized device.⁸⁰ For instance, it varies from $1.1 \mu\text{s}$ to $5.2 \mu\text{s}$ with different ratios of D35 and XY1 sensitizers in co-sensitized DSC with $[\text{Cu}(\text{tmby})_2]^{2+/1+}$ redox mediator. Moreover, the obtained regeneration efficiency remained $>99\%$ for all the different ratio being used. **Figure 1.30** shows the time-resolved laser spectroscopy of interfacial electron transfer that involve D35 and XY1 sensitizers in presence of electrolyte. Similarly, Tanaka *et al.* observed a regeneration lifetime of $1.7 \mu\text{s}$ in DSC using co-sensitized XY1 + 5T photoanode along with $[\text{Cu}(\text{tmby})_2]^{2+/1+}$ redox mediator, while 5T and XY1 sensitizers realized regeneration lifetime of $0.7 \mu\text{s}$ and $1.9 \mu\text{s}$ respectively.¹⁰⁷

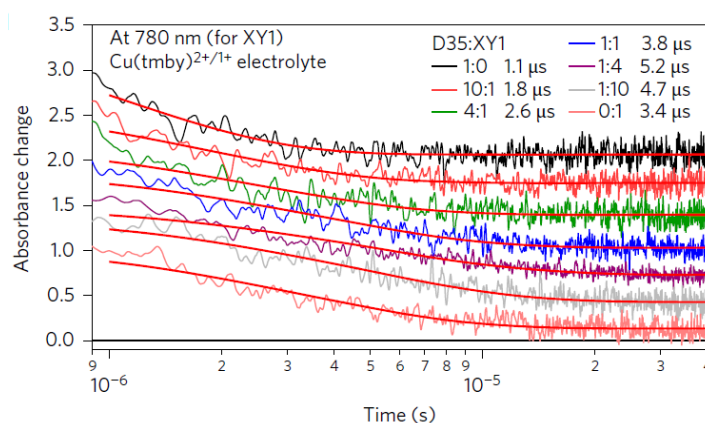


Figure 1.30 Transient absorption spectra of D35 and XY1 sensitized photoanode at various ratio in presence of $[\text{Cu}(\text{tmby})_2]^{2+/1+}$.⁸⁰

Conceptually higher concentration of Cu(I) should promote faster dye regeneration, however Michaels *et al.* found that dye regeneration is also influenced by Cu(II) concentration.¹¹⁰ The regeneration time and efficiency are summarised in **Table 1. 8**.

Table 1. 8 Regeneration times and efficiencies for Y123-sensitized photo-anodes in inert and Cu(oxabpy) electrolyte, by addition of Cu^{II} into the electrolyte

Electrolyte	$\tau_{1/2}(\mu\text{s})$	$\phi_{\text{reg}} (\%)$
Inert	104	-
Cu ^I (oxabpy)	6.19	94.0
Cu ^{II} (oxabpy) 5:1	6.33	93.9
Cu ^{II} (oxabpy) 5:2	6.70	93.5
Cu ^{II} (oxabpy) 5:3	7.39	92.9
Cu ^{II} (oxabpy) 5:4	8.52	91.8
Cu ^{II} (oxabpy) 5:5	12.6	87.9

With the increase in Cu(II) concentration, they observed a reduction in the rate of dye regeneration and they ascribed this to the hindrance caused by Cu(II) towards the regeneration process carried out by Cu(I).

1.8.6.3. Semiconductor/Electrolyte Interface

$[\text{Cu}(\text{dmp})_2]^{2+/1+}$, $[\text{Cu}(\text{dmby})_2]^{2+/1+}$ and $[\text{Cu}(\text{tmby})_2]^{2+/1+}$ are three highly efficient standard copper redox mediators used in DSCs. Saygili *et al.* observed highest lifetime for $[\text{Cu}(\text{tmby})_2]^{2+/1+}$ followed by $[\text{Cu}(\text{dmp})_2]^{2+/1+}$ and $[\text{Cu}(\text{dmby})_2]^{2+/1+}$.⁷⁴ **Figure 1. 31 (a)** shows lifetime as a function of Fermi voltage for $[\text{Cu}(\text{tmby})_2]^{2+/1+}$, $[\text{Cu}(\text{dmp})_2]^{2+/1+}$ and $[\text{Cu}(\text{dmby})_2]^{2+/1+}$. The study showed driving force dependent lifetime correlation, where $[\text{Cu}(\text{tmby})_2]^{2+/1+}$ with lower driving force owing to a redox potential of 0.87 V vs. NHE realized better lifetime, while lifetime for $[\text{Cu}(\text{dmp})_2]^{2+/1+}$ and $[\text{Cu}(\text{dmby})_2]^{2+/1+}$ decreased as driving force for recombination increased. Similarly in another study carried out by Saygili *et al.* using $[\text{Cu}(\text{beto})_2]^{2+/1+}$ and $[\text{Cu}(\text{beto}_{20\text{X}})_2]^{2+/1+}$ better lifetime was observed compared to $[\text{Cu}(\text{tmby})_2]^{2+/1+}$ as both the redox mediators possess more negative redox potential leading to lower recombination driving force.⁷³ **Figure 1. 31 (b)** shows lifetime as a function of Fermi voltage for $[\text{Cu}(\text{beto})_2]^{2+/1+}$, $[\text{Cu}(\text{beto}_{20\text{X}})_2]^{2+/1+}$ and $[\text{Cu}(\text{tmby})_2]^{2+/1+}$ electrolyte based DSCs.

Charge recombination at TiO₂/electrolyte interface also gets reduced with the increase in bulkiness of the dye or electrolyte. Zhang *et al.* studied the charge transfer of

Y123, WS70 and WS72 dyes along with $[\text{Cu}(\text{tmby})_2]^{2+/1+}$ electrolyte using EIS and found that the charge transfer resistance increases with increase in bulkiness of the dye.⁹⁸ **Figure 1. 32** shows charge transfer resistance at $\text{TiO}_2/\text{dye}/\text{electrolyte}$ interfaces for devices fabricated using Y123, WS-70 and WS-72 dyes employing $[\text{Cu}(\text{tmby})_2]^{2+/1+}$. Similarly, Jiang *et al.* proposed comparatively higher recombination resistance using HY64 that originates from its larger molecular size compared to HY63 which is effective in preventing recombination.¹⁰⁰

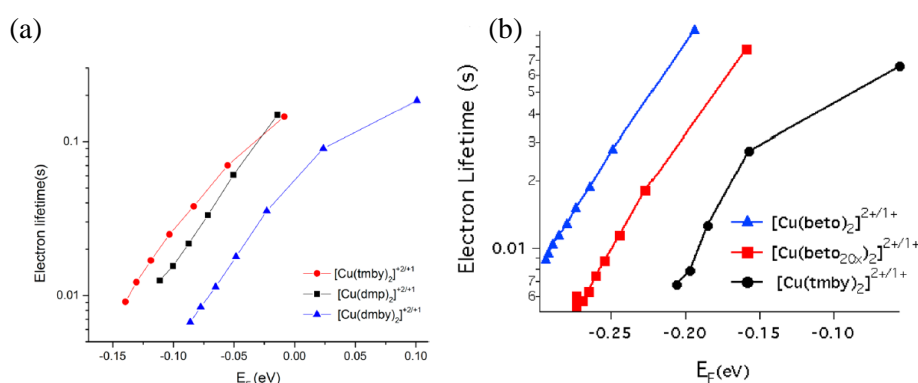


Figure 1. 31 Lifetime as a function of electron Fermi level for DSC using Y123 sensitizer along with (a) $[\text{Cu}(\text{dmp})_2]^{2+/1+}$, $[\text{Cu}(\text{dmby})_2]^{2+/1+}$ and $[\text{Cu}(\text{tmby})_2]^{2+/1+}$ (b) $[\text{Cu}(\text{beto})_2]^{2+/1+}$, $[\text{Cu}(\text{beto}_{20x})_2]^{2+/1+}$ and $[\text{Cu}(\text{tmby})_2]^{2+/1+}$.^{73,74}

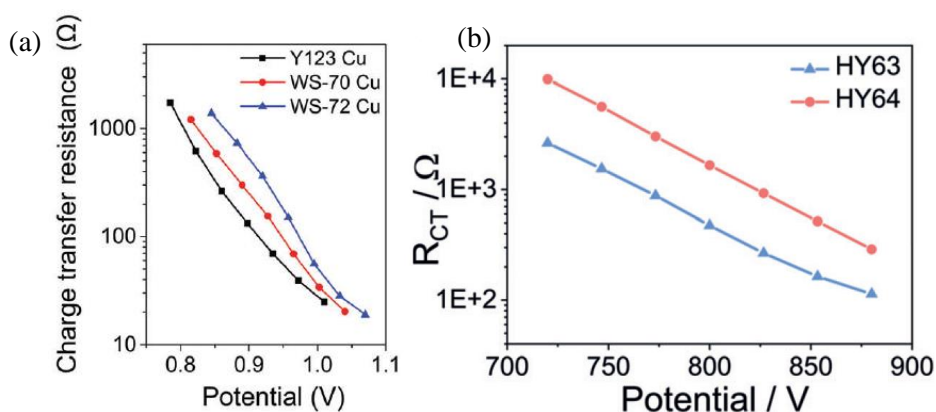


Figure 1. 32 (a) Charge transfer resistance at $\text{TiO}_2/\text{dye}/\text{electrolyte}$ interfaces for devices fabricated with dye Y123, WS-70 and WS-72 and (b) HY63 and HY64 employing $[\text{Cu}(\text{tmby})_2]^{2+/1+}$ electrolyte.^{98,100}

Wu *et al.* also observed similar trends, where comparatively larger dye, C260 delivered better lifetime than C260A.¹⁰³ Very often better lifetime is seen with co-

sensitization of dyes. For instance Freitag *et al.* observed longer lifetime with co-sensitization of XY1 and D35 dyes.⁸⁰ Michael *et al.* also realized improved lifetime with co-sensitization of L5 and XY1.¹⁰⁸ Generally, co-sensitized photoanodes contains structurally small dye molecules and bulky dye molecules, where small dye molecules fits in the vacant space available between bulky dye molecules and hence efficiently covers TiO₂ surface while bulky dye molecules keep the oxidised redox species in electrolyte away from TiO₂ surface. Overall co-sensitized photoanode reduces electron and hole interaction, leading to better lifetime.

1.8.7. Mass Transport

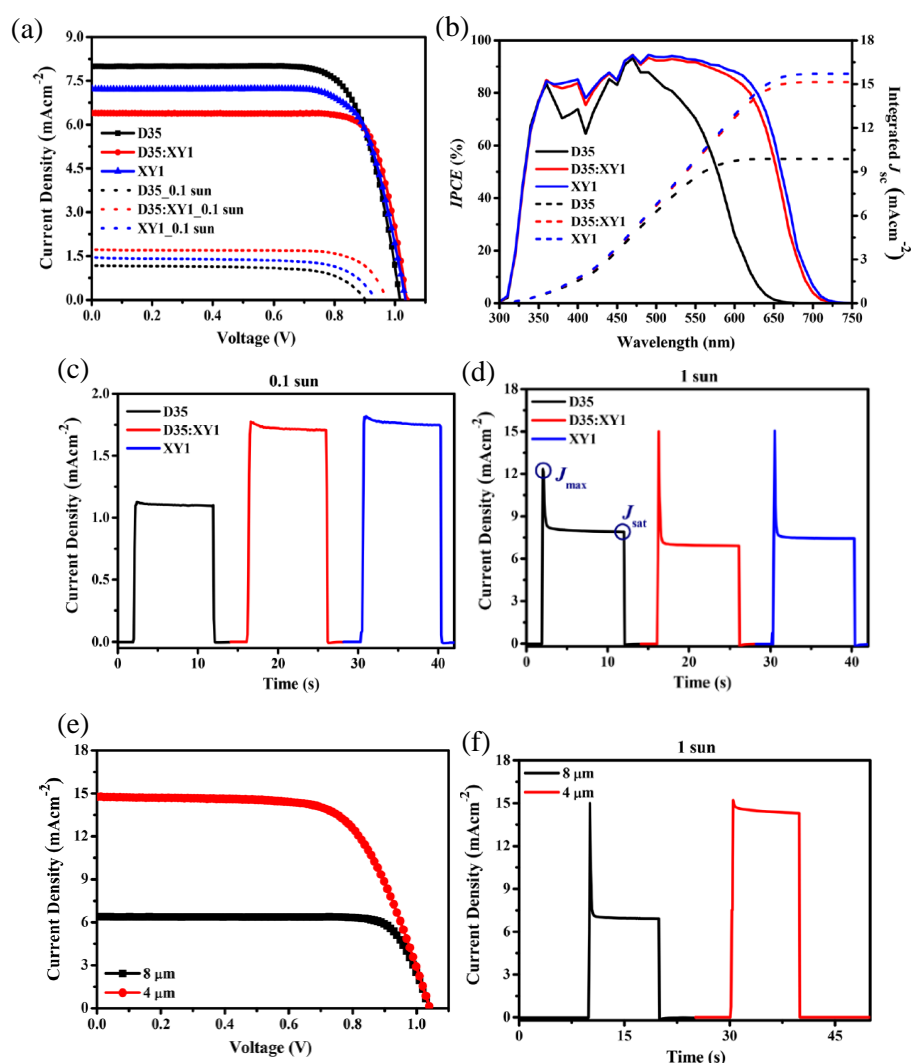


Figure 1.33 a) J - V curves for D35, D35/XY1, and XY1 at 1 sun and 0.1 sun illumination and (b) IPCE spectrum, (c,d) current transient at 0.1 sun and 1 sun for DSC with D35, D35/XY1, and XY1 along with $[\text{Cu}(\text{tmby})_2]^{2+/1+}$, (e) J - V curves for D35/XY1 with TiO₂ thickness of 4 μm and 8 μm and (f) current transient at 1 for D35/XY1 with TiO₂ thickness of 4 μm and 8 μm.¹³⁶

One of the critical charge transfer process in alternative shuttle based DSCs is mass transport. Many of the alternative redox mediators faces mass transport issues due to their-bulkiness. Mass transport is more pronounced at higher intensities. Jayadev *et al.* observed contradictory J_{sc} trend under 1 sun and 0.1 sun for DSCs with $[\text{Cu}(\text{tmby})_2]^{2+/1+}$ electrolyte- **Figure 1. 33 (a).**¹³⁶ For instance, under 1 sun illumination J_{sc} followed the trend $\text{D35} > \text{XY1} > \text{D35:XY1}$ while under 0.1 sun illumination it showed a reversal in trend, $\text{D35:XY1} > \text{XY1} > \text{D35}$. However, J_{sc} obtained from IPCE was in accordance with 0.1 sun illumination (**Figure 1. 33 (a)**). Further, current transient measurement confirmed that D35, D35:XY1 and XY1 are affected by mass transport issue at 1 sun illumination while they are free from mass transport issues under 0.1 sun illumination **Figure 1. 33 (c,d)** Further mass transport issue was addressed using thinner semiconductor layer (4 μm) in DSCs with co-sensitized D35:XY1 dyes which improved the photovoltaic performance by 47.54% **Figure 1. 33 (e)**.

Kavan *et al.* observed mass transport with the addition of tBP and was analysed it in detail using EIS of dummy cells. **Figure 1. 34 (a)** shows the Nyquist plot of symmetrical (PEDOT-PEDOT) dummy cells with $[\text{Cu}(\text{dmp})_2]^{2+/1+}$ as electrolyte.¹²⁶ The second semicircle which is the characteristic response of ion diffusion, got larger with the addition of tBP indicating higher diffusion resistance for the electrolyte. They advocated that the coordination of tBP with dmp increased the bulkiness thus leading to mass transport. In another study carried out by the same group they observed the base specific slowdown of diffusion rate.¹¹⁹ It is to be noted that the base specific slowdown of diffusion is exclusively observed in copper electrolyte while it is absent in cobalt electrolyte DSCs. They also investigated the effect of four different bases (tBP, BTBP, MOP and NOP) using symmetrical (PEDOT/PEDOT) dummy cells. The formal rate constant k_0 values are nearly invariant with base addition in Co electrolytes. On the other hand, it decreased significantly for Cu electrolytes containing tBP, NOP and MOP, but not BTBP. **Figure 1. 34** shows Nyquist plot of symmetrical (PEDOT-PEDOT) dummy cells with $[\text{Cu}(\text{tmby})_2]^{2+/1+}$ along with different bases. The estimated diffusion coefficient from EIS was found to be 3.5×10^{-5} with no base while it was 3.5×10^{-5} , 3.0×10^{-5} , 2.9×10^{-5} , 2.6×10^{-5} , 2.9×10^{-5} and 1.4×10^{-5} for MOP, tBP, NOP and BTBP respectively.

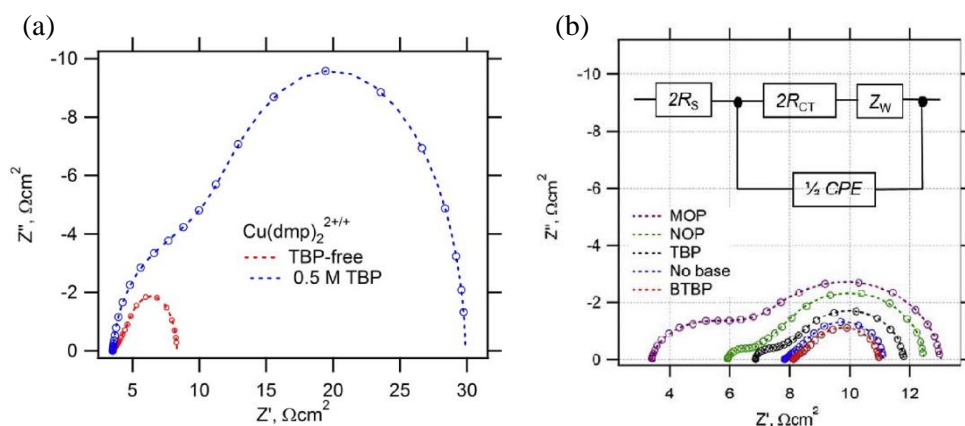


Figure 1. 34 Nyquist plot of symmetrical (PEDOT-PEDOT) dummy cells with (a) $[\text{Cu}(\text{dmp})_2]^{2+/1+}$ as electrolyte and (b) $[\text{Cu}(\text{tmby})_2]^{2+/1+}$ along with different bases. ^{119,126}

Garcia-Rodriguez *et al.* studied the mass transport issue with respect to inter electrode distance.¹³⁷ They engineered three different configuration (a) surlyn cells (b) epoxy-TiO₂ cells and (c) epoxy-TiO₂/ZrO₂ cells (**Figure 1. 35**). The third configuration was introduced to prevent direct contact of working electrode and counter electrode which very often leads to short circuit. Current transient measurement shows decrease in mass transport with decrease in inter electrode spacing.

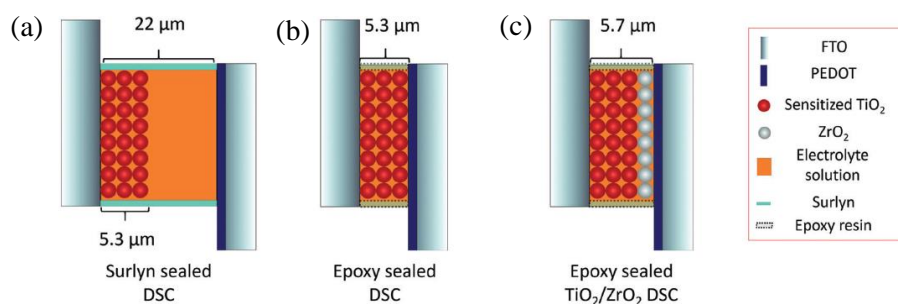


Figure 1. 35 Schematic illustration of the three different DSC configurations evaluated in this work (a) surlyn cell, (b) epoxy-TiO₂ cell and (c) epoxy-TiO₂/ ZrO₂ cell. ¹³⁷

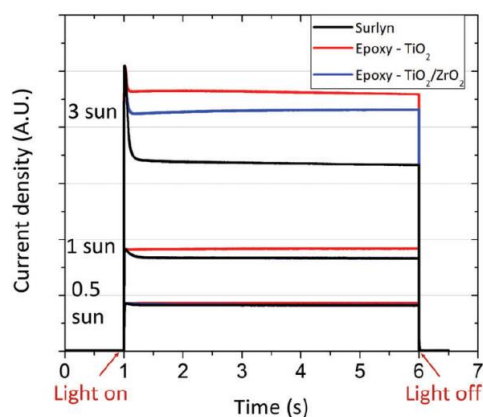


Figure 1. 36 Transient photocurrent measurements for the surlyn, epoxy-TiO₂ and epoxy-TiO₂/ZrO₂ cells. ¹³⁷

1.8.8. Innovative New Architecture used in DSCs

1.8.8.1. Zombie DSCs

Liquid electrolytes always prevents DSC to realize long term stability.¹³⁸ In a way to address stability, liquid electrolyte is replaced with solid state hole transport materials (HTMs). The most efficient HTM used in DSCs is spiro-OMeTAD, however it has many disadvantages also such as poor pore filling, low conductivity and significantly higher recombination at TiO₂/electrolyte interface.¹³⁹ Owing to these limitations, the PV performance of ssDSCs is always lower than liquid DSC. Freitag *et al.* came up with a new strategy to make ssDSC commonly known as Zombie DSCs.⁷² Zombie cells were discovered serendipitously and have a unique manufacturing process compared to typical HTM based ssDSCs. Zombie ssDSCs are fabricated by evaporating solvents from electrolyte in ambient air. With zombie DSCs, the issue of poor pore filling could be directly ruled out, thus efficient regeneration of oxidised dye could be made possible even with thicker TiO₂. **Figure 1. 37** shows the cross sectional SEM of a representative working electrode with copper based HTM, PIA spectra of ssDSCs and DSCs with LEG4 employing [Cu(dmp)₂]^{2+/1+} based HTM/redox mediator. The cross-sectional SEM image shows 2 μm thick Cu is deposited on top of the sensitized mesoporous TiO₂ layer which efficiently regenerates the oxidised dye as seen in the PIA spectrum. Additionally, the hole mobility in a solid film of [Cu(dmp)₂]⁺ ($\sim 3 \times 10^{-2} \text{ cm}^2 \text{V}^{-1} \text{s}^{-1}$) is found to be one order of magnitude higher than that of doped spiro-OMeTAD ($\sim 4 \times 10^{-3} \text{ cm}^2 \text{V}^{-1} \text{s}^{-1}$).

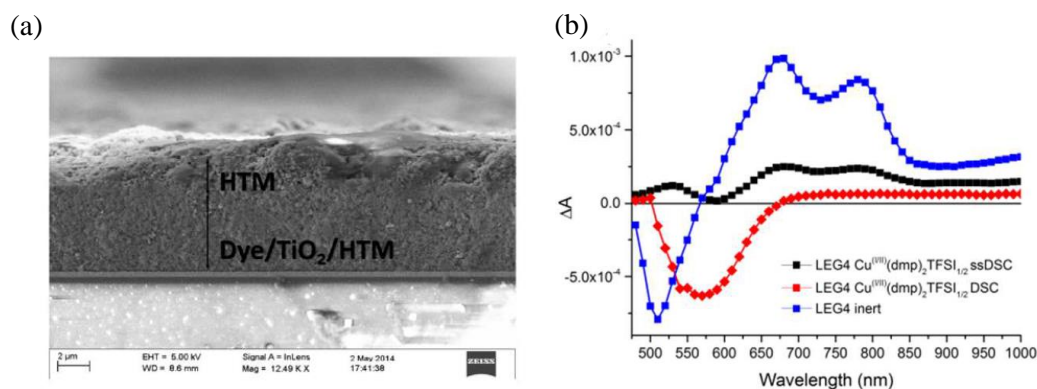


Figure 1.37 a) Cross section by SEM of a representative working electrode with copper based HTM after removal of the PEDOT coated FTO counter electrode b) PIA spectra of ssDSCs and DSCs with LEG4 employing $[\text{Cu}(\text{dmp})_2]^{2+/1+}$ based HTM or redox mediator.⁷²

Table 1.9 PV parameters derived from J - V measurements of LEG4 sensitized ssDSCs and DSCs using $[\text{Cu}(\text{dmp})_2]^{2+/1+}$ based HTM or redox mediator.

HTM or Electrolyte	V_{oc} (mV)	J_{sc} (mAcm ²)	FF	η (%)
Cu(dmp) ₂ HTM	1010	13.8	0.59	8.2
Cu(dmp) ₂ EL	1035	9.4	0.62	6.0
Spiro-OMeTAD HTM	895	9.4	0.67	5.6

Zombie DSCs outperformed both Liquid as well as ssDSC with spiro-OMeTAD HTM with maximum efficiency reaching upto 8.2% with a $V_{oc} > 1\text{V}$. The PV parameters of ssDSCs and DSCs using $[\text{Cu}(\text{dmp})_2]^{2+/1+}$ based HTM or redox mediator are summarized in **Table 1.9**. Further, Cao *et al.* was able to further enhance the efficiency up to 11.0% (V_{oc} -1.08 V, J_{sc} -13.87 mA/cm² and FF -0.73) with Y123 sensitizer and $[\text{Cu}(\text{tmb})_2]^{2+/1+}$ using modified copper electrolyte based solid state devices.⁷⁸ Here slow evaporation of solvent played a critical role in gaining higher PV performance. They found that the presence of crystalline phase of Cu HTM induces sublinear dependence of J_{sc} with passage of time. In order to curb the crystal formation, Saygili *et al.* introduced aliphatic side chains on the ligand to reduce lattice packing and crystallinity. **Figure 1.38 (a,b)** shows the molecular structure of the newly designed Cu complexes.⁷³

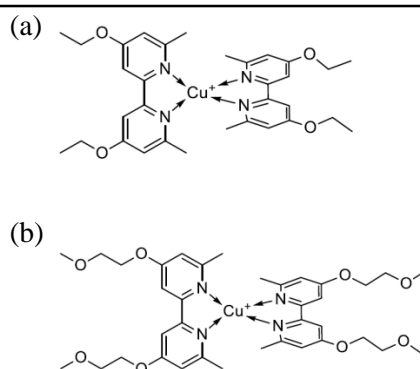


Figure 1. 38 Molecular structures of a) $[\text{Cu}(\text{beto})_2]^{2+/1+}$, b) $[\text{Cu}(\text{beto2Ox})_2]^{2+/1+}$.⁷³

Zombie DSCs made using these new complexes resulted in a lower PCE values compared to standard $[\text{Cu}(\text{tmby})_2]^{2+/1+}$ redox mediators. This is because with the new redox mediator the charge transport property reduced significantly which severely contributed to lower V_{oc} , J_{sc} and FF . With judicious selection of sensitizer (WS72) and redox mediator $[\text{Cu}(\text{tmby})_2]^{2+/1+}$ combination, Zhang *et al.* realized higher efficiency upto 11.7% (V_{oc} -1.02 V J_{sc} -13.8 mAcm^{-2} and FF -0.79).⁹⁸ They reported remarkably homogeneous infiltration of $[\text{Cu}(\text{tmby})_2]^{2+/1+}$ in the mesoscopic TiO_2 films as seen from SEM analysis (**Figure 1. 39**).

54

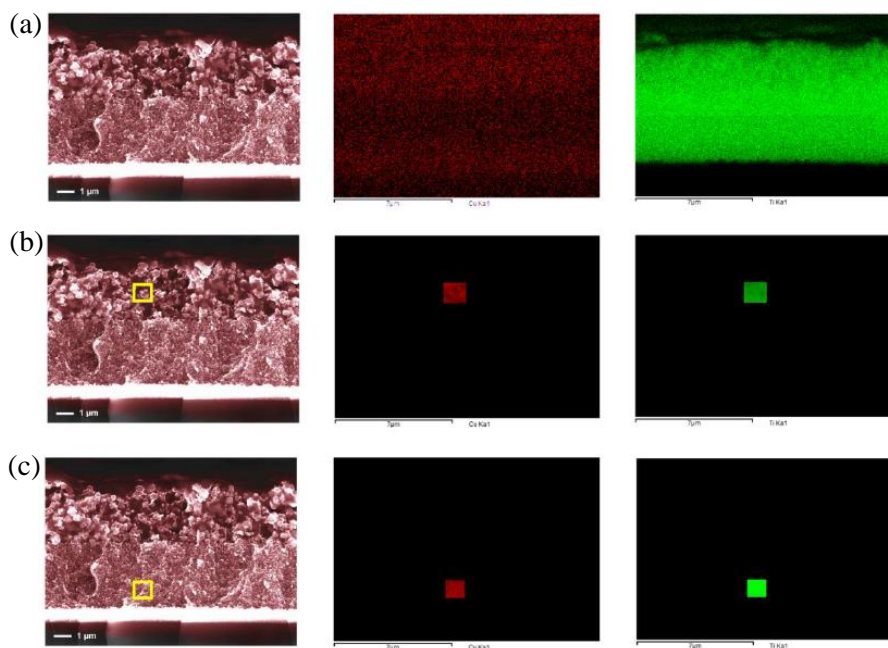


Figure 1. 39 Cross sectional image (left) of TiO_2 film sensitized by dye WS-72 infiltrated with $[\text{Cu}(\text{tmby})_2]^{2+/1+}$ based HTM. Element mapping (right) suggesting the dispersion of

Cu (red) and Ti (green) elementary in the mesoporous TiO₂ film (a, globe image; b, top image; c, bottom image).⁹⁸

Kavan *et al.* studied the zombie effect in symmetrical PEDOT-PEDOT devices filled with [Cu(tmby)₂]^{2+/1+} redox mediator.¹²⁶ FigureXX shows the electrochemical results obtained from symmetrical PEDOT-PEDOT devices. The electrochemical study reveals that the charge transfer kinetics at the counter electrode gets faster in zombie devices compared to liquid devices while mass transport issue becomes more prominent in zombies. In zombies they presumed, the hopping charge-transfer which is less important in liquid electrolyte, becomes the main hole-transport process in the solid hole conductor zombies.

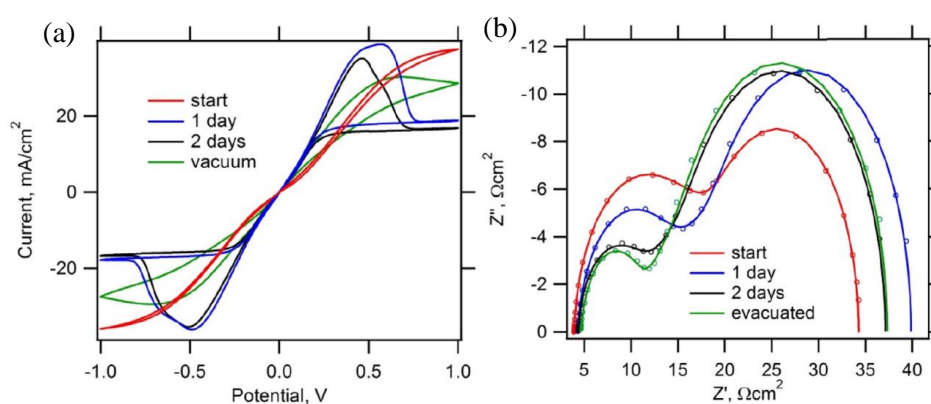


Figure 1. 40 (a) Cyclic voltammograms (b) Nyquist plots of electrochemical impedance spectra measured at 0 V from 100 kHz to 0.1 Hz. Red curve denotes pristine closed cell with liquid electrolyte solution; blue curve shows cell opened and the electrolyte solution f freely evaporated for 1 day at room temperature and pressure via two filling holes; black curve shows 2 days of free evaporation and green shows the cell with partly evaporated solution was subjected to vacuum at room temperature.¹²⁶

Kim *et al.* further explored charge transport mechanism with an in-situ solidification analysis of the charge diffusion and find that the diffusion mechanism of HTM with [Cu(dmbpy)₂]^{2+/1+} is dominated by electronic diffusion and, not ionic diffusion.¹⁴⁰ **Figure 1. 41** shows the predicted schemes of electron (hole) transport mechanism using liquid and solid copper electrolytes. They found that the solidification process reduces the energy barrier of the exchange reaction between copper complexes and increases the charge transfer reaction rate to produce the higher hole conductivity observed in HTMs compared to LEs.

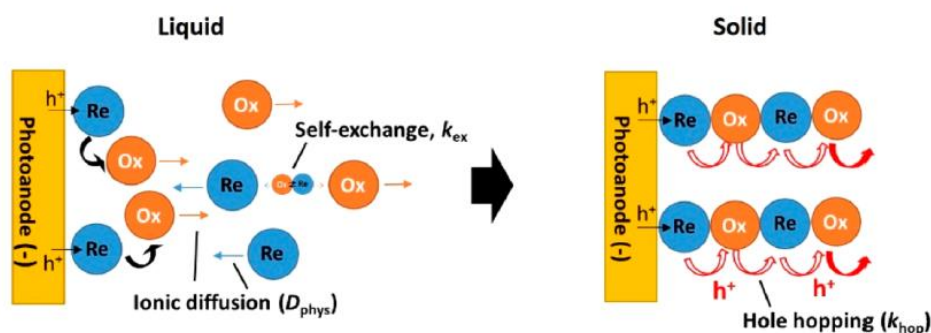


Figure 1.41 The predicted schemes of electron (hole) transport mechanism differences between the LE and HTM.¹⁴⁰

1.8.8.2. Direct Contact DSCs

The direct contact DSCs (DCD) is a new architecture introduced by Cao *et al.* where the insulating spacer is removed between the two electrodes (**Figure 1.42 (a)**).⁷⁸ The concept is originated from type II junction solar cell formed by the n-type inorganic semiconductor and the p-type polymer semiconductor. Since insulating spacer is absent, TiO₂ photoanode comes in direct contact with PEDOT counter electrode. Here PEDOT acts as hole selective electron blocking layer (**Figure 1.42 (b)**). Mass transport issue in bulk electrolyte associated with Cu redox mediators are largely minimized with DCD, subsequently photovoltaic performance is enhanced with the new DCD architecture (**Table 1.10**).

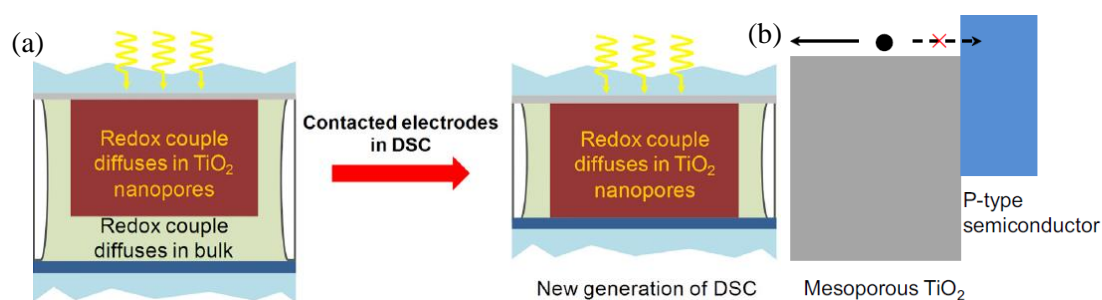


Figure 1.42 (a) Device structure of new generation DCD and normal DSC (b) Type II junction alignment of the band edges for the mesoporous TiO₂ film and a p-type semiconductor layer.⁷⁸

The remarkable improvement in PV performance is ascribed to the reduced light absorption by the electrolyte using the new DCD architecture (**Figure 1. 43**).

Table 1. 10 The photovoltaic parameters of Y123 cells with the contacted and separated electrodes tested under light projection onto either the front TiO₂ electrode or the back PEDOT electrode. The cells employ ~200 nm thick PEDOT layer counter electrode and ~4.5 μm thick nanocrystalline mesoscopic TiO₂ film without light scattering layer. With further optimization of TiO₂ thickness the efficiency of DCDs with Y123 dye reached up to 11%. Co-sensitization of Y123 with XY1 again pushed the efficiency of DCD to 13.6% under one sun illumination and 32% under indoor light conditions (1000 lux).

Table 1. 10 Photovoltaic parameter for DCD and standard DSC using Y123 dye and [Cu(tpmy)₂]^{2+/1+}

Device	Light projection into electrode	V_{oc} (mV)	J_{sc} mAcm ⁻²	FF	η (%)
DCD	Front TiO ₂	1120	11.87	0.75	10.0
	Back TiO ₂	1110	8.53	0.76	7.2
DSSC	Front TiO ₂	1115	10.88	0.74	9.0
	Back TiO ₂	1089	4.43	0.79	3.8

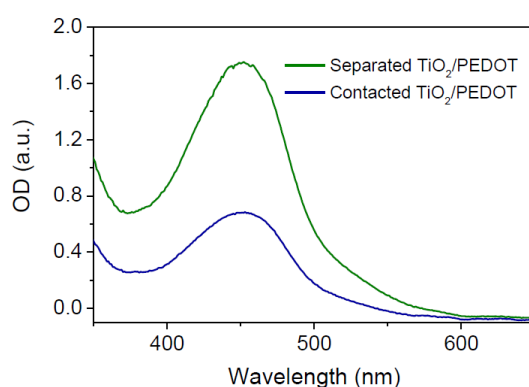


Figure 1. 43 The absorption spectra of the Cu(II)/Cu(I) redox electrolyte in the cells with the separated and contacted electrodes. The thickness of the cell with the contacted electrodes is same as the thickness of the TiO₂ film (~7 μm).⁷⁸

Further in another study that reported record efficiency of 13.6% under one sun illumination and 34.5% under indoor light condition also used direct contact architecture. Moreover, direct contact architecture is rarely seen to be used in DSCs though it has many advantages over standard spacer based DSCs.

1.8.9. Indoor/Ambient Light Harvesting using Cu Electrolyte DSCs

DSCs always remain as front-runner in indoor light harvesting since the absorption spectra of photosensitizers can be carefully tuned so as to have a perfect overlap with the entire emission spectra of indoor lights (CFL, LED) which leads to higher J_{sc} .^{141–145} Moreover, the use of copper redox mediators helped in producing higher voltage from a single junction device even under very low light illumination, which is pre-requisite requirement for being used to power IoT devices.

The competence of DSCs for harvesting indoor light caught into limelight with the demonstration by Freitag *et al.* achieving PCE upto 28.9% at an intensity of 1000 lux under illumination from a warm-white fluorescent light tube.⁸⁰ At similar light condition, GaAs solar cells showed only a PCE of 21%. **Table 1. 11** demonstrates the PV parameters. To enhance J_{sc} they used a mixture of XY1 and D35 as sensitizers, D35 absorbs mainly blue and green light, while the XY1 covers the yellow and red spectral region. Likewise, to increase V_{oc} they employed $[\text{Cu}(\text{tmby})_2]^{2+/1+}$ with redox potential very close to the HOMO of the sensitizers.

Table 1. 11 Photovoltaic metrics for DSCs and GaAs solar cells for indoor-light sources at 200 lux and 1,000 lux.

Solar cell	Light intensity (lux)	J_{sc} ($\mu\text{A cm}^{-2}$)	V_{oc} (mV)	FF	P_{in} (μWcm^{-2})	P_{out} (μWcm^{-2})	η (%)
DSC	200	27.2	732.0	0.79	61.3	15.6	25.5
DSC	1000	138.0	797.0	0.80	306.6	88.5	28.9
GaAs	200	20.1	870.0	0.75	70.6	13.1	18.6
GaAs	1000	99.0	940.0	0.80	354.0	74.5	21.0

Following this Cao *et al.* used a combination of XY1b and Y123 dyes along with $[\text{Cu}(\text{tmby})_2]^{2+/1+}$ electrolyte in new direct contact architecture and achieved a PCE of 32%

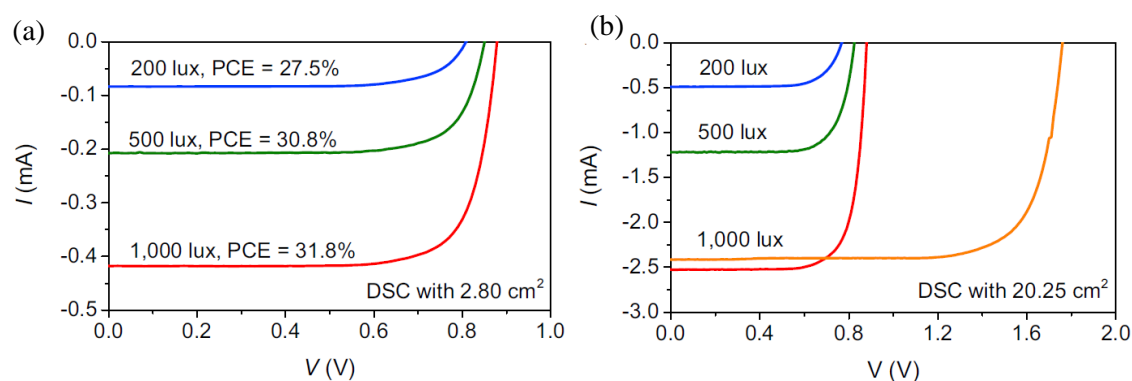


Figure 1.44 J - V characteristics of DSCs with photoactive areas of 2.80 cm^2 and 20.25 cm^2 .⁷⁸

Table 1.12 J - V parameters with photoactive areas of 2.80 cm^2 and 20.25 cm^2 .

Cell dimension	Cell performance	P_{in} of Osram 930 Warm white light (Lux or μWcm^{-2})		
		1000 (318.2)	500 (159.1)	200 (63.6)
Area: 2.8 cm^2 ; Length: 40 mm; Width: 7 mm.	P_{max} (μW)	283	132	49
	η (%)	31.8	30.8	27.5
	V_{oc} (mV)	1051	1041	981
	I_{sc} (mA cm^{-2})	0.418	0.208	0.083
	FF	0.773	0.750	0.722
Area: 20.25 cm^2 ; Length: 135 mm; Width: 15 mm.	P_{max} (μW)	1700	742	272
	η (%)	8.2	10.1	10.6
	V_{oc} (mV)	879	824	767
	J_{sc} (mA)	2.526	1.219	0.491
	FF	0.766	0.739	0.722

under 1000 lux illumination.⁷⁸ In a way to minimize the discrepancy between lab level devices and practically usable devices they demonstrated devices with an active area of 2.80 cm^2 and 20.25 cm^2 . **Figure 1.44** shows the J - V characteristics of DSC with active area of 2.80 cm^2 and 20.25 cm^2 and the parameters are summarized in **Table 1.12**.

With co-sensitization of XY1 and L1 along with $[\text{Cu}(\text{tmby})_2]^{2+/1+}$ electrolyte Mitchels *et al.* reached to an efficiency of 34% under 1000 lux illumination.¹⁰⁸ The J - V characteristics is given in **Figure 1.45** and the PV parameters are summarized in **Table 1.13**. In order to verify the practical applications, large area devices 3.2 cm^2 and 8.2 cm^2 were fabricated and demonstrated which showed PCE of 33.2% (V_{oc} -910 mV, J_{sc} -142 μAcm^{-2} and FF -0.78) and 30.6% (V_{oc} -900 mV, J_{sc} -142 μAcm^{-2} and FF -0.74) respectively.

Moreover, a small array of DSCs with a total active area of 16 cm² was used to power machine learning on wireless nodes.

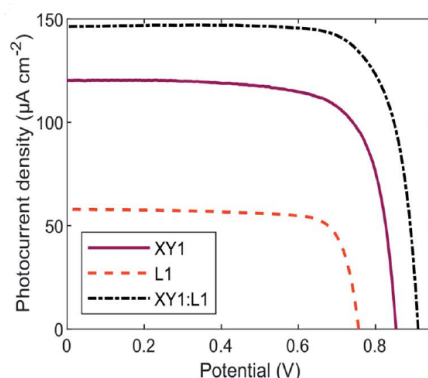


Figure 1.45 *J-V* characteristics for XY1, L1 and XY1:L1 under 1000 Lux illumination. ¹⁰⁸

Table 1. 13 *J-V* parameters at different indoor intensity for XY1, L1 and XY1:L1

Parameters	XY1 1000 lux	L1 1000 lux	XY1:L1 1000 lux	XY1:L1 500 lux	XY1:L1 200 lux
V_{oc} (mV)	850	750	910	880	840
J_{sc} (µA) (µA cm ⁻²)	30.0 (120)	14.5 (58)	36.7 (147)	18.4 (73.4)	7.2 (29.0)
FF	0.74	0.78	0.77	0.77	0.78
P_{max} (µW) (µW cm ⁻²)	18.9 (75.4)	8.6 (34.4)	25.7 (103.1)	12.4 (49.5)	4.8 (19.0)
η (%)	24.9	11.3	34.0	32.7	31.4

Zhang *et al.* recently introduced two new sensitizers named MS4 and MS5, which have the capability of reduction in recombination.¹⁰⁴ The co-sensitized devices (MS5+XY1b) with photoactive area of 2.80 cm² showcased a PCE of 34.5%, which is the highest PCE reported in indoor light under 1000 lux CFL illumination till now. Under 1000 lux illumination, devices showed a V_{oc} of 0.98 V, and I_{sc} of 0.387 mA with FF of 0.815. Similarly, 32.3% and 32.4% power conversion efficiencies were obtained for 500 lux and 200 lux illuminations respectively. The *J-V* curve is shown in the **Figure 1. 46** and the photovoltaic parameters are summarised in the **Table 1. 14**.

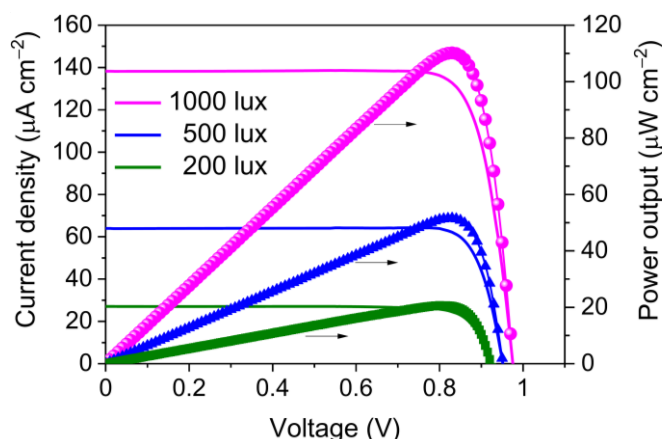


Figure 1.46 J - V characteristics for DSCs having photoactive area of 2.80 cm^2 under 1000 lux, 500 lux and 200 lux illumination condition.¹⁰⁴

Table 1.14 PV parameters of the DSC based on MS5+XY1b (active area of 2.80 cm^2) under different illumination intensities (Osram 930 Warm White fluorescent light).

Cell performance	1000 Lux (318.2)	500 Lux (159.1)	200 Lux (63.6)
P_{\max} (μW)	307.4	143.9	57.7
η (%)	34.5	32.3	32.4
V_{oc} (V)	0.98	0.95	0.92
I_{sc} (mA)	0.387	0.179	0.076
FF	0.815	0.845	0.826

Along with $[\text{Cu}(\text{dmp})_2]^{2+/1+}$ electrolyte and newly synthesised anthracene-based sensitizer CXC22 Chen *et al.* achieved an impressive PCE of 37.07% with V_{oc} of 977.57 mV, J_{sc} of $893.44 \mu\text{Acm}^{-2}$ and FF of 0.79 under 6000 lux T5 illumination.⁸² At the same time the parent sensitizer showcased a PCE of 21.34% under similar light condition. Recently, Ren *et al.* obtained a PCE of 30.1% under 1479 lux 4000 k LED illumination using copper electrolyte $\{[\text{Cu}(\text{tmby})_2]^{2+/1+}\}$.⁷⁹ To reach the feat they used preabsorber 2-(4-butoxyphenyl)-Nhydroxyacetamide (BPHA) molecules on the TiO_2 before co-sensitization of organic dye SL9 and SL10. BPHA enabled better packing density of sensitizers, which resulted in faster dye regeneration.

1.9. Statement of the Problem

Open circuit voltage (V_{oc}) in a photovoltaic cell is a crucial parameter to improve power conversion efficiency. Recently, solar cells with high V_{oc} is garnering tremendous attention as it is the key parameter to obtain higher efficiencies under ambient/indoor light illumination. In DSC the difference between Fermi potential of mesoporous semiconductor and redox potential of redox shuttle produces the V_{oc} . It can be largely improved by employing redox mediators with positive redox potentials. Conventional DSC with I^-/I_3^- redox mediator (redox potential 0.4V vs. NHE) needs ~500 mV driving force for efficient dye regeneration which limits its V_{oc} below 0.8 V. Employing alternative copper redox mediators ($Cu^{2+/1+}$) V_{oc} can be pushed above 1 V for a single functional device as it needs merely ~100 mV driving force for efficient dye regeneration. Redox potential of copper mediators ranges from 0.59 V to 0.97 V which provides an opportunity to realize theoretical V_{oc} upto 1.45 V. The very positive redox potential of copper redox mediators promotes charge recombination at semiconductor/electrolyte interface which negatively affects V_{oc} and FF leading to lower power conversion efficiency. Yet again copper redox mediators possess other issues such as slower ion diffusion, additive co-ordination and charge transfer issues at the counter electrode. Hence our motivation is to understand the interfacial charge transfer dynamics at various interfaces in DSC employing new generation alternative copper redox mediator and to engineer the devices further to improve the power conversion efficiency particularly for indoor photovoltaic applications.

1.10. Objectives of the Thesis

Chapter-2 renders a detailed comparison between DSC fabricated using classical iodide/triiodide (I^-/I_3^-), alternative cobalt $\{[Co(bpy)_3]^{3+/2+}\}$ and new generation copper $\{[Cu(dmp)_2]^{2+/1+}\}$ redox mediators. I^-/I_3^- is the highest ever used classical electrolyte with a redox potential of 0.4 V vs. NHE. $[Co(bpy)_3]^{3+/2+}$ is the one of the extensively used cobalt redox mediator with a redox potential of 0.56 V vs. NHE and $[Cu(dmp)_2]^{2+/1+}$ is one of the highly efficient copper redox mediator with redox potential 0.94 V vs. NHE. For a direct comparison we used organic dye LEG4 and PEDOT counter electrode for all the devices with the three different redox mediators. Chapter 3 deals with the comprehensive interfacial analysis of copper electrolyte based DSCs with TiO_2 working electrodes consisting of different particle size. Organic dye D35 and $Cu[(tmbpy)_2]^{2+/1+}$ redox mediator was used as the sensitizer and electrolyte for the fabrication of DSCs. Fabrication of efficient copper-

based DSCs requires an entirely new set of innovative materials and optimized device architectures. One such critical device engineering involves the uses of mesoporous titanium dioxide with particle size of 30 nm, however in standard DSC titanium dioxide particle size of 20 nm is used. We investigated DSCs with working electrode consist TiO₂ active layer of particle size of 20 nm and 30 nm respectively. To gain an in-depth understanding of interfacial charge transfer dynamics of devices, we used various electrical and optical perturbation tools. Chapter 4 deals with the investigation of charge recombination as function of dye concentration in copper electrolyte-based DSCs. Dyes are used as light harvesters in DSCs which are primarily responsible for current generation. However, the other aspect of dyes to prevent recombination leading to improvement in voltage are not been explored much. Herein, we study the role of dye in preventing recombination at TiO₂/dye/electrolyte interface in copper electrolyte-based DSC. Chapter 5 deals with the electrolyte additive engineering to improve the power conversion efficiency particularly under indoor light conditions using copper electrolyte-based DSCs. We introduced a new additive LiI in [Cu(tmby)₂]^{2+/1+} electrolyte to improve the indoor photovoltaic performance.

1.11. References

- 1 D. Helm, *Oxford Rev. Econ. Policy*, 2011, **27**, 68–91.
- 2 E. News, Energy resources will be exhausted in 40 years: Expert, Energy News, ET EnergyWorld, <https://energy.economicstimes.indiatimes.com/news/coal/energy-resources-will-be-exhausted-in-40-years-expert/57846890>, (accessed 20 December 2022).
- 3 N. A. Lee, G. E. Gilligan and J. Rochford, in *Green Chemistry: An Inclusive Approach*, 2018.
- 4 World Energy Outlook 2020 – Analysis - IEA, <https://www.iea.org/reports/world-energy-outlook-2020>, (accessed 22 March 2021).
- 5 *Advances in Solar Energy*, Springer US, 1985.
- 6 Intelligent Edge is Driving the Shift of Internet of Things (IoT), <https://www.analyticsinsight.net/intelligent-edge-is-driving-the-shift-of-internet-of-things-iot/>, (accessed 22 March 2021).
- 7 Statista, • Global IoT and non-IoT connections 2010-2025 | Statista, <https://www.statista.com/statistics/1101442/iot-number-of-connected-devices-worldwide/>, (accessed 20 December 2022).
- 8 B. A. E, *Comptes Rendus L'Academie des Sci.*, 1839, **9**, 145–149.

-
- 9 M. Li, F. Igbari, Z. Wang and L. Liao, *Adv. Energy Mater.*, 2020, **10**, 2000641.
 - 10 J. K. W. Ho, H. Yin and S. K. So, *J. Mater. Chem. A*, 2020, **8**, 1717–1723.
 - 11 M. Aftabuzzaman, S. Sarker, C. Lu and H. K. Kim, *J. Mater. Chem. A*, 2021, **9**, 24830–24848.
 - 12 A. Venkateswararao, J. K. W. Ho, S. K. So, S.-W. Liu and K.-T. Wong, *Mater. Sci. Eng. R Reports*, 2020, **139**, 100517.
 - 13 M. Okil, M. S. Salem, T. M. Abdolkader and A. Shaker, *Silicon 2021 145*, 2021, **14**, 1895–1911.
 - 14 C. L. Cutting, M. Bag and D. Venkataraman, *J. Mater. Chem. C*, 2016, **4**, 10367–10370.
 - 15 E. T. Efaz, M. M. Rhaman, S. Al Imam, K. L. Bashar, F. Kabir, M. E. Mourtaza, S. N. Sakib and F. A. Mozahid, *Eng. Res. Express*, 2021, **3**, 032001.
 - 16 X. He, J. Chen, X. Ren, L. Zhang, Y. Liu, J. Feng, J. Fang, K. Zhao and S. (Frank) Liu, *Adv. Mater.*, 2021, **33**, 2100770.
 - 17 L. Zhang and W. Hu, *Int. J. Energy Res.*, 2022, **46**, 14740–14765.
 - 18 J. Lee, K. Lee, K. Kim and N. G. Park, *Sol. RRL*, 2022, **6**, 2200623.
 - 19 F. Fu, J. Li, T. C. J. Yang, H. Liang, A. Faes, Q. Jeangros, C. Ballif and Y. Hou, *Adv. Mater.*, 2022, **34**, 2106540.
 - 20 Y. Ren, Y. Li, S. Chen, J. Liu, J. Zhang and P. Wang, *Energy Environ. Sci.*, 2016, **9**, 1390–1399.
 - 21 M. I. Asghar, J. Zhang, H. Wang and P. D. Lund, *Renew. Sustain. Energy Rev.*, 2017, **77**, 131–146.
 - 22 X. Xu, D. Li, J. Yuan, Y. Zhou and Y. Zou, *EnergyChem*, 2021, **3**, 100046.
 - 23 L. Zhang and J. M. Cole, *ACS Appl. Mater. Interfaces*, 2015, **7**, 3427–3455.
 - 24 G. Palma, L. Cozzarini, E. Capria and A. Fraleoni-Morgera, *Rev. Sci. Instrum.*, 2015, **86**, 013112.
 - 25 L. Andrade, H. A. Ribeiro and A. Mendes, in *Encyclopedia of Inorganic and Bioinorganic Chemistry*, John Wiley & Sons, Ltd, Chichester, UK, 2011.
 - 26 J. Halme, P. Vahermaa, K. Miettunen and P. Lund, *Adv. Mater.*, 2010, **22**, 210–234.
 - 27 J. J. Nelson, T. J. Amick and C. M. Elliott, *J. Phys. Chem. C*, 2008, **112**, 18255–18263.
 - 28 H. S. Kim, S. B. Ko, I. H. Jang and N. G. Park, *Chem. Commun.*, 2011, **47**, 12637–12639.
 - 29 J. Bisquert, A. Zaban, M. Greenshtein and I. Mora-Seró, *J. Am. Chem. Soc.*, 2004,

- 126**, 13550–13559.
- 30 A. Zaban, M. Greenshtein and J. Bisquert, *ChemPhysChem*, 2003, **4**, 859–864.
- 31 P. R. F. Barnes, K. Miettunen, X. Li, A. Y. Anderson, T. Bessho, M. Gratzel and B. C. O'Regan, *Adv. Mater.*, 2013, **25**, 1881–1922.
- 32 L. Peter, 2007, **599**, 233–240.
- 33 L. . Peter, N. . Duffy, R. . Wang and K. G. . Wijayantha, *J. Electroanal. Chem.*, 2002, **524–525**, 127–136.
- 34 Q. Wang, S. Ito, M. Grätzel, F. Fabregat-Santiago, I. Mora-Seró, J. Bisquert, T. Bessho and H. Imai, *J. Phys. Chem. B*, 2006, **110**, 25210–25221.
- 35 F. Fabregat-Santiago, G. Garcia-Belmonte, I. Mora-Seró and J. Bisquert, *Phys. Chem. Chem. Phys.*, 2011, **13**, 9083–9118.
- 36 M. Adachi, M. Sakamoto, J. Jiu, Y. Ogata and S. Isoda, *J. Phys. Chem. B*, 2006, **110**, 13872–13880.
- 37 J. Bisquert, I. Mora-Sero and F. Fabregat-Santiago, *ChemElectroChem*, , DOI:10.1002/celc.201300091.
- 38 J. Ondersma and T. Hamann, *J. Phys. Chem. C*, 2010, **114**, 638–645.
- 39 F. Fabregat-Santiago, J. Bisquert, G. Garcia-Belmonte, G. Boschloo and A. Hagfeldt, *Sol. Energy Mater. Sol. Cells*, 2005, **87**, 117–131.
- 40 J. Bisquert and F. Fabregat-Santiago, *Dye. Sol. Cells*, 2010, 604.
- 41 P. J. Cameron and L. M. Peter, *J. Phys. Chem. B*, 2005, **109**, 7392–7398.
- 42 A. Mishra, M. K. R. Fischer and P. Büuerle, *Angew. Chemie - Int. Ed.*, 2009, **48**, 2474–2499.
- 43 E. Palomares, N. F. Montcada, M. Méndez, J. Jiménez-López, W. Yang and G. Boschloo, in *Characterization Techniques for Perovskite Solar Cell Materials*, Elsevier, 2020, pp. 161–180.
- 44 A. B. Walker, L. M. Peter, D. Martínez and K. Lobato, *Chimia (Aarau).*, 2007, **61**, 792.
- 45 M. Pazoki, U. B. Cappel, E. M. J. Johansson, A. Hagfeldt and G. Boschloo, *Energy Environ. Sci.*, 2017, **10**, 672–709.
- 46 M. Pazoki, P. W. Lohse, N. Taghavinia, A. Hagfeldt and G. Boschloo, *Phys. Chem. Chem. Phys.*, 2014, **16**, 8503.
- 47 G. Boschloo and A. Hagfeldt, *Chem. Phys. Lett.*, 2003, **370**, 381–386.
- 48 U. B. Cappel, S. M. Feldt, J. Schöneboom, A. Hagfeldt and G. Boschloo, *J. Am. Chem. Soc.*, 2010, **132**, 9096–9101.
- 49 G. Boschloo and A. Hagfeldt, *Inorganica Chim. Acta*, 2008, **361**, 729–734.

-
- 50 B. O'Regan and M. Grätzel, *Nature*, 1991, **353**, 737–740.
- 51 M. K. Nazeeruddin, E. Baranoff and M. Grätzel, *Sol. Energy*, 2011, **85**, 1172–1178.
- 52 M. K. Nazeeruddin, P. Péchy, T. Renouard, S. M. Zakeeruddin, R. Humphry-Baker, P. Cointe, P. Liska, L. Cevey, E. Costa, V. Shklover, L. Spiccia, G. B. Deacon, C. A. Bignozzi and M. Grätzel, *J. Am. Chem. Soc.*, 2001, **123**, 1613–1624.
- 53 M. K. Nazeeruddin, F. De Angelis, S. Fantacci, A. Selloni, G. Viscardi, P. Liska, S. Ito, B. Takeru and M. Grätzel, *J. Am. Chem. Soc.*, 2005, **127**, 16835–16847.
- 54 F. Gao, Y. Wang, D. Shi, J. Zhang, M. Wang, X. Jing, R. Humphry-Baker, P. Wang, S. M. Zakeeruddin and M. Grätzel, *J. Am. Chem. Soc.*, 2008, **130**, 10720–10728.
- 55 A. Yella, H.-W. Lee, H. N. Tsao, C. Yi, A. K. Chandiran, M. K. Nazeeruddin, E. W.-G. Diao, C.-Y. Yeh, S. M. Zakeeruddin and M. Grätzel, *Science (80-.)*, 2011, **334**, 629–634.
- 56 S. Mathew, A. Yella, P. Gao, R. Humphry-Baker, B. F. E. Curchod, N. Ashari-Astani, I. Tavernelli, U. Rothlisberger, M. K. Nazeeruddin and M. Grätzel, *Nat. Chem.*, 2014, **6**, 242–247.
- 57 S. M. Feldt, E. A. Gibson, E. Gabrielsson, L. Sun, G. Boschloo and A. Hagfeldt, *J. Am. Chem. Soc.*, 2010, **132**, 16714–16724.
- 58 H. N. Tsao, C. Yi, T. Moehl, J.-H. Yum, S. M. Zakeeruddin, M. K. Nazeeruddin and M. Grätzel, *ChemSusChem*, 2011, **4**, 591–594.
- 59 K. Kakiage, Y. Aoyama, T. Yano, K. Oya, J. I. Fujisawa and M. Hanaya, *Chem. Commun.*, 2015, **51**, 15894–15897.
- 60 T. W. Hamann and J. W. Ondersma, *Energy Environ. Sci.*, 2011, **4**, 370–381.
- 61 T. W. Hamann, *Dalt. Trans.*, 2012, **41**, 3111–3115.
- 62 S. C. Pradhan, A. Hagfeldt and S. Soman, *J. Mater. Chem. A*, 2018, **6**, 22204–22214.
- 63 S. M. Feldt, G. Wang, G. Boschloo and A. Hagfeldt, *J. Phys. Chem. C*, 2011, **115**, 21500–21507.
- 64 B. A. Gregg, F. Pichot, S. Ferrere and C. L. Fields, *J. Phys. Chem. B*, 2001, **105**, 1422–1429.
- 65 S. M. Feldt, U. B. Cappel, E. M. J. Johansson, G. Boschloo and A. Hagfeldt, *J. Phys. Chem. C*, 2010, **114**, 10551–10558.
- 66 T. Daeneke, T.-H. Kwon, A. B. Holmes, N. W. Duffy, U. Bach and L. Spiccia, *Nat. Chem.*, 2011, **3**, 211–215.
- 67 T. Daeneke, A. J. Mozer, T.-H. Kwon, N. W. Duffy, A. B. Holmes, U. Bach and L. Spiccia, *Energy Environ. Sci.*, 2012, **5**, 7090.

- 68 T. C. Li, A. M. Spokoyny, C. She, O. K. Farha, C. A. Mirkin, T. J. Marks and J. T. Hupp, *J. Am. Chem. Soc.*, 2010, **132**, 4580–4582.
- 69 M. K. Nazeeruddin, E. Baranoff and M. Grätzel, *Sol. Energy*, 2011, **85**, 1172–1178.
- 70 T. W. Hamann, O. K. Farha and J. T. Hupp, *J. Phys. Chem. C*, 2008, **112**, 19756–19764.
- 71 H. Nusbaumer, J. E. Moser, S. M. Zakeeruddin, M. K. Nazeeruddin and M. Grätzel, *J. Phys. Chem. B*, 2001, **105**, 10461–10464.
- 72 M. Freitag, Q. Daniel, M. Pazoki, K. Sveinbjörnsson, J. Zhang, L. Sun, A. Hagfeldt and G. Boschloo, *Energy Environ. Sci.*, 2015, **8**, 2634–2637.
- 73 Y. Saygili, M. Stojanovic, H. S. Kim, J. Teuscher, R. Scopelliti, M. Freitag, S. M. Zakeeruddin, J. E. Moser, M. Grätzel and A. Hagfeldt, *J. Phys. Chem. C*, 2020, **124**, 7071–7081.
- 74 Y. Saygili, M. Söderberg, N. Pellet, F. Giordano, Y. Cao, A. B. Munoz-García, S. M. Zakeeruddin, N. Vlachopoulos, M. Pavone, G. Boschloo, L. Kavan, J. E. Moser, M. Grätzel, A. Hagfeldt and M. Freitag, *J. Am. Chem. Soc.*, 2016, **138**, 15087–15096.
- 75 M. Freitag, F. Giordano, W. Yang, M. Pazoki, Y. Hao, B. Zietz, M. Grätzel, A. Hagfeldt and G. Boschloo, *J. Phys. Chem. C*, 2016, **120**, 9595–9603.
- 76 S. Hattori, Y. Wada, S. Yanagida and S. Fukuzumi, *J. Am. Chem. Soc.*, 2005, **127**, 9648–9654.
- 77 Y. Bai, Q. Yu, N. Cai, Y. Wang, M. Zhang and P. Wang, *Chem. Commun.*, 2011, **47**, 4376–4378.
- 78 Y. Cao, Y. Liu, S. M. Zakeeruddin, A. Hagfeldt and M. Grätzel, *Joule*, 2018, **2**, 1108–1117.
- 79 Y. Ren, D. Zhang, J. Suo, Y. Cao, F. T. Eickemeyer, N. Vlachopoulos, S. M. Zakeeruddin, A. Hagfeldt and M. Grätzel, *Nature*, 2022, 1–6.
- 80 M. Freitag, J. Teuscher, Y. Saygili, X. Zhang, F. Giordano, P. Liska, J. Hua, S. M. Zakeeruddin, J.-E. Moser, M. Grätzel and A. Hagfeldt, *Nat. Photonics*, 2017, **11**, 372–378.
- 81 H. Michaels, M. Rinderle, R. Freitag, I. Benesperi, T. Edvinsson, R. Socher, A. Gagliardi and M. Freitag, *Chem. Sci.*, 2020, **11**, 2895–2906.
- 82 C. C. Chen, V. S. Nguyen, H. C. Chiu, Y. Da Chen, T. C. Wei and C. Y. Yeh, *Adv. Energy Mater.*, , DOI:10.1002/aenm.202104051.
- 83 P. Ferdowsi, Y. Saygili, F. Jazaeri, T. Edvinsson, J. Mokhtari, S. M. Zakeeruddin, Y. Liu, M. Grätzel and A. Hagfeldt, *ChemSusChem*, 2020, **13**, 212–220.
- 84 R. Ruess, T. H. Q. Nguyen and D. Schlottwein, *J. Electrochem. Soc.*, 2018, **165**, H3115–H3121.

-
- 85 A. Colombo, C. Dragonetti, M. Magni, D. Roberto, F. Demartin, S. Caramori and C. A. Bignozzi, *ACS Appl. Mater. Interfaces*, 2014, **6**, 13945–13955.
- 86 H. Michaels and M. Freitag, *ACS Appl. Energy Mater.*, 2022, **5**, 1933–1941.
- 87 A. Glinka, M. Gierszewski, B. Gierczyk, G. Burdziński, H. Michaels, M. Freitag and M. Ziółek, *J. Phys. Chem. C*, 2020, **124**, 2895–2906.
- 88 M. Brugnati, S. Caramori, S. Cazzanti, L. Marchini, R. Argazzi and C. A. Bignozzi, *Int. J. Photoenergy*, 2007, **2007**, 1–10.
- 89 A. Colombo, G. Di Carlo, C. Dragonetti, M. Magni, A. Orbelli Biroli, M. Pizzotti, D. Roberto, F. Tessore, E. Benazzi, C. A. Bignozzi, L. Casarin and S. Caramori, *Inorg. Chem.*, 2017, **56**, 14189–14197.
- 90 T. Higashino, H. Iiyama, I. Nishimura and H. Imahori, *Chem. Lett.*, 2020, **49**, 936–939.
- 91 A. Colombo, C. Dragonetti, F. Fagnani, D. Roberto, F. Melchiorre and P. Biagini, *Dalt. Trans.*, 2019, **48**, 9818–9823.
- 92 C. Dragonetti, M. Magni, A. Colombo, F. Fagnani, D. Roberto, F. Melchiorre, P. Biagini and S. Fantacci, *Dalt. Trans.*, 2019, **48**, 9703–9711.
- 93 M. V. Vinayak, M. Yoosuf, S. C. Pradhan, T. M. Lakshmykanth, S. Soman and K. R. Gopidas, *Sustain. Energy Fuels*, 2018, **2**, 303–314.
- 94 M. Yoosuf, S. C. Pradhan, S. Soman and K. R. Gopidas, *Sol. ENERGY*, 2019, **188**, 55–65.
- 95 M. Yoosuf, S. C. Pradhan, M. M. Sruthi, S. Soman and K. R. Gopidas, *Sol. Energy*, 2021, **216**, 151–163.
- 96 J. Cong, D. Kinschel, Q. Daniel, M. Safdari, E. Gabrielsson, H. Chen, P. H. Svensson, L. Sun and L. Kloo, *J. Mater. Chem. A*, 2016, **4**, 14550–14554.
- 97 Y. Saygili, M. Stojanovic, H. Michaels, J. Tjepelt, J. Teuscher, A. Massaro, M. Pavone, F. Giordano, S. M. Zakeeruddin, G. Boschloo, J. E. Moser, M. Grätzel, A. B. Muñoz-García, A. Hagfeldt and M. Freitag, *ACS Appl. Energy Mater.*, 2018, **1**, 4950–4962.
- 98 W. Zhang, Y. Wu, H. W. Bahng, Y. Cao, C. Yi, Y. Saygili, J. Luo, Y. Liu, L. Kavan, J.-E. Moser, A. Hagfeldt, H. Tian, S. M. Zakeeruddin, W.-H. Zhu and M. Grätzel, *Energy Environ. Sci.*, 2018, **11**, 1779–1787.
- 99 Y. Liu, Y. Cao, W. Zhang, M. Stojanovic, M. I. Dar, P. Péchy, Y. Saygili, A. Hagfeldt, S. M. Zakeeruddin and M. Grätzel, *Angew. Chemie - Int. Ed.*, 2018, **57**, 14125–14128.
- 100 H. Jiang, Y. Ren, W. Zhang, Y. Wu, E. C. Socie, B. I. Carlsen, J. E. Moser, H. Tian, S. M. Zakeeruddin, W. H. Zhu and M. Grätzel, *Angew. Chemie - Int. Ed.*, 2020, **59**, 9324–9329.
- 101 A. Grobelny, Z. Shen, F. T. Eickemeyer, N. F. Antariksa, S. Zapotoczny, S. M.

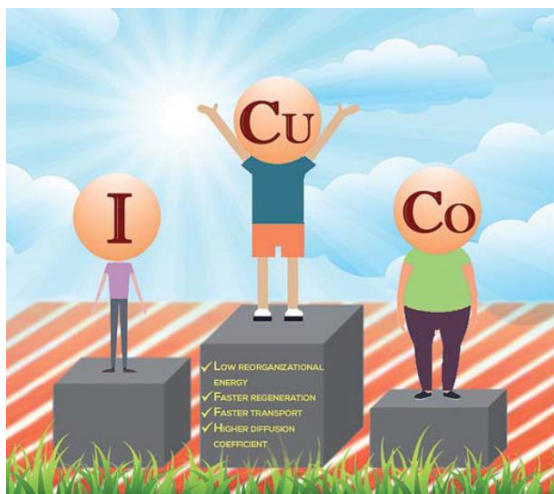
- Zakeeruddin and M. Grätzel, *Adv. Mater.*, 2022, 2207785.
- 102 Y. Ren, N. Flores-Díaz, D. Zhang, Y. Cao, J. D. Decoppet, G. C. Fish, J. E. Moser, S. M. Zakeeruddin, P. Wang, A. Hagfeldt and M. Grätzel, *Adv. Funct. Mater.*, 2020, **30**, 1–7.
- 103 H. Wu, G. Wang and B. X. Lei, *ACS Appl. Energy Mater.*, 2022, **5**, 9962–9969.
- 104 D. Zhang, M. Stojanovic, Y. Ren, Y. Cao, F. T. Eickemeyer, E. Socie, N. Vlachopoulos, J. E. Moser, S. M. Zakeeruddin, A. Hagfeldt and M. Grätzel, *Nat. Commun.*, 2021, **12**, 1–10.
- 105 J. An, X. Yang, Z. Tian, B. Cai, L. Zhang, Z. Yu, X. Wang, A. Hagfeldt and L. Sun, *Tetrahedron*, 2021, **88**, 132124.
- 106 Y. Cao, Y. Liu, M. Zakeeruddin, A. Hagfeldt, Y. Cao, Y. Liu, S. M. Zakeeruddin, A. Hagfeldt and M. Gra, 2018, 1–10.
- 107 E. Tanaka, H. Michaels, M. Freitag and N. Robertson, *J. Mater. Chem. A*, 2020, **8**, 1279–1287.
- 108 H. Michaels, M. Rinderle, R. Freitag, I. Benesperi, T. Edvinsson, R. Socher, A. Gagliardi and M. Freitag, *Chem. Sci.*, 2020, **11**, 2895–2906.
- 109 E. L. Gross, *Photosynth. Res.*, 1993, **37**, 103–116.
- 110 H. Michaels, I. Benesperi, T. Edvinsson, A. Muñoz-Garcia, M. Pavone, G. Boschloo and M. Freitag, *Inorganics*, 2018, **6**, 53.
- 111 M. Hu, J. Shen, Z. Yu, R.-Z. Liao, G. G. Gurzadyan, X. Yang, A. Hagfeldt, M. Wang and L. Sun, *ACS Appl. Mater. Interfaces*, 2018, **10**, 30409–30416.
- 112 Y. Zhao, J. Shen, Z. Yu, M. Hu, C. Liu, J. Fan, H. Han, A. Hagfeldt, M. Wang and L. Sun, *J. Mater. Chem. A*, 2019, **7**, 12808–12814.
- 113 K. Yang, X. Yang, Z. Deng, L. Zhang and J. An, *ACS Appl. Energy Mater.*, 2021, **4**, 14004–14013.
- 114 L. Li, L. Zhao, X. Jiang, Z. Yu, J. Liu, H. Rui, J. Shen, W. Sharmoukh, N. K. Allam and L. Sun, *J. Mater. Chem. A*, 2022, **10**, 4131–4136.
- 115 J. R. Jennings, F. Li and Q. Wang, *J. Phys. Chem. C*, 2010, **114**, 14664–14674.
- 116 C. J. Brabec, A. Cravino, D. Meissner, N. S. Sariciftci, T. Fromherz, M. T. Rispens, L. Sanchez and J. C. Hummelen, *Adv. Funct. Mater.*, 2001, **11**, 374–380.
- 117 S. R. Raga, E. M. Barea and F. Fabregat-Santiago, *J. Phys. Chem. Lett.*, 2012, **3**, 1629–1634.
- 118 L. Kavan, Y. Saygili, M. Freitag, S. M. Zakeeruddin, A. Hagfeldt and M. Grätzel, *Electrochim. Acta*, 2017, **227**, 194–202.
- 119 P. Ferdowsi, Y. Saygili, S. M. Zakeeruddin, J. Mokhtari, M. Grätzel, A. Hagfeldt and L. Kavan, *Electrochim. Acta*, 2018, **265**, 194–201.

-
- 120 Y. Duan, Q. Tang, J. Liu, B. He and L. Yu, *Angew. Chemie - Int. Ed.*, 2014, **53**, 14569–14574.
- 121 J. Wu, Z. Lan, J. Lin, M. Huang, Y. Huang, L. Fan, G. Luo, Y. Lin, Y. Xie and Y. Wei, *Chem. Soc. Rev.*, 2017, **46**, 5975–6023.
- 122 A. Hauch and A. Georg, *Electrochim. Acta*, 2001, **46**, 3457–3466.
- 123 E. Nasybulin, S. Wei, I. Kymissis and K. Levon, *Electrochim. Acta*, 2012, **78**, 638–643.
- 124 S. H. Seo, M. H. Kim, E. J. Jeong, S. H. Yoon, H. C. Kang, S. I. Cha and D. Y. Lee, *J. Mater. Chem. A*, 2014, **2**, 2592–2598.
- 125 G. Yue, J. Wu, Y. Xiao, M. Huang, J. Lin and J. Y. Lin, *J. Mater. Chem. A*, 2013, **1**, 1495–1501.
- 126 L. Kavan, H. Krysova, P. Janda, H. Tarabkova, Y. Saygili, M. Freitag, S. M. Zakeeruddin, A. Hagfeldt and M. Grätzel, *Electrochim. Acta*, 2017, **251**, 167–175.
- 127 S. Yun, Y. Liu, T. Zhang and S. Ahmad, *Nanoscale*, 2015, **7**, 11877–11893.
- 128 L. Fan, J. R. Jennings, S. M. Zakeeruddin, M. Grätzel and Q. Wang, *ChemElectroChem*, 2017, **4**, 1356–1361.
- 129 W. L. Hoffeditz, M. J. Katz, P. Deria, A. B. F. Martinson, M. J. Pellin, O. K. Farha and J. T. Hupp, *ACS Appl. Mater. Interfaces*, 2014, **6**, 8646–8650.
- 130 J. Ling, B. Pal, K. Chong, L. Schmidt-Mende, J. Bisquert and R. Jose, *J. Am. Ceram. Soc.*, 2019, **102**, 6337–6348.
- 131 R. R. Rodrigues, J. M. Lee, N. S. Taylor, H. Cheema, L. Chen, R. C. Fortenberry, J. H. Delcamp and J. W. Jurss, *Dalt. Trans.*, 2020, **49**, 343–355.
- 132 E. Marchini, M. Orlandi, N. Bazzanella, R. Boaretto, V. Cristino, A. Miotello, S. Caramori and S. Carli, *ACS Omega*, 2022, **7**, 29181–29194.
- 133 S. G. Hashmi, G. G. Sonai, H. Iftikhar, P. D. Lund and A. F. Nogueira, *Semicond. Sci. Technol.*, 2019, **34**, 105001.
- 134 A. Glinka, J. Kubicki and M. Ziółek, *Energies*, 2021, **14**, 407.
- 135 J. Li, X. Yang, Z. Yu, G. G. Gurzadyan, M. Cheng, F. Zhang, J. Cong, W. Wang, H. Wang, X. Li, L. Kloo, M. Wang and L. Sun, *RSC Adv.*, 2017, **7**, 4611–4615.
- 136 J. Velore, S. Chandra Pradhan, T. W. Hamann, A. Hagfeldt, K. N. N. Unni and S. Soman, *ACS Appl. Energy Mater.*, 2022, **5**, 2647–2654.
- 137 R. García-Rodríguez, R. Jiang, E. J. Canto-Aguilar, G. Oskam and G. Boschloo, *Phys. Chem. Chem. Phys.*, 2017, **19**, 32132–32142.
- 138 A. B. Muñoz-García, I. Benesperi, G. Boschloo, J. J. Concepcion, J. H. Delcamp, E. A. Gibson, G. J. Meyer, M. Pavone, H. Pettersson, A. Hagfeldt and M. Freitag, *Chem. Soc. Rev.*, 2021, **50**, 12450–12550.

- 139 I. Benesperi, H. Michaels and M. Freitag, *J. Mater. Chem. C*, 2018, **6**, 11903–11942.
- 140 T.-Y. Kim, Y. Wang, A. L. Raithel and T. W. Hamann, *ACS Energy Lett.*, 2020, **5**, 583–588.
- 141 H. Michaels, I. Benesperi and M. Freitag, *Chem. Sci.*, 2021, **12**, 5002–5015.
- 142 N. Mariotti, M. Bonomo, L. Fagiolari, N. Barbero, C. Gerbaldi, F. Bella and C. Barolo, *Green Chem.*, 2020, **22**, 7168–7218.
- 143 A. Aslam, U. Mehmood, M. H. Arshad, A. Ishfaq, J. Zaheer, A. Ul Haq Khan and M. Sufyan, *Sol. Energy*, 2020, 207, 874–892.
- 144 J. E. Ikpesu, S. E. Iyuke, M. Daramola and A. O. Okewale, *Sol. Energy*, 2020, **206**, 918–934.
- 145 M. Freitag and G. Boschloo, *Curr. Opin. Electrochem.*, 2017, **2**, 111–119.

Resurgence of DSCs with Copper Electrolyte: A Detailed Investigation of the Interfacial Charge Dynamics in Comparison with Cobalt and Iodine

2.1. Abstract



Deploying earth abundant copper as redox mediators in dye-sensitized solar cells (DSCs) is found to be a very promising strategy to achieve higher photovoltage and power conversion efficiencies in full sun (100 mW/cm^2) and in low/diffused light conditions. Achieving higher photovoltage without compromising the photocurrent helped copper electrolyte to attract much attention among the alternate electrolytes currently employed in DSC. With a very small reorganization energy between Cu(I) and Cu(II) and small molecular size helped copper in achieving unit regeneration efficiency with a driving force as low as 100 mV and a high diffusion coefficient (D_n) leading to a better diffusion length (L_n) and charge collection efficiency (η_{cc}). The mass transport issues were also found to be better in comparison to the cobalt electrolytes. Being inert to silver and other electrical contacts used in DSCs, and higher mobilities even in solid state makes copper based electrolyte a promising candidate to spearhead the commercialization of dye solar technology. In this regard a detailed evaluation of the internal electron transfer dynamics

is highly essential to understand the limiting processes in these devices. In the present manuscript we carried out a one-on-one comparison between copper, cobalt and iodine electrolyte using same dye (LEG4), semiconductor (TiO_2) and electrolyte with similar additive concentrations in a way to understand the in-depth charge transfer process leading to higher photoconversion efficiencies and also to probe the various deleterious processes taking place in copper devices which gives an opportunity to further improve its performance in future.

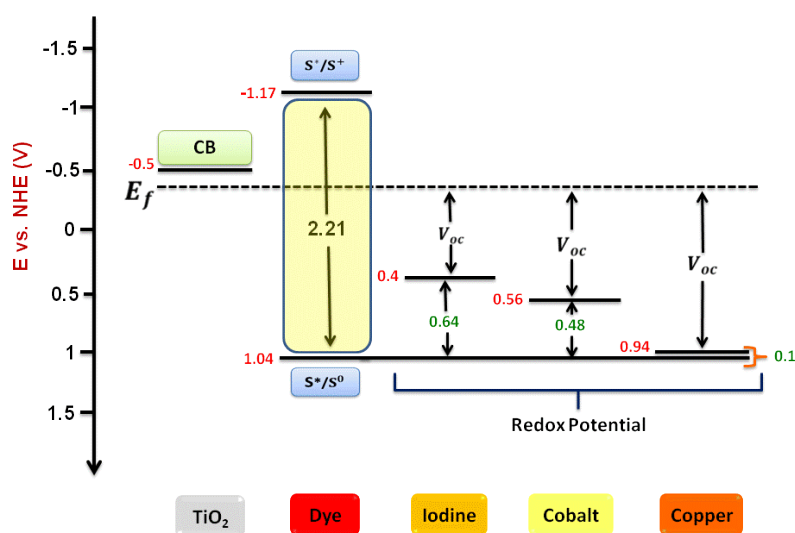
2.2. Introduction

Semiconductor, dye and electrolyte are the three major components of DSCs. Dye absorbs the light and the excited electrons are injected to the semiconductor. The oxidized dye is in-turn regenerated by the redox electrolyte. To cater to the needs of industry leading to commercialization of DSCs, there is a huge demand in developing electrolytes which are efficient and non-corrosive towards the current collector and used in modules/ panels and which are capable of delivering more voltage which is a pre-requisite for proper functioning of low power energy harvesting circuit used in Internet of things (IoT) domain. Iodide/triiodide (I/I_3^-) electrolyte serves as the most successful redox electrolyte in DSC's till date. The success of the I/I_3^- redox couple is mainly attributed to its slow recombination, fast regeneration and high solubility. But unfortunately, the mechanism involving I/I_3^- is still quite unclear which obscures the understanding of the fundamental processes. In addition to this another major drawback of I/I_3^- is the need of large driving force for regeneration which prevents in attaining higher photovoltage.

In a way to circumvent the issues related to conventional Iodide/triiodide electrolyte, metal complex based redox mediators were introduced as a viable option.^{1,2,3} Among these cobalt based redox couples occupies a prominent position. Cobalt electrolyte offers the flexibility to precisely tune the redox potential to match with dye energetics by the variation of ligands surrounding the metal center and also by introducing electron donating or withdrawing substituent to the ligands. It has successfully proved to be the best electrolyte to be used in combination with organic dyes to achieve higher voltage and higher efficiency. Even though highly efficient DSCs in literature all employ cobalt electrolyte, it is prone to high recombination coupled with mass transport issues as a result of the bulky polypyridyl ligands which are not yet solved completely. Recently, the realization of the potential of using earth abundant copper metal complexes as electrolyte has rejuvenated

the DSC research as a whole. Being a metal complex, it gives the option to fine tune the redox potential by judicious substitution of the peripheral ligands. In addition, low cost and low toxicity of these earth abundant material really pave the way for the commercialization of DSCs.

Copper redox mediators perceived to be responsible for this paradigm shift in DSC research. In the past few years, an unprecedented progression in the area of dye cells have been achieved by employing copper electrolytes in full sunlight, in indoor/lowlight/diffused light conditions. In a way to further improve the performance of DSC employing copper based electrolytes and to transform this to commercial manufacturing a more extensive understanding of the internal charge transfers dynamics evaluating the limiting processes is highly required. In this regard the present contribution involves a deeper perception on the influence of copper electrolyte to various charge transfer processes in DSC in comparison to existing iodide/triiodide (I^-/I_3^-) and cobalt electrolyte $[Co(bpy)_3]^{2+/3+}$. For direct comparison we employed the same dye (LEG4), similar electrode materials and identical device architecture for all the three electrolytes in a way to achieve uniform diffusion of the oxidized species in all three systems. Schematic representation of energetics of various components employed in the present study is given in **Scheme 2.1**.



Scheme 2.1. Representation of energetics of TiO₂ semiconductor, LEG4 dye and three different electrolytes (I^-/I_3^- , $[Co(bpy)_3]^{3+/2+}$ and $[Cu(dmp)_2]^{2+/1+}$) employed in the present study.

2.3. Experimental Section

2.3.1. Materials and Methods

All chemicals were purchased from Sigma-Aldrich unless otherwise noted. LEG4, cobalt and copper electrolytes were obtained from Dyenamo AB (Stockholm, Sweden).

2.3.2. Solar Cell Fabrication

At first the working electrodes were cleaned by sonication of 2x2 cm² FTO (Tec15, GreatCell Solar) glass with soap solution accompanied by delicate rubbing in running water followed by sonication in Millipore water and sonication in IPA and acetone for 15 minutes respectively with each step succeeded by UV-O₃ treatment. Thereafter, the substrates were immersed in 40 mM aqueous TiCl₄ solution for 30 minutes at 70°C and annealed at 500°C for 30 minutes. The mesoporous TiO₂ (30 nm particle, Dyenamo) layer was deposited by doctor blading using of a 0.3 cm² gasket on mode using 3M scotch tape followed by 100°C annealing for 10 minutes. A TiO₂ scattering layer (250 nm particle) was coated over the transparent layer followed by programmed heating at 325°C for 15 min, 375 °C for 15 min, 450°C for 15 min and 500°C for 30 minutes. Thickness of TiO₂ (active layer + scattering layer) was using a profilometer and the thickness was found to be 12 ± 03 μm. The post-blocking layer was measured subsequently deposited by heating the electrodes in 40 mM TiCl₄ solution for 30 min at 70°C succeeded by annealing at 500°C for 30 min. Cooling of the sintered photoanodes to 70°C is accompanied by immersion in LEG4 dye (Dyenamo) solutions in 1:1 acetonitrile tert-butanol (0.2 mM) mixture which were kept overnight at room temperature. The films were then rinsed in acetonitrile to remove excess dye. Counter electrodes were prepared by drilling FTO (TEC8, GreatCell Solar) glass substrates which were then cleansed using soap solution, Millipore water, and ethanol, respectively, for 45 min each, thereafter treated by UV-O₃. The preparation of PEDOT electrode involve electropolymerisation of 3,4-ethylene dioxythiophene (EDOT) from a micellar aqueous solution of 0.1 M sodium dodecyl sulfatate (SDS) and 0.01 M EDOT. Solar cells were assembled with an electrochemically deposited poly(3,4-ethylene dioxythiophene) (PEDOT) counter electrode (TEC8, GreatCell Solar) using a 30 μm thick thermoplastic Surlyn frame. The predrilled holes were sealed using a coverslip right after electrolyte was introduced. The I⁻/I₃⁻ electrolyte was obtained from Greatcell Solar (HPE electrolyte). The composition of [Co(bpy)₃]^{3+/2+} electrolyte was 0.22 M [Co(bpy)₃(PF₆)₂], 0.05 M [Co(bpy)₃(PF₆)₃], 0.1 M LiTFSI, and 0.5 M tert-butylpyridine in acetonitrile. The

$[\text{Cu}(\text{dmp})_2]^{2+/1+}$ electrolyte consists of 0.20 M $[\text{Cu}(\text{dmp})]\text{TFSI}$, 0.04 M $[\text{Cu}(\text{dmp})_2]\text{TFSI}$ Cl, 0.1 M LiTFSI, and 0.5 M 4-tert-butylpyridine in acetonitrile.

2.3.3. Solar Cell Characterization

Measurements of the devices regarding the photocurrent voltage (J - V) characteristics were carried out using a solar simulator Oriel (Model PVIV-94043A) Class-AAA solar simulator accompanied by Keithley E 2400 source meter giving light with AM 1.5 G spectral distribution which was calibrated using a certified reference solar cell to an intensity of 100 mW cm^{-2} . Circular black mask of areas 0.18 cm^2 (smaller than the active area) were used accordingly during the J - V measurements to minimize the contribution of light falling outside the active area. The measurement of incident photon-to-current conversion efficiency (IPCE) of devices were performed under DC mode using a 250 W xenon lamp integrated with a Newport monochromator, and a potentiostat, calibrated using a certified reference solar cell. Current Transient measurements were carried out under AM 1.5G illumination. The lamp was switched on and switched off manually and the photocurrent response was recorded using Autolab PGSTST302N in potentiostatic mode by applying 0 V across the device.

The Electrochemical impedance spectroscopy (EIS) was carried out using an Autolab (PGSTAT 302N) workstation equipped with FRA under forward bias in dark. The measurements were done in a frequency range from 100 mHz to 100 kHz with perturbation of 10 mV. The forward bias range for I_3^-/I_2 , $[\text{Co}(\text{bpy})_3]^{3+/2+}$ and $[\text{Cu}(\text{dmp})_2]^{2+/1+}$ systems were selected where almost same dark current was flowing in all the systems. NOVA1.11 interface software was used for carrying out measurements as well as fitting the impedance plots. Intensity-modulated photovoltage spectroscopy (IMVS) and Intensity-modulated photocurrent spectroscopy (IMPS) measurements were carried out using the electrochemical workstation (PGSTAT 302N) equipped with an FRA and LED driver to drive an array of red LED (627 nm, Thorlab). The intensity of the LED was varied by providing different current to the LED. The LED intensity was measured using a certified photodetector supplied by ThorLab. The responses of the cells were analyzed in the frequency range of 0.1 Hz to 1 kHz. The amplitude of the sinusoidal modulation for IMVS and IMPS measurements was 10% of the steady light.

2.4. Results and Discussions

2.4.1. Photovoltaic Performance Analysis

The current density-voltage ($J-V$) characteristics were measured under 100 mWcm^{-2} , AM 1.5G illumination for LEG4 sensitized solar cells using I^-/I_3^- , $[\text{Co}(\text{bpy})_3]^{3+/2+}$ and $[\text{Cu}(\text{dmp})_2]^{2+/1+}$ redox electrolytes which are shown in **Figure 2.1** and the results are summarized in **Table 2.1**. I^-/I_3^- system showed a power conversion efficiency of $5.79 \pm 0.16\%$ with an open circuit voltage (V_{oc}), short circuit current density (J_{sc}) and fill factor (FF) of $783 \pm 26 \text{ mV}$, $12.28 \pm 0.71 \text{ mAcm}^{-2}$, and 0.60 ± 0.01 respectively. Under similar conditions $[\text{Co}(\text{bpy})_3]^{3+/2+}$ delivered a V_{oc} of $868 \pm 12 \text{ mV}$, J_{sc} of $7.42 \pm 0.18 \text{ mAcm}^{-2}$, and FF of 0.7 ± 0.02 resulting in a power conversion efficiency of $4.52 \pm 0.28\%$. An improved power conversion efficiency of $6.82 \pm 0.32\%$ was recorded employing $[\text{Cu}(\text{dmp})_2]^{2+/1+}$ electrolyte resulted in V_{oc} of $902 \pm 10 \text{ mV}$, J_{sc} of $12.66 \pm 0.55 \text{ mAcm}^{-2}$ and FF of 0.6 ± 0.01 . An improvement in V_{oc} of 85 mV in $[\text{Co}(\text{bpy})_3]^{3+/2+}$ system and 119 mV for $[\text{Cu}(\text{dmp})_2]^{2+/1+}$ was realized with respect to I^-/I_3^- electrolyte. The more positive redox potential of $[\text{Co}(\text{bpy})_3]^{3+/2+}$ ($E^0 = 0.56 \text{ V vs. NHE}$) and $[\text{Cu}(\text{dmp})_2]^{2+/1+}$ ($E^0 = 0.94 \text{ V vs NHE}$) compared to I_3^-/I^- (0.4 V vs NHE) resulted in achieving higher V_{oc} employing $[\text{Co}(\text{bpy})_3]^{3+/2+}$ and $[\text{Cu}(\text{dmp})_2]^{2+/1+}$ based electrolytes. By considering the Nernst potential of the electrolyte it is expected to have an increment in voltage around 540 mV on changing from I^-/I_3^- to $[\text{Cu}(\text{dmp})_2]^{2+/1+}$ whereas the actual attained improvement was only 119 mV .

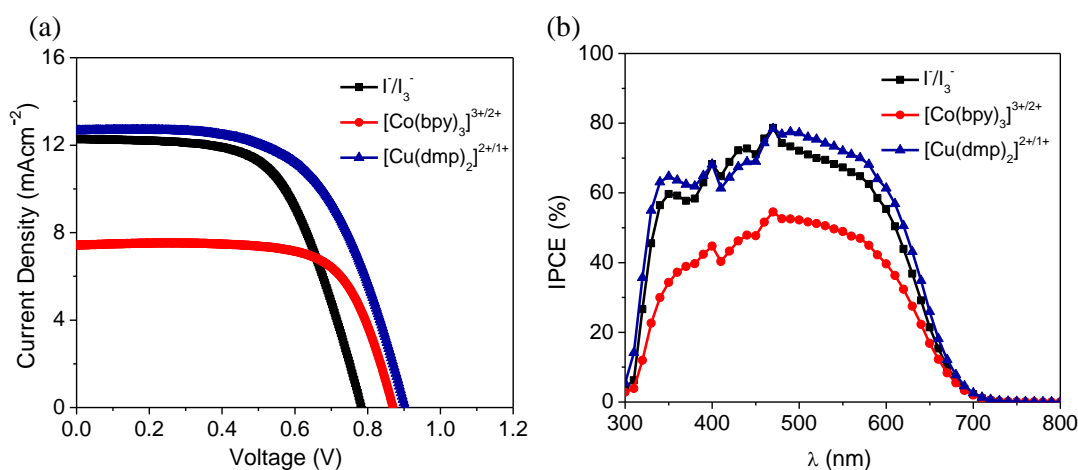


Figure 2.1 (a) Current density versus potential ($J-V$) characteristic curves and (b) IPCE of I^-/I_3^- , $[\text{Co}(\text{bpy})_3]^{3+/2+}$ and $[\text{Cu}(\text{dmp})_2]^{2+/1+}$ electrolytes employed along with LEG4 dye measured under 100 mWcm^{-2} , AM 1.5G illumination.

Table 2.1 Tabulated current-voltage characteristics of I^-/I_3^- , $[\text{Co}(\text{bpy})_3]^{3+/2+}$ and $[\text{Cu}(\text{dmp})_2]^{2+/1+}$ electrolyte with LEG4 dye measured under 100 mWcm^{-2} , AM 1.5G illumination. ${}^a\Delta G^0 = E^0_{\text{dye}} - E^0_{\text{redox}}$.

Electrolyte	V_{oc} (mV)	J_{sc} (mAcm^{-2})	FF	η (%)	ΔG^0 (mV) ^a	E^0_{redox} (mV)	IPCE at 500 nm (%)
I^-/I_3^-	783 ± 26	12.28 ± 0.71	0.60 ± 0.01	5.79 ± 0.16	640	400	72.10
$[\text{Co}(\text{bpy})_3]^{3+/2+}$	868 ± 12	7.42 ± 0.18	0.70 ± 0.02	4.52 ± 0.28	480	560	52.21
$[\text{Cu}(\text{dmp})_2]^{2+/1+}$	902 ± 10	12.66 ± 0.55	0.60 ± 0.01	6.82 ± 0.32	100	940	77.22

Similarly, there should be an improvement of 380 mV on moving from $[\text{Co}(\text{bpy})_3]^{3+/2+}$ to $[\text{Cu}(\text{dmp})_2]^{2+/1+}$, in reality only 34 mV increase in V_{oc} was achieved. This clearly points out to the fact that it is not merely the position of the redox potential of the electrolyte that determines the voltage, there are other parameters like position of conduction band (CB) and recombination of electrons which also contribute towards determining the voltage, current and photovoltaic performance. This will be discussed in detail in the following section.

While examining the variation in current density (J_{sc}), $[\text{Co}(\text{bpy})_3]^{3+/2+}$ showcased 4.86 mAcm^{-2} lesser J_{sc} than I^-/I_3^- , whereas $[\text{Cu}(\text{dmp})_2]^{2+/1+}$ exhibited almost the same J_{sc} as of I^-/I_3^- . The drop in J_{sc} for $[\text{Co}(\text{bpy})_3]^{3+/2+}$ is due to the mass transport limitation of $[\text{Co}(\text{bpy})_3]^{3+/2+}$ redox shuttle which is elaborated in the following sections. Even though with minimal driving force of 100 mV for regeneration, the reaction kinetics is fast enough to render close to 100% regeneration employing LEG4 and $[\text{Cu}(\text{dmp})_2]^{2+/1+}$ resulting in better current density.^{4,5} $[\text{Cu}(\text{dmp})_2]^{2+/1+}$ outperformed both I^-/I_3^- and $[\text{Co}(\text{bpy})_3]^{3+/2+}$ with respect to photovoltage, short circuit current and overall efficiency respectively. A better FF for $[\text{Co}(\text{bpy})_3]^{3+/2+}$ could also be due to the result of low resistive losses due to lower current density. The rationale of higher power conversion efficiency using $[\text{Cu}(\text{dmp})_2]^{2+/1+}$ electrolyte is attributed to its positive redox potential which improved V_{oc} and faster regeneration which resulted in higher J_{sc} . IPCE spectra of LEG4 devices employing all three electrolytes are shown in **Figure 2.1(b)**. IPCE was found to be in the decreasing order $[\text{Co}(\text{bpy})_3]^{3+/2+} < \text{I}^-/\text{I}_3^- < [\text{Cu}(\text{dmp})_2]^{2+/1+}$ which is in accordance with the J - V results. IPCE is given by the equation,

$$IPCE = LHE \times \eta_{inj} \times \eta_{reg} \times \eta_{coll} \quad (1)$$

where, LHE is the light harvesting efficiency, η_{inj} is the injection efficiency, η_{reg} corresponds to regeneration efficiency and η_{coll} denotes charge collection

efficiency. Using same dye, similar photoanodes materials and architecture, LHE and η_{inj} can be assumed to be unity. Then the difference in $IPCE$ is directly correlated to the regeneration and charge collection efficiencies. Copper electrolyte being the best among the series considering for η_{reg} and η_{coll} showcased a relatively higher $IPCE$. Since $IPCE$ is measured at low monochromatic light intensities, the variation in $IPCE$ between cobalt and copper complexes has a major contribution from regeneration and charge collection in addition to the mass transport limitation.

2.4.2. Mass Transport Limitations

Slower mass transport is one of the most challenging issues in alternative redox electrolyte based DSCs. Sluggish mass transport limits regeneration rate which results in reduced J_{sc} . Redox mediators diffuse either in the pores or in the bulk. Diffusion in pores is more mass transport limited than in bulk.⁶ Very often in DSCs, J_{sc} shows nonlinear relationship with increase in light irradiance. The variation of short-circuit current density (J_{sc}) with light irradiance intensity is shown in **Figure 2.2** Current density is related to input light irradiance intensity by the relation, $J_{sc} \propto I^\alpha$ where α is a constant. I/I_3^- system showcased almost linear relationship with J_{sc} yielding an α value of 0.93. $[Cu(dmp)_2]^{2+/1+}$ system was found to be comparatively more linear than $[Co(bpy)_3]^{3+/2+}$ electrolyte with α values of 0.85 and 0.53 respectively. Slow response of DSC due to long trapping and detrapping time of electrons in TiO_2 or mass transport limitation of redox mediator in electrolyte are the probable rationales for the nonlinear relationship of J_{sc} with irradiance intensity. Time lag due to trapping and detrapping can be ruled out as the TiO_2 used for I/I_3^- , $[Co(bpy)_3]^{3+/2+}$ and $[Cu(dmp)_2]^{2+/1+}$ are exactly identical. Thereupon the nonlinear increase of J_{sc} with light irradiance intensity is due to the mass transport limitations associated with the electrolyte. It is to be noted that $[Co(bpy)_3]^{3+/2+}$ electrolyte showed a better J_{sc} than I/I_3^- till 0.3 sun but the former was severely affected by mass transport limitation at illumination intensities > 0.3 sun in the present semiconductor configuration. In a way to confirm this we carried out photovoltaic measurement with just one layer of 30 nm TiO_2 particle which resulted in an efficiency of 6% for $[Co(bpy)_3]^{3+/2+}$ clearly giving evidence to mass transport problem with $[Co(bpy)_3]^{3+/2+}$ in the present architecture. In order to have similar charge population employing the three electrolytes to have a better comparison of charge transfer phenomena, we employed the same device architecture for all the three electrolytes. Basically mass transport is delayed by the steric bulk of the redox mediator.⁷ Being a six co-ordinate complex cobalt electrolyte is more bulky with three

polypyridyl ligands surrounding the metal center where as copper being a four co-ordinate complex only have two ligands and is less bulky. Also due to its smaller size copper complexes diffuse through the electrolyte much faster than its counterpart cobalt system.

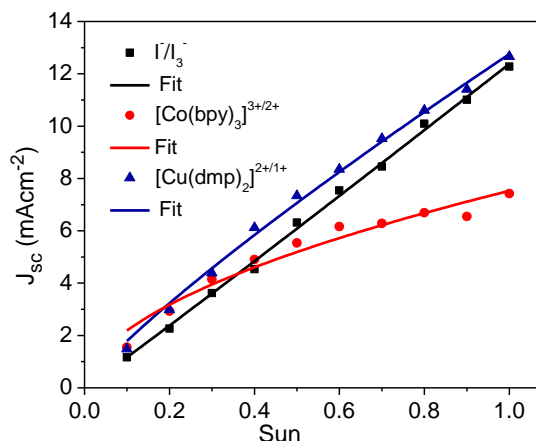


Figure 2.2 Light intensity dependence on the short circuit current density for I^-/I_3^- , $[Co(bpy)_3]^{3+/2+}$ and $[Cu(dmp)_2]^{2+/1+}$ electrolytes.

Further the mass transport was investigated by photocurrent transient measurements. **Figure 2.3 (a), (b) and (c)** shows the photocurrent transient measurements for I^-/I_3^- , $[Co(bpy)_3]^{3+/2+}$ and $[Cu(dmp)_2]^{2+/1+}$ systems. In photocurrent transient measurement the current response of the device is measured by illumination followed by switching off the light. Photocurrent transient measurements were carried out under AM 1.5G simulated light from 0.1 sun to 1 sun. With light illumination, J_{sc} reaches to a peak value (J_{max}), either it remains flat there or decays to saturation current (J_{sat}). As the light is irradiated electrons from the HOMO of the dye are excited towards the LUMO leaving behind holes in HOMO. The excited electrons are then consequently injected to the CB of TiO_2 . For further excitation of electrons, holes in HOMO need to be regenerated by the reduced species present in the electrolyte. If the regeneration rate is equivalent to the excitation rate, the current density remains flat with time ($J_{max}=J_{sat}$). Similarly, if the regeneration rate is slower than the excitation rate, current density decays with time and reaches to a saturation value ($J_{max}>J_{sat}$).

The decay of J_{sc} is mainly caused by the slow diffusion of ions in the electrolyte solution. The redox mediator in the electrolyte is capable of regenerating a certain number of oxidized dyes, thus supporting a certain J_{sc} . If the generated J_{sc} is more than the capacity of the redox mediator to maintain it, then a decay in J_{sc} is observed. Thus, J_{sc} decay is also

dye dependent as different dyes possess unlike light absorption properties. Similarly, J_{sc} decay is input light intensity dependent because J_{sc} deliberately drops with light intensity. Subsequently, the extent of J_{sc} decay also drops, and it does not decay at light intensity where generated J_{sc} matches with the capability of the redox mediator to support it.

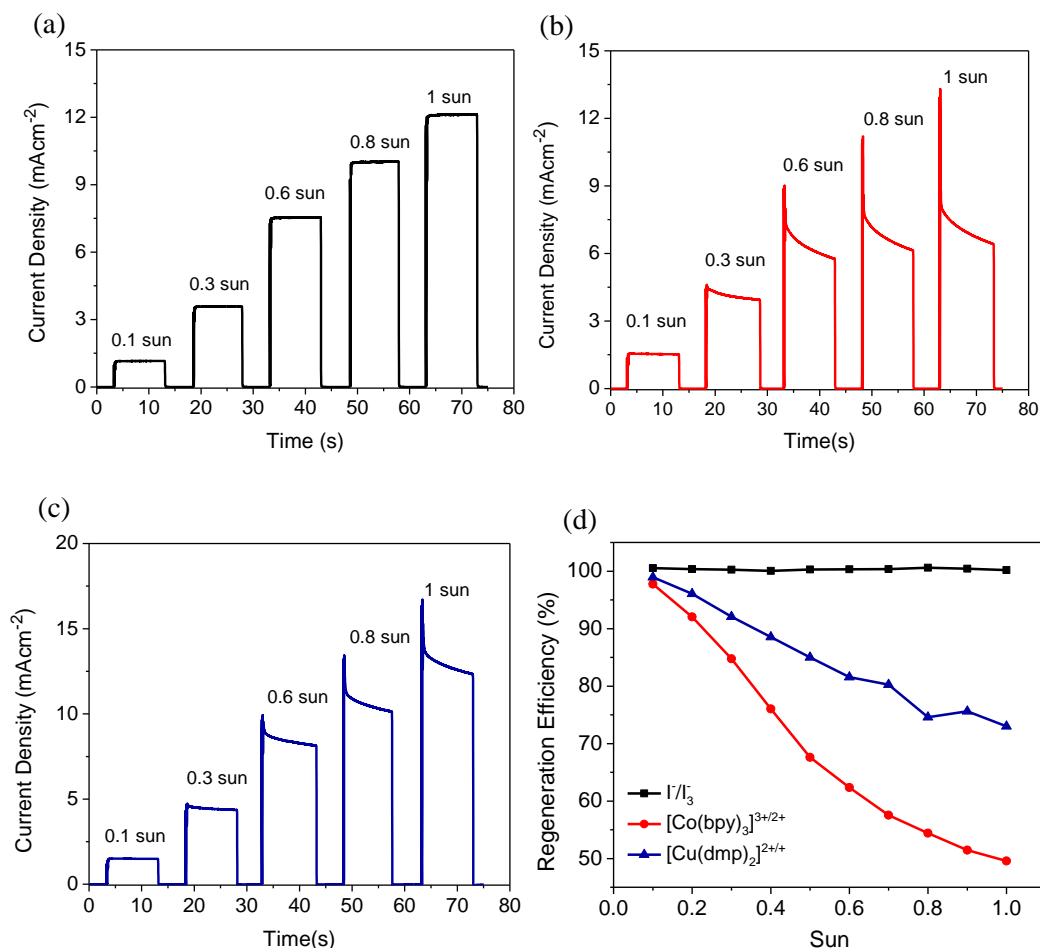


Figure 2.3 Current transients measured at AM 1.5G simulated light from 0.1 sun to 1 sun for (a) I^-/I_3^- (b) $[Co(bpy)_3]^{3+/2+}$ and (c) $[Cu(dmp)_2]^{2+/1+}$ (d) Regeneration Efficiency from 0.1 sun to 1 sun for I^-/I_3^- , $[Co(bpy)_3]^{3+/2+}$ and $[Cu(dmp)_2]^{2+/1+}$.

For device employing I^-/I_3^- the peak current was not observed which confirms that it is not limited by mass transport. The larger peak in $[Co(bpy)_3]^{3+/2+}$ compared to $[Cu(dmp)_2]^{2+/1+}$ elucidates higher mass transport limitation in $[Co(bpy)_3]^{3+/2+}$ compared to that of $[Cu(dmp)_2]^{2+/1+}$. At lower intensities mass transport limitation was hardly observed as comparatively fewer electrons were there to be regenerated by the reduced species present in the electrolyte. Slower mass transport limits the regeneration efficiency. Thereupon to investigate the consequence of mass transport limitation; regeneration efficiency is used as a useful tool. **Figure 2.3 (d)** shows regeneration efficiency at various

light intensities. With assumption of sufficient driving force for regeneration for I/I_3^- , $[Co(bpy)_3]^{3+/2+}$ and $[Cu(dmp)_2]^{2+/1+}$ electrolytes ; regeneration efficiency can be calculated from current transient by the equation, $(J_{sat}/J_{max}) \times 100$ where J_{sat} is saturated J_{sc} and J_{max} is the peak J_{sc} . For I/I_3^- based devices the regeneration efficiency was found to be 100% regardless of the light intensity. For $[Co(bpy)_3]^{3+/2+}$ and $[Cu(dmp)_2]^{2+/1+}$ electrolytes regeneration efficiency decreased with increase in light intensity as mass transport issues become more prominent at higher intensities. Regeneration efficiency was superior for $[Cu(dmp)_2]^{2+/1+}$ based electrolyte with regeneration efficiency value of 72% under 1 sun condition, compared to $[Co(bpy)_3]^{3+/2+}$ where the regeneration efficiency was only 49%.

EIS was carried out to further investigate the diffusion of redox species in I/I_3^- , $[Co(bpy)_3]^{3+/2+}$ and $[Cu(dmp)_2]^{2+/1+}$ redox shuttles. **Figure 2.4 (a)** and **(c)** shows the Nyquist plot and equivalent circuit used to fit the Nyquist plot. Nyquist plot showed two semicircles for I/I_3^- and three semicircles for $[Co(bpy)_3]^{3+/2+}$ and $[Cu(dmp)_2]^{2+/1+}$ electrolyte. The semicircle at higher frequency region corresponds to the charge transfer at the counter electrode/electrolyte interface, the second semicircle in the middle frequency region corresponds to the charge transfer at the TiO_2 /dye/electrolyte interface and the third semicircle at the lower frequency region corresponds to the diffusion of ions in the electrolyte. The Nyquist plot was fitted with transmission line model as given in **Figure 2.4 (c)**.⁸⁻¹¹ The equivalent circuit consists of resistors, capacitors and constant phase element. R_{PEDOT} and C_{PEDOT} refer to the resistance and capacitance at the counter electrode/electrolyte interface. Similarly, R_s is the sheet resistance of substrates and Z_d is the impedance of ion diffusion in the electrolyte. The transmission line model was used to fit TiO_2 /dye/electrolyte interface and it consists of three electrical parameters transport resistance (R_t), recombination resistance (R_{rec}) and chemical capacitance (C_μ). R_t corresponds to resistance for the electrons to diffuse in mesoporous TiO_2 , R_{rec} is the resistance for the recombination of electrons at the TiO_2 /electrolyte interface and C_μ is the constant phase element that represents the capacitance at the TiO_2 /electrolyte interface. Diffusion resistance (R_d) was calculated Z_d . **Figure 2.4 (b)** shows the Diffusion resistance (R_d) against potential corrected for the potential drop due to series resistance. The diffusion resistance of I/I_3^- electrolyte was so low that its resultant response in Nyquist plot was not even observed. However, a distinct semicircle at lower frequency in Nyquist plot was clearly noticed for both $[Co(bpy)_3]^{3+/2+}$ and $[Cu(dmp)_2]^{2+/1+}$ system. $[Cu(dmp)_2]^{2+/1+}$ electrolyte showed lower R_d than $[Co(bpy)_3]^{2+/3+}$. Higher R_d results in slower diffusion of

ions in the electrolyte. Recently Freitag and co-workers have successfully shown that $[\text{Cu}(\text{dmp})_2]^{2+/1+}$ complexes is having a diffusion coefficient ($25 \times 10^{-6} \text{ cm}^2\text{s}^{-1}$) which is double the value $[\text{Co}(\text{bpy})_3]^{3+/2+}$ ($9.4 \times 10^{-6} \text{ cm}^2\text{s}^{-1}$) which was determined using cyclic voltammetry.⁵ Further the smaller size of four co-ordinate copper complex helped in achieving a faster movement inside the nano porous network in comparison to the six coordinate cobalt complex achieving higher diffusion coefficient.

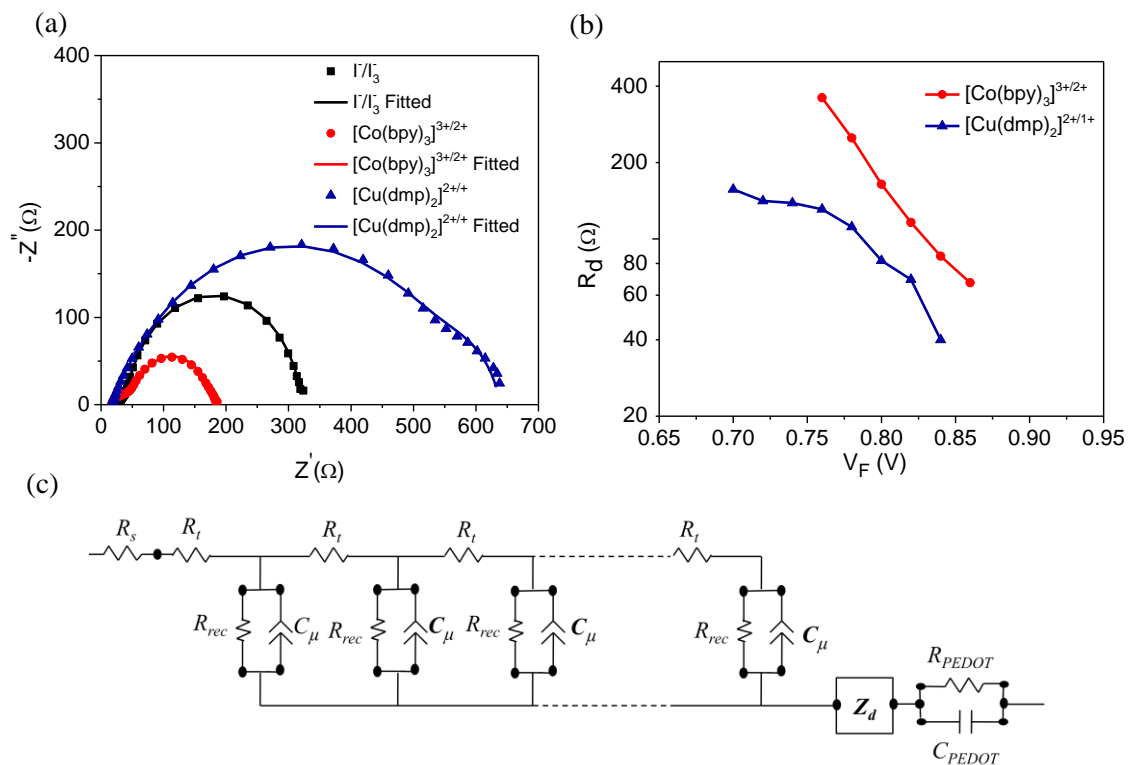


Figure 2.4 (a) Nyquist plot (b) diffusion resistance (R_d) as a function of corrected potential and (c) equivalent circuit used to fit Nyquist plot.

2.4.3. Nonlinearity and Surface state Recombination

The light intensity dependence of open-circuit potential (V_{oc}) for I/I_3^- , $[\text{Co}(\text{bpy})_3]^{3+/2+}$ and $[\text{Cu}(\text{dmp})_2]^{2+/1+}$ electrolytes are given in **Figure 2.5**. V_{oc} is related to light intensity by the relation,

$$\frac{dV_{oc}}{d \log I} = \frac{2.30mk_B T}{q} \quad (2)$$

Where, I is input light intensity, m is the ideality factor, k_B is Boltzmann's constant and T is the temperature. m is calculated from irradiance vs V_{oc} plot using the standard linear equation.^{12,13}

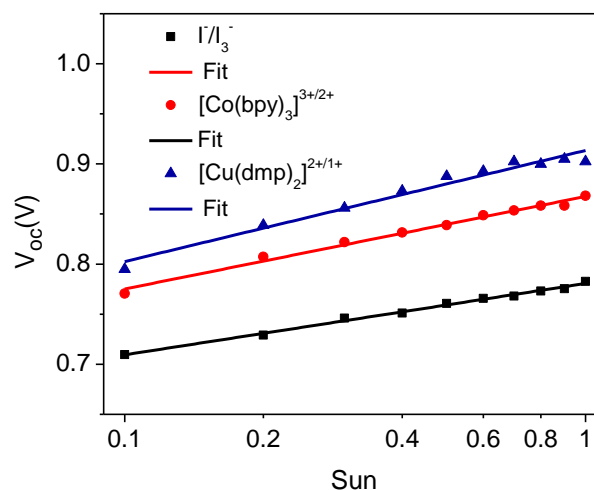


Figure 2.5 Light intensity dependence of the open-circuit voltage for I^-/I_3^- , $[Co(bpy)_3]^{3+/2+}$ and $[Cu(dmp)_2]^{2+/1+}$ electrolytes.

A non-linear dependence of V_{oc} with input irradiance was observed for I^-/I_3^- , $[Co(bpy)_3]^{3+/2+}$ and $[Cu(dmp)_2]^{2+/1+}$ electrolytes. The electron recombination at FTO/electrolyte interface results in non-ideality in DSC.^{14–16} However to block electron recombination at FTO/electrolyte interface we deposited compact TiO_2 blocking layer which significantly curbs the back electron transfer. Thereupon the non-idealities due to the back electron transfer at FTO/electrolyte interface can be ruled out to certain extent. According to Bisquert *et al.* the non-ideal characteristics is due to recombination from the exponentially distributed surface trap states located over the band gap of TiO_2 .^{17,18} There is always recombination from surface states, but the rate of recombination from surface states is slower compared to the conduction band states, thereby recombination from surface states and conduction band states are hardly distinguished experimentally. The recombination from trap states becomes more prominent when the driving force for recombination increases.¹⁹ Hamann *et al.* has already reported a significant recombination from surface trap states with reduced species of electrolyte employing $[Ru(bpy)_2(MeIm)_2]^{3+/2+}$ redox shuttle based DSC.²⁰ For I^-/I_3^- system m was found to be 1.19 which is very near to the ideal value where rate of recombination rate is very low due to the lower driving force for recombination from surface states. In $[Co(bpy)_3]^{3+/2+}$ and $[Cu(dmp)_2]^{2+/1+}$ electrolyte based DSCs, m value was found to be 1.54 and 1.89 which shows the possibility of higher recombination from surface states in $[Cu(dmp)_2]^{2+/1+}$ compared to $[Co(bpy)_3]^{2+/3+}$. We strongly believe that with proper surface state passivation using techniques like ALD where we can precisely control the passivating layer thickness, the recombination can be

controlled/modulated especially employing alternative copper redox mediators in a way to further improve its performance.

2.4.4. Investigation of Interfacial Charge Dynamics with Small Electrical and Light Perturbation Techniques

To investigate in detail, the origin of variation in open circuit potential (V_{oc}) with reference to the shift in conduction band, recombination, diffusion and transport properties we carried out Electrochemical Impedance Spectroscopy (EIS) in dark. EIS was carried out with same device architecture and analyzed using the transmission line model developed by Bisquert *et al.* **Figure 2.6 (a), (b) and (c)** shows the chemical capacitance (C_{μ}),

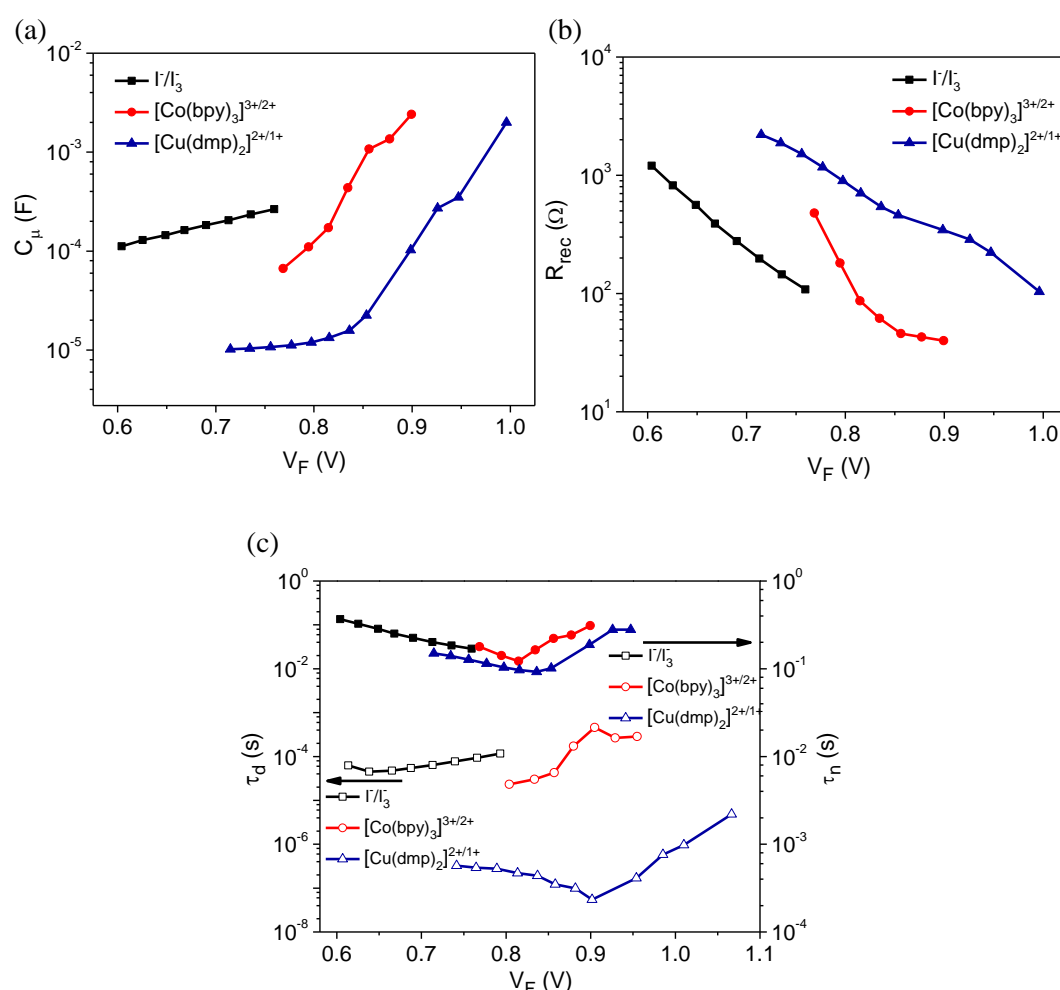


Figure 2.6 (a) Chemical capacitance (C_{μ}) (b) recombination resistance (R_{rec}) and (c) electron lifetime (τ_n) and transport time (τ_d) as a function of corrected potential employing I^-/I_3^- , $[Co(bpy)_3]^{3+/2+}$ and $[Cu(dmp)_2]^{2+/1+}$ electrolytes.

recombination resistance (R_{rec}), lifetime (τ_n) and transport time (τ_d) for I^-/I_3^- , $[Co(bpy)_3]^{3+/2+}$ and $[Cu(dmp)_2]^{2+/1+}$ electrolytes as a function of corrected potential. Chemical capacitance

(C_{μ}) is the quantification of the conduction band edge of TiO_2 . A negative shift in conduction band was observed in $[\text{Co}(\text{bpy})_3]^{3+/2+}$ and $[\text{Cu}(\text{dmp})_2]^{2+/1+}$ electrolytes with respect to I^-/I_3^- system. $[\text{Cu}(\text{dmp})_2]^{2+/1+}$ was found to be most negatively shifted in comparison to $[\text{Co}(\text{bpy})_3]^{3+/2+}$ electrolyte. Negative shift in conduction results in higher V_{oc} if the rate of recombination is unaltered. Again a more negative shift in CB of TiO_2 may lead towards an injection limitation in DSC. Here in, injection limitation due to shift in CB can be ruled out as there is ample driving force (close to 600 mV) between the excited state of LEG4 dye and TiO_2 conduction band. In addition to this by employing $[\text{Cu}(\text{dmp})_2]^{2+/1+}$ electrolyte which is more negatively shifted compared to reference I^-/I_3^- electrolyte showed similar J_{sc} which again justifies that injection has minimal influence in determining the performance in the present case which is also complimented by the fast regeneration prevailing in copper based electrolytes. From the capacitance plot it is quite obvious that the higher voltage resulted for copper based electrolyte has its contributions also from the negative shift in conduction band as the V_{oc} is said to be the difference between the redox potential of the electrolyte and the Fermi level. A similar trend was also observed in case of $[\text{Cu}(\text{dmp})_2]^{2+/1+}$ employing C218 organic dye by Wang et. al.⁸ Recombination resistance was found to be in the decreasing order of $[\text{Cu}(\text{dmp})_2]^{2+/1+} > [\text{Co}(\text{bpy})_3]^{3+/2+} > \text{I}^-/\text{I}_3^-$. Recombination resistance is given by the equation,

$$R_{rec} = R_0 \exp\left[-\frac{q\beta V_F}{k_B T}\right] \quad (3)$$

$$R_0 = \frac{k_B T}{q\beta j_0} \quad (4)$$

$$j_0 = j_{0k} \exp\left\{\frac{\beta(E_{F0} - E_C)}{k_B T}\right\} \quad (5)$$

Where, β is recombination parameter, k_B is Boltzman constant, T is temperature, q is charge, E_C corresponds to the conduction band edge. By analyzing equations 3, 4 and 5 it is quite evident that a shift in the position of CB brings to a change in j_0 , R_0 and hence R_{rec} . Thus difference observed in recombination resistance can be correlated to the difference in position of CB of TiO_2 using I^-/I_3^- , $[\text{Co}(\text{bpy})_3]^{3+/2+}$ and $[\text{Cu}(\text{dmp})_2]^{2+/1+}$ electrolytes. The time span of the average number of injected electrons in TiO_2 before it recombines with the oxidized species in electrolyte is represented as the lifetime whereas the average time required for the injected electrons to get collected at the working electrode is denoted as the transport time. Lifetime should be higher than the transport time for attaining efficient charge collection. $[\text{Cu}(\text{dmp})_2]^{2+/1+}$ resulted in a slightly lower lifetime compared to $[\text{Co}(\text{bpy})_3]^{3+/2+}$ and I^-/I_3^- electrolytes as a result of the negative shift in

conduction band coupled with more positively placed redox potential thereby leading to higher driving force for recombination from CB and sub band gap states to the oxidized species in electrolyte. In addition, a more porous 30 nm particle allows oxidized Cu^{2+} species to come closer to FTO resulting in recombination from the FTO/electrolyte interface. Recombination rate is directly proportional to the driving force for recombination. Hagfeldt *et al.* had realized Marcus normal region behavior for recombination using a range of cobalt redox shuttles with various organic dyes as well as ruthenium sensitizer.¹⁹ Recently, Freitag *et al.* has also observed a Marcus normal region behavior for recombination employing copper redox electrolytes with Y123 dye.¹⁰ In our recent contribution we also observed Marcus normal region behavior for recombination using two triphenylamine dyes TPAA4 and TPAA5 employed along with cobalt redox shuttles.²¹ As $[\text{Cu}(\text{dmp})_2]^{2+/1+}$ having higher driving force for recombination it is quite natural to have lower lifetime, interestingly $[\text{Co}(\text{bpy})_3]^{3+/2+}$ and I/I_3^- showed similar lifetime trends which can be related to the nature of semiconductor used in present case. I/I_3^- redox electrolyte is well known for its exceptionally slow recombination rate compared to $[\text{Co}(\text{bpy})_3]^{3+/2+}$ redox electrolyte but employing a more porous 30 nm particle network leaves channels for small molecules like iodine and copper to get closer to the back contact resulting in more recombination whereas for bulky cobalt species the access may be restricted to certain extent. The above mentioned behavior resulted in having a comparable lifetime for iodine and cobalt electrolyte.²² Different blocking materials were tried at $\text{TiO}_2/\text{electrolyte}$ interface in order to alleviate this recombination.²³⁻²⁸ But in majority of cases the blocking layer not only prevent recombination but also limit the injection of electron to the CB if TiO_2 . The alternative and most promising approach to restrict recombination is to structurally modify the dyes which is capable of preventing the reduced species to come closer to TiO_2 , thereby curbing recombination.^{29-31,32} In a way to control recombination without compromising the injection we employed LEG4 sensitizer in the present work. LEG4 is a structurally modified dye with dicyclopentene spacer grafted with long alkyl chains which prevents the approach of reduced species coming closer to the TiO_2 surface. In addition to this enlarged steric bulk property of redox mediator also reduces the recombination.⁷ Hamann *et al.* observed that bulky $[\text{Co}(t\text{-Bu}2\text{bpy})_3]^{3+/2+}$ acted as insulating spacer which reduced the electronic coupling due to steric hindrance, thereby reducing recombination.³³ Maybe the suitable structure of LEG4 sensitizer could effectively prevent the bulky $[\text{Co}(\text{bpy})_3]^{3+/2+}$ redox mediator in approaching closer to the TiO_2 yielding a

comparable lifetime of $[\text{Co}(\text{bpy})_3]^{3+/2+}$ and I^-/I_3^- electrolyte. It is quite exciting to note that copper redox mediator gave the shortest transport time among the series.

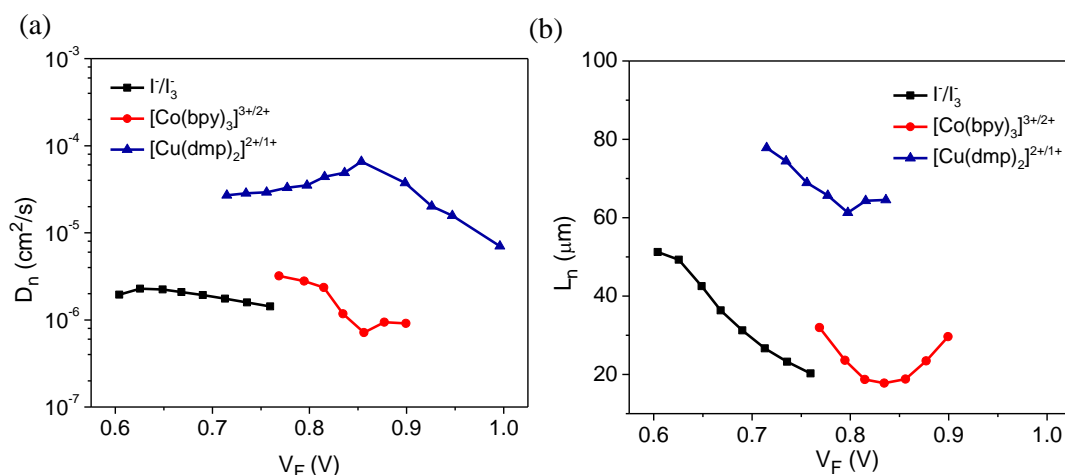


Figure 2.7 (a) Diffusion coefficient (D_n) and (b) diffusion length (L_n) as a function of corrected potential.

Diffusion coefficient (D_n) and diffusion length (L_n) as a function of corrected potential are given in **Figure 2.7**. Diffusion coefficient (D_n) is inversely proportional to transport time, as given by the equation $D_n = \frac{L^2}{\tau_d}$ where L is the thickness of the semiconductor. Diffusion coefficient (D_n) decreased in the order $[\text{Cu}(\text{dmp})_2]^{2+/1+} > [\text{Co}(\text{bpy})_3]^{3+/2+} > \text{I}^-/\text{I}_3^-$. Slightly lower lifetime for $[\text{Cu}(\text{dmp})_2]^{2+/1+}$ is compensated by the higher diffusion coefficient and hence $[\text{Cu}(\text{dmp})_2]^{2+/1+}$ exhibited longer diffusion length compared to $[\text{Co}(\text{bpy})_3]^{3+/2+}$ and I^-/I_3^- . Diffusion length (L_n) is the distance electrons can travel before ends up in recombination. Diffusion length (L_n) is given by the relation, $L_n = \sqrt{D_n \times \tau_n}$. Longer L_n results in better charge collection efficiency which in turn results in higher IPCE value. This holds completely true in the present case where copper electrolyte having a better L_n resulted in better IPCE profile. The higher D_n and L_n obtained for copper can be particularly be result of fast regeneration and slow recombination prevailing in copper compared to cobalt electrolyte.

To examine charge transfer dynamics in presence of light we carried out photo-modulated perturbation measurements such as Intensity Modulated Photovoltage Spectroscopy (IMVS) and Intensity Modulated Photocurrent Spectroscopy (IMPS). Results are shown in **Figure. 2.8**. For both the photo-modulated measurements monochromatic light (627 nm)

was used as the light source for excitation. Electron lifetime (τ_n) was determined from IMVS by the relation,⁴²

$$\tau_n = \frac{1}{2\pi f_m} \quad (6)$$

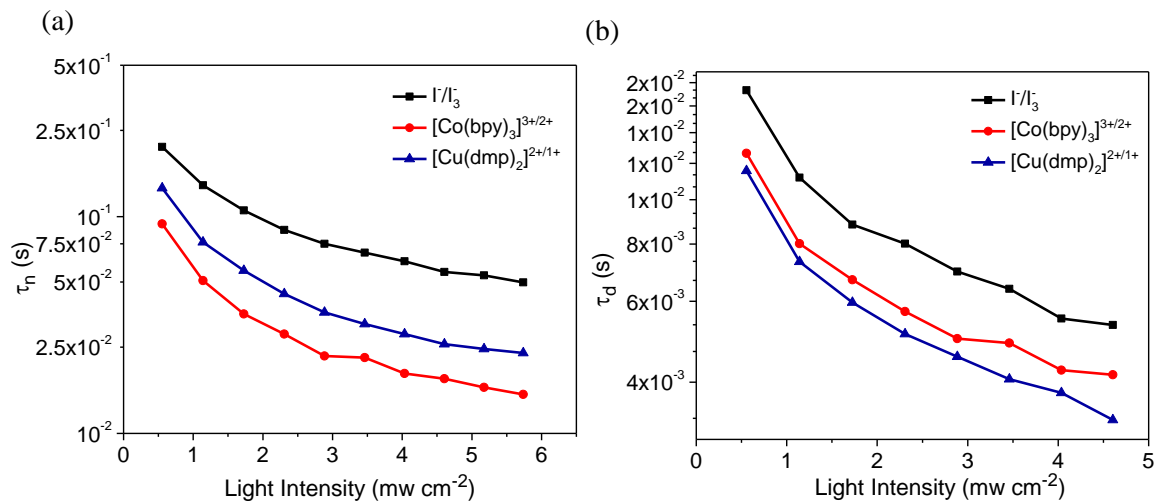


Figure 2.8 (a) Lifetime (τ_n) and (b) Transport time (τ_d) as a function of light intensity.

where, f_m is the frequency corresponding to highest value of the imaginary part ($-H''$) in Bode plot. The lifetime was found to be in decreasing order $\text{I}_3^-/\text{I}^- > [\text{Cu}(\text{dmp})_2]^{2+/1+} > [\text{Co}(\text{bpy})_3]^{3+/2+}$. The observed trend is found to be slightly different from what we came across in EIS measurements carried out in dark. This behavior is quite conclusive since under illumination mass transport limitation was quite visible for both the outer sphere cobalt and copper redox mediators. Subodh Mhaisalkar *et al.* had previously observed that the possibility of the relatively slow moving bulky redox mediator ions getting accumulate at the TiO_2 surface thereby increasing the recombination.³⁴ As discussed previously copper electrolyte showed much lower mass transport at higher light intensity which is reflected in better lifetime for copper in comparison to cobalt in light measurement. Transport lifetime (τ_d) is determined from IMPS by the relation

$$\tau_d = \frac{1}{2\pi f_m} \quad (7)$$

where f_m is the frequency corresponding to highest value of the imaginary part ($-H''$) in Bode plot. The transport time was in decreasing order $\text{I}_3^-/\text{I}^- > [\text{Co}(\text{bpy})_3]^{3+/2+} > [\text{Cu}(\text{dmp})_2]^{2+/1+}$ which resembles the transport time trend calculated from EIS. From both the dark and light measurements, it is quite clear that a lower transport time and higher

diffusion coefficient are the two major parameters which elated copper electrolyte in achieving higher photovoltaic performance.

2.5. Conclusions

Redox electrolyte plays a crucial role in determining the photovoltaic performance in DSCs. Electrolytes with positive redox potentials can serve as a viable solution for attaining higher photovoltage. In a way to study the gain and loss processes associated by changing the electrolytes, we carried out detailed interfacial charge transfer dynamics investigation using various perturbation techniques employing iodine, cobalt and copper electrolytes. Though conventional iodide/triiodide based devices were independent of mass transport issues, the Nernst potential was placed at a less positive potential in comparison to cobalt and copper electrolytes leading to lower photovoltage. Even though cobalt electrolyte is endowed with a more positive redox potential in comparison to conventional iodide electrolytes, slow regeneration and higher recombination coupled with mass transport limitations became an obstacle in realizing long term performance and stability in these devices.

It is a general trend to have an increase in voltage and decrease in current on moving to more positive redox potentials as a result of slow regeneration rates and higher recombination whereas for copper-based electrolytes a difference in trend is observed. The increase in both voltage and current simultaneously for copper based electrolyte is accomplished as a result of higher regeneration and better charge collection efficiency in addition to superior diffusion coefficient and lower mass transport issues endowed by the smaller size of copper in comparison to cobalt electrolytes. Copper is placed at a potential which is 540 mV more positive to I^-/I_3^- and 380 mV positive to $[Co(bpy)_3]^{2+/3+}$. In addition, copper electrolyte-based devices result in a negative shift in conduction band, both of which should trigger more recombination for copper in comparison to other two electrolytes. With a very fast regeneration kinetics and efficiency, copper electrolytes were able to manage the recombination reaction to a greater extent. Based on our observation, for copper based electrolytes the interception reaction takes place from the conduction band, sub-band gap states, surface states, and FTO to the oxidized Cu(II) species present in the electrolyte. Employing pre and post blocking layers can help in preventing this recombination to a greater extent. This points to the need of employing pinhole free compact blocking layers using techniques like ALD which would further improve the performance of copper based

devices. Also this indicates the requirement of structurally engineered dyes that can prevent the recombination in a better way. Mass transport is another issue that needs to be tackled for copper electrolyte. The best option being reducing the spacer thickness as recently been shown by Boschloo and Oskam which is very effective in controlling the mass transport in copper electrolyte based devices.³⁵ In addition to this a further tuning of the porosity of semiconductor is required in a way to extract the best out of copper electrolyte based solar cells. In a nutshell, being environmental friendly with easy synthesis protocols, low cost and earth abundance along with its ability to deliver higher performance in full sun and low light makes copper based redox electrolyte a promising candidate for future DSC research.

2.6. References

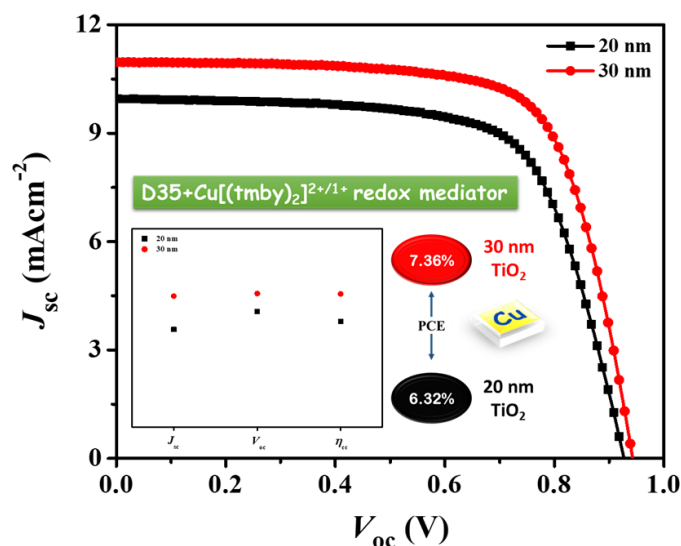
- 1 T. W. Hamann and J. W. Ondersma, 2011, 370–381.
- 2 T. W. Hamann, R. A. Jensen, A. B. F. Martinson, H. Van Ryswyk and J. T. Hupp, *Energy Environ. Sci.*, 2008, **1**, 66.
- 3 J.-H. Yum, E. Baranoff, F. Kessler, T. Moehl, S. Ahmad, T. Bessho, A. Marchioro, E. Ghadiri, J.-E. Moser, C. Yi, M. K. Nazeeruddin and M. Grätzel, *Nat. Commun.*, 2012, **3**, 631.
- 4 M. Freitag, F. Giordano, W. Yang, M. Pazoki, Y. Hao, B. Zietz, M. Grätzel, A. Hagfeldt and G. Boschloo, *J. Phys. Chem. C*, 2016, **120**, 9595–9603.
- 5 Y. Saygili, M. Söderberg, N. Pellet, F. Giordano, Y. Cao, A. B. Muñoz-García, S. M. Zakeeruddin, N. Vlachopoulos, M. Pavone, G. Boschloo, L. Kavan, J. E. Moser, M. Grätzel, A. Hagfeldt and M. Freitag, *J. Am. Chem. Soc.*, 2016, **138**, 15087–15096.
- 6 J. J. Nelson, T. J. Amick and C. M. Elliott, *J. Phys. Chem. C*, 2008, **112**, 18255–18263.
- 7 J. Kusters, S. M. Feldt, E. a. Gibson, E. Gabrielsson, L. Sun, G. Boschloo, A. Hagfeldt and J. Kusters, *J. Am. Chem. Soc.*, 2007, **1**, 2–7.
- 8 F. Fabregat-Santiago, G. Garcia-Belmonte, I. Mora-Seró and J. Bisquert, *Phys. Chem. Chem. Phys.*, 2011, **13**, 9083–9118.
- 9 E. Oommen, A. Hummel, L. Allmannsberger, D. Cuthbertson, S. Carette, C. Pagnoux, G. S. Hoffman, D. E. Jenne, N. A. Khalidi, C. L. Koenig, C. A. Langford, C. A. McAlear, L. Moreland, P. Seo, A. Sreih, S. R. Ytterberg, P. A. Merkel, U. Specks and P. A. Monach, *Clin. Exp. Rheumatol.*, 2017, **35**, 98–101.
- 10 J. Bisquert and F. Fabregat-santiago, *J. Phys. Chem. C*, 2009, **113**, 17278–17290.

-
- 11 J. Bisquert, I. Mora-Sero and F. Fabregat-Santiago, *ChemElectroChem*, DOI:10.1002/celc.201300091.
 - 12 P. Salvador, M. G. Hidalgo, A. Zaban and J. Bisquert, *J. Phys. Chem. B*, 2005, **109**, 15915–15926.
 - 13 J. Bisquert and I. Mora-Seró, *J. Phys. Chem. Lett.*, 2010, **1**, 450–456.
 - 14 S. Sasidharan, S. Soman, S. C. Pradhan, K. N. N. Unni, A. A. P. Mohamed, B. N. Nair and H. U. N. Saraswathy, *New J. Chem.*, 2017, **41**, 1007–1016.
 - 15 P. J. Cameron and L. M. Peter, *J. Phys. Chem. B*, 2005, **109**, 7392–7398.
 - 16 P. J. Cameron and L. M. Peter, 2005, 930–936.
 - 17 J. Bisquert, A. Zaban, M. Greenshtein and I. Mora-Seró, *J. Am. Chem. Soc.*, 2004, **126**, 13550–13559.
 - 18 S. Cells, N. S. Statistics and I. Electron, 2002, 8774–8782.
 - 19 S. M. Feldt, P. W. Lohse, F. Kessler, M. K. Nazeeruddin, M. Grätzel, G. Boschloo and A. Hagfeldt, *Phys. Chem. Chem. Phys.*, 2013, **15**, 7087–7097.
 - 20 J. W. Ondersma and T. W. Hamann, *J. Am. Chem. Soc.*, 2011, **133**, 8264–8271.
 - 21 S. Soman, S. C. Pradhan, M. Yoosuf, M. V. Vinayak, S. Lingamoorthy and K. R. Gopidas, *J. Phys. Chem. C*, 2018, **122**, 14113–14127.
 - 22 T. W. Hamann, *Dalt. Trans.*, 2012, **41**, 3111–3115.
 - 23 S. Lee, J. H. Noh, H. S. Han, D. K. Yim, D. H. Kim, J.-K. Lee, J. Y. Kim, H. S. Jung and K. S. Hong, *J. Phys. Chem. C*, 2009, **113**, 6878–6882.
 - 24 A. K. Chandiran, P. Comte, R. Humphry-baker, F. Kessler, C. Yi, K. Nazeeruddin and M. Grätzel, 2013, 2775–2781.
 - 25 C. Lin, F.-Y. Tsai, M.-H. Lee, C.-H. Lee, T.-C. Tien, L.-P. Wang and S.-Y. Tsai, *J. Mater. Chem.*, 2009, **19**, 2999.
 - 26 P. M. Sommeling, B. C. O'Regan, R. R. Haswell, H. J. P. Smit, N. J. Bakker, J. J. T. Smits, J. M. Kroon and J. A. M. van Roosmalen, *J. Phys. Chem. B*, 2006, **110**, 19191–19197.
 - 27 M.-H. Kim and Y.-U. Kwon, *J. Phys. Chem. C*, 2011, **115**, 23120–23125.
 - 28 X. Gao, D. Guan, J. Huo, J. Chen and C. Yuan, *Nanoscale*, 2013, **5**, 10438–10446.
 - 29 X. Jiang, K. M. Karlsson, E. Gabrielsson, E. M. J. Johansson, M. Quintana, M. Karlsson, L. Sun, G. Boschloo and A. Hagfeldt, *Adv. Funct. Mater.*, 2011, **21**, 2944–2952.
 - 30 G. Wu, F. Kong, Y. Zhang, X. Zhang, J. Li and W. Chen, DOI:10.1021/jp4124265.

- 31 A. Mahmood, *Sol. Energy*, 2016, **123**, 127–144.
- 32 M. V. Vinayak, M. Yoosuf, S. C. Pradhan, T. M. Lakshmykanth, S. Soman and K. R. Gopidas, *Sustain. Energy Fuels*, 2018, **2**, 303–314.
- 33 B. M. Klahr and T. W. Hamann, *J. Phys. Chem. C*, 2009, **113**, 14040–14045.
- 34 T. T. Trang Pham, T. M. Koh, K. Nonomura, Y. M. Lam, N. Mathews and S. Mhaisalkar, *ChemPhysChem*, 2014, **15**, 1216–1221.
- 35 R. García-Rodríguez, R. Jiang, E. J. Canto-Aguilar, G. Oskam and G. Boschloo, *Phys. Chem. Chem. Phys.*, 2017, **19**, 32132–32142.

Probing Photovoltaic Performance in Copper Electrolyte Dye-Sensitized Solar Cells of Variable TiO₂ Particle Size Using Comprehensive Interfacial Analysis

3.1. Abstract



Copper-based metal complex redox mediators proved to be an efficient, futuristic electrolyte for dye-sensitized solar cell (DSC) applications addressing many critical issues of conventional iodide/triiodide electrolyte. However, copper redox mediators being bulkier than conventional iodine electrolyte imposes movement restrictions contributing towards unfavourable charge transfer processes. In the present manuscript, we analysed the impact of TiO₂ particle size (20 nm and 30 nm) on the photovoltaic parameters of DSCs using organic D35 dye and alternate copper redox mediator, Cu[(tmby)₂]^{2+/1+}. DSC photoanodes with 20 nm TiO₂ particles realized lower power conversion efficiency (PCE) of $6.32 \pm 0.07\%$ in comparison to $7.36 \pm 0.12\%$ efficiency achieved using DSCs made with 30 nm TiO₂ particles. The improved PCE using 30 nm TiO₂ particles is associated with the enhancement in short circuit current density (J_{sc}), open-circuit potential (V_{oc}) and fill factor (FF). Furthermore, comprehensive analysis of various charge transfer processes at

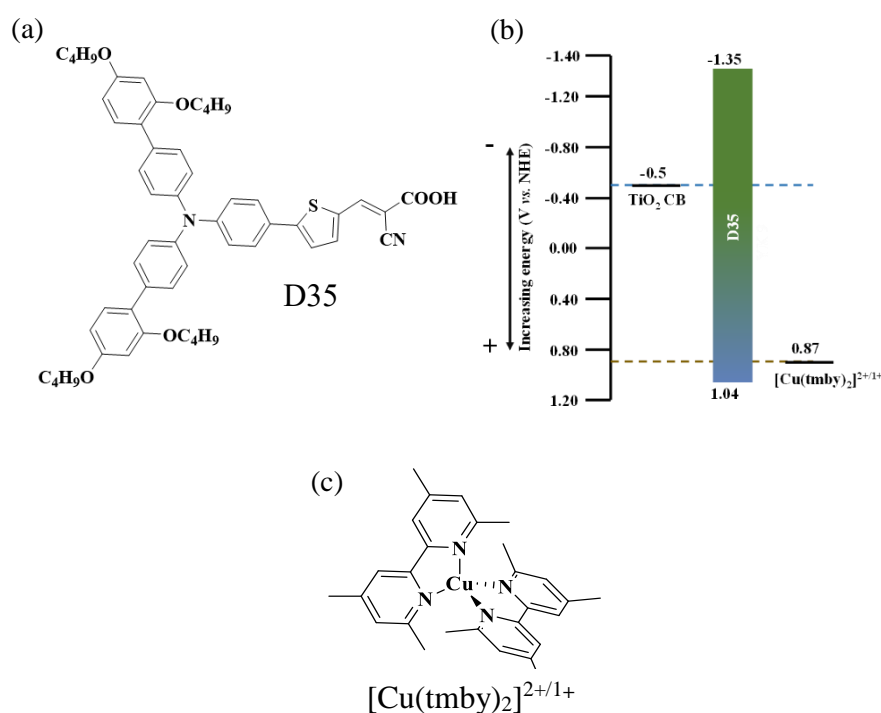
discrete interfaces in these devices reveals collective enhancement in light-harvesting, dye regeneration and charge collection efficiency that ultimately contributed towards achieving 16% improvement in PCE using 30 nm TiO₂ particles.

3.2. Introduction

Third-generation solar cells have garnered tremendous attention in recent years as a potential light-harvesting option, mainly due to their capability to work under diffused/artificial light conditions.¹⁻⁷ Among the various types of third-generation photovoltaic (PV) technologies, dye-sensitized solar cells (DSCs) are considered as one of the most promising cost-effective PV technology.

In DSCs, dye absorbs light, and correspondingly electron-hole pairs are created. The excited electrons are then injected into the semiconductor (TiO₂) and collected through the working electrode. Meanwhile, the oxidized dye is reduced by the electron-rich species present in the electrolyte. The cycle completes as the oxidized species in the electrolyte gets re-reduced at the counter electrode. The output current primarily depends upon the light-harvesting capability of the sensitizer and the voltage constitutes the Fermi energy difference between TiO₂ and redox potential of electrolyte. Since the Fermi level of TiO₂ offers fewer opportunities to modify, V_{oc} of DSCs can be increased more readily by employing electrolytes with positive redox potentials. Unfortunately, conventional I⁻/I₃⁻ redox electrolyte offers minimal flexibility to tune the redox potential (0.4 V vs NHE), limiting DSC's open-circuit potential.⁸ One of the redox complexes that successfully fulfilled the shortcomings of the I⁻/I₃⁻ redox shuttle was cobalt-based metal complex redox mediators (Co³⁺/Co²⁺).⁹ Unlike I⁻/I₃⁻, Co³⁺/Co²⁺ offers modulation of redox potential through structural changes done on the peripheral organic ligands attaining voltage close to 1 V.¹⁰ However, the reorganization energy is relatively high for cobalt redox mediators since Co(III) has a high spin state, and Co(II) has a low spin state necessitating a minimum driving force of 400-500 mV for efficient dye regeneration, limiting further improvement in V_{oc} .^{10,11} A significant advancement in voltage gain was achieved recently with the introduction of copper electrolyte where merely 100 mV driving force was sufficient enough for efficient dye regeneration leading to $V_{oc}>1$ V from a single junction device.¹²⁻¹⁶ Recently, using Cu[(tmby)₂]^{2+/1+} Hagfeldt and co-workers achieved an outstanding V_{oc} of 1.24 V from a single junction device leading to a power conversion efficiency of 13.5%.¹⁷ Fabrication of efficient copper-based DSCs and optimized device architectures.

One such critical device engineering parameter involves the use of mesoporous titanium dioxide particles with variable particle sizes. In standard I^-/I_3^- electrolyte based DSC, mesoporous TiO_2 with an average particle size of 20 nm is commonly used as active layer, which provides a balance between dye uptake and charge transport. However, in copper electrolyte DSCs, mesoporous TiO_2 with an average particle size of 30 nm is primarily preferred over 20 nm. Ferdowsi *et al.* used TiO_2 particles size of 20 nm and 30 nm size with $[Cu(tmby)_2]^{2+/1+}$ electrolyte and newly synthesized sensitizers L156 and L224 sensitizers, which showed improvement in efficiency.¹⁸ Cao *et al.* also observed an improvement in PCE by replacing 20 nm with 30 nm TiO_2 particles under one sun illumination using copper electrolyte.¹⁹ Though the difference between 20 nm and 30 nm TiO_2 particle is minimal, it critically alters surface area and porosity, which further influences the charge transfer process at TiO_2 /electrolyte interface.²⁰ For instance, lower surface area for 30 nm particles reduces electron-hole recombination at TiO_2 /electrolyte



Scheme 3.1 Representation of (a) structure of D35 dye, (b) energetics of TiO_2 semiconductor, and (c) structure of $[Cu(tmby)_2]^{2+/1+}$ employed in the present study.

interface with compromised dye loading.²¹ Similarly, better porosity for 30 nm particles facilitates easy movement of alternative bulky electrolytes.²² Unlike I^-/I_3^- redox mediators,

Cu²⁺/Cu¹⁺ ions are bulky with a higher tendency for interfacial recombination. Thus a slight change in porosity or surface area may substantially influence photovoltaic parameters. Moreover, a detail investigation on the gain in PCE using mesoporous TiO₂ of variable particle sizes are not explored in detail for DSC using copper electrolytes. In the present study, we carried out a comprehensive interfacial analysis of DSCs fabricated using 20 nm and 30 nm TiO₂ particles along with the organic D35 sensitizer and Cu[(tmbpy)₂]^{2+/1+} redox mediator. **Scheme 3.1** shows the molecular structure of D35 dye, Cu[(tmbpy)₂]^{2+/1+} electrolyte and the energy level diagram of TiO₂, dye and electrolyte.

3.3. Experimental Section

3.3.1. General Methods

The solvents and materials used for device fabrication were of HPLC grade purchased from Sigma-Aldrich, Merck, GreatCell Solar and used without further purification. D35 organic dye and [Cu(tmbpy)₂]^{2+/1+} copper complexes were obtained from Dyenamo AB (Stockholm, Sweden). 20 nm 18 NRT TiO₂ paste was obtained from GreatCell Solar and 30 nm TiO₂ paste was obtained from Dyenamo AB.

3.3.2. Fabrication of DSCs

Working electrode preparation starts with cutting of FTO glasses (TEC15, GreatCell Solar) into 1.5 × 1.5 cm² pieces. Thereupon FTO glasses were sonicated in detergent for 30 minutes followed by gentle scrubbing in water and again sonication in deionized (DI) water for 30 minutes, followed by sonication in IPA and acetone for 15 minutes each. To further remove any other organics, processed FTOs were annealed at 500 °C for 15 minutes in a muffle furnace followed by UV-Ozone cleaning. A compact TiO₂ blocking layer was created over FTO using TiCl₄ treatment followed by annealing at 500 °C for 30 minutes. TiCl₄ treatment includes dipping cleaned FTO in 53 mM TiCl₄ bath for 30 min at 70 °C followed by rinsing of FTO using DI water and ethanol. Following this, either a 20 nm TiO₂ particle layer (18NRT, GreatCell Solar) or 30 nm (Dyenamo, Sweden) was deposited by screen printing with a total thickness of 4 μm. Further TiO₂ coated substrates were annealed at 325 °C for 5 minutes, 375 °C for 5 minutes, 400 °C for 5 minutes and 500 °C for 15 minutes. Again, TiCl₄ treatment was done on electrodes followed by annealing at 500 °C for 30 minutes to create a compact TiO₂ post-blocking layer over the mesoporous TiO₂. The electrodes were then kept inside the dye bath overnight. The dye

solution consists of 0.2 mM D35 (Dyename, Sweden) in 1:1 acetonitrile and tert-butanol. For counter electrodes, predrilled $1.5 \times 1.5 \text{ cm}^2$ FTO glasses (TEC8, GreatCell Solar) were sonicated in detergent, DI water, and ethanol for 45 minutes and consequently annealed at $500 \text{ }^\circ\text{C}$ for 15 minutes. Prior to PEDOT [poly (3,4-ethylene dioxythiophene)] deposition, electrodes were treated using UV- O_3 for 15 min. Preparation of PEDOT counter electrode involves electropolymerisation of 3,4-ethylene dioxythiophene (EDOT) from a micellar aqueous solution of 0.1 M sodium dodecyl sulfate (SDS) and 0.01 M EDOT.^{23,24} The electrodes were assembled using a $30 \text{ }\mu\text{m}$ surllyn spacer and heat pressing at $110 \text{ }^\circ\text{C}$. $[\text{Cu}(\text{tmby})_2]^{2+/1+}$ electrolyte, which consists of 0.20 M Cu(I), 0.04 M Cu(II), 0.1 M LiTFSI, and 0.6 M 4-tert-butylpyridine in acetonitrile was injected through the predrilled holes and the holes were subsequently sealed using a cover glass.

3.3.3. Solar Cell Characterization

Photocurrent voltage (J - V) characteristics were carried out using the Oriel Class-AAA solar simulator (Model PVIV- 94043A) accompanied with Keithley 2440 power source. The intensity of irradiation was measured using a certified calibrated Si solar cell. For indoor light measurement was carried out inside a dark box with white CFL as source of illumination. The indoor J - V responses were recorded using Dyename potentiostat (DN-AE05). The intensity of the light was measured using radiometrically calibrated Ocean optics Jaz spectrometer. A circular black mask of areas 0.1256 cm^2 (smaller than the active area) was used during the J - V measurements to minimize the contribution of light falling outside the active area. Incident photon-to-current conversion efficiency ($IPCE$) of devices were performed under DC mode using a 300 W Xenon lamp integrated with a Newport monochromator and power meter, controlled using the Oriel software. Both current transient and open-circuit voltage decay (OCVD) measurements were carried out under AM 1.5G illumination. For current transient measurement, the lamp was sequentially switched on and switched off in intervals of 10 seconds, and the photocurrent response was recorded using Autolab PGSTAT302N by applying 0 V across the device. In OCVD measurement, the device was illuminated for 30 seconds, and then the light was switched off, and the photovoltage decay was recorded. Further from the photovoltage the decay lifetime was calculated.^{25,26} Photo induced absorption spectroscopy (PIA) was recorded using Dyename DN-AE02. It uses 1W blue light-emitting LED ($\lambda=470 \text{ nm}$) as a pump and a 20 W tungsten halogen lamp as a probe. The transmitted light through the sample falls on

the monochromator and is detected by a UV enhanced Si detector connected to a lock-in amplifier (SR830) via a current amplifier. The PIA spectra of the devices were recorded using excitation by LED, which has a square wave with a modulation frequency of 9.3 Hz. For PIA measurement TiO₂ thickness of devices was 4 μm. Transient photovoltage decay, transient photocurrent decay, and charge extraction were measured using DYNAMO Toolbox set-up (DN-AE01). It generates light using white LED, and current or voltages response is recorded using a digital acquisition board. For transient photovoltage and photocurrent decay, a small amplitude square wave perturbations involving different light intensities are given to the device, and the response is recorded at open circuit and short circuit respectively. In charge extraction measurement, the device is illuminated to attain V_{oc} , simultaneously the light is switched off and the device is short-circuited, and the current response is recorded. Electrochemical Impedance Spectroscopy (EIS) of DSCs were carried out under dark condition with perturbation of amplitude 10 mV, frequency ranges from 100 mHz to 100 kHz using Autolab (PGSTAT302N). For LHE study absorption of dye-soaked electrodes were carried out using Ocean Optics Jaz spectrometer. For dye loading study dye desorption was done using 0.1 M NaOH in ethanol and absorption of desorbed dye solutions were recorded using Ocean Optics Jaz spectrometer.

3.4. Results and Discussion

3.4.1. Photovoltaic Performance Analysis

Current density - voltage (J - V) characterization was carried out under one sun illumination (AM 1.5G, 100 mWcm⁻²). **Figure 3.1** shows the J - V and $IPCE$ plots for DSCs fabricated using 20 nm, and 30 nm TiO₂ particles and the resultant photovoltaic parameters are summarized in Table 1 employing D35 sensitizer and [Cu(tmby)₂]^{2+/1+} electrolyte. DSCs with 20 nm particles delivered an open-circuit voltage (V_{oc}) of 928 ± 2 mV, short circuit current density (J_{sc}) of 9.95 ± 0.09 mA/cm² and fill factor (FF) of 0.68 ± 0.01, leading to a power conversion efficiency (η) of 6.32 ± 0.07%. Under similar conditions, DSCs with 30 nm particles exhibited a V_{oc} of 948 ± 3 mV and J_{sc} of 10.96 ± 0.10 mA/cm² and FF of 0.71 ± 0.01 realizing an improved η of 7.36 ± 0.12%. DSCs with 30 nm TiO₂ particles showed 16% improvement in PCE with respect to devices fabricated using 20 nm TiO₂ particles.

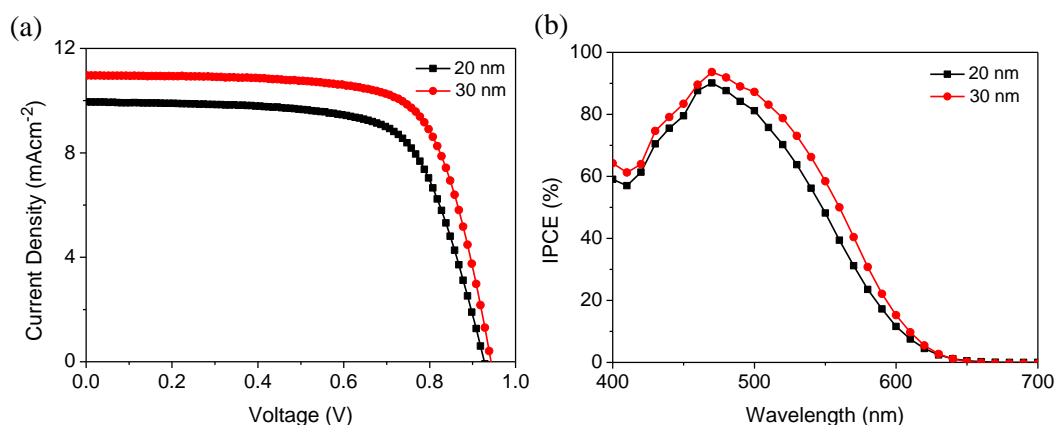


Figure 3.1. (a) Current density - voltage (J - V) and (b) Incident photon current conversion efficiency (IPCE) plot of DSCs fabricated with 20 nm and 30 nm TiO_2 particles employing D35 sensitizer and $[\text{Cu}(\text{tmby})_2]^{2+/1+}$ redox mediator.

Table 3.1. J - V parameters of DSCs fabricated using 20 nm and 30 nm TiO_2 particles using D35 sensitizer and $[\text{Cu}(\text{tmby})_2]^{2+/1+}$ electrolyte.

Device	V_{oc} (mV)	J_{sc} (mAcm^{-2})	FF	η (%)
20 nm	928 ± 2	9.95 ± 0.09	0.68 ± 0.01	6.32 ± 0.07
30 nm	948 ± 3	10.96 ± 0.10	0.71 ± 0.01	7.36 ± 0.12

The improvement in efficiency was also observed under indoor light illumination. **Figure 3.2** shows J - V characteristic of DSCs using 20 nm, and 30 nm TiO_2 particles under 200 lux, 500 lux and 1000 lux illumination and the resultant indoor photovoltaic parameters are summarized in Table 3.2 employing D35 sensitizer and $[\text{Cu}(\text{tmby})_2]^{2+/1+}$ electrolyte. DSCs with 20 nm particles delivered maximum efficiency of $8.83 \pm 0.11\%$ while with 30 nm particles delivered maximum efficiency of $10.37 \pm 0.26\%$. With decrease in indoor light intensity efficiency decreased irrespective of TiO_2 particle, however the efficiency with 30 nm was higher than 20 nm under all light intensities.

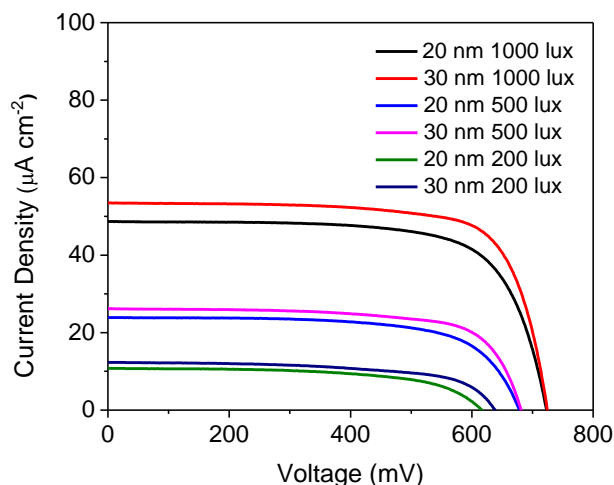


Figure 3.2. Current density - voltage (J - V) of DSCs fabricated with 20 nm and 30 nm TiO₂ particles employing D35 sensitizer and [Cu(tmby)₂]^{2+/1+} redox mediator under compact fluorescent light (CFL) light.

Table 3.2. Indoor photovoltaic parameter of DSCs fabricated with 20 nm and 30 nm TiO₂ particles employing D35 sensitizer and [Cu(tmby)₂]^{2+/1+} redox mediator under CFL light.

Device	Input power lux ($\mu\text{W}/\text{cm}^2$)	V_{oc} (mV)	J_{sc} ($\mu\text{A}/\text{cm}^2$)	FF	P_{max} ($\mu\text{W}/\text{cm}^2$)	η (%)
20 nm	1000 (283)	722 ± 1	48.68 ± 0.26	0.71 ± 0.33	25.01 ± 0.31	8.83 ± 0.11
	500 (143)	679 ± 4	23.92 ± 0.23	0.67 ± 0.37	10.88 ± 0.23	7.61 ± 0.16
	200 (59)	617 ± 2	10.79 ± 0.22	0.60 ± 0.25	3.98 ± 0.27	6.74 ± 0.14
30 nm	1000 (283)	727 ± 3	53.74 ± 0.22	0.75 ± 0.45	$29.36 \pm .74$	10.37 ± 0.26
	500 (143)	687 ± 3	26.54 ± 0.20	0.74 ± 0.80	13.49 ± 0.20	9.43 ± 0.14
	200 (59)	639 ± 2	12.33 ± 0.10	0.61 ± 0.55	4.84 ± 0.33	8.21 ± 0.22

3.4.2. Probing Light Harvesting Efficiency

Light-harvesting efficiency (LHE) demonstrates the capability of the device to absorb light and is the first step in the photon to electrical energy conversion process. During this process, light is absorbed, and electron-hole pairs are created. In DSCs, sensitizer/dye serves the role of light harvester; thus, the absorption capability and molar extinction coefficient of dyes primarily determines the light-harvesting capability.

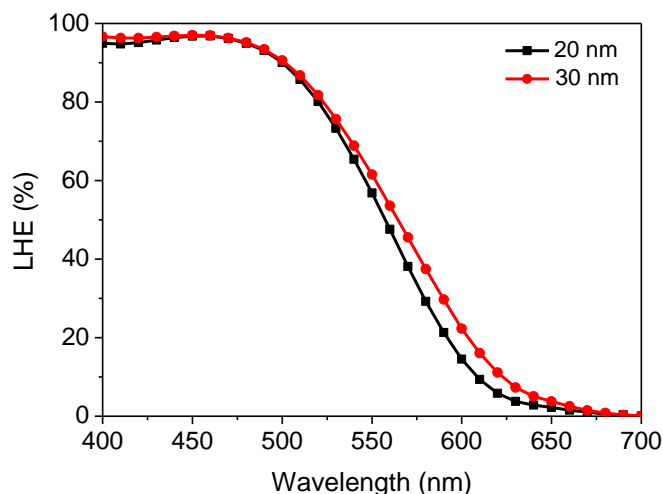


Figure 3.3. Light-harvesting efficiency (*LHE*) of dye soaked TiO₂ electrodes with 20 nm and 30 nm TiO₂ particles as a function of wavelength. The thickness of TiO₂ layer is 4 μm.

Light-harvesting efficiency is given by the equation (2)^{27,28}

$$LHE = 1 - 10^{-abs} \quad (2)$$

Here *abs* is the absorbance. **Figure 3.3.** shows the *LHE* of dye soaked TiO₂ electrodes using 20 nm and 30 nm TiO₂ particles as a function of wavelength. *LHE* of the dye-soaked electrodes with 30 nm TiO₂ particles got marginally red-shifted. The redshift in *LHE* particularly at higher wavelengths (>500 nm) can be attributed to the better light scattering induced by the higher particle size and roughness provided by 30 nm particles. From the AFM image analysis, the roughness was found to be 129 nm for TiO₂ films with 20 nm particles, whereas the roughness value for 30 nm TiO₂ films was found to be 339 nm. Larger roughness contributed towards higher dye loading for 30 nm TiO₂ particles (1.3×10^{-7} Mol cm⁻² for 30 nm and 1.2×10^{-7} Mol cm⁻² for 20 nm). Thus the larger-sized particles with higher roughness improved the scattering and dye intake thereby contributing towards better *LHE* for devices fabricated using 30 nm TiO₂ particles, particularly in the red region.^{29,30}

3.4.3. Probing Recombination

The most critical process that determines the performance of DSCs is the back electron transfer/recombination, at the TiO₂/electrolyte interface. At this interface, the injected electrons in the conduction band (CB) and sub-bandgap states of TiO₂ recombines

with the oxidised species/holes present in the electrolyte. Recombination is more prominent in copper electrolyte-based devices since the redox potentials of Cu^I/Cu^{II} systems are more positively placed than the conventional iodide electrolyte, resulting in larger driving force for recombination. Thus, minor alterations at TiO₂/electrolyte interface remarkably impacts the rate of recombination in copper electrolyte-based DSC. We first analyzed the location of CB in both 20 nm and 30 nm devices using charge extraction measurement.

Figure 3.4 shows V_{oc} as a function of extracted charge for DSCs with 20 nm and 30 nm TiO₂ particles, respectively. As apparent from **Figure 3.4**, at analogous charge density, V_{oc} for 30 nm device is lower than 20 nm, which indicates that the CB of TiO₂ using 30 nm TiO₂ particles shifted towards more positive potentials compared to 20 nm.

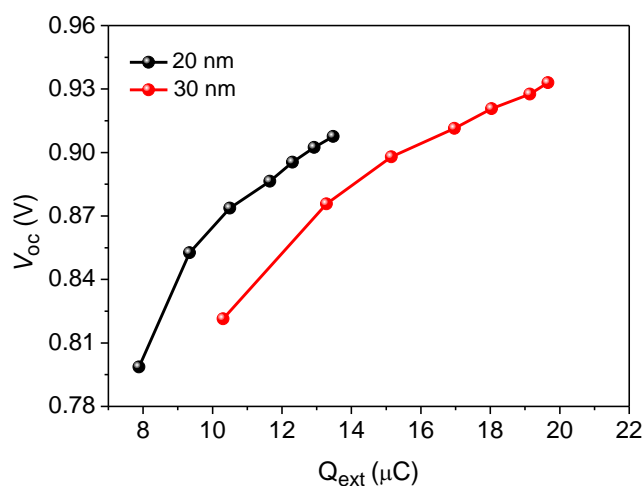


Figure 3.4. V_{oc} as a function of extracted charge for DSCs with 20 nm and 30 nm TiO₂ particles.

After locating the CB of TiO₂, the recombination at TiO₂/electrolyte interface using transient photovoltage decay and open-circuit voltage decay (OCVD) were measured (**Figure 3.5**). Employing these two perturbation techniques, we estimated the lifetime, which provides the information on recombination.

Nevertheless, the CB of TiO₂ in 30 nm devices are also placed at lower potentials than 20 nm, which aids in reducing recombination as a result of a lower recombination-

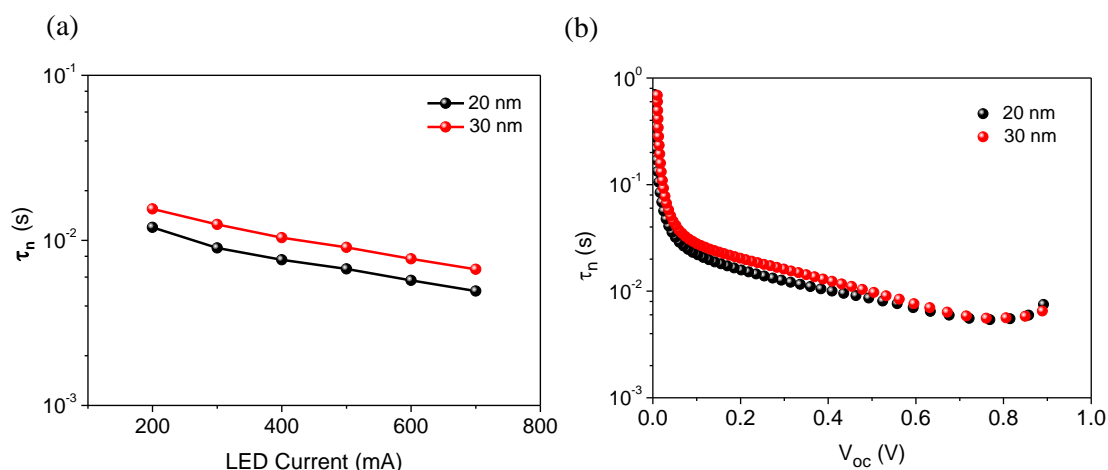


Figure 3.5. Lifetime (τ_n) measurements using (a) Transient photovoltage decay and (b) Open circuit voltage decay (OCVD) for DSCs with 20 nm and 30 nm TiO_2 particles.

driving force. Owing to the improved lifetime, DSCs fabricated using 30 nm TiO_2 particles showed higher V_{oc} and fill factor than the devices fabricated using 20 nm TiO_2 particles.

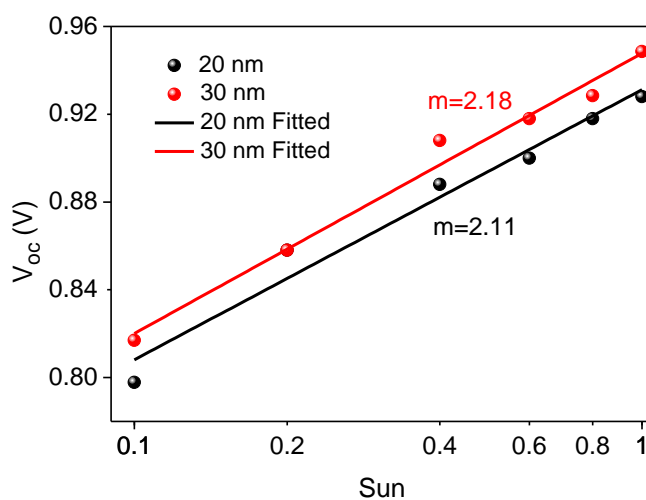


Figure 3.6. V_{oc} as a function light intensity for DSCs with 20 nm and 30 nm TiO_2 particles.

Recombination from the sub-bandgap states of TiO_2 also cannot be ignored for devices using $[\text{Cu}(\text{tmb})_2]^{2+/1+}$ electrolyte with a positive redox potential of 0.87 V vs. *NHE* that leads to non-ideality.^{31,32} We estimated the ideality factor from the V_{oc} vs. light intensity plot (**Figure 3.6**) using the relation,³³

$$\frac{dV_{oc}}{d \log I} = \frac{2.30mk_B T}{q} \quad (3)$$

Where, I is input light intensity, m is the ideality factor, k_B is Boltzmann's constant, and T is the temperature. Using equation 3, m was found to be 2.11 and 2.18 for devices fabricated using 20 nm and 30 nm TiO₂ particles. It is to be noted that the ideal value of m is 1. The non-ideal value in both cases indicates recombination from sub-bandgap states. The extent of non-ideality is nearly similar; thus, the recombination from sub-bandgap states is likely to be identical for both 20 nm and 30 nm TiO₂ particles.

3.4.4. Probing Injection, Regeneration and Mass Transport

The injection and regeneration studies were carried out using photo induced absorption measurements (PIA). **Figure 3.7** shows the PIA spectra of dye-soaked electrodes and copper electrolyte filled devices. For dye-soaked electrodes, the ground state bleaching was detected around 580 nm; meanwhile, absorption of the oxidised D35 dye

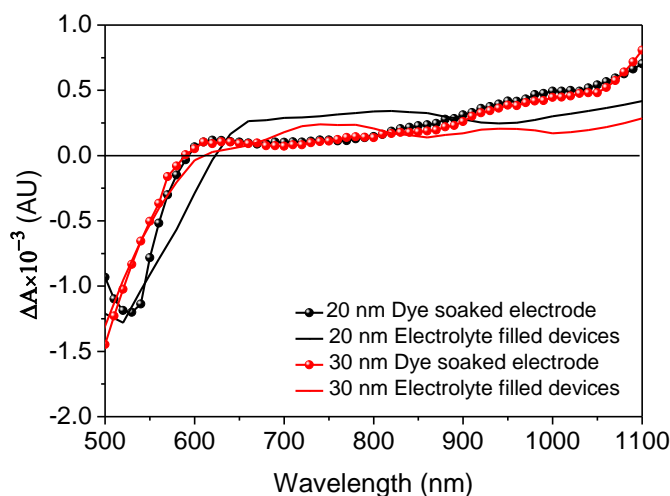


Figure 3.7. PIA spectra for DSCs with TiO₂ electrodes with 20 nm and 30 nm TiO₂ particles.

was observed beyond 800 nm wavelength, showing effective injection of electrons to TiO₂ dye excited state.^{27,34,35} The PIA spectrum of devices fabricated with both the 20 nm and 30 nm TiO₂ particles overlap with each other, indicating similar injection. The absorption spectra of the oxidised D35 dye was quenched with addition of electrolyte electrolyte, suggesting effective regeneration of oxidized dye ground state.⁶ Moreover, faster

regeneration can be anticipated qualitatively for devices using 30 nm TiO₂ particles with respect to devices using 20 nm TiO₂ particles, as the extent of absorption quenching is more in the former case. Dye regeneration can also be influenced by the slower diffusion of ions present in the electrolyte, particularly in DSCs employing alternative redox electrolytes due to the molecular bulkiness of the transition metal complexes.^{36–38}

We carried out intensity dependent J_{sc} measurement and current transient measurements to explore the mass transport limitation in these devices. **Figure 3.8(a)** shows J_{sc} as a function of light intensity. Current density is related to the irradiation intensity by the relation, $J_{sc} \propto I^\alpha$ where α is a constant. $\alpha=1$ suggests ideal relationship between J_{sc} and input light intensity. Using 20 nm and 30 nm TiO₂ particle, α was found to be unity which suggest that both the devices are free from mass transport limitation irrespective of the difference in the size of the TiO₂ particles being used in respective devices. This is applicable to devices using dyes of similar architecture as D35. This may not hold the same using bulky dyes or while employing co-sensitized approach. **Figure 3.8(b)** displays the current transient measurement for DSCs fabricated using photoanodes having 20 nm and 30 nm TiO₂ particles. Current transient measurements were carried out under one sun illumination (100 mW/cm², AM 1.5G). Once the light is irradiated, the current response of the device reached to a maximum current (J_{max}) followed by a decay reaching to a saturation (J_{sat}) current over the passage of a few

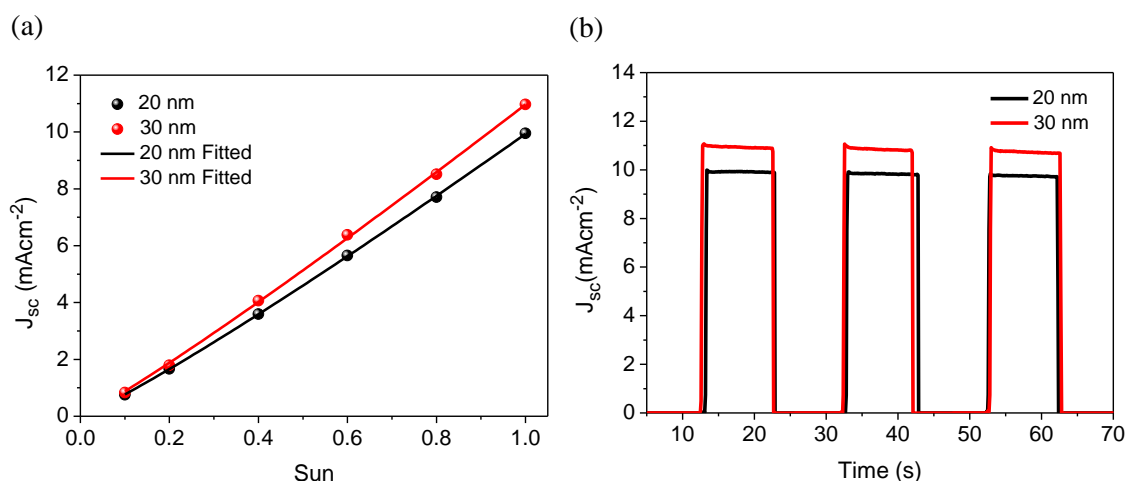


Figure 3.8. (a) Light intensity dependence on J_{sc} for DSCs with 20 nm and 30 nm TiO₂ particles and (b) Current transient plot measured at AM 1.5G simulated light for DSCs fabricated using 20 nm and 30 nm TiO₂ particles.

seconds. As apparent from **Figure 3.8(b)** J_{\max} and J_{sat} are nearly equal using the present dye-electrolyte combination (D35-[Cu(tmby)₂]^{2+/1+}), which further confirms that devices fabricated with both 20 nm and 30 nm TiO₂ particles are free from mass transport limitations.

3.4.5. Probing Charge Collection

Once electrons are injected, they must be collected at the respective electrodes to generate current. The ratio of the number of electrons injected to the number of electrons collected determines the charge collection efficiency (η_{cc}).^{39,40} For efficient charge collection, diffusion length (L_n) must be longer than the thickness of TiO₂.^{41,42}

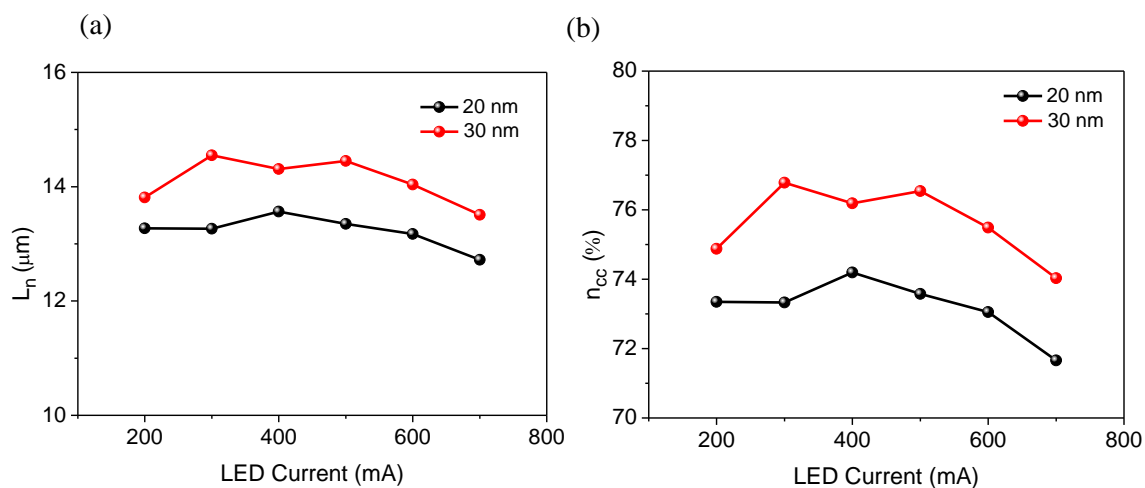


Figure 3.9. (a) Diffusion length (L_n) and (b) charge collection efficiency (η_{cc}) as a function of LED current for DSCs using 20 nm and 30 nm TiO₂ particles.

Figure 3.9 shows diffusion length (L_n) and charge collection efficiency (η_{cc}) as a function of LED current. Diffusion length (L_n) and charge collection efficiency (η_{cc}) was estimated from equations (4) and (5),^{39,43,44}

$$L_n = L \sqrt{\frac{\tau_d}{\tau_n}} \quad (4)$$

$$\eta_{cc} = 1 / \left(1 + \frac{\tau_d}{\tau_n} \right) \times 100 \quad (5)$$

Where L is thickness of TiO_2 , τ_d is transport time and τ_n is lifetime. Lifetime and transport time were determined from transient photovoltage decay and transient photo current decay measurements.

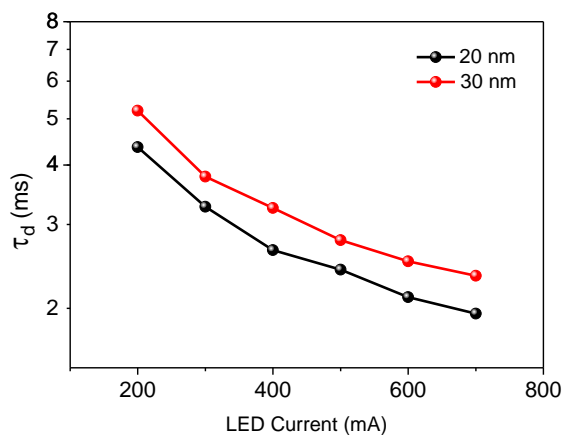


Figure 3.10. Transport time (τ_d) measurements using transient photocurrent decay for DSCs with 20 nm and 30 nm TiO_2 particles.

Transient photo current decay is given in **Figure 3.10**. As shown in **Figure 3.9(a)**, for devices fabricated using 20 nm and 30 nm TiO_2 particles, the diffusion length is three times longer than the thickness to TiO_2 film ($\sim 4 \mu\text{m}$ irrespective of the particle size), which is large enough for efficient charge collection. L_n remains approximately constant irrespective of light intensity while DSCs with 30 nm TiO_2 particles showcased longer diffusion length than DSCs fabricated using 20 nm TiO_2 particles. Longer diffusion length in 30 nm TiO_2 particles can be attributed to the improved lifetime which resulted in comparatively better charge collection efficiency for 30 nm TiO_2 particle-based devices (**Figure 3.9 (b)**).

3.5. Conclusions

We systematically studied the effect of photoanode comprising of 20 nm and 30 nm TiO_2 particle respectively, employing $\text{Cu}[(\text{tmbpy})_2]^{2+/1+}$ as redox mediator with organic D35 sensitizer. The device fabricated using 30 nm TiO_2 particles showed an improvement of 16% in PCE compared to the device fabricated with 20 nm TiO_2 particles. The improvement in PCE is attributed to the enhancement of current density (J_{sc}), open-circuit potential (V_{oc}) and fill factor (FF). The gain in V_{oc} and FF is mainly attributed to the improved lifetime. The diode quality factor (m) was found to be non-ideal for DSCs using both 20 nm and 30 nm TiO_2 particles, indicating the possibility of recombination from surface states. To

provide a more detailed justification on enhancement in J_{sc} , we analysed parameters such as η_{LHE} , η_{inj} , η_{reg} and η_{cc} . LHE was marginally improved at higher wavelength for photoanodes using 30 nm TiO₂ particles as a result of higher roughness, better dye loading and improved scattering. PIA result suggests better regeneration for devices fabricated using 30 nm TiO₂ particles. Further, devices fabricated using 20 nm and 30 nm TiO₂ particles were free from mass transport with an ideal α value of 1. Devices fabricated using 30 nm TiO₂ particles realized longer lifetime and diffusion length contributing to a better charge collection efficiency. In a nutshell, the collective enhancement in LHE , dye regeneration, and charge collection efficiency assisted in bringing higher J_{sc} , V_{oc} , FF and improved PCE for devices fabricated using 30 nm TiO₂ particles employing D35 sensitizer and Cu[(tmbpy)₂]^{2+/1+} as the redox mediator.

3.6. References

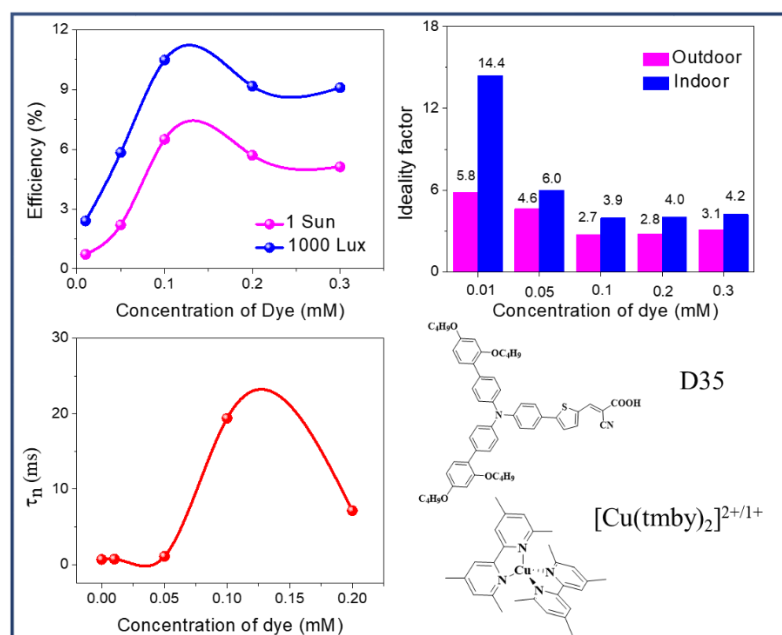
- 1 Mikko Kokkonen, Parisa Talebi, Jin Zhou, Somayyeh Asgari, S. Ahmed Soomro, Farid Elsehrawy, Janne Halme, Shahzada Ahmad, Anders Hagfeldt and S. Ghufuran Hashmi, *J. Mater. Chem. A*, 2021, **9**, 10527–10545.
- 2 P. R. Nitha, S. Soman and J. John, *Mater. Adv.*, 2021, **2**, 6136–6168.
- 3 G. Gokul, S. C. Pradhan and S. Soman, in *Advances in Solar Energy Research*, Springer, Singapore, 2019, pp. 281–316.
- 4 A. Aslam, U. Mehmood, M. H. Arshad, A. Ishfaq, J. Zaheer, A. Ul Haq Khan and M. Sufyan, *Sol. Energy*, 2020, 207, 874–892.
- 5 Q. Hualmé, V. M. Mwalukuku, D. Joly, J. Liotier, Y. Kervella, P. Maldivi, S. Narbey, F. Oswald, A. J. Riquelme, J. A. Anta and R. Demadrille, *Nat. Energy* 2020 56, 2020, **5**, 468–477.
- 6 E. Tanaka, H. Michaels, M. Freitag and N. Robertson, *J. Mater. Chem. A*, 2020, **8**, 1279–1287.
- 7 H. Michaels, I. Benesperi and M. Freitag, *Chem. Sci.*, 2021, **12**, 5002–5015.
- 8 T. W. Hamann, *Dalt. Trans.*, 2012, **41**, 3111–3115.
- 9 M. Yoosuf, S. C. Pradhan, M. M. Sruthi, S. Soman and K. R. Gopidas, *Sol. Energy*, 2021, **216**, 151–163.
- 10 S. M. Feldt, E. A. Gibson, E. Gabrielsson, L. Sun, G. Boschloo and A. Hagfeldt, *J. Am. Chem. Soc.*, 2010, **132**, 16714–16724.
- 11 Y. Hao, W. Yang, L. Zhang, R. Jiang, E. Mijangos, Y. Saygili, L. Hammarström, A.

-
- Hagfeldt and G. Boschloo, *Nat. Commun.* 2016 71, 2016, **7**, 1–8.
- 12 Y. Saygili, M. Söderberg, N. Pellet, F. Giordano, Y. Cao, A. B. Munoz-García, S. M. Zakeeruddin, N. Vlachopoulos, M. Pavone, G. Boschloo, L. Kavan, J. E. Moser, M. Grätzel, A. Hagfeldt and M. Freitag, *J. Am. Chem. Soc.*, 2016, **138**, 15087–15096.
- 13 M. Freitag, F. Giordano, W. Yang, M. Pazoki, Y. Hao, B. Zietz, M. Grätzel, A. Hagfeldt and G. Boschloo, *J. Phys. Chem. C*, 2016, **120**, 9595–9603.
- 14 S. Hattori, Y. Wada, S. Yanagida and S. Fukuzumi, *J. Am. Chem. Soc.*, 2005, **127**, 9648–9654.
- 15 W. Zhang, Y. Wu, H. W. Bahng, Y. Cao, C. Yi, Y. Saygili, J. Luo, Y. Liu, L. Kavan, J. E. Moser, A. Hagfeldt, H. Tian, S. M. Zakeeruddin, W. H. Zhu and M. Grätzel, *Energy Environ. Sci.*, 2018, **11**, 1779–1787.
- 16 P. S. Gangadhar, A. Jagadeesh, A. S. George, G. Reddy, S. Prasanthkumar, S. Soman and L. Giribabu, *Mol. Syst. Des. Eng.*, 2021, **6**, 779–789.
- 17 D. Zhang, M. Stojanovic, Y. Ren, Y. Cao, F. T. Eickemeyer, E. Socie, N. Vlachopoulos, J. E. Moser, S. M. Zakeeruddin, A. Hagfeldt and M. Grätzel, *Nat. Commun.*, 2021, **12**, 1–10.
- 18 P. Ferdowsi, Y. Saygili, F. Jazaeri, T. Edvinsson, J. Mokhtari, S. M. Zakeeruddin, Y. Liu, M. Grätzel and A. Hagfeldt, *ChemSusChem*, 2020, **13**, 212–220.
- 19 Y. Cao, Y. Liu, S. M. Zakeeruddin, A. Hagfeldt and M. Grätzel, *Joule*, 2018, **2**, 1108–1117.
- 20 Y. J. Son, J. S. Kang, J. Yoon, J. Kim, J. Jeong, J. Kang, M. J. Lee, H. S. Park and Y.-E. Sung, *J. Phys. Chem. C*, 2018, **122**, 7051–7060.
- 21 K. Park, Q. Zhang, D. Myers and G. Cao, *ACS Appl. Mater. Interfaces*, 2013, **5**, 1044–1052.
- 22 H. S. Kim, S. B. Ko, I. H. Jang and N. G. Park, *Chem. Commun.*, 2011, **47**, 12637–12639.
- 23 H. Ellis, N. Vlachopoulos, L. Häggman, C. Perruchot, M. Jouini, G. Boschloo and A. Hagfeldt, *Electrochim. Acta*, 2013, **107**, 45–51.
- 24 S. Soman, S. C. Pradhan, M. Yoosuf, M. V Vinayak, S. Lingamoorthy and K. R. Gopidas, *J. Phys. Chem. C*, 2018, **122**, 14113–14127.
- 25 S. Sasidharan, S. Soman, S. C. Pradhan, K. N. N. Unni, A. A. P. Mohamed, B. N. Nair and H. U. N. Saraswathy, *New J. Chem.*, 2017, **41**, 1007–1016.

- 26 J. Bisquert, A. Zaban, M. Greenshtein and I. Mora-Seró, *J. Am. Chem. Soc.*, 2004, **126**, 13550–13559.
- 27 M. Pazoki, U. B. Cappel, E. M. J. Johansson, A. Hagfeldt and G. Boschloo, *Energy Environ. Sci.*, 2017, **10**, 672–709.
- 28 Q. Wu, J. Hou, H. Zhao, Z. Liu, X. Yue, S. Peng and H. Cao, *Dalt. Trans.*, 2018, **47**, 2214–2221.
- 29 S. Sasidharan, S. C. Pradhan, A. Jagadeesh, B. N. Nair, A. A. P. Mohamed, N. U. K. N, S. Soman and U. N. S. Hareesh, *ACS Appl. Energy Mater.*, 2020, **3**, 12584–12595.
- 30 K. Zhu, N. Kopidakis, N. R. Neale, J. Van De Lagemaat and A. J. Frank, *J. Phys. Chem. B*, 2006, **110**, 25174–25180.
- 31 J. Halme, P. Vahermaa, K. Miettunen and P. Lund, *Adv. Mater.*, 2010, **22**, 210–234.
- 32 J. Bisquert, A. Zaban and P. Salvador, *J. Phys. Chem. B*, 2002, **106**, 8774–8782.
- 33 P. Salvador, M. G. Hidalgo, A. Zaban and J. Bisquert, *J. Phys. Chem. B*, 2005, **109**, 15915–15926.
- 34 M. Freitag, J. Teuscher, Y. Saygili, X. Zhang, F. Giordano, P. Liska, J. Hua, S. M. Zakeeruddin, J.-E. Moser, M. Grätzel and A. Hagfeldt, *Nat. Photonics*, 2017, **11**, 372–378.
- 35 R. Haridas, J. Jayadev, S. C. Pradhan, V. Asarikal, Y. Karuvath, S. Soman, N. U. K N and A. Ajayaghosh, *Mater. Adv.*, , DOI:10.1039/d1ma00829c.
- 36 T. W. Hamann and J. W. Ondersma, *Energy Environ. Sci.*, 2011, **4**, 370–381.
- 37 B. M. Klahr and T. W. Hamann, *J. Phys. Chem. C*, 2009, **113**, 14040–14045.
- 38 S. C. Pradhan, A. Hagfeldt and S. Soman, *J. Mater. Chem. A*, 2018, **6**, 22204–22214.
- 39 K. Zhu, S. R. Jang and A. J. Frank, *J. Phys. Chem. Lett.*, 2011, **2**, 1070–1076.
- 40 K. Zhu, N. R. Neale, A. Miedaner and A. J. Frank, *Nano Lett.*, 2006, **7**, 69–74.
- 41 J. Ondersma and T. Hamann, *J. Phys. Chem. C*, 2010, **114**, 638–645.
- 42 F. Fabregat-Santiago, J. Bisquert, G. Garcia-Belmonte, G. Boschloo and A. Hagfeldt, *Sol. Energy Mater. Sol. Cells*, 2005, **87**, 117–131.
- 43 M. Adachi, M. Sakamoto, J. Jiu, Y. Ogata and S. Isoda, *J. Phys. Chem. B*, 2006, **110**, 13872–13880.
- 44 J. Van De Lagemaat, N. G. Park and A. J. Frank, *J. Phys. Chem. B*, 2000, **104**, 2044–2052.

Fundamental Understanding of Interfacial Charge Dynamics in Copper Electrolyte Based Dye-Sensitized Solar Cells as a Function of Dye Coverage Under Outdoor/Indoor Illuminations

4.1. Abstract



Modern dye-sensitized solar cells (DSCs) with copper redox mediators are gaining wider attention owing to its higher photovoltaic (PV) performance both under natural and artificial lights. Dyes played a crucial role in the evolution of modern DSCs. Dyes were custom designed in a way not only to harvest light but also to act as blocking layers to prevent recombination. To explore the role of dye coverage on the photovoltaic parameters while used along with the new generation copper electrolyte based DSCs, we systematically controlled the dye coverage on TiO_2 using D35 organic dye solutions of different concentrations. Dye loading/surface coverage of dye was found to increase with the increase in dye concentrations and it reached to a saturation around 0.2 mM of D35

concentration. However, 0.1 mM was found to be an optimum dye concentration in terms of photovoltaic performance both under indoor and outdoor light illuminatiuons. Maximum power conversion efficiency (PCE) of $6.50 \pm 0.25\%$ (V_{oc} -1002 \pm 3 mV, J_{sc} -10.22 \pm 0.25 mA/cm², FF-0.63 \pm 0.01) under outdoor (AM 1.5 G, 100 mW/cm²) and 10.48 \pm 0.30 % (V_{oc} -773 \pm 3 mV, J_{sc} -48.8 \pm 0.9 mA/cm² and FF-0.78 \pm 0.02) under indoor light (1000 lux, WW CFL) was obtained using 0.1 mM D35 dye concentration. Dark current and ideality factor (m) was also found to be minimum at 0.1 mM dye concentration. Furthermore, m was found to be more non-ideal under indoor light condition than outdoor illumination. To exclusively study the role of dye, charge dynamics of DSCs were explored using electrochemical impedance spectroscopy (EIS) under dark conditions. Lifetime obtained from EIS measurement was found to be in line with the ideality factor (m) and dark current. Electron injectin, dye regeneration, charge collection and ion diffusion was found to be independent of the dye coverage.

4.2. Introduction

Dye-sensitized solar cells (DSCs) are considered to be one among the most promising cost-effective and environmentally friendly photovoltaic technologies.^{1,2} DSCs are endowed with many striking features such as colour tunability, transparency, flexibility, and superior performance under indoor/artificial illuminations which makes it attractive to develop self-powered, battery-free smart devices.³⁻⁷ During the last three decades, DSCs have significantly transformed to a stage capable to realize market penetration. Modern DSCs are exclusively among the few technologies that work efficiently under indoor/ambient light conditions with PCE > 30% and are now commercialized by many industries globally as the energy source for various internet of things (IoT) based electronic devices.⁸⁻¹⁰ Furthermore, it also started to make its presence in the building integrated photovoltaic (BIPV) sector.¹¹⁻¹⁵

Unlike conventional DSCs, that constitutes ruthenium metal complex sensitizers and iodide-triiodide (I^-/I_3^-) redox mediators, modern DSCs rely on organic dyes with alternate transition metal complexes ($Co^{3+/2+}/Cu^{2+/+}$) redox mediators.¹⁶⁻¹⁸ Alternate redox mediators render an opportunity to modify the redox potential and thereby minimizing voltage loss leading to higher open circuit potential (V_{oc}). Likewise, organic sensitizers possess higher molar extinction coefficient which helps in better light harvesting properties contributing towards improved J_{sc} using thin TiO₂ layers. The combination of organic dyes

and alternate electrolytes generate enormous opportunities to fine tune the device properties and to meet the end-user requirements.¹⁹ For instance, recently Naim *et al.* successfully realized fully transparent DSCs using a selective near-infrared sensitizer based on a polymethine cyanine dye along with cobalt redox mediator.²⁰ Yet again Hualme *et al.* were able to realize photochromic dye-sensitized solar cells that can change colour with self-adjustable light transmittance when irradiated.²¹ Moreover, presently DSCs have already reached an efficiency of 15.2% using co-sensitized organic dyes (SL9 and SL10) along with copper electrolyte ($[\text{Cu}(\text{tmby})_2]^{2+/1+}$) under outdoor/ 1 sun illumination (AM 1.5G, 100 mW).²² Similarly, an impressive power conversion efficiency of 34.5% is already achieved using co-sensitized XY1+MS5 dye combination along with $[\text{Cu}(\text{tmby})_2]^{2+/1+}$ electrolyte under 1000 lux CFL illumination.²³

Earth-abundant copper redox mediators played a significant role in the evolution of modern DSCs, particularly for indoor photovoltaics (IPV).^{16,24–26} Copper redox shuttles are cost-effective and environmentally friendly, thus possessing adequate potential for industrialization and mass production. More importantly, copper based redox mediators can sufficiently regenerate the oxidized dye molecules with efficiencies close to unity even with a driving force as low as 0.1 V.^{27–29} Using $\text{Cu}^{\text{I/II}}$ redox couples, $V_{oc} > 1$ V can easily be realized without compromising J_{sc} . It is to be noted that a notable V_{oc} of 1.24 V from a single junction device has already been realized using $[\text{Cu}(\text{tmby})]^{2+/1+}$ redox mediator. The ground breaking efficiency of 28.9% under indoor light (1000 lux CFL) was achieved using $[\text{Cu}(\text{tmby})_2]^{2+/1+}$ redox mediator, which paved the way towards further development of DSCs in the area of indoor photovoltaics.³⁰ Presently efficiency up to 34.5% under 1000 lux and 37% under 6000 lux has been realized using organic dye-copper electrolyte combinations.^{23,31} In classical DSCs, dye is responsible for the current generation through light absorption, however, in modern DSCs the role of dye is not merely limited to light absorption, it also plays a pivotal role in preventing recombination at $\text{TiO}_2/\text{electrolyte}$ interface.^{32–35} Employing alternate redox mediators like copper complexes having positive redox potentials recombination is a critical issue. Further, under low indoor/artificial light illuminations, recombination becomes essentially more crucial where even a small increase in recombination can subsequently hamper the efficiency in a bigger way. Addressing recombination using additional blocking layers has already proved to be an efficient and conventional method, but possesses several bottlenecks in scale-up. Thus, modifying the dye coverage on TiO_2 and thereby controlling recombination offers better possibility to

realize higher V_{oc} and PCEs. To enhance our knowledge on the fundamental understanding of various charge transfer process as a function of dye coverage, D35 organic dye in different concentrations are used to control the dye loading on TiO_2 and investigated in detail its effect on PV parameters using $[Cu(tmby)_2]^{2+/1+}$ electrolyte both under 1 sun (AM 1.5 G, 100 mW/cm^2) and indoor illumination (1000 lux, WW CFL).

4.3. Experimental Section

4.3.1. General Methods

The solvents and materials used for device fabrication were of HPLC grade purchased from Sigma-Aldrich, Merck, GreatCell Solar and used without further purification. D35 organic dye, $[Cu(tmby)_2]^{2+/1+}$ copper complexes and 30 nm TiO_2 paste were obtained from Dynamo AB (Stockholm, Sweden).

4.3.2. Fabrication of DSCs

FTO glasses (TEC15, GreatcellSolar) were cut into 1.5 × 1.5 cm^2 and used as substrates for both working and counter electrodes. FTO substrates were sonicated in detergent for 30 minutes followed by gentle scrubbing in flowing water and again sonication in deionized (DI) water for 30 minutes, followed by sonication in IPA and acetone for 15 minutes each. Further FTOs were annealed at 500 °C for 15 minutes in a muffle furnace followed by UV-Ozone cleaning. A compact TiO_2 blocking layer was deposited over FTO using $TiCl_4$ treatment followed by annealing at 500 °C for 30 minutes. $TiCl_4$ treatment includes dipping cleaned FTO substrates in 53 mM $TiCl_4$ bath for 30 min at 70 °C followed by rinsing of FTO using DI water and ethanol. TiO_2 paste consists of 30 nm particles (Dyename, Sweden) was deposited by screen printing and annealed at 325 °C for 5 minutes, 375 °C for 5 minutes, 400 °C for 5 minutes and 500 °C for 15 minutes. Again, $TiCl_4$ treatment was done on electrodes followed by annealing at 500 °C for 30 minutes to create a compact TiO_2 post-blocking layer over the mesoporous TiO_2 . The electrodes were then kept inside the dye bath overnight. The dye solution consists of 0.2 mM D35 dye (Dyename, Sweden) in 1:1 acetonitrile and tert-butanol mixture. For counter electrodes, predrilled FTO glasses (TEC8, GreatCell Solar) were sonicated in detergent, DI water, and ethanol for 45 minutes and consequently annealed at 500 °C for 15 minutes. Prior to PEDOT [poly (3,4-ethylene dioxythiophene)] deposition, electrodes were treated using UV-O₃ for 15 min. Preparation of PEDOT counter electrode involves electropolymerisation of 3,4-ethylene dioxythiophene (EDOT) from a micellar aqueous

solution of 0.1 M sodium dodecyl sulfate (SDS) and 0.01 M EDOT.^{36,37} The electrodes were assembled using a 25 μm surlyn spacer and heat pressed at 110 $^{\circ}\text{C}$. $[\text{Cu}(\text{tmby})_2]^{2+/1+}$ electrolyte, consisting of 0.20 M Cu(I), 0.04 M Cu(II), 0.1 M LiTFSI, and 0.6 M 4-tert-butylpyridine in acetonitrile was injected through the predrilled holes and the holes were subsequently sealed using a cover glass.

4.3.3. Solar Cell Characterization

Photocurrent voltage (J - V) characteristics were carried out using the Oriel Class-AAA solar simulator (Model PVIV- 94043A) accompanied with Keithley 2440 power source. The intensity of irradiation was measured using a certified calibrated Si solar cell. Indoor light measurement was carried out inside a dark box with white CFL as source of illumination. The indoor J - V responses were recorded using Dyenamo potentiostat (DN-AE05). The intensity of the light was measured using radiometrically calibrated Ocean optics Jaz spectrometer. A circular black mask of areas 0.1256 cm^2 (smaller than the active area) was used during the J - V measurements to minimize the contribution of light falling outside the active area. Incident photon-to-current conversion efficiency ($IPCE$) of devices were performed under DC mode using IPCE equipment having a 300 W Xenon lamp integrated with a Newport monochromator and power meter, controlled using the Oriel software. Electrochemical Impedance Spectroscopy (EIS) of DSCs were carried out under dark condition with an amplitude perturbation of 10 mV and frequency ranging from 100 mHz to 100 kHz using Autolab (PGSTAT302N). The DC voltage was given from 0.85V to 1.0V. For dye loading studies dye desorption was carried out using 0.1 M NaOH in ethanol and absorption of desorbed dye solutions were recorded using Ocean Optics Jaz spectrometer. Photo induced absorption spectroscopy (PIA) was recorded using Dyenamo DN-AE02. It uses 1W blue light emitting LED ($\lambda=470$ nm) as pump and 20 W tungsten halogen lamp as a probe. The transmitted light through the sample falls on the monochromator and is detected by a UV enhanced Si detector connected to a lock-in amplifier (SR830) via a current amplifier. The PIA spectra of the devices were recorded using excitation by LED, which has a square wave with a modulation frequency of 9.3 Hz.

4.4. Results and Discussion

4.4.1. Solar Cell Characteristics under Full Sun and Indoor light

For the photovoltaic studies, we fabricated DSCs employing organic D35 dye along with $[\text{Cu}(\text{tmby})_2]^{2+/1+}$ redox mediator keeping the rest of parameters constant. **Figure 4.1 (a)** shows the structure of D35 dye and $[\text{Cu}(\text{tmby})_2]^{2+/1+}$ redox mediator along with its energetics. As shown in **Figure 4.1 (b)**, D35 dye and $[\text{Cu}(\text{tmby})_2]^{2+/1+}$ redox mediator possesses favorable energetics for efficient charge injecting and dye regeneration. D35 dye was selected for the present study as it is free from dye aggregation, providing a platform to exclusively study the charge recombination at TiO_2 /electrolyte interface using Cu(I/II) electrolyte.^{38,39} We quantified the amount of dye on TiO_2 by desorption study (**Figure 4.1 (c)**). In all fabricated DSCs, TiO_2 photoanodes with a thickness of 4 μm and dye loading time of 15 hours was used. As apparent in **Figure 4.1 (c)**, dye loading reached to saturation using 0.2 mM D35 concentration.

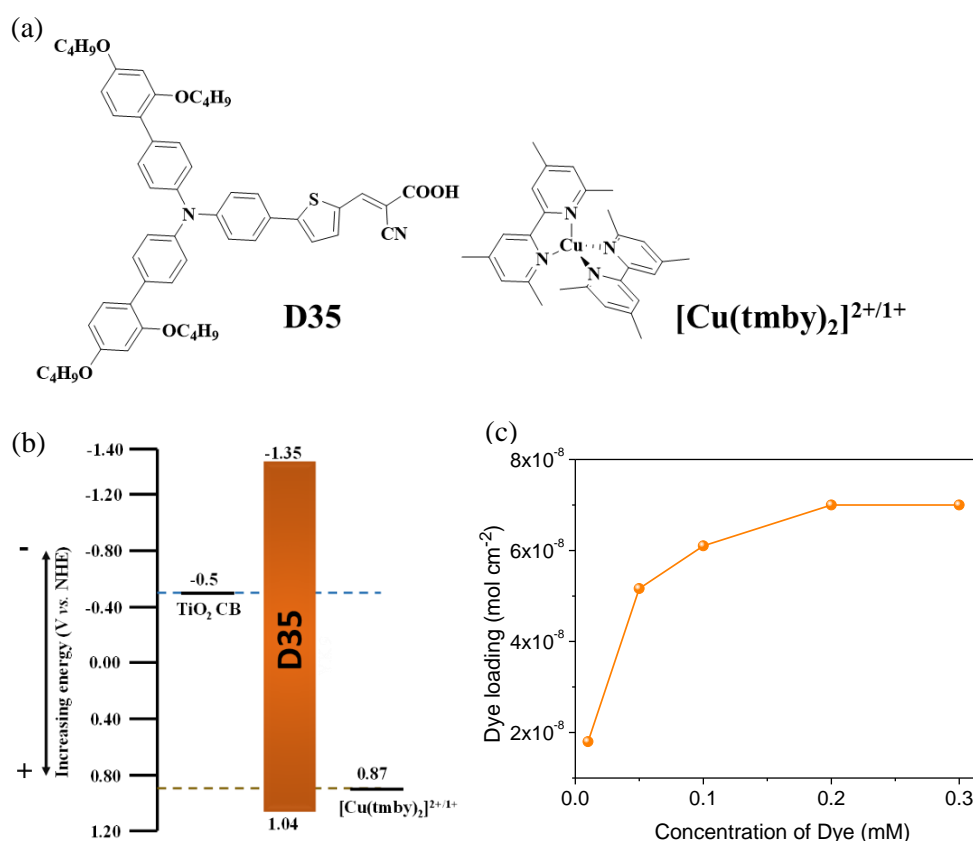


Figure 4.1. (a) Structure of D35 dye and $[\text{Cu}(\text{tmby})_2]^{2+/1+}$ redox mediator (b) energetics and (c) dye loading as a function of dye concentration on TiO_2 films.

Current density–voltage (J – V) characteristics carried out under AM 1.5G one sun (100 mW/cm^2) illumination and the corresponding IPCE plots for DSCs fabricated with various dye concentrations (0.01 mM, 0.05 mM, 0.1 mM, 0.2 mM, 0.3 mM) are given in **Figure 4.2** and the resultant photovoltaic parameters are summarized in **Table 4.1**. The J_{sc} obtained from J – V measurements followed the similar trend to that of the IPCE response (**Figure 4.2**). We observed improvement in V_{oc} , J_{sc} , FF and hence PCE with increase in dye concentration. The optimum PCE of $6.50 \pm 0.25 \%$ (V_{oc} – $1002 \pm 3 \text{ mV}$, J_{sc} – $10.22 \pm 0.25 \text{ mA/cm}^2$ and FF – 0.63 ± 0.01) was obtained for DSCs fabricated using 0.1 M D35 dye concentration. Further increase in dye concentration contributed towards drop in V_{oc} , J_{sc} and PCE, whereas FF remained almost constant over the higher dye concentrations. A similar trend was observed for DSCs at various light intensities ranging from 0.1 sun to 1 sun (**Figure 4.3**).

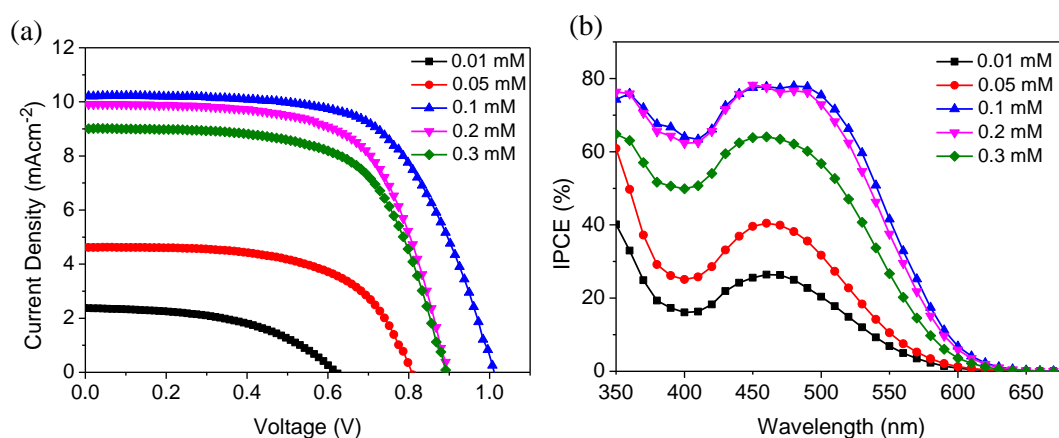


Figure 4.2. (a) Current density–voltage (J – V) and (b) incident photon current conversion efficiency (IPCE) plot of DSCs fabricated with various D35 dye concentrations along with $[\text{Cu}(\text{tmby})_2]^{2+/1+}$ redox mediator.

Table 4.1. Photovoltaic parameters of DSCs fabricated with various D35 dye concentrations along with $[\text{Cu}(\text{tmby})_2]^{2+/1+}$ redox mediator.

D35 Concentration (mM)	V_{oc} (mV)	J_{sc} (mAcm^{-2})	FF	η (%)
0.01	622 ± 2	2.40 ± 0.48	0.49 ± 0.02	0.73 ± 0.12
0.05	803 ± 3	4.62 ± 0.37	0.60 ± 0.01	2.22 ± 0.18
0.1	1002 ± 3	10.22 ± 0.25	0.63 ± 0.01	6.50 ± 0.25
0.2	898 ± 4	9.91 ± 0.28	0.64 ± 0.03	5.70 ± 0.26
0.3	895 ± 6	9.09 ± 0.27	0.64 ± 0.02	5.12 ± 0.21

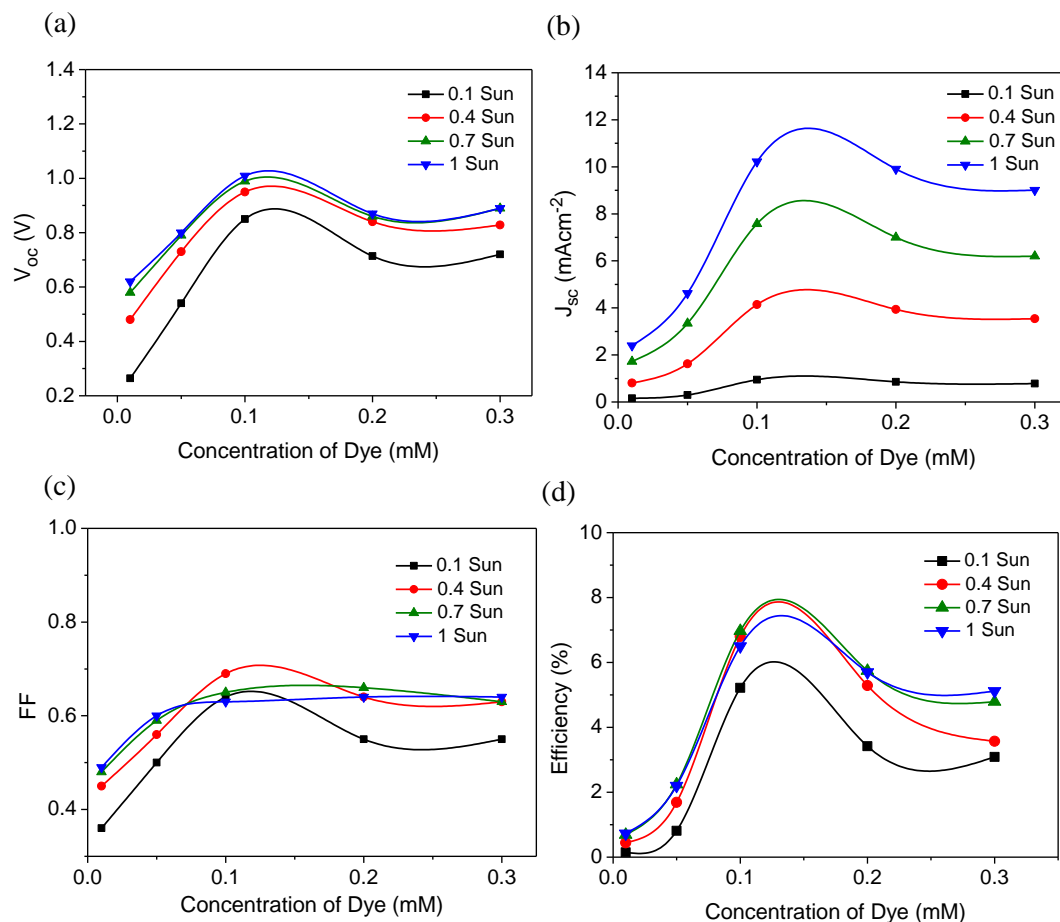


Figure 4.3. Solar cell characteristics of DSCs with D35 sensitizer and $[\text{Cu}(\text{tmby})_2]^{2+/1+}$ electrolyte (a) V_{oc} , (b) J_{sc} , (c) FF and (d) efficiency from 0.1 sun to 1 sun as a function of dye concentration (0.01 mM, 0.05 mM, 0.1 mM, 0.2 mM, and 0.3 mM).

Indoor photovoltaic characterization was carried out using a homemade indoor light simulator using warm white CFL light source. **Figure 4.4** shows the current density–voltage (J – V) and power curves for DSCs fabricated using various dye concentrations under 1000 lux CFL illumination. The indoor photovoltaic parameters are summarized in **Table 4.2**. The photovoltaic performance under 1000 lux illumination also followed the same trend as that of 1 sun, but with enhanced efficiencies. Higher efficiency under CFL illumination is attributed to the better spectral overlap of CFL light with the absorption of D35 sensitizer. Highest PCE of $10.48 \pm 0.30\%$ (V_{oc} -773 \pm 3 mV, J_{sc} -48.8 \pm 0.9 μAcm^{-2} and FF-0.78 \pm 0.02) was realized using a concentration of 0.1 mM D35 dye similar to the trend in results observed under 1 sun. Compared to one sun condition, under 1000 lux illumination better fill factor was recorded using all the different dye concentrations except at a very lower dye concentration of 0.01 mM. This is because recombination under 1000 lux

illumination one sun illumination is lower compared to that of 1 sun due to less charge density being populated at the TiO₂ under indoor 1000 lux illumination.

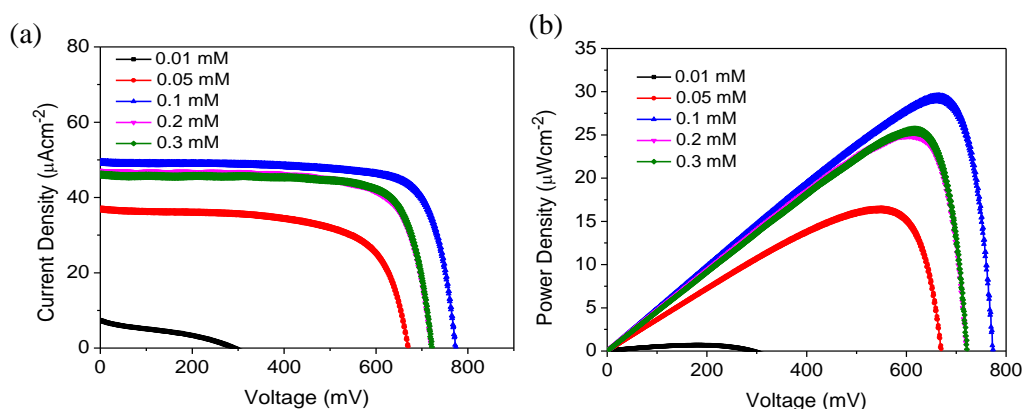


Figure 4.4. (a) Current density-voltage (J - V) and (b) power curve for DSCs fabricated with different D35 dye concentrations along with $[\text{Cu}(\text{tmby})_2]^{2+/1+}$ redox mediator under 1000 lux illumination.

Table 4.2. Photovoltaic parameters of DSCs fabricated with different D35 dye concentrations and $[\text{Cu}(\text{tmby})_2]^{2+/1+}$ electrolyte under 1000 lux illumination.

D35 Concentration (mM)	V_{oc} (mV)	J_{sc} (μAcm^{-2})	FF	η (%)
0.01	292 ± 6	7.4 ± 0.8	0.32 ± 0.02	2.40 ± 0.22
0.05	670 ± 2	37.0 ± 0.9	0.66 ± 0.03	5.84 ± 0.13
0.1	773 ± 3	48.8 ± 0.9	0.78 ± 0.02	10.48 ± 0.30
0.2	721 ± 2	47.6 ± 0.3	0.76 ± 0.01	9.17 ± 0.12
0.3	721 ± 2	46.4 ± 0.2	0.77 ± 0.08	9.09 ± 0.70

4.4.2. Interfacial Charge Transfer Study

Interfacial charge transfer analysis of the fabricated dye-sensitized solar cells provides better understanding of the fundamental processes happening at various interfaces that dictates the PV performance. In the present study, we relied on various electro-optical perturbations, and pump prob techniques along with steady state current-voltage (I - V) measurements to gain more insight on the fundamental process as a function of the amount of dye on semiconductor using Cu(II/I) electrolyte. As copper redox mediators are often limited by mass transport, we initially analyzed the J_{sc} vs. light intensity measurements under full sun (100 mW/cm^2 , AM 1.5G) to probe the mass transport. (**Figure 4.5**).

Current density increases with increasing input light illumination by the relation, $J_{sc} \propto I^\alpha$ where α is the power constant. α was found to be unity for DSCs with different dye loading amounts suggesting minimal influence of dye loading on the mass transport of these devices. We observed similar results in our previous study also where D35 dye along with $[\text{Cu}(\text{tmby})_2]^{2+/1+}$ was found to be free from mass transport.⁴⁰ This could be attributed to the smaller size of the D35 sensitizer which provides ample space for the electrolyte to penetrate in a working device.

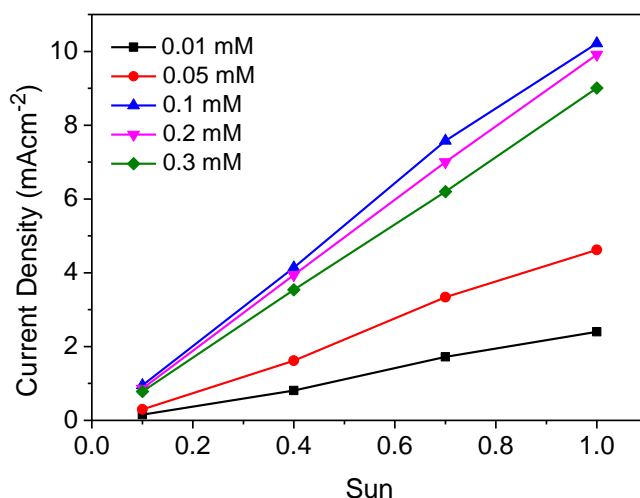


Figure 4.5. Current density as a function of light intensity for DSCs fabricated with various D35 dye concentrations using $[\text{Cu}(\text{tmby})_2]^{2+/1+}$ electrolyte.

The difference between the Fermi energy level of TiO_2 and redox potential of electrolyte accounts for the V_{oc} and is related to the light intensity by the equation,^{41,42}

$$\frac{dV_{oc}}{d \log I} = \frac{2.30mk_B T}{q} \quad (1)$$

Where I is the intensity of the light, m is the ideality factor k_B is Boltzmann constant, T is temperature and q is the charge. **Figure 4.6 (a)** represents V_{oc} as a function of irradiance in mW/cm^2 measured under 1 sun (AM 1.5G, $100 \text{ mW}/\text{cm}^2$) and **Figure 4.6 (b)** displays V_{oc} as function of illuminance in lux measured using CFL light of varying intensities respectively. Generally, employing alternate redox mediators like cobalt and copper, the relation between V_{oc} and I was found to be non-ideal owing to more recombination. From **Figure 4.6 (a, b)** it is quite evident that under the indoor light illumination conditions the relationship between V_{oc} and I is found to be more non-ideal than that under the solar light illumination. It is to be noted that ideally m should be unity. The ideality factor (m) calculated at various dye concentrations under both 1 sun and 1000 lux CFL illumination

is given in **Figure 4.6 (c)**. From **Figure 4.6 (c)**, it is observed that a close to ideal m values are obtained using an optimum dye concentration of 0.1 mM both under 1 sun and indoor illumination. At lower concentrations due to lesser amount of dyes on TiO_2 surface, recombination is expected to be more intense, leading to higher m values. It is also to be noted that the deviation from ideal behavior is more pronounced under indoor light illumination which clearly indicates the need to arrest recombination to realize higher photovoltaic performance under indoor/artificial illuminations. According to Bisquert *et al.* the non-ideal characteristics observed are related to the electron recombination not only from the conduction band of TiO_2 but also from the surface states and trap states distributed exponentially in the band gap of TiO_2 .^{43,44} Further, Zhang *et al.* also observed a deviation in ideality factor for DSCs using different organic sensitizers, for instance, DSCs with NT5 sensitizer showed an m value of 1.7 while MS4 and MS5 showed an m value 1.26 and 1.04 respectively.²³ The difference in ideality factor was mainly attributed to the reduction in interfacial charge recombination from the surface and trap states. Thus, in the present context, it can be said that higher concentration of dye molecules on TiO_2 passivates the surface states subsequently leading to lower recombination and better photovoltaic performance. To clarify this further, we measured the dark current for the devices (**Figure 4.6 (d)**) with various dye loading amounts. Herein we also included a device without any dye in a way to quantify the role of dyes in preventing interfacial charge recombination. In DSCs without the dye, dark current drops rapidly with voltage, and with the increase in dye concentration dark current gets better and reached to an optimum value at 0.1 mM dye concentration and again started to drop with further increase in dye concentration. The trend in dark current aligns with the calculated ideality factor (**Figure 4.6 (c)**), which confirms that the dye molecules is capable of reregulating recombination and a careful optimization of dye concentration is inevitable to extract the best performance from these devices particularly employing alternate Cu(II/I) redox mediators.

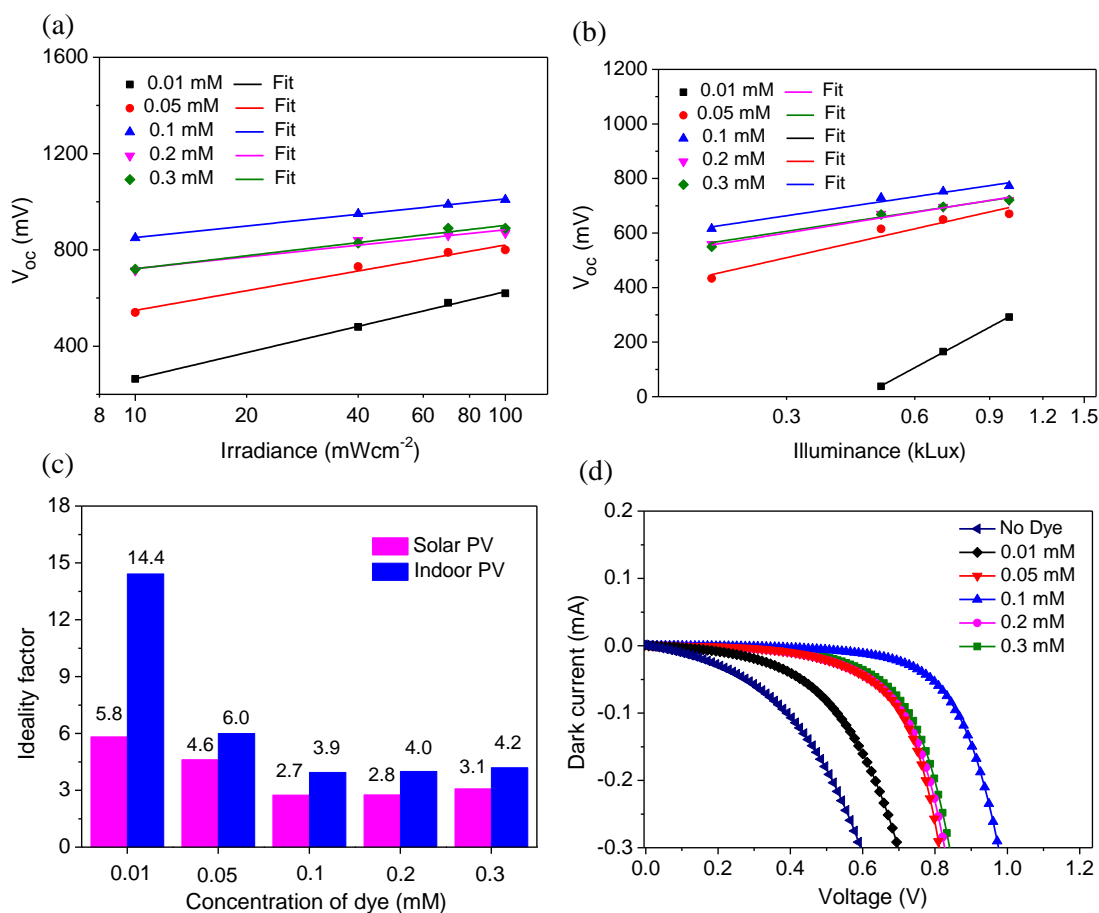


Figure 4.6. V_{oc} as a function of (a) Irradiance (mW/cm^2) under 1 sun irradiation ($100 \text{ mW}/\text{cm}^2$), (b) illuminance (lux) under indoor light illuminations (c) ideality factor calculated as a function of D35 dye concentration under solar and indoor CFL illumination and (d) dark current as a function of of D35 dye concentration.

For a detailed interfacial charge transfer study, we further used electrochemical impedance spectroscopic (EIS) measurements carried out under dark conditions. In TiO_2 photoanode, electron diffusion to the FTO and charge recombination of injected electrons in TiO_2 with the oxidized species of redox mediator occur simultaneously. As the dye is placed in between the TiO_2 and electrolyte, undoubtedly it influences the charge dynamics at $\text{TiO}_2/\text{dye}/\text{electrolyte}$ interface. To gain a better understanding of the role of dye in DSSCs and its influence on various charge transfer processes, we also carried out measurements on devices without the sensitizer.

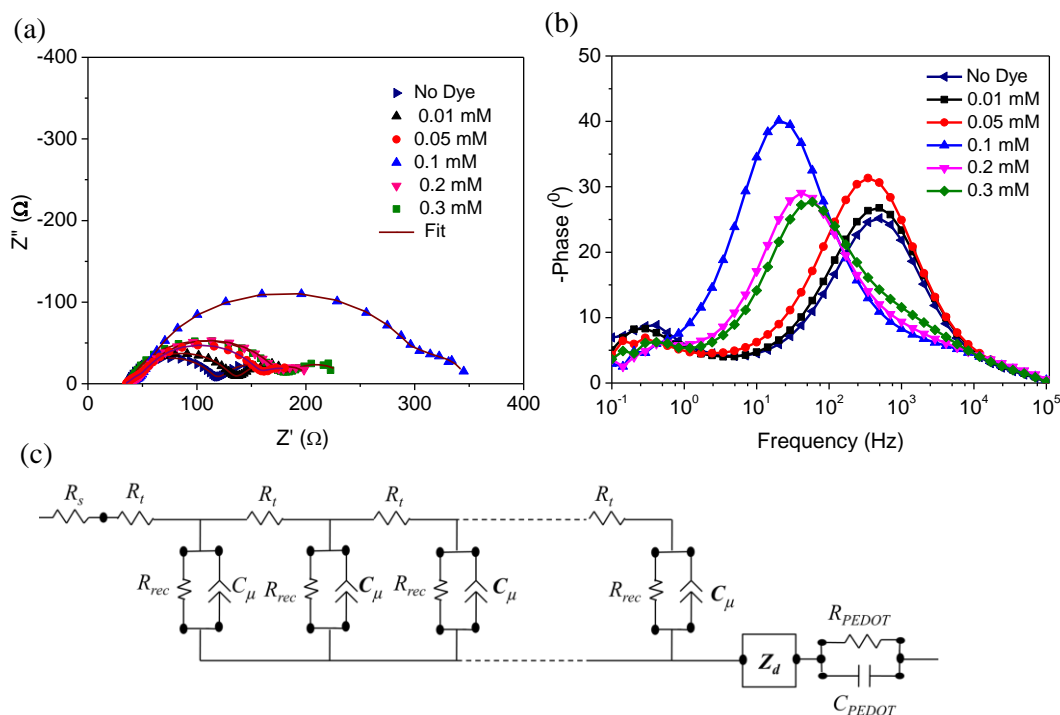


Figure 4.7. (a) Nyquist plot, (b) Bode plot and (c) equivalent circuit used for fitting the obtained Nyquist plot for DSCs with different D35 concentration employing $[Cu(tmby)_2]^{2+/1+}$ electrolyte.

EIS is a highly trusted characterization tool, as both transport time and lifetime can be simultaneously extracted at the same Fermi level position which allows for direct comparisons, while in other perturbation tools like lifetime is measured at open circuit conditions and transport time is measured at short circuit condition. EIS measurements were carried out at different steady-state voltages with a constant perturbation amplitude of 10 mV at frequencies starting from 100 mHz to 100 kHz. The representative Nyquist plot and Bode plot at 0.85 V for different D35 dye concentrations are given in **Figure 4.7 (a,b)**. The impedance plots were fitted using an equivalent circuit transmission line model given in **Figure 4.7 (c)**.^{45,46} Nyquist plot consists of three semicircles, first semicircle at higher frequency corresponds to the charge transfer at the counter/electrolyte interface, the second semicircle at intermediate frequency corresponds to charge transfer at TiO_2 /dye/electrolyte interface and the semicircle at the lower frequency region represents the diffusion of the ions in the bulk electrolyte. The equivalent circuit consists of resistors, capacitors and constant phase element. R_{PEDOT} and C_{PEDOT} refer to resistance and capacitance at the counter electrode/electrolyte interface. Similarly, R_s corresponds to the sheet resistance of the substrates and Z_d represents the impedance towards ion diffusion in the electrolyte. The

transmission line model (**Figure 4.7 (c)**) was used to fit TiO₂/dye/electrolyte interface and it consists of mainly three electrical parameters transport resistance (R_t), recombination resistance (R_{rec}) and chemical capacitance (C_μ). R_t corresponds to the resistance of electrons to diffuse in mesoporous TiO₂, R_{rec} is the charge transfer resistance at the TiO₂/dye/electrolyte interface and C_μ is the constant phase element that represents the capacitance of TiO₂/electrolyte interface. As apparent in **Figure 4.7(a)**, the size of the first semicircle and third semicircle remains unaltered with change in dye concentration which suggests that charge transfer at the counter electrode/electrolyte interface and ion diffusion in the electrolyte bulk are not influenced by the change in dye concentrations. A significant change in the middle semicircle is seen which suggests that the charge transfer at the TiO₂/dye/electrolyte interface is largely influenced by changing dye concentrations. A similar feature can also be observed in Bode plot where peaks at low and high frequency remains unchanged while a significant change in peaks at intermediate frequency was observed.

The accumulation of electrons at TiO₂/electrolyte interface is quantified with capacitance. Here constant phase element is used in place of capacitance to obtain better fitting. **Figure 4.8 (a)**, shows C_μ as a function of Fermi voltage (V_F). V_F is calculated from the equation,

$$V_F = V_{applied} - IR_{eqv} \quad (2)$$

where $V_{applied}$ is the steady state voltage applied across the device during EIS measurement, I is the obtained current and R_{eqv} is the total series resistance (i.e summation of sheet resistance (R_s), counter electrode resistance (R_{pedot}) and diffusion resistance (R_d)). C_μ is generally used to locate the conduction band of TiO₂. The conduction band of TiO₂ for DSCs with 0 mM, 0.01 mM and 0.05 mM dye concentration lies at similar energy levels. Likewise, the conduction band of TiO₂ for DSCs with higher dye concentrations of 0.1 mM, 0.2 mM and 0.3 mM also lies at similar energy levels, though they are shifted to more positive potentials compared to the device at lower concentrations. As the dye molecules binds to the TiO₂, it releases protons which further shifts the TiO₂ conduction band to more positive potentials.⁴⁷ Thus by using higher dye concentrations (0.1 mM, 0.2 mM, 0.3 mM), the released protons were sufficient enough to shift the CB of TiO₂ to positive potentials.

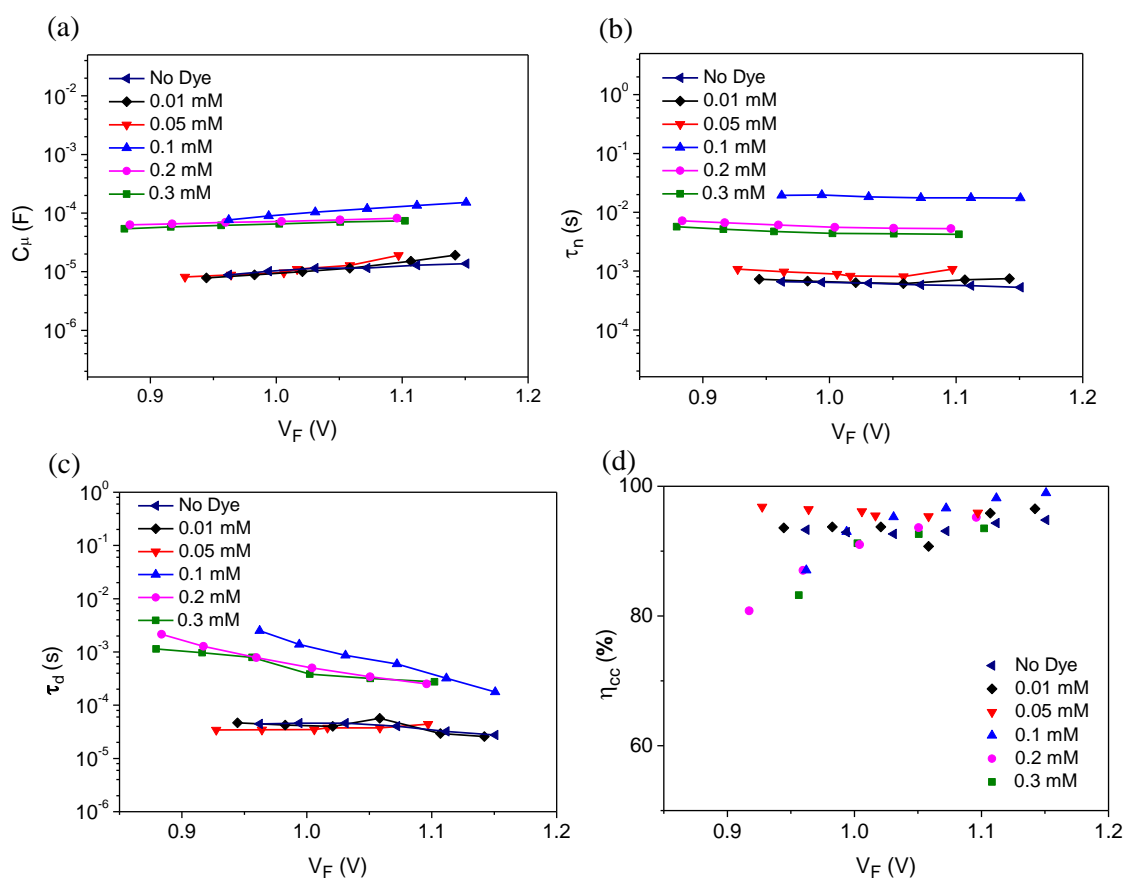


Figure 4.8. (a) Chemical capacitance (C_μ), (b) lifetime (τ_n), (c) transport time (τ_d) and (d) charge collection efficiency (η_{cc}) as a function of V_F for DSCs with different dye concentrations using D35 sensitizer and $[\text{Cu}(\text{tmb})_2]^{2+/1+}$ electrolyte.

Very often positive shift in TiO_2 CB helps to improve J_{sc} by providing better driving force for electron injection from LUMO of the sensitizer to TiO_2 . In the present study by using D35 sensitizer having more negative excited state potentials (-1.35 V, **Figure 4.1(b)**), we didn't expect to have major influence in J_{sc} from the CB shift, which was qualitatively studied in detail using photo induced absorption (PIA) spectroscopy and will be discussed in detail. Thus, the improvement in J_{sc} is mainly associated with the higher dye loading at higher concentrations. The recombination lifetime obtained at different dye concentrations as a function of Fermi voltage is provided in **Figure 4.8(b)**. It is quite evident from the graph that the lifetime was found to increase with increase in dye concentration and a maximum lifetime was obtained using 0.1mM D35 dye concentration, which dropped further with increase in dye concentration. The same trend is also observed from the Bode plot, where the peak at the intermediate frequency region got shifted to higher frequencies with the increase in dye concentration and reached to a maximum at 0.1 mM dye

concentration which then further moved to lower frequency regions at higher concentrations. A similar trend in recombination was also previously observed by Boschloo and co-workers in DSCs fabricated using D35 dye and $[\text{Co}(\text{bpy})_3]^{3+/2+}$ redox mediator.⁴⁸ The increasing trend in lifetime with increased dye loading is mainly attributed to better coverage of dyes over the TiO_2 surface. Additionally, at higher D35 concentrations (0.1mM, 0.2mM and 0.3 mM) there is a positive shift in CB as evident from the capacitance plot (**Figure 4.8(a)**), which reduces the driving force of recombination. Recombination from the bandgap and sub bandgap states are more prominent in copper electrolyte DSCs. Thus, reducing the recombination driving force along with better passivation of TiO_2 by dyes helped in controlling the PV performance. Optimum performance was delivered by DSCs using 0.1mM D35 dye concentration. With further increase in concentration (> 0.1 mM) we observed a reduction in lifetime. But we didn't observe any change in CB at higher concentrations (**Figure 4.8(a)**), which clearly indicates that the observed decrease in lifetime is associated with more recombination at higher concentrations. The trend in lifetime was also reflected and related to the observed open circuit potential (V_{oc}) (**Table 4.1**). DSCs fabricated with 0.1 mM D35 dye solution provided uniform surface coverage of TiO_2 that spatially separates the oxidized Cu(II) species getting closer to TiO_2 . Additionally, devices fabricated using 0.1 mM D35 dye resulted in lowest recombination driving force. Both the above factors contributed to higher photovoltaic performance at 0.1 mM D35 concentration. Lifetime also followed the same trend as that of ideality factor and dark current (**Figure 4.6 (c)**). The transport time measured by EIS (**Figure 4.8 (c)**) shows faster transport for devices with lower concentration of dyes. The charge collection efficiency obtained from EIS also showed better collection employing 0.1 mM D35.

We further used photo induced absorption spectroscopy (PIA) to analyze the electron injection and dye regeneration of DSCs fabricated with different D35 concentrations. **Figure 4.9(a, b)** shows PIA as a function of wavelength for dye soaked photoanodes in the absence and presence of $[\text{Cu}(\text{tmby})_2]^{2+/1+}$ redox mediator respectively. The absorption of oxidized D35 dye under different dye concentrations were observed after 700 nm wavelength region (**Figure 4.9(a)**). Further in presence of redox mediator, absorption response got quenched which reflects efficient dye regeneration. As the PIA spectra for all the dye concentrations overlaps with and without electrolyte, a similar rate of electron injection and dye regeneration is expected for DSCs with various dye concentrations. In short, it can be said that variation of dye content over the TiO_2 surface have little influence on injection and regeneration and does not likely modify the structural

and energetic behavior of DSCs so as to influence the J_{sc} employing D35 sensitizer and $[\text{Cu}(\text{tmby})_2]^{2+/1+}$ electrolyte, thus the variation of J_{sc} undeniably rely on the difference in dye loading and associated variation in light harvesting properties of the sensitizer.

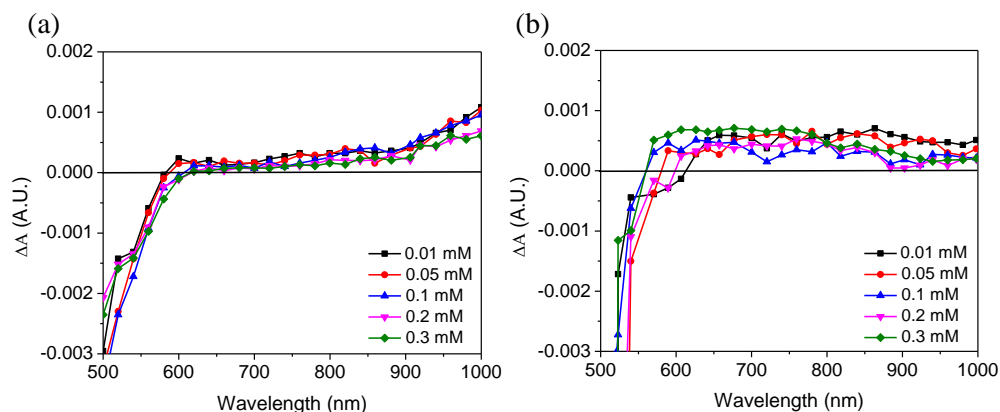


Figure 4.9. (a) Injection and (b) regeneration plot measured using photo-induced absorption (PIA) spectroscopy for devices fabricated using D35 sensitizer and $[\text{Cu}(\text{tmby})_2]^{2+/1+}$ electrolyte under various dye concentrations.

4.5. Conclusions

We studied the role of dye molecules in regulating the charge transfer dynamics of DSCs employing alternate copper redox mediator. In the present study, D35 organic dye at various dye concentrations (0.01 mM, 0.05 mM, 0.1 mM, 0.2 mM and 0.3 mM) was used along with $[\text{Cu}(\text{tmby})_2]^{2+/1+}$ redox mediator. With the increase in dye concentration, dye loading over TiO_2 surface was found to increase and reached to a saturation at 0.2 mM D35 concentration. However, 0.1 mM dye concentration was found to be optimal in terms of photovoltaic performance. A maximum power conversion of $6.50 \pm 0.25\%$ under the full sun (100 mW/cm^2) and $10.48 \pm 0.30\%$ under indoor illumination (1000 lux CFL) was obtained for devices fabricated using 0.1 mM D35 concentration. The calculated ideality factor (m) was also found to be more reasonable at 0.1 mM D35 concentration both under full sun and indoor light illuminations. It is important to note that DSCs showed more deviation from ideal behaviour under indoor illumination than under full sun, indicating the importance of addressing recombination at lower illumination intensities. Further ideality factor was also found in line with the obtained dark current results. EIS was carried out under dark conditions for devices fabricated without the dye and with variable dye concentrations to gain better knowledge on interfacial charge transfer dynamics as a function of concentration of dyes. The conduction band of TiO_2 was found to shift towards

positive potentials with increase in dye concentrations (0.1 mM, 0.2 mM and 0.3 mM). Likewise, lifetime was also found to increase with dye concentration, and the best lifetime was showcased by devices fabricated using 0.1 mM dye which was found to further drop at higher dye concentrations (0.2 mM and 0.3 mM). The increase in lifetime is mainly attributed to the better dye coverage and reduced recombination driving force associated with the positive shift in CB, whereas the drop in lifetime at very higher dye concentrations is attributed to disorder dye distribution due to rapid dye loading. Moreover, 0.1 mM dye concentration also delivered the best charge collection efficiency among the series. The electron injection was found to be quite similar under various concentrations. The targeted application under indoor photovoltaic domain demands for higher V_{oc} and a better control on V_{oc} achieved by changing dye concentration provides better insights, to further improved the V_{oc} in organic dye-copper electrolyte DSCs. With the optimal surface coverage achieved using 0.1 mM D35 dye concentration, DSCs delivered a V_{oc} of 1 V. In nutshell, variation of dye content over TiO_2 surface not only modifies J_{sc} but also changes V_{oc} and FF of DSC. Thus an optimum dye concentration is essential to realize better photovoltaic performance employing organic dye- copper electrolyte combination both under full sun and indoor illumination.

4.6. References

- 1 A. Sohani, S. Memon, S. Hoseinzadeh, D. A. Garcia, F. Schoden, J. Detzmeier, A. K. Schnatmann, T. Blachowicz and E. Schwenzfeier-Hellkamp, *Sustain.* 2022, Vol. 14, Page 5670, 2022, **14**, 5670.
- 2 T. H. Syed and W. Wei, *Inorganics*, 2022, **10**, 191.
- 3 A. Aslam, U. Mehmood, M. H. Arshad, A. Ishfaq, J. Zaheer, A. Ul Haq Khan and M. Sufyan, *Sol. Energy*, 2020, **207**, 874–892.
- 4 N. Mariotti, M. Bonomo, L. Fagiolari, N. Barbero, C. Gerbaldi, F. Bella and C. Barolo, *Green Chem.*, 2020, **22**, 7168–7218.
- 5 E. Sadow, P. Raut, V. Kishnani, K. Mondal, A. Gupta and S. C. Jana, *Micromachines* 2022, Vol. 13, Page 680, 2022, **13**, 680.
- 6 T. H. Syed and W. Wei, *Inorganics* 2022, Vol. 10, Page 191, 2022, **10**, 191.

-
- 7 Mikko Kokkonen, Parisa Talebi, Jin Zhou, Somayyeh Asgari, S. Ahmed Soomro, Farid Elsehrawy, Janne Halme, Shahzada Ahmad, Anders Hagfeldt and S. Ghufuran Hashmi, *J. Mater. Chem. A*, 2021, **9**, 10527–10545.
 - 8 D. Zhang, M. Stojanovic, Y. Ren, Y. Cao, F. T. Eickemeyer, E. Socie, N. Vlachopoulos, J. E. Moser, S. M. Zakeeruddin, A. Hagfeldt and M. Grätzel, *Nat. Commun.*, 2021, **12**, 1–10.
 - 9 H. Michaels, M. Rinderle, R. Freitag, I. Benesperi, T. Edvinsson, R. Socher, A. Gagliardi and M. Freitag, *Chem. Sci.*, 2020, **11**, 2895–2906.
 - 10 R. Haridas, J. Velore, S. C. Pradhan, A. Vindhyasarumi, K. Yoosaf, S. Soman, K. N. N. Unni and A. Ajayaghosh, *Mater. Adv.*, 2021, **2**, 7773–7787.
 - 11 A. Roy, A. Ghosh, S. Bhandari, P. Selvaraj, S. Sundaram and T. K. Mallick, *J. Phys. Chem. C*, 2019, **123**, 23834–23837.
 - 12 H. M. Lee and J. H. Yoon, *Appl. Energy*, 2018, **225**, 1013–1021.
 - 13 B. R. Park, E. J. Choi, Y. J. Choi and J. W. Moon, *KIEAE J.*, 2020, **20**, 121–128.
 - 14 H. Kim, J. Jo, G. Lee, M. Shin and J.-C. Lee, *Sol. Energy*, 2017, **155**, 585–592.
 - 15 J. Barichello, L. Vesce, P. Mariani, E. Leonardi, R. Braglia, A. Di Carlo, A. Canini and A. Reale, *Energies*, 2021, **14**, 6393.
 - 16 A. B. Muñoz-García, I. Benesperi, G. Boschloo, J. J. Concepcion, J. H. Delcamp, E. A. Gibson, G. J. Meyer, M. Pavone, H. Pettersson, A. Hagfeldt and M. Freitag, *Chem. Soc. Rev.*, 2021, **50**, 12450–12550.
 - 17 R. Jiang, H. Michaels, N. Vlachopoulos and M. Freitag, in *Dye-Sensitized Solar Cells*, Elsevier, 2019, pp. 285–323.
 - 18 A. Yella, R. Humphry-Baker, B. F. E. Curchod, N. Ashari Astani, J. Teuscher, L. E. Polander, S. Mathew, J.-E. Moser, I. Tavernelli, U. Rothlisberger, M. Grätzel, M. K. Nazeeruddin and J. Frey, *Chem. Mater.*, 2013, **25**, 2733–2739.
 - 19 W. Zhang, Y. Wu, H. W. Bahng, Y. Cao, C. Yi, Y. Saygili, J. Luo, Y. Liu, L. Kavan,

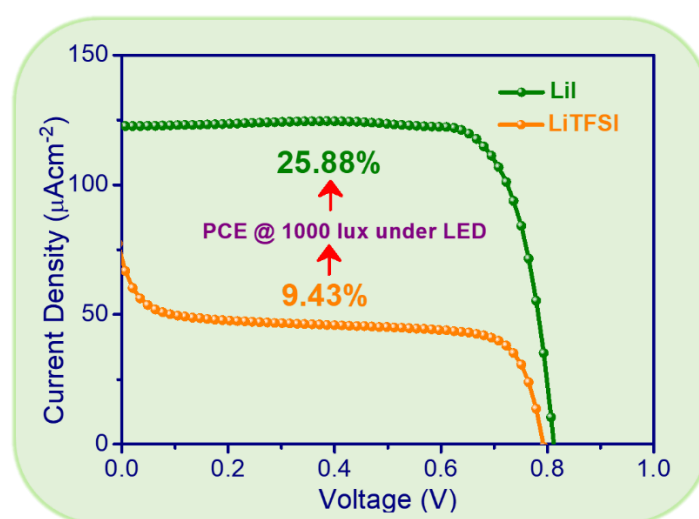
- J.-E. Moser, A. Hagfeldt, H. Tian, S. M. Zakeeruddin, W.-H. Zhu and M. Grätzel, *Energy Environ. Sci.*, 2018, **11**, 1779–1787.
- 20 W. Naim, V. Novelli, I. Nikolinakos, N. Barbero, I. Dzeba, F. Grifoni, Y. Ren, T. Alnasser, A. Velardo, R. Borrelli, S. Haacke, S. M. Zakeeruddin, M. Graetzel, C. Barolo and F. Sauvage, *JACS Au*, 2021, **1**, 409–426.
- 21 Q. Huaultmé, V. M. Mwalukuku, D. Joly, J. Liotier, Y. Kervella, P. Maldivi, S. Narbey, F. Oswald, A. J. Riquelme, J. A. Anta and R. Demadrille, *Nat. Energy*, 2020, **5**, 468–477.
- 22 Y. Ren, D. Zhang, J. Suo, Y. Cao, F. T. Eickemeyer, N. Vlachopoulos, S. M. Zakeeruddin, A. Hagfeldt and M. Grätzel, *Nature*, 2022, 1–6.
- 23 D. Zhang, M. Stojanovic, Y. Ren, Y. Cao, F. T. Eickemeyer, E. Socie, N. Vlachopoulos, J. E. Moser, S. M. Zakeeruddin, A. Hagfeldt and M. Grätzel, *Nat. Commun.*, 2021, **12**, 2–11.
- 24 H. Michaels, I. Benesperi and M. Freitag, *Chem. Sci.*, 2021, **12**, 5002–5015.
- 25 M. Freitag and G. Boschloo, *Curr. Opin. Electrochem.*, 2017, **2**, 111–119.
- 26 H. Michaels, M. Rinderle, R. Freitag, I. Benesperi, T. Edvinsson, R. Socher, A. Gagliardi and M. Freitag, *Chem. Sci.*, 2020, **11**, 2895–2906.
- 27 Y. Saygili, M. Söderberg, N. Pellet, F. Giordano, Y. Cao, A. B. Muñoz-García, S. M. Zakeeruddin, N. Vlachopoulos, M. Pavone, G. Boschloo, L. Kavan, J.-E. Moser, M. Grätzel, A. Hagfeldt and M. Freitag, *J. Am. Chem. Soc.*, 2016, **138**, 15087–15096.
- 28 M. Freitag, F. Giordano, W. Yang, M. Pazoki, Y. Hao, B. Zietz, M. Grätzel, A. Hagfeldt and G. Boschloo, *J. Phys. Chem. C*, 2016, **120**, 9595–9603.
- 29 J. Li, X. Yang, Z. Yu, G. G. Gurzadyan, M. Cheng, F. Zhang, J. Cong, W. Wang, H. Wang, X. Li, L. Kloo, M. Wang and L. Sun, *RSC Adv.*, 2017, **7**, 4611–4615.
- 30 M. Freitag, J. Teuscher, Y. Saygili, X. Zhang, F. Giordano, P. Liska, J. Hua, S. M. Zakeeruddin, J. E. Moser, M. Grätzel and A. Hagfeldt, *Nat. Photonics*, 2017, **11**,

- 372–378.
- 31 C. Chen, V. S. Nguyen, H. Chiu, Y. Chen, T. Wei and C. Yeh, *Adv. Energy Mater.*, 2022, **12**, 2104051.
- 32 H. Wu, G. Wang and B. X. Lei, *ACS Appl. Energy Mater.*, 2022, **5**, 9962–9969.
- 33 A. Grobelny, Z. Shen, F. T. Eickemeyer, N. F. Antariksa, S. Zapotoczny, S. M. Zakeeruddin and M. Grätzel, *Adv. Mater.*, 2022, 2207785.
- 34 E. Tanaka, H. Michaels, M. Freitag and N. Robertson, *J. Mater. Chem. A*, 2020, **8**, 1279–1287.
- 35 Y. Bai, Q. Yu, N. Cai, Y. Wang, M. Zhang and P. Wang, *Chem. Commun.*, 2011, **47**, 4376–4378.
- 36 H. Ellis, N. Vlachopoulos, L. Häggman, C. Perruchot, M. Jouini, G. Boschloo and A. Hagfeldt, *Electrochim. Acta*, 2013, **107**, 45–51.
- 37 S. Soman, S. C. Pradhan, M. Yoosuf, M. V. Vinayak, S. Lingamoorthy and K. R. Gopidas, *J. Phys. Chem. C*, 2018, **122**, 14113–14127.
- 38 S. M. Feldt, E. A. Gibson, E. Gabrielsson, L. Sun, G. Boschloo and A. Hagfeldt, *J. Am. Chem. Soc.*, 2010, **132**, 16714–16724.
- 39 V. Dryza and E. J. Bieske, *J. Photochem. Photobiol. A Chem.*, 2015, **302**, 35–41.
- 40 S. C. Pradhan, J. Velore, A. Hagfeldt and S. Soman, *J. Mater. Chem. C*, 2022, **10**, 3929–3936.
- 41 P. Salvador, M. G. Hidalgo, A. Zaban and J. Bisquert, *J. Phys. Chem. B*, 2005, **109**, 15915–15926.
- 42 J. Bisquert and I. Mora-Seró, *J. Phys. Chem. Lett.*, 2010, **1**, 450–456.
- 43 J. Bisquert, A. Zaban, M. Greenshtein and I. Mora-Seró, *J. Am. Chem. Soc.*, 2004, **126**, 13550–13559.
- 44 J. Bisquert, A. Zaban and P. Salvador, *J. Phys. Chem. B*, 2002, **106**, 8774–8782.

- 45 F. Fabregat-Santiago, G. Garcia-Belmonte, I. Mora-Seró and J. Bisquert, *Phys. Chem. Chem. Phys.*, 2011, **13**, 9083–9118.
- 46 J. Bisquert and F. Fabregat-santiago, *J. Phys. Chem. C*, 2009, **113**, 17278–17290.
- 47 M. K. Nazeeruddin, R. Humphry-Baker, P. Liska and M. Grätzel, *J. Phys. Chem. B*, 2003, **107**, 8981–8987.
- 48 M. Pazoki, P. W. Lohse, N. Taghavinia, A. Hagfeldt and G. Boschloo, *Phys. Chem. Chem. Phys.*, 2014, **16**, 8503.

Additive Engineering in Copper Electrolyte Based Dye-sensitized Solar Cells for Indoor Photovoltaics

5.1. Abstract



Dye-sensitized Solar Cells (DSCs) are highly appreciated for their impressive performance under indoor/artificial light conditions. Recent developments in this area with the introduction of new generation of copper electrolytes and co-sensitized organic dyes helped DSCs to occupy a major position in indoor photovoltaics. A less discussed but imperative modification that plays a critical role in achieving higher indoor photovoltaic performance in copper electrolyte based DSCs is the selection of appropriate additives used in the preparation of electrolyte. Here in we introduced a new additive, lithium iodide (LiI) in copper electrolyte DSCs that improved the photovoltaic performance exceptionally well particularly under indoor light illumination (1000 lux CFL/LED). $[\text{Cu}(\text{tmby})_2]^{2+/1+}$ electrolyte containing LiI along with XY1 sensitizer showed a maximum PCE of 25.88% under 1000 lux warm white LED illumination whereas devices fabricated using the standard lithium bis(trifluoromethylsulphonyl)imide (LiTFSI) only showed an efficiency of 9.43%. Taking advantage of the co-sensitization approach by using a 1:1 XY1:D35 sensitizers, we were able to further enhance the power conversion efficiency to 30.61%

under 1000 lux LED illumination. Mini-modules fabricated with an active area of 1.92 cm² was able to generate a power output of 177 μ W which was sufficient enough to realize autonomous operation of multitude of sensors and actuators under the smart Internet of Things (IoT) network.

5.2. Introduction

With the rapid industrialization, we are marching towards a global climate emergency. The impact of climate change is already visible across the globe. United Nations Climate Change Conference of all Parties (COP2021) expresses severe concern over the increasing global warming rate as a result of human activities.¹ Furthermore, with the advancement in the connected device technologies, a revolution in “Internet of Things” (IoTs) was seen in recent years. Undeniably, IoTs are going to bring about a substantial transformation in the modern smart world. It is anticipated that 30 billion IoTs will exist by 2025; conversely, it will bring an unintended environmental impact of the used batteries powering these devices contributing towards carbon waste.² To avoid a global climatic emergency, we need to develop affordable, sustainable, reliable and modern energy for all. Since light is present everywhere, photovoltaic technology by harvesting sunlight and converting it to useful power is one of the highly appreciated technologies used to produce clean energy to meet the global energy demand. The first generation silicon solar photovoltaic technology is the front runner in solar light harvesting.^{3,4} Similarly, third generation molecular photovoltaic technologies have emerged as outstanding candidate for indoor photovoltaics.⁵⁻⁷

Dye-sensitized solar cells (DSCs) are one among the most studied third generation PV technology, which was attracting attention since 1991 owing to its low cost, flexibility, and aesthetics.⁸⁻¹⁰ Recently with the introduction of judicious combination of co-sensitized organic dyes and copper redox mediators, impressive power conversion efficiency of 15.2% under one sun illumination (AM 1.5G, 100 mW/cm²) and 34.5% under indoor light illumination (1000 lux CFL) was achieved in DSCs using [Cu(tmby)]^{2+/1+} redox mediator.^{11,12} The progress in DSCs with copper redox mediators was mainly attributed to the exploration of newly designed, structurally modified redox mediators and also with the use of newly designed sensitizers.¹³⁻¹⁵ Yet gain, additives used in electrolyte even though are key materials that plays critical role in realizing higher photovoltaic performance by controlling the conduction band and recombination, it never received prime attention in

comparison to the other DSC components. The best copper electrolyte formulation contains lithium additives such as LiTFSI or LiCLO₄ and Lewis base such as 4-tertbutyl pyridine (TBP) along with appropriate concentration of use Cu(I) and Cu(II).^{16–20} However, in recent times, use of a wide variety of additives was also seen in copper electrolyte formulations. For instance, Freitag *et al.* used LiTFSI and tributyl phosphate (TBP) realizing an efficiency upto 28.9% under indoor CFL light illumination.²¹ Further Zhang *et al.* used copper electrolyte formulation with 0.1 M LiTFSI, and 0.6 M 1-methylbenzimidazole (NMBI) achieving an efficiency of 34.5% under 1000 lux CFL illumination and 13.5% under AM 1.5G 1 sun (100 mW/cm²) illumination.¹² Recently Ren *et al.* used 0.1 M Sodium bis(trifluoromethylsulphonyl)imide (NaTFSI) and 0.45M 5-chloro-1-ethyl-2-methylimidazole (CEMI) to reach the record PCE of 15.2% under one sun and 30.2% under 1000 lux LED illumination.¹¹ Even though additives were not given any exclusive importance in any of these state-of-art scientific reports, the role of additives in improving the power conversion efficiency of DSCs particularly under indoor/artificial light conditions cannot be ignored.

In the present study, we introduced a new additive lithium iodide (LiI) replacing the conventional LiTFSI in [Cu(tmby)₂]^{2+/1+} redox mediator. We systematically varied the LiI concentration in the electrolyte formulation and studied the photovoltaic performance using XY1 sensitizer. **Figure 5.1.** shows structure and energetics of sensitizers D35, XY1 and redox mediator [Cu(tmby)₂]^{2+/1+} used in the present study. Under one sun (100 mW/cm²) illumination, DSCs without LiI showed the maximum PCE of 9.42%, while under indoor 1000 lux LED illumination, an impressive efficiency of 25.88% was realized using DSC fabricated with 0.3M LiI which is 64% higher PCE compared to standard electrolyte with LiTFSI. Interfacial charge transfer dynamics studied using charge extraction, open circuit voltage decay and electrochemical impedance spectroscopy provided better understanding of the charge recombination at various interfaces. Further, by employing the co-sensitization of XY1 and D35 sensitizers we successfully achieved an impressive power conversion efficiency of 30.6% under 1000 lux LED illumination. Larger area mini-modules with an active area of 1.92 cm² was able to retain the same PCE and delivered a power of 177 μW under 1000 lux LED illumination. Here in we particularly used LED in place of CFL (compact florescent lamp) for all indoor light measurements as popularity of LED is growing and CFL is hardly used.

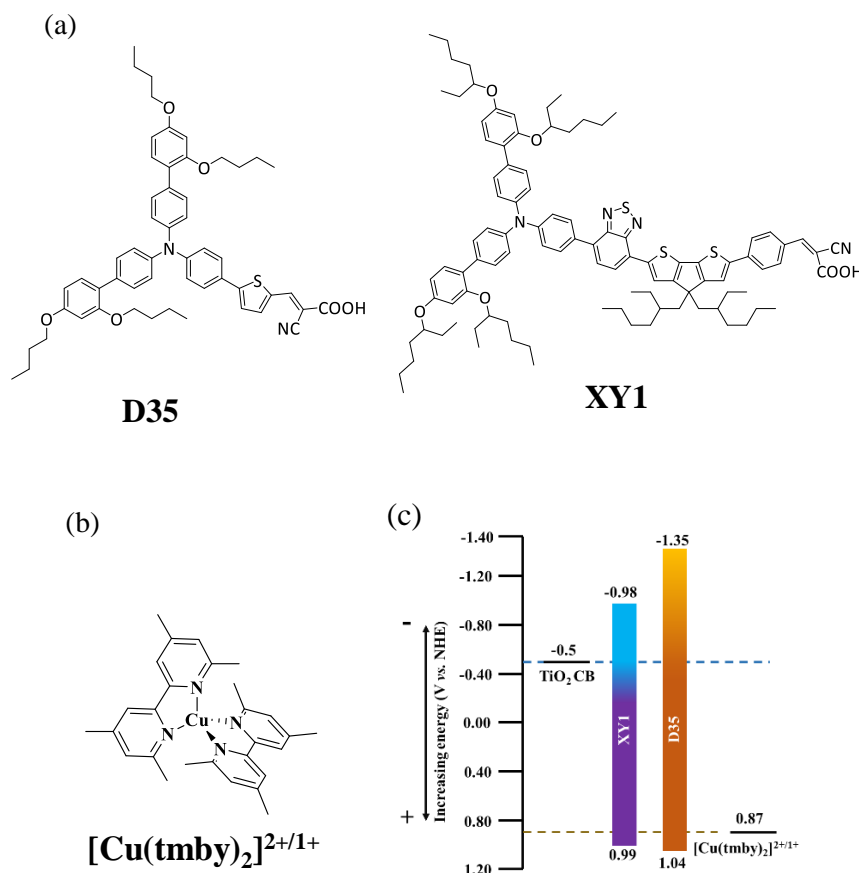


Figure 5.1. (a) Structures of D35, XY1 sensitizers (b) $[\text{Cu}(\text{tmby})_2]^{2+/1+}$ electrolyte and (c) energetics of the sensitizers and electrolyte used in the present study.

5.3. Experimental Section

5.3.1. General Methods

The solvents and materials used for device fabrication were of HPLC grade purchased from Sigma-Aldrich, Merck, GreatCell Solar and used without further purification. D35 and XY1 organic dye, $[\text{Cu}(\text{tmby})_2]^{2+/1+}$ copper complexes and TiO_2 paste were obtained from Dynamo AB (Stockholm, Sweden).

5.3.2. Fabrication of DSCs

Preparation of working electrode starts with cutting of large size FTO glass into square size (1.5 cm \times 1.5) cm using glass cutting machine, while, for master plates the size was 1.4 cm \times 2.4 cm. FTO glass substrates were sequentially sonicated in detergent (30 minutes), DI water (30 minutes), isopropyl alcohol (15 minutes) and acetone (15 minutes)

followed by annealing at 500 °C for 30 minutes. The substrates were further taken for UV ozone cleaning followed by blocking layer deposition. For blocking layer deposition, the electrodes were immersed in 40 mM TiCl₄ at 70 °C for 30 minutes and then rinsed in DI water and ethanol multiple times followed by 500 °C for 30 minutes. Mesoporous TiO₂ (30NRD, Greatcell solar) was screen printed using 77T screen and dried by annealing at 100 °C. Further scattering layer (18NRAO, Greatcell solar) was screen printed using 77T screen and annealed at 325 °C for 5 minutes, 375 °C for 5 minutes, 400 °C for 5 minutes and 500 °C for 30 minutes. The total thickness of active layer was found to be around 7 μm. Further a blocking layer was deposited over TiO₂ by TiCl₄ treatment in the similar way as discussed earlier. The electrodes were immersed in dye solution for 16 hours in dark environment at room temperature. Both XY1 and D35 dye solution were prepared in acetonitrile and tertbutynol solution in 1:1 ratio with 0.1 M molar concentration. The co-sensitized XY1 and D35 dye solution were made in 1:1 ratio. The dye soaked electrodes were rinsed in acetonitrile and dried in nitrogen. For counter electrodes, hole drilled square size TEC 8 FTO glass were sequentially sonicated in detergent (45 minutes), DI water (45 minutes) and ethanol (45 minutes) and annealed at 500 °C for 30 minutes. The electrodes were treated with UV ozone for 15 minutes prior to PEDOT deposition. PEDOT electrodes were prepared by electropolymerisation of 3,4-ethylene dioxythiophene (EDOT) from a micellar aqueous solution of 0.1 M sodium dodecyl sulfate (SDS) and 0.01 M EDOT.^{22–24} The detail of PEDOT counter electrode is given elsewhere. The photoanode and counter electrode were assembled together using threebond UV epoxy. Electrolyte was injected into the devices through back holes and holes were further sealed with cover glass. The electrolyte consists of 0.1 M Cu(I), 0.04 M Cu(II), 0.6 M 4-tert-butylpyridine and different concentrations of either LiTFSi and LiI salt in acetonitrile.

5.3.3. Solar Cell Characterization

Current-Voltage (*J-V*) measurements were carried out using Oriel Class-AAA solar simulator (Model PVIV- 94043A) using Keithley 2441 source meter which is controlled using computer through LabView software. The intensity of light from solar simulator was calibrated using certified reference Si solar cell. Indoor light measurements were carried out using homemade indoor light simulator with a white LED as the source of illumination. The indoor *J-V* responses were recorded using Dyenamo potentiostat (DN-AE05). The intensity of the light was measured using radiometrically calibrated Ocean optics Jaz

spectrometer. A square black mask of area 0.34 cm^2 (similar size as that of active area) was used during the J - V measurements to minimize the contribution of light falling outside the active area. Photon-to-Current Efficiency (IPCE) measurement was carried using Oriel (model) preconfigured setup. It consists of 300 W Xenon arc lamp and monochromator. The input intensity is measured using a power meter coupled with a certified photo detector. Entire equipment is controlled by computer through TRAQ basic software. IPCE was carried in the wavelength range of 300 to 1000 nm in DC mode. Current transient and open circuit voltage decay (OCVD) measurements were carried out under AM 1.5 illumination. For current transient measurement studies, the shutter of solar simulator was closed and opened alternatively for multiple times and the current response was measured using Autolab (PGSTAT302N workstation). Similarly, to perform OCVD the shutter of solar simulator was opened for 20 seconds and further closed to measure the voltage decay using Autolab. Charge extraction measurements were carried out using Dyenamo Toolbox. EIS measurements were carried out at 0 V DC bias and 10 mv perturbation using a frequency range of 100 mHz to 100 kHz. Nyquist plots were fitted in Z-view software using the standard equivalent circuit models.

5.4. Results and Discussion

5.4.1. Photovoltaic Performance under Full Sun

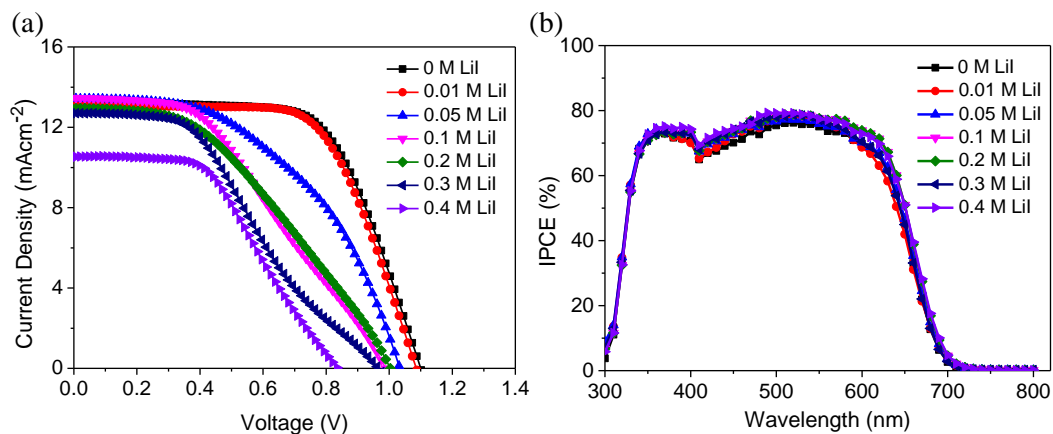


Figure 5.2. (a) J - V characteristics under AM 1.5G one sun illumination (100 mW/cm^2) and (b) IPCE response with various LiI concentrations using devices fabricated using XY1 sensitizer and $[\text{Cu}(\text{tmby})_2]^{2+/1+}$ electrolyte.

Table 5.1. Photovoltaic parameters of DSCs fabricated using XY1 sensitizer and $[\text{Cu}(\text{tmby})_2]^{2+/1+}$ electrolyte having different LiI concentrations.

Irradiance (Sun)	LiI Con. (M)	V_{oc} (V)	J_{sc} (mAcm^{-2})	FF	η (%)	Integrated J_{sc} (mAcm^{-2})
1	0	1.10 ± 0.01	13.20 ± 0.07	0.65 ± 0.01	9.41 ± 0.13	12.47
	0.01	1.08 ± 0.05	13.00 ± 0.15	0.66 ± 0.04	9.24 ± 0.02	12.42
	0.05	1.03 ± 0.05	13.40 ± 0.11	0.49 ± 0.01	6.77 ± 0.11	12.74
	0.1	0.99 ± 0.09	13.45 ± 0.26	0.41 ± 0.07	5.41 ± 0.20	13.16
	0.2	1.00 ± 0.01	12.95 ± 0.17	0.41 ± 0.03	5.28 ± 0.15	13.16
	0.3	0.98 ± 0.03	12.83 ± 0.09	0.38 ± 0.10	4.73 ± 0.29	12.81
	0.4	0.85 ± 0.06	10.50 ± 0.22	0.47 ± 0.08	4.21 ± 0.31	13.17
0.1	0	0.93 ± 0.03	1.11 ± 0.13	0.56 ± 0.09	5.75 ± 0.25	--
	0.01	0.93 ± 0.04	1.14 ± 0.12	0.66 ± 0.07	7.05 ± 0.22	--
	0.05	0.93 ± 0.04	1.26 ± 0.19	0.72 ± 0.07	8.37 ± 0.14	--
	0.1	0.83 ± 0.06	1.42 ± 0.15	0.72 ± 0.08	8.48 ± 0.20	--
	0.2	0.86 ± 0.03	1.32 ± 0.21	0.73 ± 0.02	8.33 ± 0.11	--
	0.3	0.86 ± 0.01	1.33 ± 0.20	0.68 ± 0.08	7.8 ± 0.19	--
	0.4	0.76 ± 0.04	1.48 ± 0.16	0.72 ± 0.06	8.15 ± 0.15	--

Current density–voltage (J – V) characteristics of the fabricated DSCs were measured under one sun illumination (AM 1.5G, 100 mWcm^{-2}). The J – V characteristics of the DSCs using copper electrolytes at various concentration of LiI is shown in **Figure 5.2 (a)** and the photovoltaic parameters are listed in **Table 5.1**. The highest efficiency of 9.41 ± 0.13 (V_{oc} - $1.10 \pm 0.01\text{V}$, J_{sc} - $13.20 \pm 0.07 \text{ mAcm}^{-2}$ and FF - 0.65 ± 0.01) was obtained for DSCs employing Cu(I/II) electrolyte without LiI. The photovoltaic performance decreased with increase in LiI concentration. It is well known that the presence of Li^+ in the electrolyte positively shifts the conduction band of TiO_2 through Li^+ intercalation reducing the V_{oc} .^{25,26} Similarly, increase in Γ in electrolyte concentration can consequently shift the redox potential towards negative potential leading to lower V_{oc} .^{27,28} Moreover, both Li^+ cation and Γ anion can affect simultaneously to reduce the V_{oc} . In this regard we carried out a detailed interfacial charge transfer study using various perturbation techniques which is discussed in the following sections to probe the charge transfer dynamics as a function of LiI concentration.

A nominal improvement in J_{sc} was observed initially with increase in LiI concentration (from 0.01M to 0.1M) and a maximum J_{sc} of 13.45 mAcm^{-2} was obtained with LiI concentration of 0.1 M. Further increase in LiI concentration resulted in J_{sc} drop. In contrary, IPCE response of DSC with various LiI concentration was found to overlap with each other (**Figure 5.2 (b)**). Subsequently the J_{sc} obtained by integrating IPCE spectra showed similar value. According to Jayadev *at el.* discrepancy in J_{sc} obtained from J - V and IPCE measurement is an indication of mass transport issue.²⁹ The variation in J_{sc} obtained from J - V and IPCE measurement is largely visible in 0.4 M LiI concentration, where J_{sc} from J - V measurement is 10.5 mAcm^{-2} while integrated J_{sc} from IPCE was 13.17 mAcm^{-2} (**Table 5.1**). This point towards mass transport issues in DSCs at very high concentration of LiI. Mass transport issue is further discussed in the following section. Further, FF was also largely affected with the increase in concentration of LiI in electrolyte. Increase in LiI concentration severely damaged both V_{oc} and FF of the devices under 1 sun illumination and hence the power conversion efficiency (η) also got reduced with increasing concentration of LiI under 1 sun illumination.

Photovoltaic performance was also measured at a lower illumination intensity of 0.1 sun illumination (10 mW/cm^2) which showed contradictory results to that obtained under full sun (100 mW/cm^2) (**Figure 5.3, Table 5.1**). V_{oc} showed similar trend under 0.1 sun as that of 1 sun, where it dropped with increase in LiI concentrations. Whereas both J_{sc}

and FF increased with increase in LiI concentration under 0.1 sun illumination contributing towards an increase in PCE with increase in LiI concentration under 0.1 sun illumination.

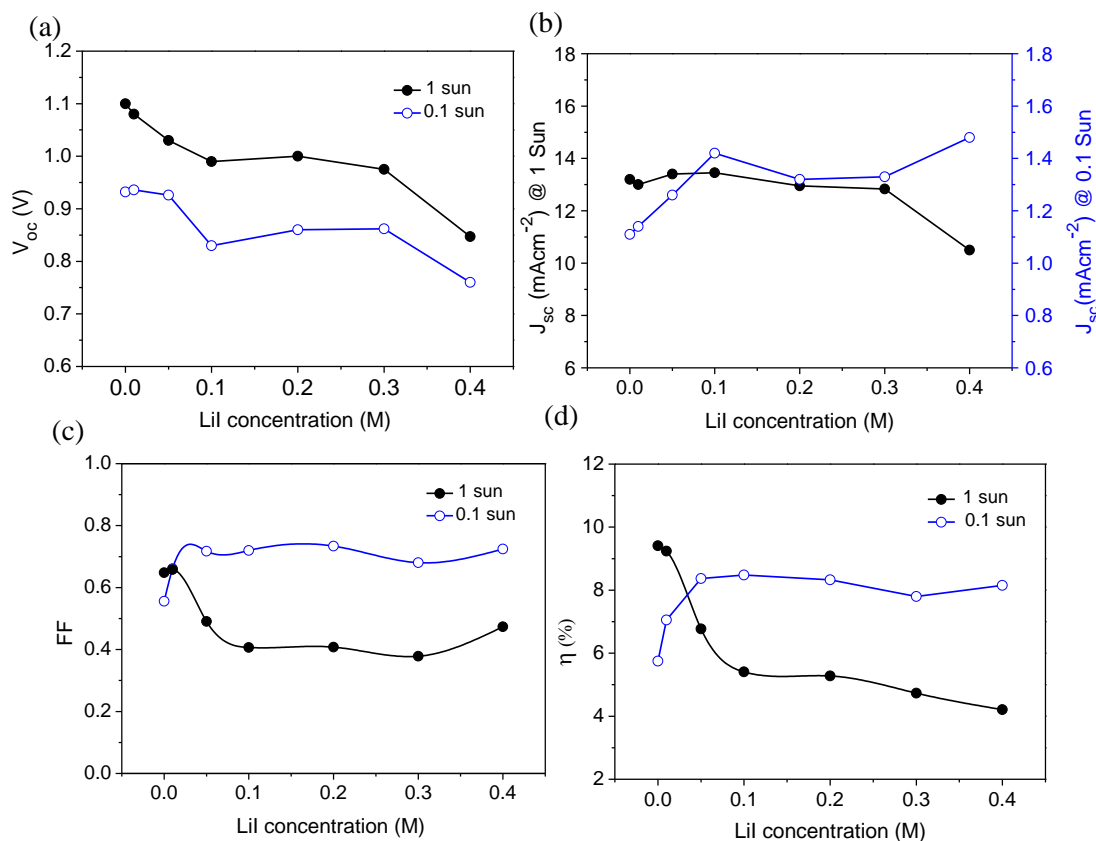


Figure 5.3. Trend in (a) V_{oc} (b) J_{sc} (c) FF and (d) η as a function of LiI concentration under 1 sun and 0.1 sun illumination (100 mW/cm^2 and 10 mW/cm^2) using DSCs fabricated using XY1 sensitizer and $[\text{Cu}(\text{tmby})_2]^{2+/1+}$ electrolyte.

5.4.2. Interfacial Charge Transfer Study

The indication of mass transport limitation as initially observed from *IPCE* plot (**Figure 5.1 (b)**) was further investigated in detail using intensity dependent J_{sc} and current transient measurements. **Figure 5.4 (a)** shows J_{sc} as a function of light intensity and current density as a function of time (**Figure 5.4 (b)**). J_{sc} is related to light intensity (I) by the relation, $J_{sc} \propto I^\alpha$ where α is the power coefficient. The α value obtained by fitting J_{sc} vs. light intensity was close to unity for 0 M, 0.01 M, 0.1 M and 0.2 M LiI while it deviated from ideality (0.94 and 0.77 for 0.3 M and 0.4 M) at higher LiI concentrations. The same trend was also observed in current transient plot (**Figure 5.4 (b)**) where we observed a

sudden drop in J_{sc} followed by light illumination at higher concentrations of 0.3M and 0.4M LiI. The loss in J_{sc} at higher LiI concentration originates mainly from the mass transport limitations.

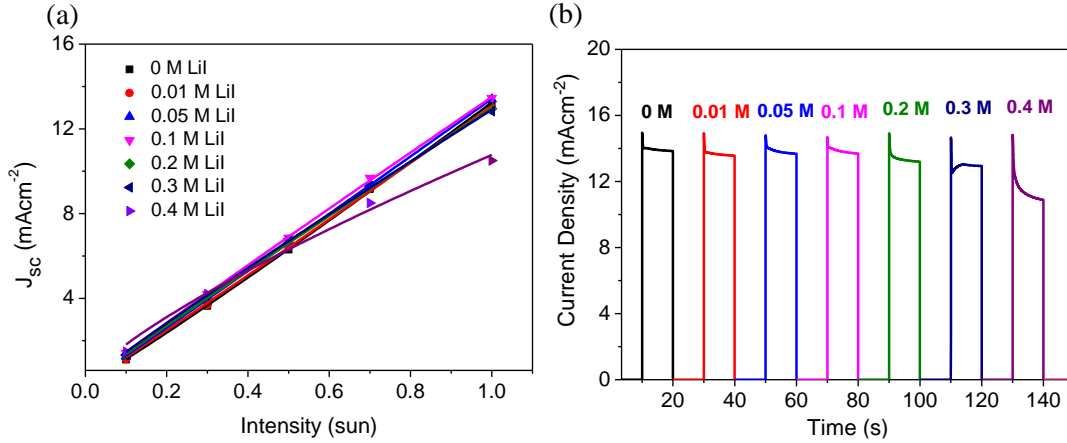


Figure 5.4. (a) J_{sc} as function of light intensity and (b) current transient measurements of DSCs with various concentrations of LiI using XY1 dye and $[\text{Cu}(\text{tmby})_2]^{2+/1+}$ electrolyte.

The limitation in FF is mainly associated with the resistive losses at the counter electrode/electrolyte interface.³⁰⁻³² To understand this further, we studied CE-CE dummy cells using electrochemical impedance spectroscopy (EIS). **Figure 5.5 (a,b and c)** shows the Nyquist plot of CE-CE dummy cells, equivalent circuit used to fit the Nyquist plots and the derived equivalent resistance ($R_{ct,eqv}$) at various LiI concentrations. The Nyquist plot of CE-CE dummy cells shows three semicircles, first semicircle corresponds to the diffusion of ions in the porous electrode, second semicircle represents the charge transfer at the PEDOT/electrolyte interface and the third semicircle indicates the diffusion of ions in the electrolyte.^{22,33} The equivalent circuit as given in **Figure 5.5 (b)** consists of resistors (R), constant phase elements (CPE) and Warburg element (W_s). R_s is the series resistance of substrate, R_{porous} is the resistance for ion diffusion at the porous electrode and R_{ct} is the resistance for charge transfer at the PEDOT/electrolyte interface. Similarly, CPE_{porous} and CPE_{ct} are the capacitance owing to diffusion of electrons at the porous electrodes and charge transfer at the PEDOT/electrolyte interface. Moreover, the summation of R_{porous} and R_{ct} corresponds to the equivalent resistance ($R_{ct,eqv}$) for charge transfer at the PEDOT/electrolyte interface. As shown in **Figure 5.5 (c)**, $R_{ct,eqv}$ is similar at 0 M and 0.01M LiI concentration and it increased significantly with further increase in LiI concentration.

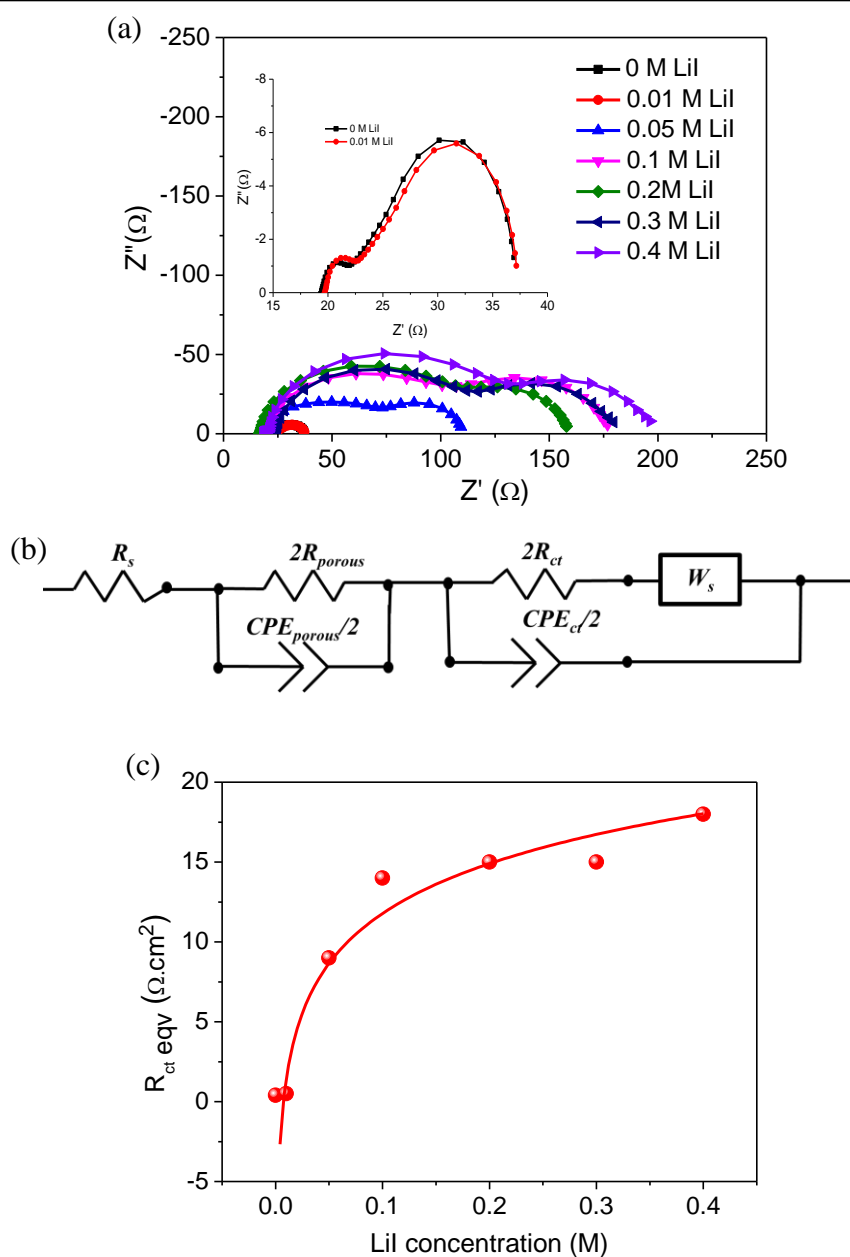


Figure 5.5. (a) Nyquist plot of CE-CE dummy cells at various LiI concentration, (b) equivalent circuit used for fitting Nyquist plot and (c) Equivalent charge transfer resistance as a function of LiI concentrations.

This was clearly reflected in the FF of DSCs, where a sudden drop in FF was observed starting from 0.05 M LiI concentration. Even though FF under 1 sun illumination was severely affected with increased concentration of LiI, it remained uninfluenced for measurements carried out under 0.1 sun illumination (**Figure 5.3 (c)**).

Charge transfer at the $\text{TiO}_2/\text{dye}/\text{electrolyte}$ interface significantly influences both V_{oc} and J_{sc} of DSCs and it was examined in detail using charge extraction and open circuit voltage decay (OCVD) measurements. As evident from the charge extraction

measurements (**Figure 5.6 (a)**), the CB of TiO₂ shifted towards more positive potentials with increase in LiI concentration which is attributed to the Li⁺ intercalation with TiO₂.^{34,35} However, under 1 sun illumination the positive shift in CB didn't materialize towards better injection and higher J_{sc} as the performance was severely masked by mass transport at higher intensity. Charge recombination at TiO₂/dye/electrolyte interface was measured using OCVD and the lifetime was calculated from the voltage decay plot using the equation,^{36,37}

$$\tau_n = -\frac{k_B T}{e} \left(\frac{dV_{OC}}{dt} \right)^{-1} \quad (1)$$

Figure 5.6 (b) shows the lifetime as a function of voltage. Lifetime was found to increase with increase in LiI concentrations. LiI in electrolyte forms Li⁺ which shift the CB of TiO₂ to more positive potentials and thereby reducing the driving force for charge recombination from TiO₂ CB and sub-bandgap states to the oxidized species in electrolyte (Cu²⁺) leading to improved lifetime. Improvement in lifetime generally contributes towards higher V_{oc} , however, in the present case the trend in V_{oc} better aligns with the results obtained from charge extraction measurement aligning more with the shift in TiO₂ CB with increased concentration of LiI.

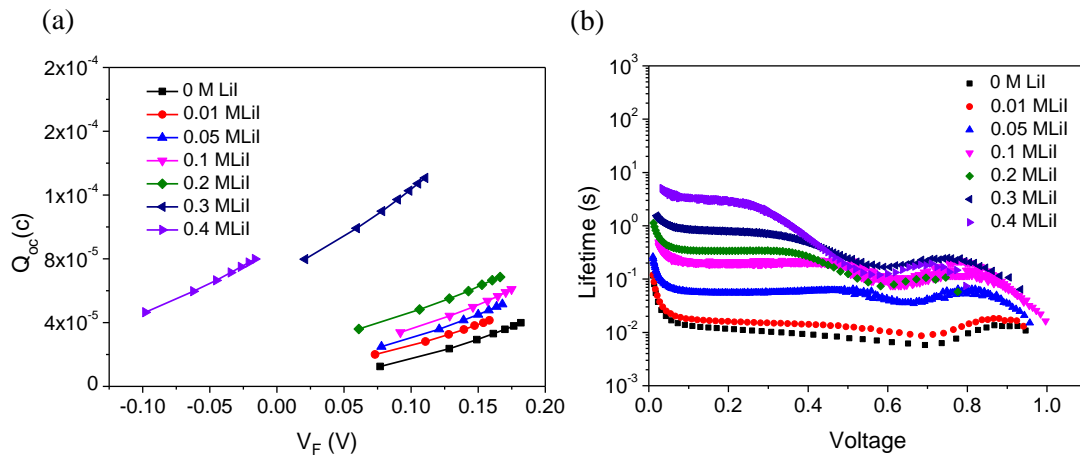


Figure 5.6 (a) Extracted charge as function Fermi voltage (V_F) measured using charge extraction (b) Lifetime as function of voltage measured using OCVD at various LiI concentration in devices fabricated using XY1 dye and [Cu(tmby)₂]^{2+/1+} electrolyte.

5.4.3. Photovoltaic Performance under Indoor LED Illumination

Indoor photovoltaic parameters of the fabricated DSCs were measured under 1000 lux illumination using light emitting diode (LED). **Figure 5.7** shows the J - V characteristics under 1000 lux illumination using DSCs fabricated with XY1 dye and [Cu(tmby)₂]^{2+/1+}

electrolyte using different LiI concentrations and the obtained photovoltaic parameters are summarized in **Table 5.2**. The trend in photovoltaic parameters obtained under indoor 1000 lux illumination showed similar trend as that of the results obtained under 0.1 sun (**Table 5.1**), but displayed a difference in trend compared to the results obtained under 1 sun illumination (**Table 5.1**). This difference observed is mainly attributed to the variation

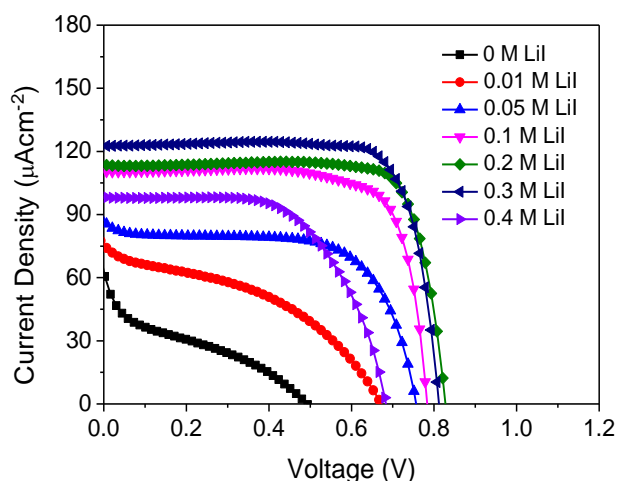


Figure 5.7. *J-V* characteristics measured under 1000 lux LED illumination for DSCs fabricated using XY1 dye and $[\text{Cu}(\text{tmby})_2]^{2+/1+}$ electrolyte with different LiI concentrations.

Table 5.2. Photovoltaic parameters of DSCs fabricated using XY1 dye and $[\text{Cu}(\text{tmby})_2]^{2+/1+}$ electrolyte under 1000 lux LED illumination using various concentrations of LiI.

LiI Conc. (M)	V_{oc} (V)	J_{sc} (μAcm^{-2})	FF	η (%)
0	0.49 ± 0.04	63 ± 1.7	0.23 ± 0.03	2.39 ± 0.11
0.01	0.67 ± 0.03	75 ± 1.0	0.41 ± 0.03	6.78 ± 0.08
0.05	0.75 ± 0.03	88 ± 1.5	0.63 ± 0.07	13.76 ± 0.13
0.1	0.78 ± 0.01	110 ± 1.3	0.76 ± 0.02	21.71 ± 0.10
0.2	0.82 ± 0.07	113 ± 2.0	0.81 ± 0.05	24.72 ± 0.21
0.3	0.81 ± 0.01	122 ± 1.4	0.79 ± 0.02	25.88 ± 0.10
0.4	0.68 ± 0.05	98 ± 1.0	0.62 ± 0.01	13.57 ± 0.09

in charge transfer at various interfaces in DSCs under 1 sun and indoor illumination. Under low intensity indoor light illumination, mass transport issues and charge transfer at the counter electrode which are bottlenecks to realize higher performance under full sun becomes less likely to affect the solar cell performance. Under LED illumination, V_{oc} , J_{sc}

and FF increased with increase in LiI concentration and a maximum power conversion efficiency of $25.88 \pm 0.10\%$ (V_{oc} - 0.81 ± 0.01 V, J_{sc} - $122 \pm 1.4 \mu\text{Acm}^{-2}$ and FF - 0.79 ± 0.02) was achieved using 0.3 M LiI concentration. The improvement in V_{oc} and FF with LiI is mainly attributed to the higher electron lifetime (**Figure 5.6 (b)**). Similarly, an increase in J_{sc} was observed with increasing LiI concentration which could be due to better injection owing to improved driving force for injection with a positively shifted CB. However, at a higher LiI concentration of 0.4 M, drastic drop in photovoltaic parameters and power conversion efficiency was observed which may be due to the presence of excessive concentration of I⁻ in the electrolyte leading to multiple intermediators and recombination pathways.

5.4.4. LiTFSi vs. LiI

Systematically we carried out a comparative study of DSCs containing conventional LiTFSI and the newly introduced LiI in $[\text{Cu}(\text{tmby})_2]^{2+/1+}$ electrolyte formulation to evaluate the impact on various charge transfer processes. **Figure 5.8 (a)** shows the J - V characteristics of DSCs measured under 1000 lux LED illumination using XY1 dye along with $[\text{Cu}(\text{tmby})_2]^{2+/1+}$ containing 0.1 M LiTFSI and 0.1 M LiI in the electrolyte and the indoor photovoltaic parameters are summarized in **Table 5.3**. Under 1000 lux LED illumination, 0.1M LiTFSI based DSCs showed a maximum power conversion efficiency of $9.43 \pm 0.17\%$ while DSCs with similar LiI concentration showed an improved power conversion efficiency $21.71 \pm 0.10\%$. Under similar concentration of 0.1 mM, efficiency of DSC with LiTFSI is 57% lesser compared to DSC with LiI. Yet again, efficiency of DSC with LiTFSI is 64% lesser than the efficiency delivered by DSCs employing 0.3 M LiI ($25.88 \pm 0.10\%$). With decrease in light intensity power conversion efficiency continuously dropped and it did not perform under 200 lux illumination. To investigate this further, we examined the shift in CB and recombination lifetime as a function of both the additives used under similar concentration of 0.1M. As evident from the charge extraction plot (**Figure 5.8. (b)**), the TiO_2 CB is shifted to positive potentials in presence of LiI. This could have helped in better injection and also contributed to better electron lifetime (**Figure 5.8 (c)**) as a result of reduced driving force for recombination.

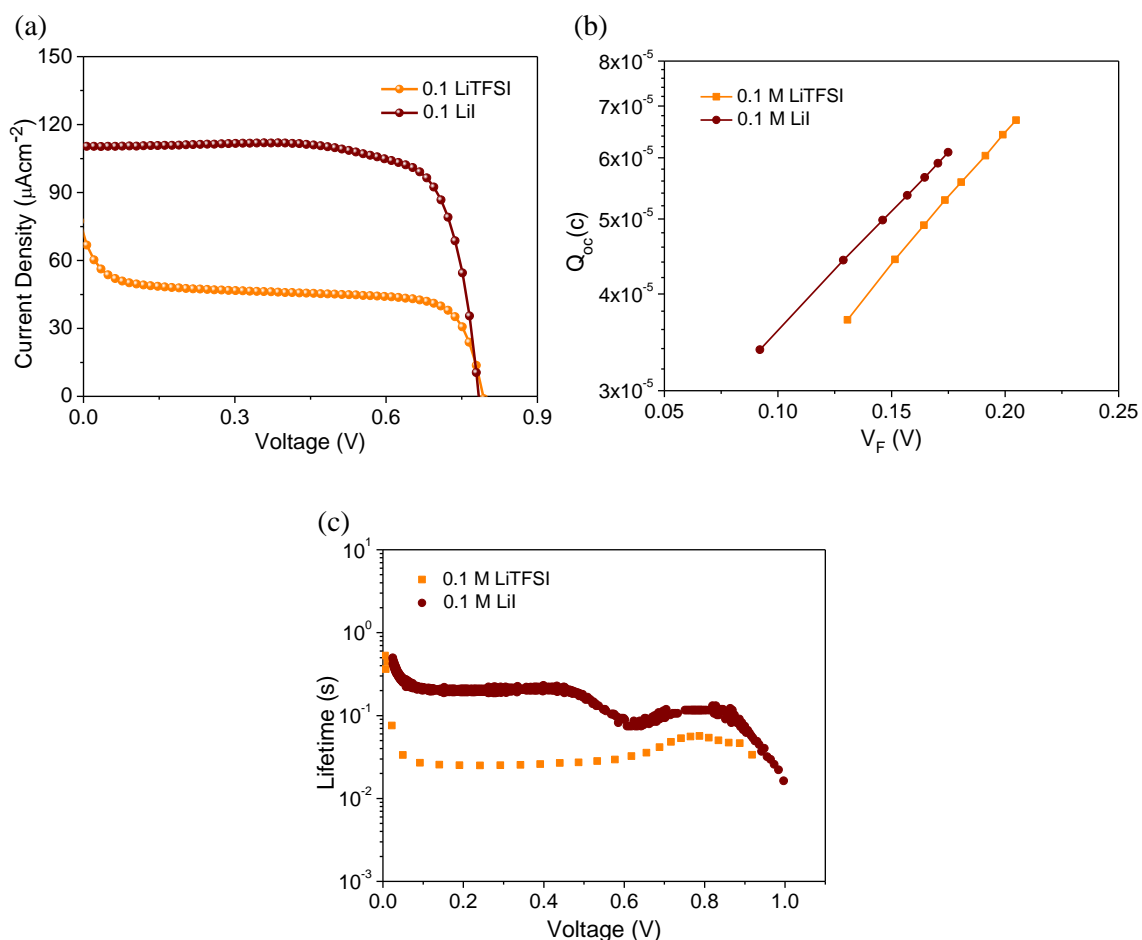


Figure 5.8 (a) J - V characteristics of DSCs under LED illumination using XY1 dye along with $[\text{Cu}(\text{tmby})_2]^{2+/1+}$ containing 0.1 M LiTFSI, (b) extracted charge as a function of V_F and (c) lifetime as a function of voltage for DSCs using $[\text{Cu}(\text{tmby})_2]^{2+/1+}$ containing 0.1 M LiTFSI and 0.1 M LiI.

Table 5.3. Photovoltaic parameters of DSCs fabricated with XY1 dye along with $[\text{Cu}(\text{tmby})_2]^{2+/1+}$ containing 0.1 M LiTFSI and 0.1 M LiI under 1000 lux LED illumination ($303 \mu\text{W}/\text{cm}^2$).

Dye	Additive	V_{oc} (mV)	J_{sc} (μAcm^{-2})	FF	η (%)
XY1	LiTFSI	789 ± 30	78 ± 0.5	0.55 ± 0.03	9.43 ± 0.17
	LiI	784 ± 28	110 ± 1.3	0.76 ± 0.02	21.71 ± 0.10

5.4.5. Co-sensitization Strategy for Indoor Photovoltaic Performance Enhancement

Co-sensitization of organic sensitizers is used as an innovative approach to improve the photovoltaic performance of DSCs under indoor/ambient light illuminations.^{38,39} Co-sensitization involves use of a smaller dye along with a larger sensitizer which occupies spatial positions between the larger dye, thus passivating recombination as well as help to realize better absorption characteristic to match with the spectra of indoor light sources. In order to further improve the photovoltaic performance under LED illumination, we co-sensitized XY1 dye with standard D35 sensitizer in 1:1 ratio along with best optimized LiI concentration (0.3 M). **Figure 5.9 (a, b, c)** shows the J - V characteristics of D35, XY1 and

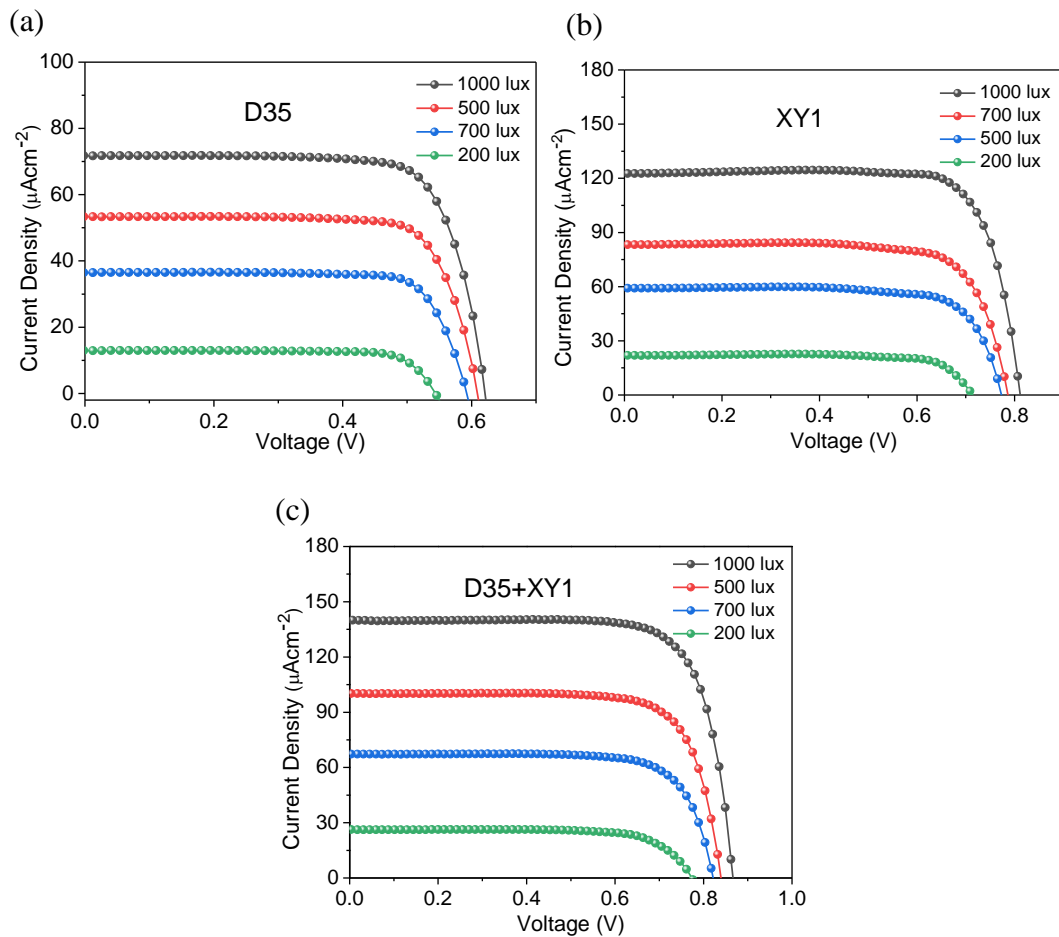


Figure 5.9. J - V characteristics of DSCs with (a)D35, (b) XY1 and (c) D35+XY1 sensitizers with $[\text{Cu}(\text{tmby})_2]^{2+/1+}$ containing 0.3 M LiI under LED illumination.

Table 5.4. Indoor photovoltaic parameters of DSCs with D35, XY1 and co-sensitized D35+XY1 dye combinations with $[\text{Cu}(\text{tmby})_2]^{2+/1+}$ electrolyte containing 0.3 M LiI under LED illumination of variable intensities (1000 lux, 700 lux, 500 lux, 200 lux)

Dye	Light Intensity (lux)	Input Power Density (μWcm^{-2})	V_{oc} (mV)	J_{sc} (μAcm^{-2})	FF	η (%)
D35	1000	303	620 ± 27	72 ± 1.3	0.75 ± 0.02	11.17 ± 0.16
	700	195	607 ± 25	53 ± 0.9	0.72 ± 0.02	11.93 ± 0.11
	500	150	592 ± 19	36 ± 1.0	0.74 ± 0.07	11.30 ± 0.14
	200	65	545 ± 20	12 ± 0.3	0.73 ± 0.05	8.56 ± 0.17
XY1	1000	303	806 ± 0.13	122 ± 1.4	0.79 ± 0.02	25.88 ± 0.10
	700	195	779 ± 0.16	83 ± 1.1	0.77 ± 0.05	25.82 ± 0.14
	500	150	0.764 ± 0.15	59 ± 0.9	0.77 ± 0.07	23.07 ± 0.13
	200	65	0.708 ± 0.20	22 ± 1.6	0.77 ± 0.04	18.67 ± 0.18
XY1 + D35	1000	303	866 ± 70	140 ± 3.1	0.76 ± 0.03	30.6 ± 0.11
	700	195	837 ± 55	100 ± 2.0	0.76 ± 0.06	30.5 ± 0.10
	500	150	820 ± 77	67 ± 1.2	0.75 ± 0.03	27.7 ± 0.31
	200	65	774 ± 59	26 ± 0.5	0.74 ± 0.05	23.1 ± 0.25

D35+XY1 sensitized devices under LED illumination of variable intensities (1000 lux, 700 lux, 500 lux and 200 lux) with $[\text{Cu}(\text{tmby})_2]^{2+/1+}$ electrolyte containing 0.3 M LiI and the photovoltaic parameters are summarized in **Table 5.4**. Under standard 1000 lux illumination DSCs with D35 dye showed a maximum efficiency of $11.17 \pm 16\%$ (V_{oc} - 620 ± 27 mV J_{sc} - 72 ± 1.3 μAcm^{-2} and FF - 0.75 ± 0.02). Under similar light condition DSCs with XY1 sensitizer showed maximum efficiency of $25.88 \pm 0.01\%$ (V_{oc} - 806 ± 13 mV J_{sc} - 122 ± 1.4 μAcm^{-2} and FF - 0.79 ± 0.02) and co-sensitized (D35+XY1) DSCs showed an impressive power conversion efficiency of $30.6 \pm 0.11\%$ (V_{oc} - 866 ± 70 mV, J_{sc} of 140 ± 3.1 μAcm^{-2} and FF - 0.76 ± 0.03). Even at a lower LED illumination intensity of 200 lux, D35 +

XY1 co-sensitized device was able to realize a PCE of $23.1 \pm 0.25\%$ (V_{oc} - 774 ± 59 mV, J_{sc} of $26 \pm 0.5 \mu\text{Acm}^{-2}$ and FF - 0.74 ± 0.05).

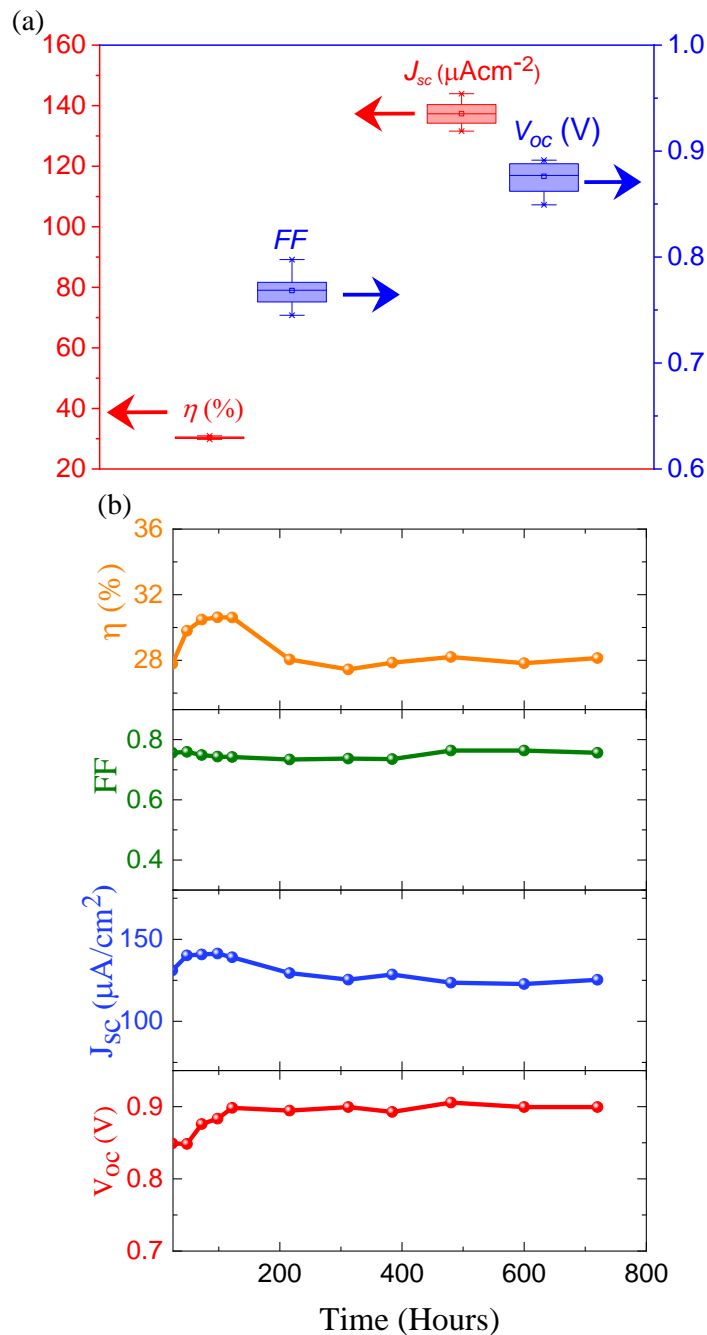


Figure 5.10 (a) Error plot for V_{oc} , J_{sc} , FF and η evaluated by measuring 14 DSCs under 1000 lux LED illumination and (b) stability test under 1000 lux LED illumination up to 700 hours for DSCs fabricated using co-sensitized (D35+XY1) dyes and $[\text{Cu}(\text{tmby})_2]^{2+/1+}$ electrolyte.

To confirm the repeatability of the photovoltaic performance, we fabricated 14 devices with best performing combination consisting of D35+XY1 co-sensitized

photoanodes and $[\text{Cu}(\text{tmby})_2]^{2+/1+}$ electrolyte containing 0.3 M LiI and evaluated the performance. **Figure 5.10 (a)** provides the error plot for various photovoltaic parameters measured under 1000 lux LED illumination. Further, we also carried out J - V measurement under standard 1000 lux illumination for a period of upto 700 hours (**Figure 5.10 (b)**). The devices used for stability were kept in open circuit condition under room light. Power conversion efficiency reached to a maximum value after 72 hours which further gets slightly reduced and then got stabilized and maintained the initial PCE by 95% even after 700 hours. V_{oc} and FF remains unchanged even after 700 hours however, slight drop in J_{sc} was observed which contributed to drop in PCE with passage of time.

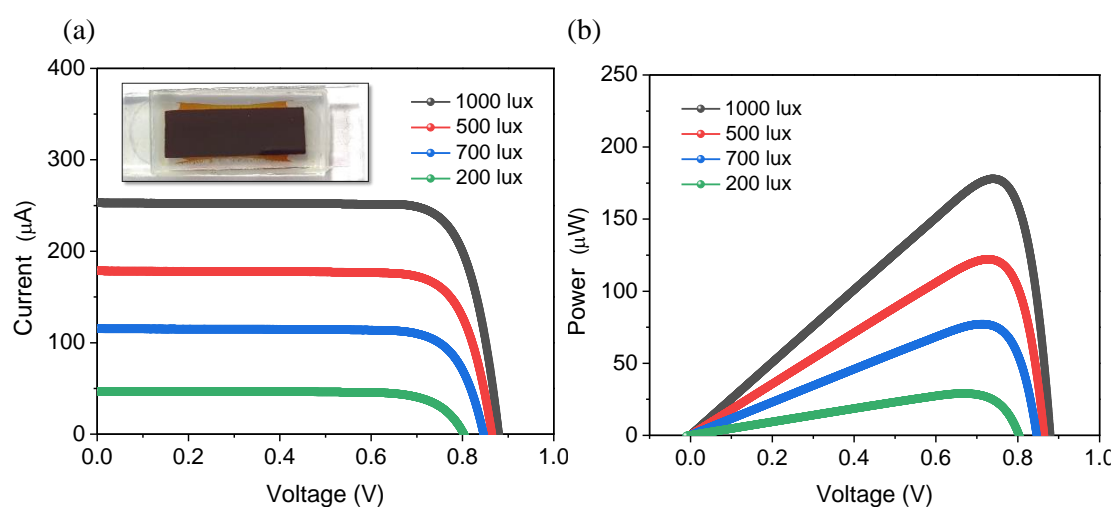


Figure 5.11 – (a) I - V characteristics and (b) P - V characteristics for DSC masterplates with an active area of 1.92 cm² under LED illumination using co-sensitized (D35+XY1) dyes and $[\text{Cu}(\text{tmby})_2]^{2+/1+}$ electrolyte. Inset: 1.92 cm² DSC.

Table 5.5 Indoor photovoltaic parameters of large area (active area 1.92 cm²) DSC masterplate with cosensitized D35+XY1 dyes under LED illumination of different intensities using $[\text{Cu}(\text{tmby})_2]^{2+/1+}$ electrolyte containing 0.3 M LiI.

Light Intensity (lux)	Input Power Density (μWcm^{-2})	Output Power (μW)	V_{oc} (mV)	I_{sc} (μA)	FF	η (%)
1000	303	177	880 ± 43	252 ± 21	0.80 ± 0.01	30.62 ± 0.12
700	192	122	865 ± 55	178 ± 49	0.79 ± 0.03	30.59 ± 0.15
500	150	77	846 ± 39	115 ± 23	0.79 ± 0.01	26.79 ± 0.12
200	65	29	803 ± 16	47 ± 09	0.77 ± 0.07	23.24 ± 0.14

To meet the power requirements of various IoT applications such as sensors and actuators, we require devices of larger active area. We optimized indoor DSC masterplates

of 1.92 cm² active area. The current-voltage and power curve for DSC masterplates with an active area of 1.92 cm² under LED illumination of variable intensities ranging from 1000 lux to 200 lux are given in **Figure 5.11** and the photovoltaic parameters are summarized in **Table 5.5**. With proper optimizations, we were able to fabricate large area DSC master plates without performance drop. Under 1000 LED lux illumination, DSC master plates produced 177 μW power with an efficiency of 30.62±0.12%. Even under a lower illumination intensity of 200 lux, it produced a power output of 29 μW which is enough to drive many of the IoT devices autonomous free of batteries. As of today, our results are the highest reported performance under LED illumination for DSCs. Notably, the highest power conversion efficiency under LED illumination is 30.2 % which is recently reported by Gratzel and coworker.¹¹ Further optimizations are under progress and we expect to realize efficiency >35% through innovative device engineering strategies.

5.5. Conclusions

In conclusion, we introduced a new additive lithium Iodide (LiI) in [Cu(tmby)]^{2+/1+} electrolyte formulation which showed promising results under indoor illumination. Under one sun illumination, DSCs with XY1 dye and [Cu(tmby)]^{2+/1+} electrolyte without LiI showed the maximum performance realizing a PCE of 9.41±0.13%. We observed a reduction in power conversion efficiency with increase in LiI concentration under 1 sun (100 mW/cm²) illumination; however, a reverse in photovoltaic trend was observed under 0.1 sun illumination (10 mW/cm²), which indicated its potential under indoor/artificial light sources. The origin of photovoltaic parameters as a function of LiI concentration was discussed using various perturbation tools such as current transient, charge extraction, OCVD and EIS measurements. With increase in LiI concentration conduction band of TiO₂ shifted to more positive potential while lifetime of electron in TiO₂ improved simultaneously. Under standard 1000 lux LED illumination, DSCs fabricated with XY1 sensitizer alone, used with an electrolyte formulation containing 0.3 M LiI realized maximum efficiency of 25.88±0.10%. To evaluate the difference in photovoltaic performance by changing the lithium salts, we fabricated devices using both LiTFSI and LiI keeping the rest of the parameters the same. DSC with standard LiTFSI showed a maximum power conversion efficiency of 9.43±0.17%, which is 64% lesser than the efficiency delivered by DSCs employing 0.3 M LiI (25.88±0.10%). The superiority of LiI

over LiTFSI under indoor light illumination is mainly attributed to the longer lifetime of electrons in TiO₂. To improve the power conversion efficiency of DSCs using the newly developed electrolyte composition, we co-sensitized XY1 with D35 sensitizer which further enhanced the power conversion efficiency to 30.6±0.11% under 1000 lux LED illumination and maintained the initial efficiency even after 700 hours. Further optimization of DSC masterplates were done through an active area of 1.92 cm² and it generated a power output of 177 μW maintaining the power conversion efficiency of 30.6±0.11% under standard 1000 lux LED illumination which proves its immense potential for commercialization leading to the development of self-powered smart devices and applications.

5.6. References

- 1 IEA, *Int. Energy Agency*.
- 2 B. Charan Patel, R. Shankar Tripathi and N. Goel, *Int. J. Comput. Appl. Technol. Res.*, 2021, **10**, 119–122.
- 3 E. T. Efaz, M. M. Rhaman, S. Al Imam, K. L. Bashar, F. Kabir, M. E. Mourtaza, S. N. Sakib and F. A. Mozahid, *Eng. Res. Express*, 2021, **3**, 032001.
- 4 T. G. Allen, J. Bullock, X. Yang, A. Javey and S. De Wolf, *Nat. Energy* 2019 **411**, 2019, **4**, 914–928.
- 5 J. K. W. Ho, H. Yin and S. K. So, *J. Mater. Chem. A*, 2020, **8**, 1717–1723.
- 6 M. Li, F. Igbari, Z. Wang and L. Liao, *Adv. Energy Mater.*, 2020, **10**, 2000641.
- 7 H. Michaels, I. Benesperi and M. Freitag, *Chem. Sci.*, 2021, **12**, 5002–5015.
- 8 B. O'Regan and M. Grätzel, *Nature*, 1991, **353**, 737–740.
- 9 I. Benesperi, H. Michaels and M. Freitag, *J. Mater. Chem. C*, 2018, **6**, 11903–11942.
- 10 A. Yella, H.-W. Lee, H. N. Tsao, C. Yi, A. K. Chandiran, M. K. Nazeeruddin, E. W.-G. Diao, C.-Y. Yeh, S. M. Zakeeruddin and M. Gratzel, *Science (80-.)*, 2011, **334**, 629–634.
- 11 Y. Ren, D. Zhang, J. Suo, Y. Cao, F. T. Eickemeyer, N. Vlachopoulos, S. M. Zakeeruddin, A. Hagfeldt and M. Grätzel, *Nature*, 2022, 1–6.
- 12 D. Zhang, M. Stojanovic, Y. Ren, Y. Cao, F. T. Eickemeyer, E. Socie, N. Vlachopoulos, J. E. Moser, S. M. Zakeeruddin, A. Hagfeldt and M. Grätzel, *Nat. Commun.*, 2021, **12**, 1–10.
- 13 K. S. Srivishnu, S. Prasanthkumar and L. Giribabu, *Mater. Adv.*, 2021, **2**, 1229–

- 1247.
- 14 A. Colombo, C. Dragonetti, D. Roberto and F. Fagnani, *Molecules*, 2021, **26**, 194.
- 15 J. Conradie, *Electrochem. commun.*, , DOI:10.1016/j.elecom.2021.107182.
- 16 P. Ferdowsi, Y. Saygili, S. M. Zakeeruddin, J. Mokhtari, M. Grätzel, A. Hagfeldt and L. Kavan, *Electrochim. Acta*, 2018, **265**, 194–201.
- 17 A. Colombo, C. Dragonetti, F. Fagnani, D. Roberto, F. Melchiorre and P. Biagini, *Dalt. Trans.*, 2019, **48**, 9818–9823.
- 18 Y. Saygili, M. Söderberg, N. Pellet, F. Giordano, Y. Cao, A. B. Muñoz-García, S. M. Zakeeruddin, N. Vlachopoulos, M. Pavone, G. Boschloo, L. Kavan, J.-E. Moser, M. Grätzel, A. Hagfeldt and M. Freitag, *J. Am. Chem. Soc.*, 2016, **138**, 15087–15096.
- 19 S. O. Furer, R. A. Milhuisen, M. K. Kashif, S. R. Raga, S. S. Acharya, C. Forsyth, M. Liu, L. Frazer, N. W. Duffy, C. A. Ohlin, A. M. Funston, Y. Tachibana and U. Bach, *Adv. Energy Mater.*, 2020, **10**, 2002067.
- 20 H. Rui, J. Shen, Z. Yu, L. Li, H. Han and L. Sun, *Angew. Chemie*, 2021, **133**, 16292–16299.
- 21 M. Freitag, J. Teuscher, Y. Saygili, X. Zhang, F. Giordano, P. Liska, J. Hua, S. M. Zakeeruddin, J.-E. Moser, M. Grätzel and A. Hagfeldt, *Nat. Photonics*, 2017, **11**, 372–378.
- 22 S. C. Pradhan and S. Soman, *Results in Surfaces and Interfaces*, 2021, **5**, 100030–100035.
- 23 S. Ahmad, J.-H. Yum, Z. Xianxi, M. Grätzel, H.-J. Butt and M. K. Nazeeruddin, *J. Mater. Chem.*, 2010, **20**, 1654–1658.
- 24 J. Kwon and J. H. Park, *J. Electrochem. Sci. Technol.*, 2013, **4**, 89–92.
- 25 S. Taya, S. Kuwahara, Q. Shen, T. Toyoda and K. Katayama, *RSC Adv.*, 2014, **4**, 21517–21520.
- 26 S. Zhang, M. Yanagida, X. Yang and L. Han, *Appl. Phys. Express*, 2011, **4**, 042301.
- 27 G. Boschloo and A. Hagfeldt, *Acc. Chem. Res.*, , DOI:10.1021/ar900138m.
- 28 Y. Liu, A. Hagfeldt, X. R. Xiao and S. E. Lindquist, *Sol. Energy Mater. Sol. Cells*, 1998, **55**, 267–281.
- 29 J. Velore, S. Chandra Pradhan, T. W. Hamann, A. Hagfeldt, K. N. N. Unni and S. Soman, *ACS Appl. Energy Mater.*, 2022, **5**, 2647–2654.
- 30 J. Halme, P. Vahermaa, K. Miettunen and P. Lund, *Adv. Mater.*, 2010, **22**, 210–234.

-
- 31 F. Fabregat-Santiago, G. Garcia-Belmonte, I. Mora-Seró and J. Bisquert, *Phys. Chem. Chem. Phys.*, 2011, **13**, 9083–9118.
- 32 J. Wu, Z. Lan, J. Lin, M. Huang, Y. Huang, L. Fan, G. Luo, Y. Lin, Y. Xie and Y. Wei, *Chem. Soc. Rev.*, 2017, **46**, 5975–6023.
- 33 S. G. Hashmi, G. G. Sonai, H. Iftikhar, P. D. Lund and A. F. Nogueira, *Semicond. Sci. Technol.*, 2019, **34**, 105001.
- 34 R. Li, D. Liu, D. Zhou, Y. Shi, Y. Wang and P. Wang, *Energy Environ. Sci.*, 2010, **3**, 1765.
- 35 S. R. Raga, E. M. Barea and F. Fabregat-Santiago, *J. Phys. Chem. Lett.*, 2012, **3**, 1629–1634.
- 36 S. Sasidharan, S. Soman, S. C. Pradhan, K. N. N. Unni, A. A. P. Mohamed, B. N. Nair and H. U. N. Saraswathy, *New J. Chem.*, 2017, **41**, 1007–1016.
- 37 A. Zaban, M. Greenshtein and J. Bisquert, *ChemPhysChem*, 2003, **4**, 859–864.
- 38 M. A. Saeed, H. C. Kang, K. Yoo, F. K. Asiam, J.-J. Lee and J. W. Shim, *Dye. Pigment.*, 2021, **194**, 109624.
- 39 J. M. Cole, G. Pepe, O. K. Al Bahri and C. B. Cooper, *Chem. Rev.*, 2019, **119**, 7279–7327.

Summary and Future Scope

Dye-sensitized Solar Cells (DSCs) are gaining popularity as one of the most promising technologies for Indoor Photovoltaics (IPV) in recent years. One of the key modifications realized in DSC contributing towards higher efficiencies under indoor illumination is by introducing new generation of copper redox electrolytes. The present thesis provides a strong foundation for fabricating highly efficient copper electrolyte based DSCs, particularly for indoor photovoltaic applications, along with providing an in-depth understanding of the interfacial charge dynamics at various interfaces in those devices. The thesis comprises of five chapters, Chapter 1 provides a brief introduction of copper electrolyte DSCs and indoor photovoltaics. To improve the photovoltaic performance of copper based DSC, a fundamental understanding exploring the gain and loss process is highly essential. In this regard Chapter-2 provides a detailed understanding through one to one comparison of DSCs fabricated using classical iodine (I^-/I_3^-), alternative cobalt $\{[Co(bpy)_3]^{3+/2+}\}$ and new generation copper $\{[Cu(dmp)_2]^{2+/1+}\}$ redox electrolytes. DSC with copper electrolyte emerged as best performing photovoltaic device owing improved transport time of electrons and longer diffusion length. However, mass transport limitation and surface or sub band gap recombination are some of the key issues associated with copper electrolyte based DSCs that needs detailed investigation. Fabrication of efficient copper-based DSCs needs new innovative materials and optimized device architectures. One such critical device engineering parameter involves the replacement of conventional TiO_2 layer with particle size of 20 with 30 nm. A detailed investigation exploring the interfacial charge dynamics of DSC with particle size of 20 with 30 nm is required for future modification of DSC. Thus in Chapter 3 we analyzed the impact of TiO_2 particle size (20 nm and 30 nm) on the photovoltaic performance of DSCs using organic D35 dye and $Cu[(tmbpy)_2]^{2+/1+}$ redox mediator. The device fabricated using 30 nm TiO_2 particles showed an improvement of 16% in PCE compared to the device fabricated with 20 nm TiO_2 particles. The collective enhancement in *LHE*, dye regeneration, and charge collection efficiency assisted in bringing higher J_{sc} , V_{oc} , *FF* and improved PCE for devices fabricated using 30 nm TiO_2 particles. Employing alternate redox mediators like copper complexes having positive redox potentials recombination is a critical issue. Recombination can be effectively prevented by efficiently covering TiO_2 surface dye molecules. In Chapter 4 we explored the role of dye coverage in regulating the recombination at the TiO_2 /electrolyte interface in DSC using organic D35 dye and $Cu[(tmbpy)_2]^{2+/1+}$ redox mediator. Here we

systematically controlled the dye coverage on TiO₂ by changing the concentration dye (0.01 mM, 0.05 mM, 0.1 mM, 0.2 mM and 0.3 mM) and investigated the role of dye coverage using various electrical and optical perturbation and pump-probe methods. Though 0.2 mM and 0.3 mM dye concentration achieved the highest dye loading, DSCs fabricated with 0.1 mM dye concentration showcased highest photovoltaic performance as it excellently arrested recombination. This shows the importance of having uniform and pin-hole free dye loading which is more important than having highest dye loading. Additive engineering in electrolyte is a powerful tool to improve photovoltaic performance. In Chapter 5 we introduced new additive, lithium iodide (LiI) in copper electrolyte based DSCs that improved the photovoltaic performance exceptionally well particularly under indoor light illumination (1000 lux LED). We achieved maximum power conversion efficiency of 30.6±0.11% under 1000 lux LED illumination. Further, DSC masterplates with an active area of 1.92 cm² generated a power output of 177 μW under 1000 lux LED illumination which proves its immense potential for commercialization leading to the development of self-powered smart devices and applications, free of batteries.

Copper electrolyte based DSCs have a promising future in the field of indoor photovoltaics. While J_{sc} has already reached an optimal value, there is still a significant room for improving the V_{oc} . It is theoretically possible to achieve voltage in the range of 1.3 to 1.4 V without compromising J_{sc} , though it has only reached maximum voltage of 1 V under 1000 lux illumination till date. An improvement in voltage can be achieved by reducing the recombination at TiO₂/electrolyte interface. One effective strategy to reduce recombination is to maintain an optimal special separation between the photoinduced electrons in TiO₂ and the oxidized species present in the electrolyte. This can be accomplished by using a blocking layer on the TiO₂ surface or by adding suitable additives to copper electrolyte. Very often, coordination of Lewis base, such as tBP, with the oxidized species of copper electrolyte can result in a reduction in overall redox potential of the electrolyte. Therefore, an alternative Lewis base that does not coordinate with the oxidized species is necessary, which at the same time controls the energetics in positive way thereby increasing the voltage as well as the net output power of the device.

In order to improve the indoor photovoltaic performance, new device architectures need to be adopted, and one such architecture with high potential is the multijunction device approach. However, the presence of holes in such devices presents a significant challenge. Holes not only block light but also create air gaps between devices, which leads to light

loss. The new architecture called hole-free, spacer-free (HF-SF) has the potential to be a breakthrough in this regard. HF-SF architecture not only eliminates holes but also reduces the amount of electrolyte in the device which results in a reduction in light absorption loss. Furthermore, the HF-SF DSC can achieve an active area to total device area $> 90\%$, which not only helps in increasing the output power but also contributes to the aesthetics of the device with lower production cost.

One of the critical parameters in terms of commercialization is the stability of the devices. To reach and achieve stability as per the commercial standard we need to replace the conventional liquid electrolyte with solid state/ quasi solid state electrolytes. Zombie DSC using copper electrolyte is also an innovative approach by slow evaporation of solution present in electrolyte that can meet the standard stability requirements. Similarly, copper based gel electrolytes can also be used as a strategy to prepare highly stable electrolyte.

Moreover, to meet the voltage and current requirements required to support the IoT indoor illuminations, we may need to interconnect the devices in serial/parallel fashion to increase the V_{oc}/J_{sc} . Here monolithic serial connection, Z-type serial connection and W-type serial connection seems to serve the purpose. Yet again serially connected DSC module can eliminate the use of voltage booster circuit in an IoT device, which will further reduce the cost of the product.

Overall, the present research conducted as part of the thesis along with the future possibilities it has presented will provide a foundation for developing innovative and sustainable alternatives to batteries, thereby contributing to a greener world.

ABSTRACT

Name of the Student: **Mr. Sourava Chandra Pradhan** Registration No.: 20EE18A39022
Faculty of Study: Engineering Sciences Year of Submission: 2023
AcSIR academic centre/CSIR Lab: CSIR-National Name of the Supervisor(s): Dr. Suraj Soman
Institute for Interdisciplinary Science and
Technology (CSIR-NIIST)
Title of the thesis: **Probing Interfacial Charge Dynamics in Dye-sensitized Solar Cells using Copper Electrolytes for Indoor Photovoltaics**

Chapter 1 provides a brief introduction of copper electrolyte-based dye-sensitized solar cells (DSCs) and indoor photovoltaics.

Chapter-2 renders a detailed comparison between DSCs fabricated using classical iodine (I/I_3^-), alternative cobalt $\{[Co(bpy)_3]^{3+/2+}\}$ and new generation copper $\{[Cu(dmp)_2]^{2+/1+}\}$ redox mediators. DSCs with $[Cu(dmp)_2]^{2+/1+}$ delivered a maximum power conversion efficiency of $6.82 \pm 0.32\%$ whereas $[Co(bpy)_3]^{3+/2+}$ and I/I_3^- based device delivered efficiencies of $4.52 \pm 0.28\%$ and $5.79 \pm 0.16\%$ respectively. To understand the origin performance variations, we carried out detailed interfacial measurements. I/I_3^- was found to be free of mass transport with an α value near to 1, while $[Cu(dmp)_2]^{2+/1+}$ was moderately affected by mass transport with an α value of 0.83 and $[Co(bpy)_3]^{3+/2+}$ was severely affected by mass transport with α value of 0.54. A negative shift in conduction band was observed for $[Co(bpy)_3]^{3+/2+}$ and $[Cu(dmp)_2]^{2+/1+}$ electrolytes with respect to I/I_3^- system. Further using $[Cu(dmp)_2]^{2+/1+}$ electrolyte we observed more recombination due lower lifetime as a result of the negative shift in conduction band as well as more recombination driving force from negative shift in conduction band. However, $[Cu(dmp)_2]^{2+/1+}$ redox mediator gave the shortest transport time among the series followed by $[Co(bpy)_3]^{3+/2+}$ and I/I_3^- . Slightly lower lifetime for $[Cu(dmp)_2]^{2+/1+}$ is compensated by the higher diffusion (L_n) coefficient and hence $[Cu(dmp)_2]^{2+/1+}$ exhibited longer diffusion length compared to $[Co(bpy)_3]^{3+/2+}$ and I/I_3^- . Longer L_n results in better charge collection efficiency which in turn results in higher J_{sc} and power conversion efficiency.

Chapter 3 provides a detailed analysis of the impact of TiO_2 particle size (20 nm and 30 nm) on the photovoltaic performance of DSCs using organic D35 dye and alternate copper redox mediator, $Cu[(tmby)_2]^{2+/1+}$. DSC photoanodes with 30 nm TiO_2 particles realized a higher power conversion efficiency (PCE) of $7.36 \pm 0.12\%$ in comparison to $6.32 \pm 0.07\%$ efficiency achieved using DSCs made with 20 nm TiO_2 particles. The improved PCE using 30 nm TiO_2 particles is associated with the enhancement in short circuit current density (J_{sc}), open-circuit potential (V_{oc}) and fill factor (FF). Furthermore, comprehensive analysis of various charge transfer processes at the interfaces in these devices reveals collective enhancement in light-harvesting, dye regeneration and charge collection efficiency that ultimately contributed towards achieving 16% improvement in PCE using 30 nm TiO_2 particles.

Chapter 4 explores the role of dye coverage on the photovoltaic parameters while used along with the new generation copper electrolyte based DSCs. Here we systematically controlled the dye coverage on TiO_2 using D35 organic dye solutions of different concentrations. Dye loading/surface coverage of dye was found to increase with the increase in dye concentrations and it reached to a saturation around 0.2 mM of D35 concentration. However, 0.1 mM was found to be an optimum dye concentration in terms of photovoltaic performance both under indoor and outdoor light illuminations. Maximum power conversion efficiency of $6.50 \pm 0.25\%$ under outdoor (100 mW/cm^2) and $10.48 \pm 0.30\%$ under indoor light (1000 lux, WW CFL) was obtained using 0.1 mM D35 dye concentration. Dark current and ideality factor (m) was also found to be minimum at 0.1 mM dye concentration. The conduction band of TiO_2 was found to shift towards positive potentials with increase in dye concentrations (0.1 mM, 0.2 mM and 0.3 mM). Likewise, lifetime was also found to increase with dye concentration, and the best lifetime was showcased by devices fabricated using 0.1 mM dye which was found to further drop at higher dye concentrations (0.2mM and 0.3mM). Electron injection, dye regeneration, charge collection and ion diffusion was found to be independent of the dye coverage.

Chapter 4 introduces a new additive, lithium iodide (LiI) in copper electrolyte DSCs that improved the photovoltaic performance exceptionally well particularly under indoor light illumination (1000 lux LED). $[Cu(tmby)_2]^{2+/1+}$ electrolyte containing LiI along with XY1 sensitizer showed a maximum PCE of 25.88% under 1000 lux warm white LED illumination whereas devices fabricated using the standard lithium bis(trifluoromethylsulphonyl)imide (LiTFSI) only showed an efficiency of 9.43%. Taking advantage of the co-sensitization approach by using XY1:D35 sensitizers, we were able to further enhance the power conversion efficiency to 30.61% under 1000 lux LED illumination. Mini-modules fabricated with an active area of 1.92 cm^2 was able to generate a power output of $177 \mu\text{W}$ which was sufficient enough to realize autonomous operation of multitude of sensors and actuators under the smart Internet of Things (IoT) network.

List of Publications

Details of Publications Emanating from the Thesis Work

Published

- (1) **Pradhan, S. C.**; Velore, J.; Hagfeldt, A.; Soman, S. Probing Photovoltaic Performance in Copper Electrolyte Dye-Sensitized Solar Cells of Variable TiO₂ Particle Size Using Comprehensive Interfacial Analysis. *J. Mater. Chem. C* **2022**, 10 (10), 3929–3936. <https://doi.org/10.1039/D1TC05803G>.
- (2) **Pradhan, S. C.**; Hagfeldt, A.; Soman, S. Resurgence of DSCs with Copper Electrolyte: A Detailed Investigation of Interfacial Charge Dynamics with Cobalt and Iodine Based Electrolytes. *J. Mater. Chem. A* **2018**, 6 (44), 22204–22214. <https://doi.org/10.1039/C8TA06948D>.

Manuscripts Submitted/Under Preparation

- (1) **Pradhan, S. C.**, Velore, J., Sruthi, M. M. Hagfeldt, A. & Soman, S. Charge recombination as function of dye concentration in copper-based Dye Sensitized Solar Cell, *manuscript under preparation*
- (2) **Pradhan, S. C.**, Velore, J., Hagfeldt, A. Unni, N. Grätzel, M. & Soman, S. Electrolyte additive engineering to improve indoor photovoltaic performance in Dye Sensitized Solar Cell, *manuscript under preparation*.
- (3) **Pradhan, S. C.**, Sruthi, M. M., Hagfeldt, A. & Soman, S. Copper Electrolyte based Dye Sensitized Solar Cell, *manuscript under preparation*.

List of Publications from Other Related Works

- (1) Velore, J.; **Pradhan, S. C.**; Hamann, T. W.; Hagfeldt, A.; Unni, K. N. N.; Soman, S. Understanding Mass Transport in Copper Electrolyte-Based Dye-Sensitized Solar Cells. *ACS Appl. Energy Mater.* **2022**, 5 (3), 2647–2654. <https://doi.org/10.1021/acsaem.1c04121>.
- (2) Sivasankaran, L.; **Pradhan, S. C.**; Mishra, R. K.; Soman, S.; Ajayaghosh, A. Role of Alkyl Groups Regulating Recombination and Mass Transport at Cobalt Electrolyte-Dye Interface in Dye Sensitized Solar Cells. *Sol. Energy* **2022**, 236 (February), 182–194. <https://doi.org/10.1016/j.solener.2022.03.001>.
- (3) Enaganti, P. K.; Soman, S.; Devan, S. S.; **Pradhan, S. C.**; Srivastava, A. K.; Pearce, J. M.; Goel, S. Dye-sensitized Solar Cells as Promising Candidates for Underwater Photovoltaic Applications. *Prog. Photovoltaics Res. Appl.* **2022**, No. December 2021, 1–8. <https://doi.org/10.1002/pip.3535>.
- (4) **Pradhan, S. C.**; Soman, S. Effect of Thickness on Charge Transfer Properties of Conductive Polymer Based PEDOT Counter Electrodes in DSSC. *Results in Surfaces and Interfaces* **2021**, 5 (October), 100030. <https://doi.org/10.1016/j.rsurfi.2021.100030>.
- (5) Haridas, R.; Velore, J.; **Pradhan, S. C.**; Vindhyasarumi, A.; Yoosaf, K.; Soman, S.; Unni, K. N. N.; Ajayaghosh, A. Indoor Light-Harvesting Dye-Sensitized Solar Cells Surpassing 30% Efficiency without Co-Sensitizers. *Mater. Adv.* **2021**, 2 (23), 7773–7787. <https://doi.org/10.1039/D1MA00829C>.
- (6) Maniarasu, S.; Karthikeyan, V.; Korukonda, T. B.; **Pradhan, S. C.**; Soman, S.; Ramasamy, E.; Veerappan, G. Ambient Processed Perovskite Sensitized Porous TiO₂ Nanorods for Highly Efficient and Stable Perovskite Solar Cells. *J. Alloys Compd.* **2021**, 884, 161061. <https://doi.org/10.1016/j.jallcom.2021.161061>.
- (7) Sasidharan, S.; Jagadeesh, A.; **Pradhan, S. C.**; Nair, B. N.; Azeez Peer Mohamed, A.; Narayanan Unni, K. N.; Soman, S.; Nair Saraswathy Hareesh, U. ZnO Hierarchical Structures as Sacrificial Inclusions for Enhanced Performance under Full Sun and

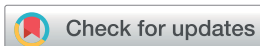
- Indoor Light in Bifacial Dye Sensitized Solar Cells. *Sol. Energy* **2021**, 226, 214–224. <https://doi.org/10.1016/j.solener.2021.08.030>.
- (8) Yoosuf, M.; **Pradhan, S. C.**; Sruthi, M. M.; Soman, S.; Gopidas, K. R. Propellar Shaped Triple Bond Rigidified D-A- π -A Triphenylamine Dye as Back Electron Interceptor in Iodine and Cobalt Electrolyte DSSCs under Full Sun and Indoor Light. *Sol. Energy* **2021**, 216, 151–163. <https://doi.org/10.1016/j.solener.2021.01.001>.
- (9) Nitha, P. R.; Jayadev, V.; **Pradhan, S. C.**; Divya, V. V.; Suresh, C. H.; John, J.; Soman, S.; Ajayaghosh, A. Regulating Back Electron Transfer through Donor and Π -Spacer Alterations in Benzothieno[3,2-b]Indole-based Dye-sensitized Solar Cells. *Chem. – An Asian J.* **2020**, 15 (21), 3503–3512. <https://doi.org/10.1002/asia.202000808>.
- (10) Sasidharan, S.; **Pradhan, S. C.**; Jagadeesh, A.; Nair, B. N.; Mohamed, A. A. P.; K. N., N. U.; Soman, S.; Hareesh, U. N. S. Bifacial Dye-Sensitized Solar Cells with Enhanced Light Scattering and Improved Power Conversion Efficiency under Full Sun and Indoor Light Conditions. *ACS Appl. Energy Mater.* **2020**, 3 (12), 12584–12595. <https://doi.org/10.1021/acsaem.0c02500>.
- (11) Santhini, P. V; V., J.; **Pradhan, S. C.**; Lingamoorthy, S.; P. R., N.; M. V., C.; Mishra, R. K.; K. N., N. U.; John, J.; Soman, S. Indolo[3,2- b]Indole Donor-Based D- π -A Dyes for DSCs: Investigating the Role of π -Spacers towards Recombination. *New J. Chem.* **2019**, 43 (2), 862–873. <https://doi.org/10.1039/C8NJ04561E>.
- (12) Yoosuf, M.; **Pradhan, S. C.**; Soman, S.; Gopidas, K. R. Triple Bond Rigidified Anthracene-Triphenylamine Sensitizers for Dye-Sensitized Solar Cells. *Sol. Energy* **2019**, 188, 55–65. <https://doi.org/10.1016/j.solener.2019.05.051>.
- (13) Gokul, G.; **Pradhan, S. C.**; Soman, S. Dye-Sensitized Solar Cells as Potential Candidate for Indoor/Diffused Light Harvesting Applications: From BIPV to Self-Powered IoTs. In *Advances in Solar Energy Research*; Springer, Singapore, **2019**; pp 281–316. https://doi.org/10.1007/978-981-13-3302-6_9.
- (14) Vinayak, M. V.; Yoosuf, M.; **Pradhan, S. C.**; Lakshmykanth, T. M.; Soman, S.; Gopidas, K. R. A Detailed Evaluation of Charge Recombination Dynamics in Dye Solar

- Cells Based on Starburst Triphenylamine Dyes. *Sustain. Energy Fuels* **2018**, 2 (1), 303–314. <https://doi.org/10.1039/C7SE00257B>.
- (15) Soman, S.; **Pradhan, S. C.**; Yoosuf, M.; Vinayak, M. V; Lingamoorthy, S.; Gopidas, K. R. Probing Recombination Mechanism and Realization of Marcus Normal Region Behavior in DSSCs Employing Cobalt Electrolytes and Triphenylamine Dyes. *J. Phys. Chem. C* **2018**, 122 (25), 14113–14127. <https://doi.org/10.1021/acs.jpcc.8b01325>.
- (16) Hemavathi, B.; Jayadev, V.; **Pradhan, S. C.**; Gokul, G.; Jagadish, K.; Chandrashekhara, G. K.; Ramamurthy, P. C.; Pai, R. K.; Narayanan Unni, K. N.; Ahipa, T. N.; Soman, S.; Geetha Balakrishna, R. Aggregation Induced Light Harvesting of Molecularly Engineered D-A- π -A Carbazole Dyes for Dye-Sensitized Solar Cells. *Sol. Energy* **2018**, 174, 1085–1096. <https://doi.org/10.1016/j.solener.2018.09.073>.
- (17) Nikolaou, V.; Charisiadis, A.; Chalkiadaki, S.; Alexandropoulos, I.; **Pradhan, S. C.**; Soman, S.; Panda, M. K.; Coutsolelos, A. G. Enhancement of the Photovoltaic Performance in D 3 A Porphyrin-Based DSCs by Incorporating an Electron Withdrawing Triazole Spacer. *Polyhedron* **2018**, 140, 9–18. <https://doi.org/10.1016/j.poly.2017.09.024>.
- (18) Sasidharan, S.; Soman, S.; **Pradhan, S. C.**; Unni, K. N. N.; Mohamed, A. A. P.; Nair, B. N.; Saraswathy, H. U. N. Fine Tuning of Compact ZnO Blocking Layers for Enhanced Photovoltaic Performance in ZnO Based DSSCs: A Detailed Insight Using β Recombination, EIS, OCVD and IMVS Techniques. *New J. Chem.* **2017**, 41 (3), 1007–1016. <https://doi.org/10.1039/C6NJ03098J>.

List of Conference Presentations

- (1) Oral presentation on “Comprehensive analysis of Copper based Dye Sensitized Solar Cell consisting of TiO₂ photo anode with particle size of 20 nm and 30 nm” in National Webinar on Recent Advances in the Physics of Materials (RAPM-2021), December 9-10, 2021.
- (2) Poster presentation on “Effect of thickness on charge transfer properties of conductive polymer based PEDOT counter electrode in DSSC” in Solar-Power-Tech International Conference – SPTech 21, July 5-8, 2021.
- (3) Oral presentation on “Comprehensive interfacial analysis probing the role of dye and TiO₂ in regulating the performance of dye cells” in 5th International Conference on Nanoscience and Nanotechnology (ICONN19) held at SRM University Chennai, 27-19 Feb, 2019.
- (4) Poster presentation on “Investigating the role of PEDOT thickness in determining photovoltaic performance in DSSC” in International Conference on Optoelectronics and Nano Materials for Advanced technology (icONMAT 2019) held at Cochin University of Science and Technology, Kochi, India in January 2-5, 2019.

SCI Publications



Cite this: *J. Mater. Chem. A*, 2022, 10, 1596

DOI: 10.1039/d1ta90272e

rsc.li/materials-a

Correction: Resurgence of DSCs with copper electrolyte: a detailed investigation of interfacial charge dynamics with cobalt and iodine based electrolytes

Sourava C. Pradhan,^{ac} Anders Hagfeldt^b and Suraj Soman^{*ac}

Correction for 'Resurgence of DSCs with copper electrolyte: a detailed investigation of interfacial charge dynamics with cobalt and iodine based electrolytes' by Sourava C. Pradhan *et al.*, *J. Mater. Chem. A*, 2018, 6, 22204–22214, DOI: 10.1039/C8TA06948D.

The authors regret that one of the affiliations (affiliation *c*) was incorrectly shown in the original manuscript. Affiliation *c* has been amended. The correct affiliations are as shown here.

The Royal Society of Chemistry apologises for these errors and any consequent inconvenience to authors and readers.

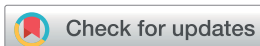
^aPhotosciences and Photonics Section, Chemical Sciences and Technology Division, CSIR-National Institute for Interdisciplinary Science and Technology (CSIR-NIIST), Thiruvananthapuram, 695019, India. E-mail: suraj@niist.res.in; suraj.csir@gmail.com

^bLaboratory of Photomolecular Science, Institute of Chemical Sciences & Engineering, Ecole Polytechnique Federale de Lausanne, Lausanne 1015, Switzerland

^cAcademy of Scientific and Innovative Research (AcSIR), Ghaziabad-201002, India



PAPER

Cite this: *J. Mater. Chem. A*, 2018, 6, 22204

Resurgence of DSCs with copper electrolyte: a detailed investigation of interfacial charge dynamics with cobalt and iodine based electrolytes†

Sourava C. Pradhan,^{ac} Anders Hagfeldt^{id}^b and Suraj Soman^{id}^{*ac}

Deploying earth abundant copper as a redox mediator in dye-sensitized solar cells (DSCs) has been found to be a very promising strategy to achieve higher photovoltage and power conversion efficiencies in full sun (100 mW cm⁻²) and in low/diffuse light conditions. Achieving higher photovoltage without compromising photocurrent helped copper electrolyte attract considerable attention among alternate electrolytes currently employed in DSCs. The very small reorganization energy between Cu(I) and Cu(II) and small molecular size helped copper achieve unit regeneration efficiency, with a driving force as low as 100 mV and a high diffusion coefficient (D_n), leading to better diffusion length (L_n) and charge collection efficiency (η_{cc}). Mass transport issues were also found to be improved for copper electrolytes in comparison with cobalt electrolytes. As it is inert to silver and other electrical contacts used in DSCs and possesses higher mobility even in solid state, copper-based electrolyte is a promising candidate to spearhead the commercialization of dye solar technology. In this regard, a detailed evaluation of internal electron transfer dynamics is highly essential to understand the limiting processes in these devices. In the present study, we performed a comparison between copper, cobalt and iodine electrolytes using the same dye (LEG4), semiconductor (TiO₂) and additive concentrations to understand in detail the charge transfer processes leading to higher photoconversion efficiencies and also probe the various deleterious processes taking place in copper devices that provide opportunities to further improve its performance in future.

Received 18th July 2018
Accepted 28th August 2018

DOI: 10.1039/c8ta06948d

rsc.li/materials-a

Introduction

Dye-sensitized solar cells (DSCs) have allured the photovoltaic community since their invention by Brian O'Regan and Michael Grätzel due to their cost effectiveness, ease of fabrication, and aesthetics. Power conversion efficiencies above 14% have already been achieved under full sun AM 1.5G irradiation using DSCs.¹ Recently, Michael Grätzel and Anders Hagfeldt successfully showcased this solar technology as superior in

comparison with all the existing first and second generation technologies for indoor light harvesting applications, delivering an efficiency of 32% (1000 lux, CFL), thus causing a resurgence in efforts of commercializing dye-sensitized solar cells.^{2,3} Semiconductor, dye and electrolyte are the three major components of DSCs. The dye absorbs light and the excited electrons are injected into the semiconductor. Then, the oxidized dye is regenerated by the redox electrolyte. To cater to the needs of industry for commercialization of DSCs, there is a great demand to develop electrolytes that are efficient and non-corrosive towards current collectors used in modules/panels and capable of delivering more voltage, which is a pre-requisite for the smooth functioning of low power energy harvesting circuits used in the Internet of Things (IoT) domain. Iodide/triiodide (I^-/I_3^-) electrolyte has been the most successful redox electrolyte in DSCs till date. The success of I^-/I_3^- redox couple is mainly attributed to its slow recombination, fast regeneration and high solubility. Unfortunately, the mechanism involving I^-/I_3^- is still unclear, which obscures the understanding of the fundamental processes. Another major drawback of I^-/I_3^- is the requirement of large driving force for regeneration, which prevents attainment of higher photovoltage.

^aPhotosciences and Photonics Section, Chemical Sciences and Technology Division, CSIR-National Institute for Interdisciplinary Science and Technology (CSIR-NIIST), Thiruvananthapuram 695019, India. E-mail: suraj@niist.res.in; suraj.csir@gmail.com

^bLaboratory of Photomolecular Science, Institute of Chemical Sciences & Engineering, Ecole Polytechnique Federale de Lausanne, Lausanne 1015, Switzerland

^cAcademy of Scientific and Innovative Research (AcSIR), CSIR-NIIST Campus, Thiruvananthapuram 695019, India

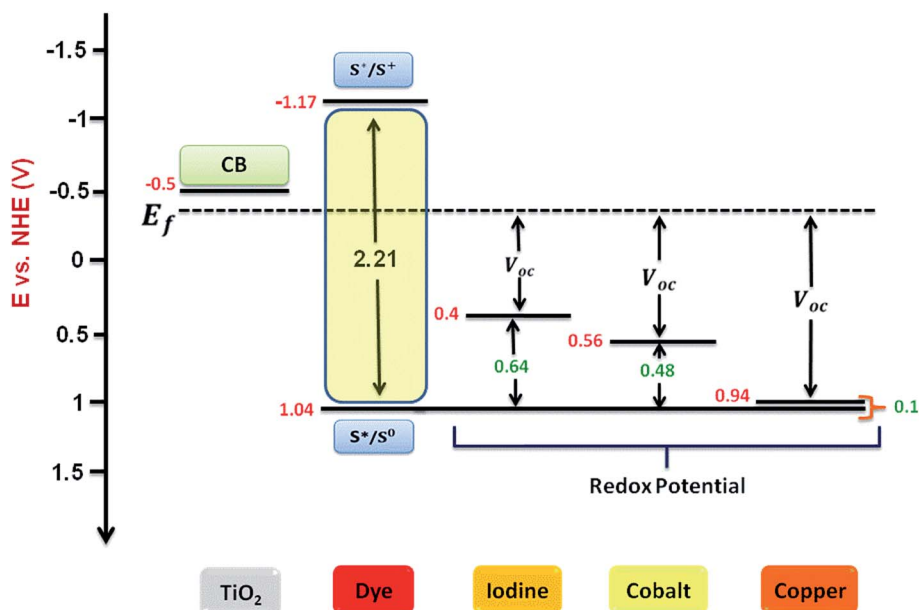
† Electronic supplementary information (ESI) available: Tabulated $J-V$ data for lower light intensities, dark current obtained from EIS and Nyquist plot for I^-/I_3^- , $[Co(bpy)_3]^{2+/3+}$ and $[Cu(dmp)]_2^{1+/2+}$ electrolytes at a constant current of 1.8 mA, Bode plot, equivalent circuit used for fitting the EIS data, Nyquist plots obtained for IMVS and IMPS and current transient measurements are given in the supporting information. See DOI: 10.1039/c8ta06948d

To circumvent the issues related to the conventional I^-/I_3^- electrolyte, metal complex based redox mediators were introduced as a viable option.⁴⁻⁶ Among these, cobalt-based redox couples occupy a prominent position. Cobalt electrolyte offers flexibility to precisely tune the redox potential to match the dye energetics by varying the ligands surrounding the metal center and also by introducing electron donating or withdrawing substituents to the ligands. It was successfully proved to be the best electrolyte in combination with organic dyes to achieve higher voltage and efficiency. Although cobalt electrolyte is employed in all the highly efficient DSCs reported in literature, it is prone to high recombination coupled with mass transport issues as a result of bulky polypyridyl ligands, which are not yet completely solved.

Recently, the realization of the potential of using earth abundant copper metal complexes as electrolytes has rejuvenated DSC research. Being a metal complex, it allows fine tuning of the redox potential by judicious substitution of peripheral ligands. In addition, the low cost and low toxicity of these earth abundant materials pave the way for commercialization of DSCs. Copper redox electrolyte [Cu(I)/(II)] was first used by Fukuzumi *et al.*, giving an efficiency of 1.4% using bis(2,9-dimethyl-1,10-phenanthroline) Cu(I)/(II) [Cu(dmp)₂]^{1+/2+} and N719 dye in 1 sun as well as improved performance of 2.2% in low-light intensities ($\sim 20 \text{ mW cm}^{-2}$).⁷ A few years later, in 2011, Wang *et al.* reported an improved efficiency of 7% at 100 mW cm^{-2} and 8.3% at 23 mW cm^{-2} in AM 1.5G light employing [Cu(dmp)₂]^{1+/2+} with C218 organic dye.⁸ This was followed by the breakthrough contribution from Freitag *et al.* where efficiency of above 10% was reported using new copper based redox shuttle at 100 mW cm^{-2} in AM 1.5G light.⁹ Modified copper electrolytes employing substituted ligands [Cu(I) (II)/bpye and Cu(I) (II)/dmbp] were successfully employed with LEG4 and Y123

dyes, surpassing the record 10% efficiency.⁴¹ By employing a “cocktail” organic dye mixture of D35 and XY1 along with Cu(I) (II)/(tmbp) as the redox shuttle, Hagfeldt and Grätzel achieved a very high open circuit photovoltage of 1.1 V, resulting in efficiency of 11.3% in AM 1.5G light and 28.9% under 1000 lux (indoor CFL illumination), corresponding to a power output of $88.5 \mu\text{W cm}^{-2}$.³ Earlier this year, the same group came up with a new modified architecture for copper based electrolyte completely devoid of spacer, leading to a record PCE of 13.1% under standard AM 1.5G simulated light and 32% in artificial indoor light (Osram 1000 lux 930 warm white fluorescent tube light), giving power output of $283 \mu\text{W cm}^{-2}$ using an active area of 2.80 cm^2 .² The amount of power generated even in such a small area is sufficient to make electronic devices completely autonomous, thus opening up a wide area of applications in self powered e-readers, tablets and IoT-related applications.

Copper redox mediators are perceived to be responsible for this paradigm shift in DSC research. In the past few years, unprecedented progress in the area of dye cells has been achieved by employing copper electrolytes in full sunlight and indoor/lowlight/diffused light conditions. To further improve the performance of DSCs employing copper-based electrolytes and to scale up such DSCs to commercial manufacturing scale, a more extensive understanding of internal charge transfer dynamics and evaluation of the limiting processes are required. In this regard, the present contribution involves a deeper perception into the influence of copper electrolyte on various charge transfer processes in DSCs in comparison with existing DSCs employing iodide/triiodide and cobalt electrolytes. For direct comparison, we employed the same dye (LEG4), similar electrode materials, identical device architecture and uniform electrolyte composition for all the three electrolytes to achieve uniform diffusion of the oxidized species in all the three



Scheme 1 Representation of energetics of TiO_2 semiconductor, LEG4 dye and three different electrolytes (I^-/I_3^- , $[\text{Co}(\text{bpy})_3]^{2+/3+}$ and $[\text{Cu}(\text{dmp})_2]^{1+/2+}$) employed in the present study.

systems. Schematic representation of energetics of various components employed in the present study is given in Scheme 1.

Experimental section

General methods

All chemicals were purchased from Sigma-Aldrich unless otherwise noted. LEG4, and cobalt and copper electrolytes were obtained from Dyenamo AB (Stockholm, Sweden).

Solar cell fabrication

First, the working electrodes of $2 \times 2 \text{ cm}^2$ FTO (Tec15, GreatCell Solar) glass were cleaned by sonication with soap solution, accompanied by delicate rubbing in running water and followed by sonication in Millipore water and sonication in IPA and acetone for 15 minutes, sequentially, with each step succeeded by UV- O_3 treatment. Then, the substrates were immersed in 40 mM aqueous TiCl_4 solution for 30 minutes at 70°C and annealed at 500°C for 30 minutes. The mesoporous TiO_2 (30 nm particles, Dyenamo) layer was deposited by doctor blading using of a 0.3 cm^2 gasket on mode using 3M scotch tape followed by 100°C annealing for 10 minutes. A TiO_2 scattering layer (250 nm particles) was coated over the transparent layer, followed by programmed heating at 325°C for 15 min, 375°C for 15 min, 450°C for 15 min and 500°C for 30 minutes. Thickness of the TiO_2 (active layer + scattering layer) film was measured using profilometer and was found to be $12 \pm 03 \mu\text{m}$. The post-blocking layer was subsequently deposited by heating the electrodes in 40 mM TiCl_4 solution for 30 min at 70°C , succeeded by annealing at 500°C for 30 min. Cooling of the sintered photoanodes to 70°C was accompanied by immersion in LEG4 dye (Dyenamo) solution in 1 : 1 acetonitrile *tert*-butanol (0.2 mM) mixture; then, the photoanodes were kept undisturbed overnight at room temperature. The photoanodes were then rinsed in acetonitrile to remove excess dye. Counter electrodes were prepared by drilling FTO (TEC8, GreatCell Solar) glass substrates, which were then cleansed using soap solution, Millipore water, and ethanol, sequentially, for 45 min each, followed by UV- O_3 treatment. Preparation of PEDOT electrode involved electropolymerisation of 3,4-ethylene dioxathiophene (EDOT) from a micellar aqueous solution of 0.1 M sodium dodecyl sulfate (SDS) and 0.01 M EDOT. Solar cells were assembled with an electrochemically deposited poly(3,4-ethylene dioxathiophene) (PEDOT) counter electrode (TEC8, GreatCell Solar) using a $30 \mu\text{m}$ -thick thermoplastic Surlyn frame. The predrilled holes were sealed using a coverslip immediately after introduction of electrolyte. The I^-/I_3^- electrolyte was obtained from GreatCell Solar and contained 0.1 M lithium iodide and 0.5 M 4-*tert*-butylpyridine with 0.5 M 1-butyl-3-methylimidazolium iodide, 0.1 M guanidine thiocyanate and iodine in acetonitrile and valeronitrile mixed solvent. The composition of $[\text{Co}(\text{bpy})_3]^{2+/3+}$ electrolyte was 0.22 M $[\text{Co}(\text{bpy})_3(\text{PF}_6)_2]$, 0.05 M $[\text{Co}(\text{bpy})_3(\text{PF}_6)_3]$, 0.1 M LiTFSI, and 0.5 M *tert*-butylpyridine in acetonitrile. The $[\text{Cu}(\text{dmp})_2]^{1+/2+}$ electrolyte comprised 0.20 M $[\text{Cu}(\text{dmp})]\text{TFSI}$, 0.04 M $[\text{Cu}(\text{dmp})_2]$

TFSI Cl, 0.1 M LiTFSI, and 0.5 M 4-*tert*-butylpyridine in acetonitrile.

Solar cell characterization

Measurements of photocurrent voltage (J - V) characteristics of the devices were performed using a solar simulator Oriel (Model PVIV-94043A) Class-AAA solar simulator, accompanied by a Keithley E 2400 source meter providing light at an intensity of 100 mW cm^{-2} with AM 1.5 G spectral distribution, which was calibrated using a certified reference solar cell. Circular black masks of area 0.18 cm^2 (smaller than the active area) were used during J - V measurements to minimize the contribution of light falling outside the active area. Measurements of incident photon-to-current conversion efficiency (IPCE) of devices were performed under DC mode using a 250 W xenon lamp integrated with a Newport monochromator and a potentiostat, which was calibrated using a certified reference solar cell. Current transient measurements were performed under AM 1.5G illumination. The lamp was switched on and off manually, and the photocurrent response was recorded using Autolab PGSTAT 302N in potentiostatic mode by applying 0 V across the device.

Electrochemical impedance spectroscopy (EIS) was performed using an Autolab (PGSTAT 302N) workstation equipped with FRA under forward bias in dark. Measurements were conducted in a frequency range from 100 mHz to 100 kHz with perturbation of 10 mV. Forward bias ranges for I^-/I_3^- , $[\text{Co}(\text{bpy})_3]^{2+/3+}$ and $[\text{Cu}(\text{dmp})_2]^{1+/2+}$ systems were selected, where almost the same dark current was flowing in all the systems (Fig. S2, ESI †). NOVA1.11 interface software was used for performing measurements as well as fitting the impedance plots. Intensity-modulated photovoltage spectroscopy (IMVS) and intensity-modulated photocurrent spectroscopy (IMPS) measurements were performed using an electrochemical workstation (PGSTAT 302N) equipped with an FRA and LED driver to drive an array of red LEDs (627 nm, Thorlab). The intensity of the LED was varied by providing different currents. LED intensity was measured using a certified photo-detector supplied by ThorLab. Cell responses were analyzed in the frequency range from 0.1 Hz to 1 kHz. Amplitude of sinusoidal modulation for IMVS and IMPS measurements was 10% of the steady light.

Results and discussion

Photovoltaic performance analysis

Current density-voltage (J - V) characteristics were measured under 100 mW cm^{-2} and AM 1.5G illumination for LEG4 sensitized solar cells using I^-/I_3^- , $[\text{Co}(\text{bpy})_3]^{2+/3+}$ and $[\text{Cu}(\text{dmp})_2]^{1+/2+}$ redox electrolytes, as shown in Fig. 1; the results are summarized in Table 1. I^-/I_3^- system showed a power conversion efficiency of 5.79% with an open circuit voltage (V_{oc}), short circuit current density (J_{sc}) and fill factor (FF) of $783 \pm 26 \text{ mV}$, $12.28 \pm 0.71 \text{ mA cm}^{-2}$, and 0.60 ± 0.01 , respectively. Under similar conditions, $[\text{Co}(\text{bpy})_3]^{2+/3+}$ delivered a V_{oc} of $868 \pm 12 \text{ mV}$, J_{sc} of $7.42 \pm 0.18 \text{ mA cm}^{-2}$, and FF of 0.7 ± 0.02 ,

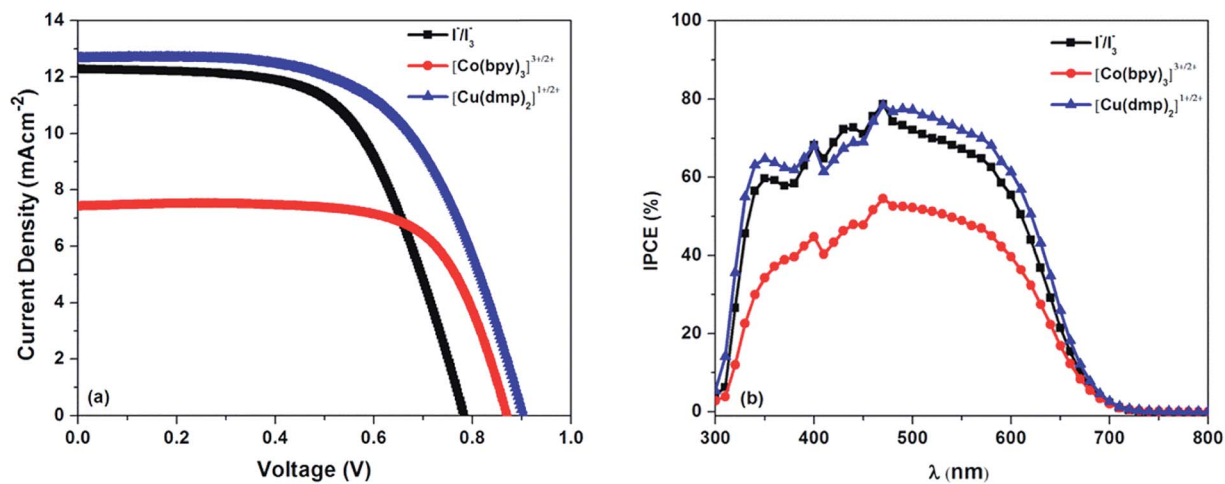


Fig. 1 (a) Current density versus potential (J - V) characteristic curves and (b) IPCE of I^-/I_3^- , $[Co(bpy)_3]^{2+/3+}$ and $[Cu(dmp)_2]^{1+/2+}$ electrolytes with LEG4 dye measured under 100 mW cm^{-2} and AM 1.5G illumination.

Table 1 Tabulated current–voltage characteristics of I^-/I_3^- , $[Co(bpy)_3]^{2+/3+}$ and $[Cu(dmp)_2]^{1+/2+}$ electrolyte with LEG4 dye measured under 100 mW cm^{-2} and AM 1.5G illumination

Electrolyte	V_{oc} (mV)	J_{sc} (mA cm^{-2})	FF	Efficiency (%)	ΔG^{0a} (mV)	E_{redox}^0 (mV)	IPCE at 500 nm (%)
I^-/I_3^-	783 ± 26	12.28 ± 0.71	0.60 ± 0.01	5.79 ± 0.16	640	400	72.10
$[Co(bpy)_3]^{2+/3+}$	868 ± 12	7.42 ± 0.18	0.70 ± 0.02	4.52 ± 0.28	480	560	52.21
$[Cu(dmp)_2]^{1+/2+}$	902 ± 10	12.66 ± 0.55	0.60 ± 0.01	6.82 ± 0.32	100	940	77.22

$$^a \Delta G^0 = E_{dye}^0 - E_{redox}^0.$$

resulting in power conversion efficiency of 4.52%. Improved power conversion efficiency of $6.82 \pm 0.32\%$ was recorded employing $[Cu(dmp)_2]^{1+/2+}$ electrolyte, resulting in V_{oc} of 902 ± 10 mV, J_{sc} of $12.66 \pm 0.55 \text{ mA cm}^{-2}$ and FF of 0.6 ± 0.01 . An improvement in V_{oc} of 85 mV in $[Co(bpy)_3]^{2+/3+}$ system and 119 mV for $[Cu(dmp)_2]^{1+/2+}$ was realized with respect to I^-/I_3^- electrolyte. The more positive redox potentials of $[Co(bpy)_3]^{2+/3+}$ ($E^0 = 0.56 \text{ V vs. NHE}$) and $[Cu(dmp)_2]^{1+/2+}$ ($E^0 = 0.94 \text{ V vs. NHE}$) compared with that of I_3^-/I^- (0.4 V vs. NHE) resulted in achieving higher V_{oc} on employing $[Co(bpy)_3]^{2+/3+}$ and $[Cu(dmp)_2]^{1+/2+}$ -based electrolytes. The Nernst potential of the electrolytes was expected to increase by around 540 mV on changing the electrolyte from I^-/I_3^- to $[Cu(dmp)_2]^{1+/2+}$, whereas the actual improvement was only 119 mV. Similarly, there should be an improvement of 380 mV on changing the electrolyte from $[Co(bpy)_3]^{2+/3+}$ to $[Cu(dmp)_2]^{1+/2+}$. However, only 34 mV increase in V_{oc} was achieved. This clearly indicates that it is not merely the redox potential of the electrolyte that determines voltage; there are other parameters, such as position of conduction band (CB) and recombination of electrons, which also contribute towards determining the voltage, current and photovoltaic performance. These will be discussed in detail in the following sections.

While examining the variation in J_{sc} , $[Co(bpy)_3]^{2+/3+}$ showed 4.86 mA cm^{-2} lower J_{sc} than I^-/I_3^- , whereas $[Cu(dmp)_2]^{1+/2+}$ exhibited almost the same J_{sc} as that of I^-/I_3^- . The drop in J_{sc} for

$[Co(bpy)_3]^{2+/3+}$ is due to the mass transport limitation of $[Co(bpy)_3]^{2+/3+}$ redox shuttle, which is elaborated in the following sections. Even with minimal driving force of 100 mV for regeneration, the reaction kinetics are fast enough to render close to 100% regeneration on employing LEG4 and $[Cu(dmp)_2]^{1+/2+}$, resulting in better current density.^{9,10} $[Cu(dmp)_2]^{1+/2+}$ outperformed both I^-/I_3^- and $[Co(bpy)_3]^{2+/3+}$ with respect to J_{sc} , V_{oc} and overall efficiency. Better FF for $[Co(bpy)_3]^{2+/3+}$ could be due to low resistive losses from lower current density. Higher power conversion efficiency using $[Cu(dmp)_2]^{1+/2+}$ electrolyte is attributed to its positive redox potential, which improved V_{oc} and faster regeneration, resulting in higher J_{sc} . IPCE spectra of LEG4 devices employing all three electrolytes are shown in Fig. 1(b). IPCE was found to increase in the order $[Co(bpy)_3]^{2+/3+} < I^-/I_3^- < [Cu(dmp)_2]^{1+/2+}$, which is in accordance with the J - V results. IPCE is given by the equation

$$IPCE = LHE \times \eta_{inj} \times \eta_{reg} \times \eta_{coll}$$

where LHE is the light harvesting efficiency, η_{inj} is the injection efficiency, η_{reg} corresponds to regeneration efficiency and η_{coll} denotes charge collection efficiency. Using the same dye and similar photoanode materials and architecture, LHE and η_{inj} can be assumed to be unity. Therefore, the difference in IPCE is directly correlated to regeneration and charge collection efficiencies. Copper electrolyte, being the best among the series

considering η_{reg} and η_{coll} , exhibited a relatively higher IPCE. Copper electrolyte also proved to be the best among the three for power conversion efficiency in low light. Details are given in Table S1 and Fig. S1, ESI.† Since IPCE is measured at low monochromatic light intensities, variation in IPCE between cobalt and copper complexes has a major contribution from regeneration and charge collection, in addition to the mass transport limitation.

Mass transport limitations

Slower mass transport is one of the most challenging issues in alternative redox electrolyte based DSCs. Sluggish mass transport limits regeneration rate, resulting in reduced J_{sc} . Redox mediators diffuse either in the pores or in the bulk. Diffusion in pores is more mass transport-limited than in bulk.¹¹ Very often in DSCs, J_{sc} shows a non-linear relationship with the increase in light irradiance. The variation in J_{sc} values with light irradiance is shown in Fig. 2. Current density is related to input light irradiance intensity by the relation $J_{\text{sc}} \propto I^\alpha$, where α is a constant. Γ^-/I_3^- system showed an almost linear relationship with J_{sc} , yielding an α value of 0.93. The $[\text{Cu}(\text{dmp})_2]^{1+/2+}$ system was found to be comparatively more linear than $[\text{Co}(\text{bpy})_3]^{2+/3+}$ electrolyte, with α values of 0.85 and 0.53, respectively. The slow response of DSC due to long trapping and de-trapping times of electrons in TiO_2 or mass transport limitation of redox mediator in electrolyte are the probable rationales for the non-linear relationship of J_{sc} with irradiance intensity. Time lag due to trapping and de-trapping can be ruled out, as TiO_2 used for Γ^-/I_3^- , $[\text{Co}(\text{bpy})_3]^{2+/3+}$ and $[\text{Cu}(\text{dmp})_2]^{1+/2+}$ systems is identical. Therefore, the non-linear increase in J_{sc} with light irradiance intensity is due to mass transport limitations associated with the electrolyte. It should be noted that $[\text{Co}(\text{bpy})_3]^{2+/3+}$ electrolyte showed better J_{sc} than Γ^-/I_3^- until 0.3 sun, but was severely affected by mass transport limitation at illumination intensities >0.3 sun in the present semiconductor configuration. To confirm this, we performed photovoltaic measurements with just one layer of 30 nm TiO_2 particles, which resulted in an

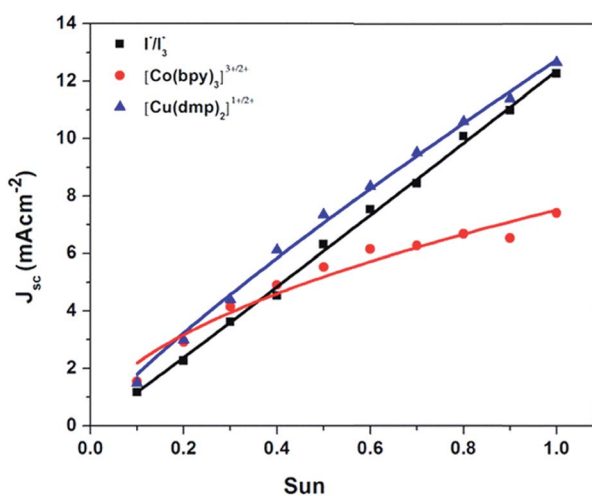


Fig. 2 Light intensity dependence on short circuit current density for Γ^-/I_3^- , $[\text{Co}(\text{bpy})_3]^{2+/3+}$ and $[\text{Cu}(\text{dmp})_2]^{1+/2+}$ electrolytes.

efficiency of 6% for $[\text{Co}(\text{bpy})_3]^{2+/3+}$, clearly giving evidence to the mass transport problem with $[\text{Co}(\text{bpy})_3]^{2+/3+}$ in the present architecture. In order to have similar CB position on employing all the three electrolytes for a better comparison of charge transfer phenomena, we employed the same device architecture for all the three electrolytes. Generally, mass transport is delayed by steric bulk of the redox mediator.¹² A six co-ordinate cobalt complex electrolyte with three polypyridyl ligands surrounding the metal centre is bulkier than a four co-ordinate copper complex with only two ligands. In addition, due to its smaller size, copper complexes diffuse through the electrolyte much faster than the counterpart cobalt system.

Furthermore, mass transport was investigated by photocurrent transient measurements. Fig. 3 shows the photocurrent transient measurements for Γ^-/I_3^- , $[\text{Co}(\text{bpy})_3]^{2+/3+}$ and $[\text{Cu}(\text{dmp})_2]^{1+/2+}$ systems. In photocurrent transient measurement, current response of the device is measured by illumination followed by switching off the light. Photocurrent transient measurements were performed under AM 1.5G simulated light from 0.1 sun to 1 sun. With the increase in light illumination, J_{sc} reaches a peak value (J_{max}); then, it either remains plateaued or decays to saturation current (J_{sat}). As the light is irradiated, electrons from the HOMO of the dye are excited towards the LUMO, leaving behind holes in HOMO. The excited electrons are then injected into the CB of TiO_2 . For further excitation of electrons, holes in the HOMO need to be regenerated by the reduced species present in the electrolyte. If the regeneration rate is equivalent to the excitation rate, the current density remains constant with time ($J_{\text{max}} = J_{\text{sat}}$). If the regeneration rate is slower than the excitation rate, current density decays with time and reaches a saturation value ($J_{\text{max}} > J_{\text{sat}}$).

For the device employing Γ^-/I_3^- electrolyte, peak current was not observed, which confirms that the current is not limited by mass transport. The larger peak in $[\text{Co}(\text{bpy})_3]^{2+/3+}$ compared with that in $[\text{Cu}(\text{dmp})_2]^{1+/2+}$ illustrates higher mass transport limitation in $[\text{Co}(\text{bpy})_3]^{2+/3+}$ than in $[\text{Cu}(\text{dmp})_2]^{1+/2+}$. At lower intensities, mass transport limitation was scarcely observed, as comparatively fewer electrons were required to be regenerated by the reduced species present in the electrolyte. Slower mass transport limits regeneration efficiency. For a better comparison at various light intensities, the overlapped data was plotted, as shown in Fig. S10, ESI.† Furthermore, to investigate the consequences of mass transport limitation, regeneration efficiency is a useful tool. Fig. 3(d) shows the regeneration efficiency at various light intensities. With the assumption of sufficient driving force for regeneration for Γ^-/I_3^- , $[\text{Co}(\text{bpy})_3]^{2+/3+}$ and $[\text{Cu}(\text{dmp})_2]^{1+/2+}$ electrolytes, regeneration efficiency can be calculated from transient current by the equation $(J_{\text{sat}}/J_{\text{max}}) \times 100$, where J_{sat} is saturated J_{sc} and J_{max} is the peak J_{sc} . For Γ^-/I_3^- -based devices, regeneration efficiency was found to be 100% regardless of light intensity. For $[\text{Co}(\text{bpy})_3]^{2+/3+}$ and $[\text{Cu}(\text{dmp})_2]^{1+/2+}$ electrolytes, regeneration efficiency decreased with an increase in light intensity as mass transport issues become more prominent at higher intensities. Regeneration efficiency was superior for the $[\text{Cu}(\text{dmp})_2]^{1+/2+}$ -based device, with regeneration efficiency value of 72% under 1 sun condition, compared with the $[\text{Co}(\text{bpy})_3]^{2+/3+}$ -based device, where

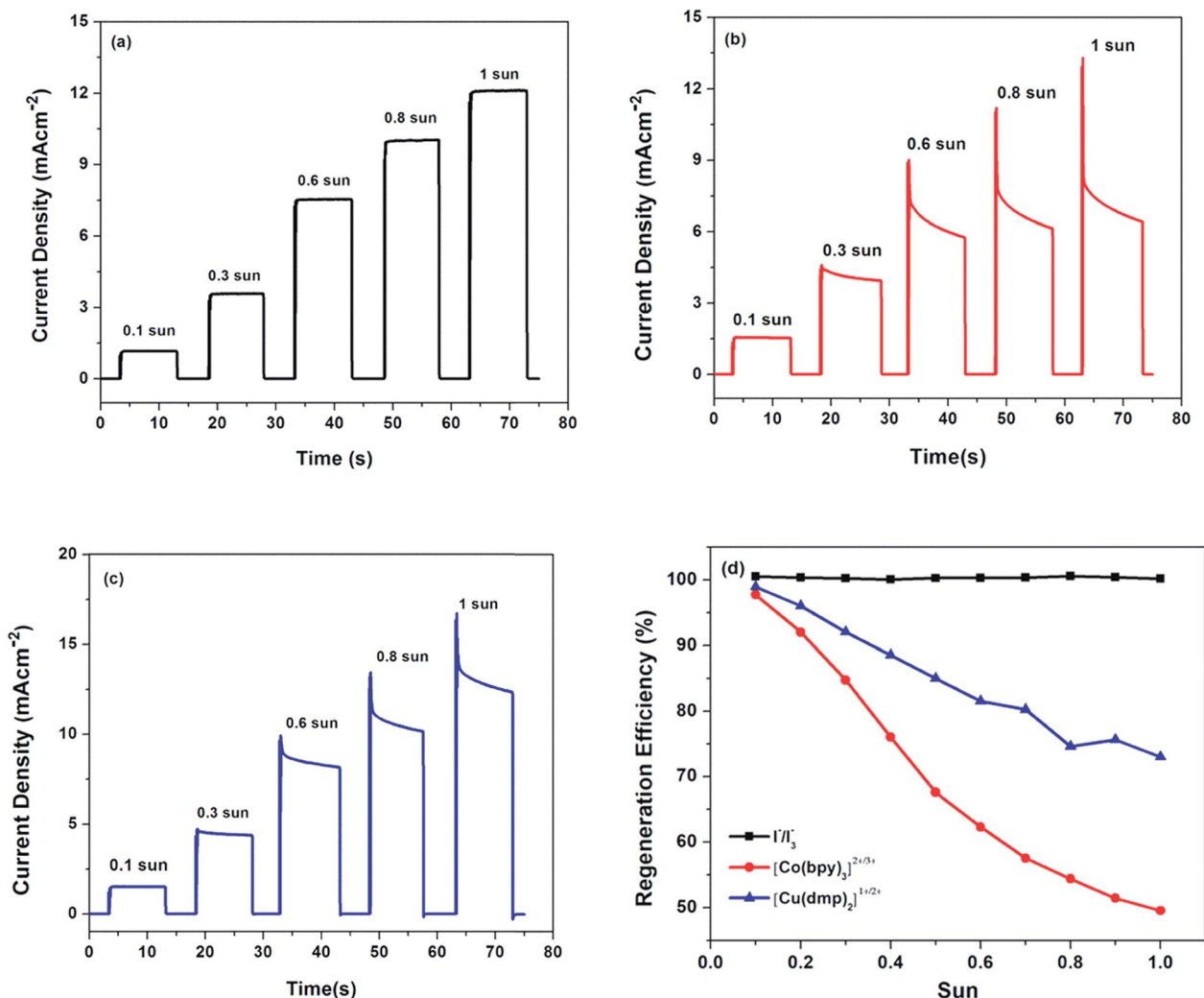


Fig. 3 Current transients measured at AM 1.5G simulated light from 0.1 sun to 1 sun for (a) I^-/I_3^- , (b) $[Co(bpy)_3]^{2+/3+}$ and (c) $[Cu(dmp)_2]^{1+/2+}$ and (d) regeneration efficiency from 0.1 sun to 1 sun for I^-/I_3^- , $[Co(bpy)_3]^{2+/3+}$ and $[Cu(dmp)_2]^{1+/2+}$.

regeneration efficiency was only 49%. This is interesting as copper electrolyte with only 100 mV driving force for regeneration reduces the ground state of the dye much faster than cobalt electrolyte with 480 mV driving force. High self-exchange rate for electron transfer and low reorganization energy helps copper attain higher regeneration yield even with low driving force. Furthermore, EIS was performed to study diffusion resistance (R_d) associated with I^-/I_3^- , $[Co(bpy)_3]^{2+/3+}$ and $[Cu(dmp)_2]^{1+/2+}$ redox shuttles. A distinct semicircle at low frequency is observed due to the diffusion of ions in the electrolyte. R_d was calculated from the Nyquist plot fitted with equivalent transmission line model. Fig. 4 shows the plot of R_d against potential corrected for potential drop due to series resistance. R_d of I^-/I_3^- electrolyte was so low that its resultant response in Nyquist plot was not observed. A distinct semicircle at low frequency in the Nyquist plot and Bode plot was clearly noticed for both $[Co(bpy)_3]^{2+/3+}$ and $[Cu(dmp)_2]^{1+/2+}$ systems (Fig. S3 and S4, ESI†). $[Cu(dmp)_2]^{1+/2+}$ electrolyte showed lower R_d than $[Co(bpy)_3]^{2+/3+}$ electrolyte. Higher R_d results in slower diffusion of ions in the electrolyte. Recently, Freitag *et al.*

successfully showed that $[Cu(dmp)_2]^{1+/2+}$ complex has a diffusion coefficient (D_n) of $25 \times 10^{-6} \text{ cm}^2 \text{ s}^{-1}$, which is double the value of $[Co(bpy)_3]^{2+/3+}$ complex ($9.4 \times 10^{-6} \text{ cm}^2 \text{ s}^{-1}$), which was

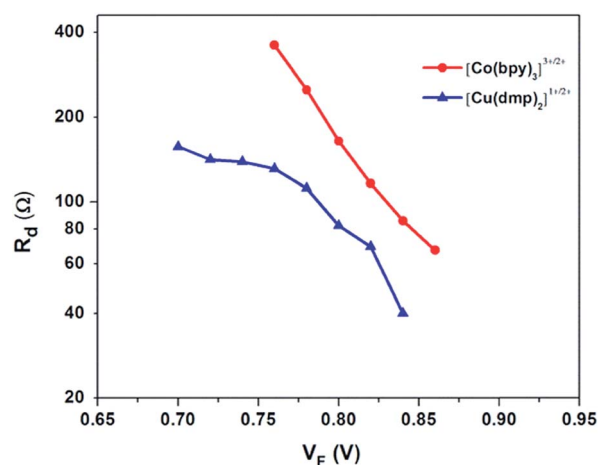


Fig. 4 Diffusion resistance (R_d) as a function of corrected potential.

determined using cyclic voltammetry.⁹ Furthermore, the smaller size of four co-ordinate copper complex helped achieve faster movement inside the nanoporous network in comparison with the six co-ordinate cobalt complex, achieving higher diffusion coefficient.

Non-linearity and surface state recombination

Light intensity dependence of V_{oc} for Γ^-/I_3^- , $[Co(bpy)_3]^{2+/3+}$ and $[Cu(dmp)_2]^{1+/2+}$ electrolytes is given in Fig. 5. V_{oc} is related to light intensity by the relation

$$\frac{dV_{oc}}{d \log I} = \frac{2.30mk_B T}{q} \quad (1)$$

where I is input light intensity, m is the ideality factor, k_B is Boltzmann's constant and T is the temperature. m is calculated from irradiance vs. V_{oc} plot using the standard linear equation.^{13,14}

Non-linear dependence of V_{oc} with input irradiance was observed for Γ^-/I_3^- , $[Co(bpy)_3]^{2+/3+}$ and $[Cu(dmp)_2]^{1+/2+}$ electrolytes. Electron recombination at the FTO/electrolyte interface results in non-ideality in DSCs.^{15–17} To block electron recombination at FTO/electrolyte interface, we deposited a compact TiO_2 blocking layer, which significantly curbed the back electron transfer. Therefore, non-idealities due to back electron transfer at FTO/electrolyte interface can be ruled out to a certain extent. According to Bisquert *et al.*, non-ideal characteristics arise due to recombination from exponentially distributed surface trap states located over the band gap of TiO_2 .^{18,19} There is always recombination from surface states, but the rate of recombination from surface states is slower compared with that from the conduction band states; therefore, recombination from surface states and conduction band states are hardly distinguishable experimentally. Recombination from trap states becomes more prominent when the driving force for recombination increases.²⁰ Hamann *et al.* have reported significant recombination from surface trap states with reduced species of electrolyte employing $[Ru(bpy)_2(MeIm)_2]^{2+/3+}$ redox

shuttle based DSC.²¹ For Γ^-/I_3^- system, m was found to be 1.19, which is very near to the ideal value where recombination rate is very low due to lower driving force for recombination from surface states. In $[Co(bpy)_3]^{2+/3+}$ and $[Cu(dmp)_2]^{1+/2+}$ electrolyte-based DSCs, m values were found to be 1.54 and 1.89, respectively, which shows the possibility of higher recombination from surface states in $[Cu(dmp)_2]^{1+/2+}$ compared with that in $[Co(bpy)_3]^{2+/3+}$. We strongly believe that with proper surface state passivation using techniques such as ALD where we can precisely control passivating layer thickness, recombination can be controlled/modulated, particularly by employing alternative copper redox mediators to further improve the performance of DSCs.

Investigation of interfacial charge dynamics with small electrical and light perturbation techniques

Furthermore, to investigate in detail the origin of variation in V_{oc} with reference to the shift in CB, recombination, diffusion and transport properties, we performed electrochemical impedance spectroscopy (EIS) in dark. EIS was performed with same device architecture and analyzed using the transmission line model developed by Bisquert *et al.*^{22–25,42} Fig. 6 shows the chemical capacitance (C_{μ}), recombination resistance (R_{rec}), lifetime (τ_n) and transport time (τ_d) for Γ^-/I_3^- , $[Co(bpy)_3]^{2+/3+}$ and $[Cu(dmp)_2]^{1+/2+}$ electrolytes as a function of corrected potential; the equivalent circuit comprising a transmission line model used to fit the data is provided in Fig. S5, ESI.† Chemical capacitance (C_{μ}) is the quantification of the conduction band edge of TiO_2 . A negative shift in conduction band was observed in $[Co(bpy)_3]^{2+/3+}$ and $[Cu(dmp)_2]^{1+/2+}$ electrolytes with respect to Γ^-/I_3^- system. The conduction band of $[Cu(dmp)_2]^{1+/2+}$ electrolyte was found to be most negatively shifted in comparison with that of $[Co(bpy)_3]^{2+/3+}$ electrolyte. Negative shift in CB results in higher V_{oc} if the rate of recombination is unaltered. Again, a more negative shift in CB of TiO_2 may lead to injection limitation in DSCs. Herein, injection limitation due to shift in CB can be ruled out as there is ample driving force (close to 600 mV) between the excited state of LEG4 dye and TiO_2 conduction band. In addition, by employing $[Cu(dmp)_2]^{1+/2+}$ electrolyte, whose CB is more negatively shifted than that of the reference Γ^-/I_3^- electrolyte, showed similar J_{sc} , which confirmed that injection has minimal influence in determining the performance in the present case, and is complimented by the fast regeneration prevailing in copper based electrolytes. From the capacitance plot, it is clear that the higher voltage resulting for the copper-based electrolyte is attributed to the negative shift in CB as V_{oc} is the difference between redox potential of the electrolyte and the Fermi level. A similar trend was also observed by Wang *et al.* in the case of $[Cu(dmp)_2]^{1+/2+}$ on employing C218 organic dye.⁸ Recombination resistance was found to be decreasing in the order $[Cu(dmp)_2]^{1+/2+} > [Co(bpy)_3]^{2+/3+} > \Gamma^-/I_3^-$. Recombination resistance is given by the equations

$$R_{rec} = R_0 \exp \left[-\frac{q\beta V_F}{k_B T} \right] \quad (2)$$

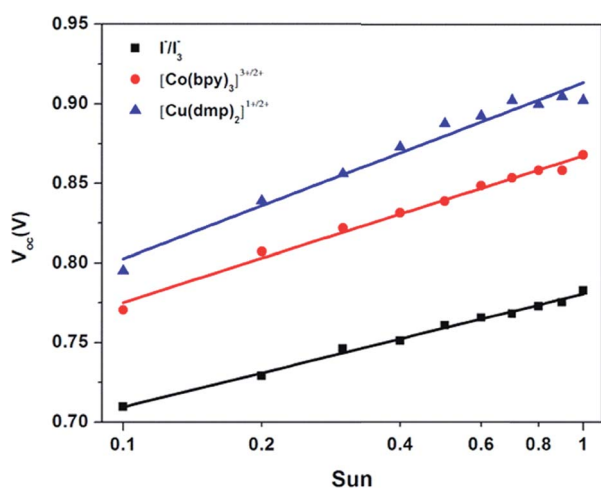


Fig. 5 Light intensity dependence of V_{oc} for Γ^-/I_3^- , $[Co(bpy)_3]^{2+/3+}$ and $[Cu(dmp)_2]^{1+/2+}$ electrolytes.

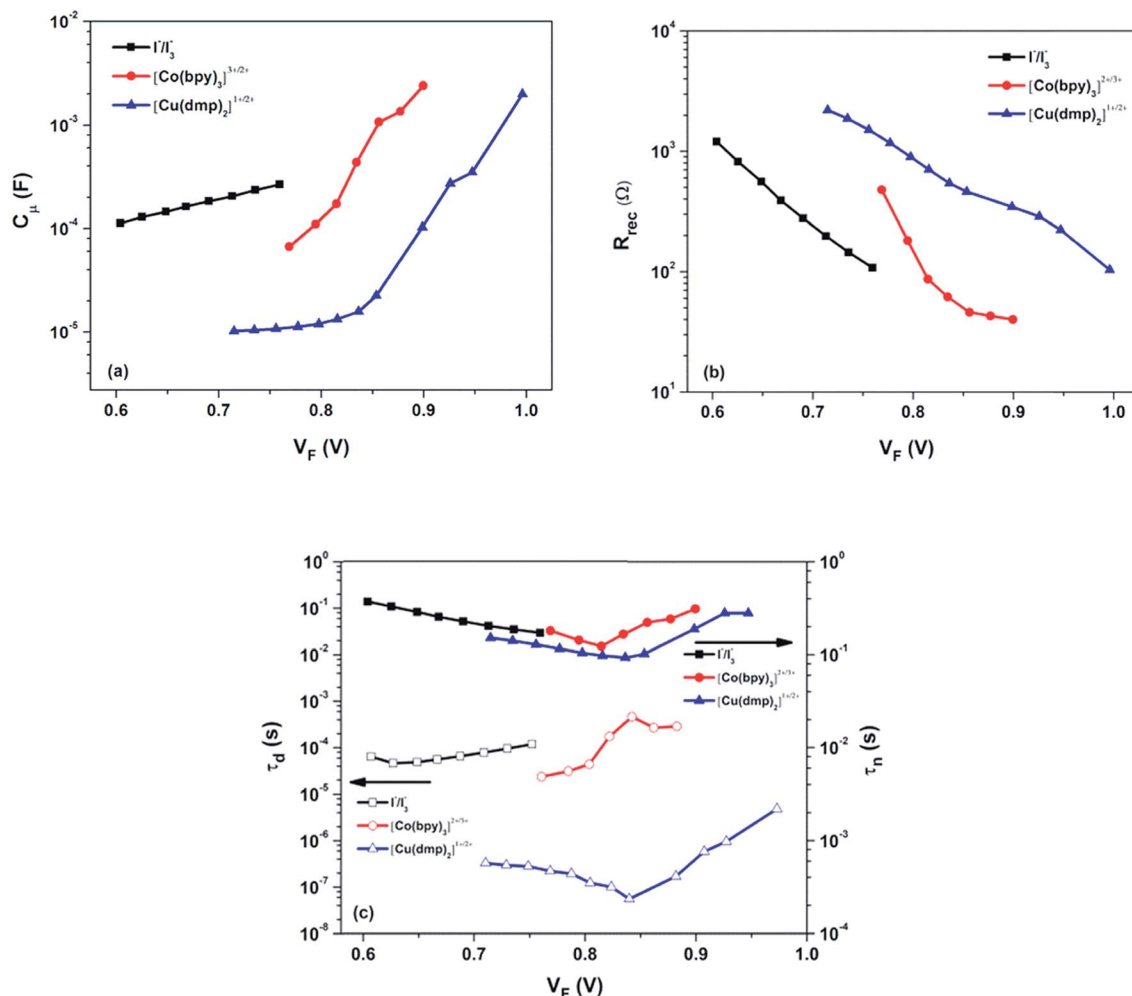


Fig. 6 (a) Chemical capacitance (C_μ), (b) recombination resistance (R_{rec}), (c) electron lifetime (τ_n) and transport time (τ_d) as a function of corrected potential employing I^-/I_3^- , $[Co(bpy)_3]^{2+/3+}$ and $[Cu(dmp)_2]^{1+/2+}$ electrolytes.

$$R_0 = \frac{k_B T}{q \beta j_0} \quad (3)$$

$$j_0 = j_{0k} \exp\left\{\frac{\beta(E_{F0} - E_C)}{k_B T}\right\} \quad (4)$$

where β is recombination parameter, k_B is Boltzmann constant, T is temperature, q is charge and E_C corresponds to the conduction band edge. By analyzing eqn (2)–(4), it is evident that a shift in the position of CB brings a change in j_0 , R_0 and hence R_{rec} . Thus, the difference observed in recombination resistance can be correlated to the difference in position of CB of TiO_2 using I^-/I_3^- , $[Co(bpy)_3]^{2+/3+}$ and $[Cu(dmp)_2]^{1+/2+}$ electrolytes. The time span for the average number of injected electrons in TiO_2 before recombining with the oxidized species in the electrolyte is represented as the lifetime, whereas the average time required for the injected electrons to be collected at the working electrode is denoted as the transport time. Lifetime should be higher than the transport time for attaining efficient charge collection. $[Cu(dmp)_2]^{1+/2+}$ resulted in a slightly lower lifetime compared to $[Co(bpy)_3]^{2+/3+}$ and I^-/I_3^- electrolytes as a result of the negative shift in conduction band coupled

with a more positive redox potential, thus leading to higher driving force for recombination from CB and sub band gap states to the oxidized species in electrolyte. In addition, a more porous 30 nm particle allows oxidized Cu^{2+} species to come closer to FTO, resulting in recombination from the FTO/electrolyte interface. Recombination rate is directly proportional to the driving force for recombination. Hagfeldt *et al.* had achieved Marcus normal region behavior for recombination using a range of cobalt redox shuttles with various organic dyes as well as a ruthenium sensitizer.²⁰ Recently, Freiteg *et al.* also observed Marcus normal region behavior for recombination employing copper redox electrolytes with Y123 dye.¹⁰ In our recent contribution, we also observed Marcus normal region behavior for recombination using two triphenylamine dyes TPAA4 and TPAA5 with cobalt redox shuttles.²⁶ As $[Cu(dmp)_2]^{1+/2+}$ has higher driving force for recombination, it is natural to have lower lifetime; interestingly, $[Co(bpy)_3]^{2+/3+}$ and I^-/I_3^- showed similar lifetime trends, which can be related to the nature of the semiconductor used in the present case. I^-/I_3^- redox electrolyte is well known for its exceptionally slow recombination rate compared with the $[Co(bpy)_3]^{2+/3+}$ redox electrolyte. However,

employing a more porous 30 nm particle network leaves channels for small molecules such as iodine and copper to approach the back contact, resulting in more recombination, whereas for bulky cobalt species, access may be restricted to a certain extent. The above-mentioned behavior resulted in comparable lifetimes for Γ^-/I_3^- and $[\text{Co}(\text{bpy})_3]^{2+/3+}$ electrolytes.²⁷ Different blocking materials were tested at the $\text{TiO}_2/\text{electrolyte}$ interface to alleviate this recombination.^{28–33} However, in majority of the cases, the blocking layer not only prevented recombination, but also limited the injection of electrons to the CB of TiO_2 . The alternative and most promising approach to restrict recombination is to structurally modify the dyes, which prevents the reduced species from approaching TiO_2 , thus curbing recombination.^{34–37} To control recombination without compromising injection, we employed LEG4 sensitizer in the present study. LEG4 is a structurally modified dye with dicyclopentene spacer grafted with long alkyl chains which prevent the approach of reduced species to the TiO_2 surface. In addition, enlarged steric bulk property of redox mediator also reduces the recombination.¹² Hamann *et al.* observed that bulky $[\text{Co}(t\text{-Bu}2\text{bpy})_3]^{2+/3+}$ electrolyte acted as an insulating spacer and reduced the electronic coupling due to steric hindrance, thus reducing recombination.³⁸ Possibly, the suitable structure of LEG4 sensitizer could effectively prevent bulky $[\text{Co}(\text{bpy})_3]^{2+/3+}$ redox mediator from approaching TiO_2 , yielding the comparable lifetimes of $[\text{Co}(\text{bpy})_3]^{2+/3+}$ and Γ^-/I_3^- electrolytes. It is exciting to note that copper redox mediator gave the shortest transport time among the series of complexes.

Diffusion coefficient (D_n) and diffusion length (L_n) as a function of corrected potential are given in Fig. 7. D_n is inversely proportional to transport time, as given by the equation $D_n = \frac{L^2}{\tau_d}$, where L is the thickness of the semiconductor. D_n decreased in the order $[\text{Cu}(\text{dmp})_2]^{1+/2+} > [\text{Co}(\text{bpy})_3]^{2+/3+} > \Gamma^-/I_3^-$. Slightly lower lifetime for $[\text{Cu}(\text{dmp})_2]^{1+/2+}$ is compensated by higher D_n and hence, $[\text{Cu}(\text{dmp})_2]^{1+/2+}$ exhibited longer diffusion length (L_n) compared with $[\text{Co}(\text{bpy})_3]^{2+/3+}$ and Γ^-/I_3^- . L_n is the distance that electrons can travel before recombination. L_n is given by the relation $L_n = \sqrt{D_n \times \tau_n}$. Longer L_n results in better

charge collection efficiency, which in turn results in higher IPCE value. This holds true in the present case, where copper electrolyte with better L_n resulted in better IPCE profile. Higher D_n and L_n obtained for copper might be a result of fast regeneration and slow recombination prevailing in copper compared to cobalt electrolyte.

To examine charge transfer dynamics in the presence of light, we performed photo-modulated perturbation measurements, such as intensity modulated photovoltage spectroscopy (IMVS) and intensity modulated photocurrent spectroscopy (IMPS). Results are shown in Fig. 8 and the obtained Nyquist and Bode plots are given in Fig. S6–S9 (ESI†). For both photo-modulated measurements, monochromatic light (627 nm) was used as the light source for excitation. Electron lifetime (τ_n) was determined from IMVS by the relation

$$\tau_n = \frac{1}{2\pi f_m} \quad (5)$$

where f_m is the frequency corresponding to the highest value of the imaginary part ($-H''$) in Bode plot. The lifetime was found to decreasing in the following order: $\Gamma^-/I_3^- > [\text{Cu}(\text{dmp})_2]^{1+/2+} > [\text{Co}(\text{bpy})_3]^{2+/3+}$. The observed trend is found to be slightly different than EIS measurements performed in dark. This behavior is conclusive since under illumination, mass transport limitation was visible for both the outer sphere cobalt and copper redox mediators. Mhaisalkar *et al.* had previously observed the possibility of relatively slow moving bulky redox mediator ions accumulating at the TiO_2 surface, thereby increasing recombination.³⁹ As discussed previously, $[\text{Cu}(\text{dmp})_2]^{1+/2+}$ electrolyte showed much lower mass transport at higher light intensities, which is reflected in better lifetime for $[\text{Cu}(\text{dmp})_2]^{1+/2+}$ in comparison with $[\text{Co}(\text{bpy})_3]^{2+/3+}$ in light measurement. Transport lifetime (τ_d) is determined from IMPS by the relation⁴³

$$\tau_d = \frac{1}{2\pi f_m} \quad (6)$$

where f_m is the frequency corresponding to the highest value of the imaginary part ($-H''$) in Bode plot. τ_d was, in decreasing

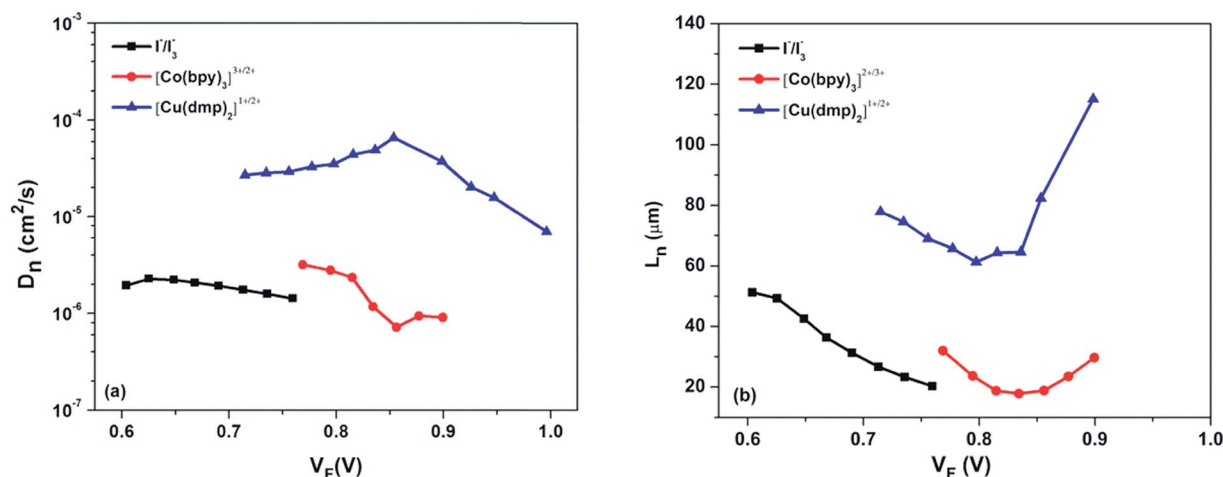


Fig. 7 (a) Diffusion coefficient (D_n) and (b) diffusion length (L_n) as a function of corrected potential.

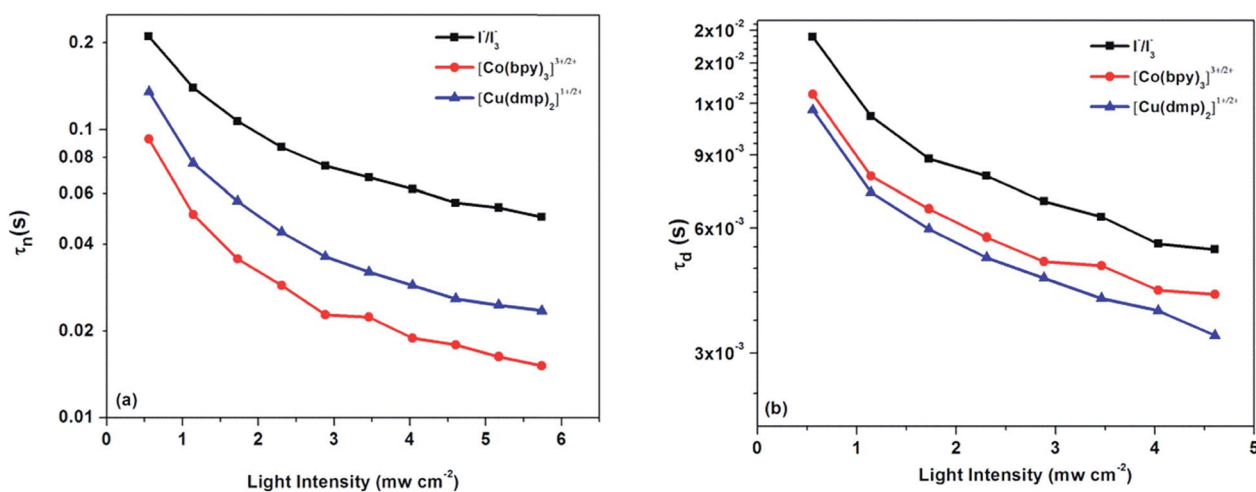


Fig. 8 (a) Lifetime (τ_n) and (b) transport time (τ_d) as a function of light intensity.

order, $I^-/I_3^- > [\text{Co}(\text{bpy})_3]^{2+/3+} > [\text{Cu}(\text{dmp})_2]^{1+/2+}$, which resembles the τ_d trend calculated from EIS measurements. From both dark and light measurements, it is clear that lower τ_d and higher D_n are the two major parameters which allowed copper electrolyte to achieve higher photovoltaic performance.

Conclusion

Redox electrolyte plays a crucial role in determining photovoltaic performance in DSCs. Electrolytes with positive redox potentials can serve as a viable solution to attain higher photovoltage. To study the gain and loss processes associated with changing electrolytes, we performed a detailed interfacial charge transfer dynamics investigation using various perturbation techniques employing I^-/I_3^- , $[\text{Co}(\text{bpy})_3]^{2+/3+}$ and $[\text{Cu}(\text{dmp})_2]^{1+/2+}$ electrolytes. Though conventional I^-/I_3^- based devices were free of mass transport issues, their Nernst potential was less positive in comparison with those of $[\text{Co}(\text{bpy})_3]^{2+/3+}$ and $[\text{Cu}(\text{dmp})_2]^{1+/2+}$ electrolyte-based devices, leading to lower photovoltage. Although $[\text{Co}(\text{bpy})_3]^{2+/3+}$ electrolyte is endowed with more positive redox potential in comparison with conventional I^-/I_3^- electrolyte, slow regeneration and higher recombination coupled with mass transport limitations became an obstacle in realizing long term performance and stability in these devices.

Generally, an increase in voltage and decrease in current are indicated by more positive redox potentials as a result of slow regeneration rates and higher recombination, whereas for $[\text{Cu}(\text{dmp})_2]^{1+/2+}$ based electrolytes, a different trend is observed. The simultaneous increase in both voltage and current for $[\text{Cu}(\text{dmp})_2]^{1+/2+}$ based electrolyte is a result of higher regeneration rate and better charge collection efficiency in addition to superior diffusion coefficient and lower mass transport issues endowed by the smaller size of copper in comparison to $[\text{Co}(\text{bpy})_3]^{2+/3+}$ electrolytes. $[\text{Cu}(\text{dmp})_2]^{1+/2+}$ is placed at a potential of 540 mV more positive than I^-/I_3^- and 380 mV more positive than $[\text{Co}(\text{bpy})_3]^{2+/3+}$. In addition, $[\text{Cu}(\text{dmp})_2]^{1+/2+}$ electrolyte based devices result in a negative shift in conduction band, both conditions which should trigger more recombination for

$[\text{Cu}(\text{dmp})_2]^{1+/2+}$ -based devices in comparison with the other two electrolytes. With fast regeneration kinetics and efficiency, $[\text{Cu}(\text{dmp})_2]^{1+/2+}$ was able to manage the recombination reaction to a greater extent. Based on our observations, for $[\text{Cu}(\text{dmp})_2]^{1+/2+}$ -based electrolytes, the interception reaction takes place from the conduction band, sub-band gap states, surface states, and FTO to the oxidized $\text{Cu}(\text{II})$ species present in the electrolyte. Employing pre- and post-blocking layers can help prevent this recombination to a greater extent. This points to the need to employ pinhole-free compact blocking layers using techniques such as ALD, which would further improve the performance of the $[\text{Cu}(\text{dmp})_2]^{1+/2+}$ -based devices. In addition, this indicates the requirement for structurally engineered dyes to help effectively prevent recombination. Mass transport is another issue that needs to be addressed for the $[\text{Cu}(\text{dmp})_2]^{1+/2+}$ electrolyte. The best option is reducing the spacer thickness, as recently shown by Boschloo and Oskam, which is effective in controlling mass transport in $[\text{Cu}(\text{dmp})_2]^{1+/2+}$ electrolyte based devices.⁴⁰ In addition, further tuning of the porosity of the semiconductor is required to achieve the best performance from $[\text{Cu}(\text{dmp})_2]^{1+/2+}$ electrolyte-based solar cells. In summary, being environmentally friendly with easy synthesis protocols, low cost and earth abundance along with the ability to deliver higher performance in full sun and low light makes $[\text{Cu}(\text{dmp})_2]^{1+/2+}$ based redox electrolyte a promising candidate for future DSC research.

Conflicts of interest

The authors declare no competing financial interest.

Acknowledgements

S. S. gratefully acknowledges financial support from DST-INSPIRE Faculty Award (IFA 13-CH-115). We also thank DST for the DST-SERI Project [DST/TM/SERI/D46(G)]. S. C. P. thank DST-SERI for research fellowships. S. S. also acknowledges Dr Henrik Pettersson, Dyename AB, Sweden for generously providing the 30 nm TiO_2 paste, LEG4 and copper redox

electrolytes. We also extend our thanks to Ms Arya, Mr Gokul and Mr Godwin Paul for their support with the manuscript preparation. S. S. also acknowledges the motivation and support from Dr A. Ajayaghosh, Director, CSIR-NIIST.

References

- 1 K. Kakiage, Y. Aoyama, T. Yano, K. Oya, J. Fujisawa and M. Hanaya, *Chem. Commun.*, 2015, **51**, 15894–15897.
- 2 Y. Cao, Y. Liu, S. M. Zakeeruddin, A. Hagfeldt and M. Grätzel, *Joule*, 2018, **2**, 1–10.
- 3 M. Freitag, J. Teuscher, Y. Saygili, X. Zhang, F. Giordano, P. Liska, J. Hua, S. M. Zakeeruddin, J. E. Moser, M. Grätzel and A. Hagfeldt, *Nat. Photonics*, 2017, **11**, 372–378.
- 4 T. W. Hamann and J. W. Ondersma, *Energy Environ. Sci.*, 2011, **4**, 370–381.
- 5 T. W. Hamann, R. A. Jensen, A. B. F. Martinson, H. Van Ryswyk and J. T. Hupp, *Energy Environ. Sci.*, 2008, **1**, 66–68.
- 6 J.-H. Yum, E. Baranoff, F. Kessler, T. Moehl, S. Ahmad, T. Bessho, A. Marchioro, E. Ghadiri, J.-E. Moser, C. Yi, M. K. Nazeeruddin and M. Grätzel, *Nat. Commun.*, 2012, **3**, 631.
- 7 S. Hattori, Y. Wada, S. Yanagida and S. Fukuzumi, *J. Am. Chem. Soc.*, 2005, **127**, 9648–9654.
- 8 Y. Bai, Q. Yu, N. Cai, Y. Wang, M. Zhang and P. Wang, *Chem. Commun.*, 2011, **47**, 4376–4378.
- 9 M. Freitag, F. Giordano, W. Yang, M. Pazoki, Y. Hao, B. Zietz, M. Grätzel, A. Hagfeldt and G. Boschloo, *J. Phys. Chem. C*, 2016, **120**, 9595–9603.
- 10 Y. Saygili, M. Söderberg, N. Pellet, F. Giordano, Y. Cao, A. B. Muñoz-García, S. M. Zakeeruddin, N. Vlachopoulos, M. Pavone, G. Boschloo, L. Kavan, J. E. Moser, M. Grätzel, A. Hagfeldt and M. Freitag, *J. Am. Chem. Soc.*, 2016, **138**, 15087–15096.
- 11 J. J. Nelson, T. J. Amick and C. M. Elliott, *J. Phys. Chem. C*, 2008, **112**, 18255–18263.
- 12 J. Kusters, S. M. Feldt, E. a. Gibson, E. Gabrielsson, L. Sun, G. Boschloo, A. Hagfeldt and J. Kusters, *J. Am. Chem. Soc.*, 2007, **1**, 2–7.
- 13 P. Salvador, M. G. Hidalgo, A. Zaban and J. Bisquert, *J. Phys. Chem. B*, 2005, **109**, 15915–15926.
- 14 J. Bisquert and I. Mora-Seró, *J. Phys. Chem. Lett.*, 2010, **1**, 450–456.
- 15 S. Sasidharan, S. Soman, S. C. Pradhan, K. N. N. Unni, A. A. P. Mohamed, B. N. Nair and H. U. N. Saraswathy, *New J. Chem.*, 2017, **41**, 1007–1016.
- 16 P. J. Cameron and L. M. Peter, *J. Phys. Chem. B*, 2005, **109**, 7392–7398.
- 17 P. J. Cameron and L. M. Peter, *J. Phys. Chem. B*, 2005, **109**, 930–936.
- 18 J. Bisquert, A. Zaban, M. Greenshtein and I. Mora-Seró, *J. Am. Chem. Soc.*, 2004, **126**, 13550–13559.
- 19 J. Bisquert, A. Zaban and P. Salvador, *J. Phys. Chem. B*, 2002, **106**, 8774–8782.
- 20 S. M. Feldt, P. W. Lohse, F. Kessler, M. K. Nazeeruddin, M. Grätzel, G. Boschloo and A. Hagfeldt, *Phys. Chem. Chem. Phys.*, 2013, **15**, 7087–7097.
- 21 J. W. Ondersma and T. W. Hamann, *J. Am. Chem. Soc.*, 2011, **133**, 8264–8271.
- 22 F. Fabregat-Santiago, G. Garcia-Belmonte, I. Mora-Seró and J. Bisquert, *Phys. Chem. Chem. Phys.*, 2011, **13**, 9083–9118.
- 23 J. Bisquert and R. A. Marcus, *Top. Curr. Chem.*, 2014, **352**, 325–396.
- 24 J. Bisquert, F. F.-S. I. Mora-Seró, G. Garcia-Belmonte and S. Giménez, *J. Phys. Chem. C*, 2009, **113**, 17278–17290.
- 25 J. Bisquert, I. Mora-Seró and F. Fabregat-Santiago, *ChemElectroChem*, 2014, **1**, 289–296.
- 26 S. Soman, S. C. Pradhan, M. Yoosuf, M. V. Vinayak, S. Lingamoorthy and K. R. Gopidas, *J. Phys. Chem. C*, 2018, **122**, 14113–14127.
- 27 T. W. Hamann, *Dalton Trans.*, 2012, **41**, 3111–3115.
- 28 S. Lee, J. H. Noh, H. S. Han, D. K. Yim, D. H. Kim, J.-K. Lee, J. Y. Kim, H. S. Jung and K. S. Hong, *J. Phys. Chem. C*, 2009, **113**, 6878–6882.
- 29 A. K. Chandiran, P. Comte, R. Humphry-baker, F. Kessler, C. Yi, K. Nazeeruddin and M. Grätzel, *Adv. Funct. Mater.*, 2013, **23**, 2775–2781.
- 30 C. Lin, F.-Y. Tsai, M.-H. Lee, C.-H. Lee, T.-C. Tien, L.-P. Wang and S.-Y. Tsai, *J. Mater. Chem.*, 2009, **19**, 2999–3003.
- 31 P. M. Sommeling, B. C. O'Regan, R. R. Haswell, H. J. P. Smit, N. J. Bakker, J. J. T. Smits, J. M. Kroon and J. A. M. van Roosmalen, *J. Phys. Chem. B*, 2006, **110**, 19191–19197.
- 32 M.-H. Kim and Y.-U. Kwon, *J. Phys. Chem. C*, 2011, **115**, 23120–23125.
- 33 X. Gao, D. Guan, J. Huo, J. Chen and C. Yuan, *Nanoscale*, 2013, **5**, 10438–10446.
- 34 X. Jiang, K. M. Karlsson, E. Gabrielsson, E. M. J. Johansson, M. Quintana, M. Karlsson, L. Sun, G. Boschloo and A. Hagfeldt, *Adv. Funct. Mater.*, 2011, **21**, 2944–2952.
- 35 G. Wu, F. Kong, Y. Zhang, X. Zhang, J. Li and W. Chen, *J. Phys. Chem. C*, 2014, **118**, 8756–8765.
- 36 A. Mahmood, *Sol. Energy*, 2016, **123**, 127–144.
- 37 M. V. Vinayak, M. Yoosuf, S. C. Pradhan, T. M. Lakshmykanth, S. Soman and K. R. Gopidas, *Sustainable Energy Fuels*, 2018, **2**, 303–314.
- 38 B. M. Klahr and T. W. Hamann, *J. Phys. Chem. C*, 2009, **113**, 14040–14045.
- 39 T. T. Trang Pham, T. M. Koh, K. Nonomura, Y. M. Lam, N. Mathews and S. Mhaisalkar, *ChemPhysChem*, 2014, **15**, 1216–1221.
- 40 R. García-Rodríguez, R. Jiang, E. J. Canto-Aguilar, G. Oskam and G. Boschloo, *Phys. Chem. Chem. Phys.*, 2017, **19**, 32132–32142.
- 41 (a) J. Cong, D. Kinschel, Q. Daniel, M. Safdari, E. Gabrielsson, H. Chen, P. H. Svensson, L. Sun and L. Kloo, *J. Mater. Chem. A*, 2016, **4**, 14550–14554; (b) J. Li, X. Yang, Z. Yu, G. G. Gurzadyan, M. Cheng, F. Zhang, J. Cong, W. Wang, H. Wang, X. Li, L. Kloo, M. Wang and L. Sun, *RSC Adv.*, 2017, **7**, 4611–4615.
- 42 F. Q. Liu, J. Su, W. Wang, W. H. Li, H. Q. Hu, L. Wang and R. X. Li, *J. Mater. Chem. A*, 2015, **3**, 3136–3143.
- 43 F. Q. Liu, K. Zhu, T. Li and T. Xu, *J. Phys. Chem. C*, 2014, **118**, 9951–9957.

Resurgence of DSCs with copper electrolyte: A detailed investigation of the interfacial charge dynamics in comparison with cobalt and iodine

Sourava C. Pradhan,^{ac} Anders Hagfeldt^b and Suraj Soman^{*ac}

^aPhotosciences and Photonics Section, Chemical Sciences and Technology Division, CSIR-National Institute for Interdisciplinary Science and Technology (CSIR-NIIST), Thiruvananthapuram 695019, India. ^bLaboratory of Photomolecular Science, Institute of Chemical Sciences & Engineering, Ecole Polytechnique Federale de Lausanne, Lausanne 1015, Switzerland. ^cAcademy of Scientific and Innovative Research (AcSIR), CSIR-NIIST Campus, Thiruvananthapuram 695019, India.

Table S1. *J-V* parameters at various light intensities.

	Light Intensity	V_{oc} (mV)	J_{sc} (mAcm ⁻²)	FF	Efficiency (%)
I ₃ ⁻ /I ⁻	1 Sun	783	12.28	0.60	5.79
	0.5 Sun	761	6.31	0.66	6.32
	0.1 Sun	709	1.17	0.73	6.07
[Co(bpy) ₃] ^{2+/3+}	1 Sun	868	7.42	0.70	4.52
	0.5 Sun	839	5.53	0.58	5.36
	0.1 Sun	771	1.54	0.52	6.23
[Cu(dmp) ₂] ^{1+/2+}	1 Sun	902	12.66	0.60	6.82
	0.5 Sun	888	7.34	0.62	8.13
	0.1 Sun	795	1.49	0.60	7.14

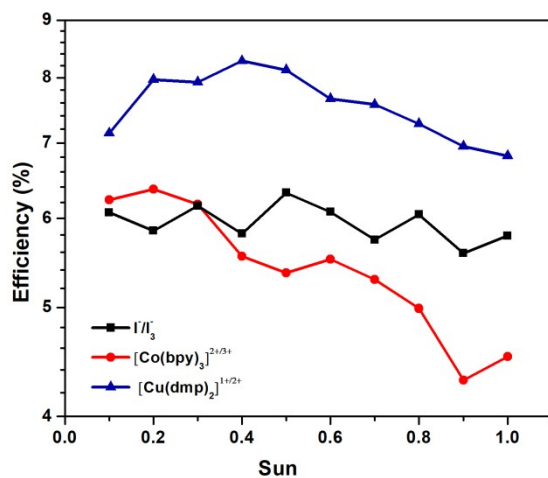


Figure S1. Efficiency at various light intensities employing I^-/I_3^- , $[Co(bpy)_3]^{2+/3+}$ and $[Cu(dmp)_2]^{1+/2+}$ electrolytes.

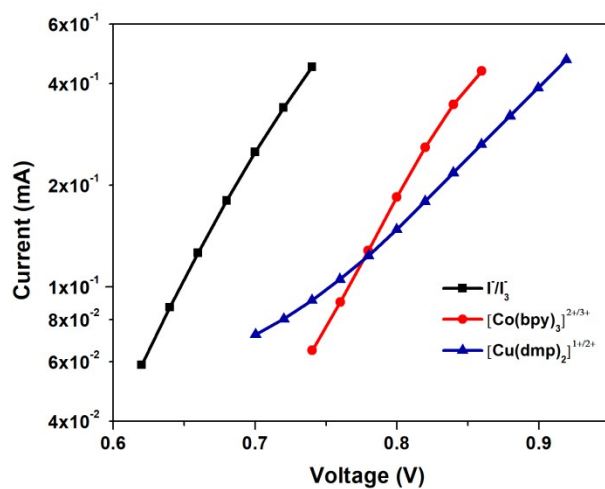


Figure S2. Dark current from EIS.

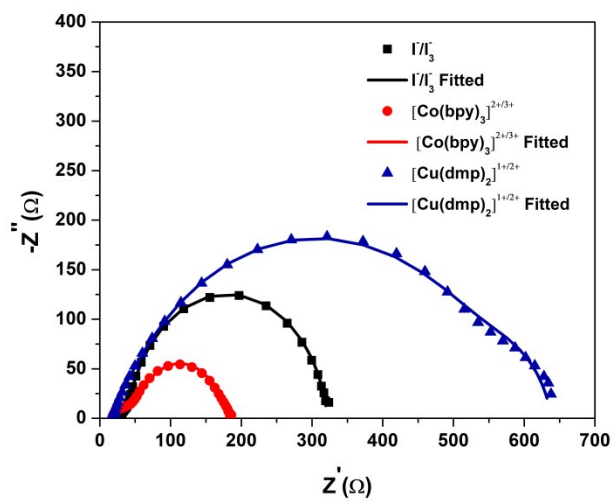


Figure S3. Nyquist plot of I^-/I_3^- , $[Co(bpy)_3]^{2+/3+}$ and $[Cu(dmp)_2]^{1+/2+}$ electrolytes.

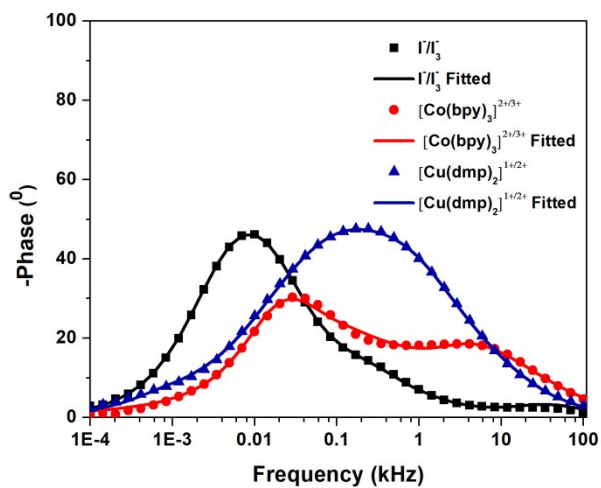


Figure S4. Bode plot of I^-/I_3^- , $[Co(bpy)_3]^{2+/3+}$ and $[Cu(dmp)_2]^{1+/2+}$ electrolytes.

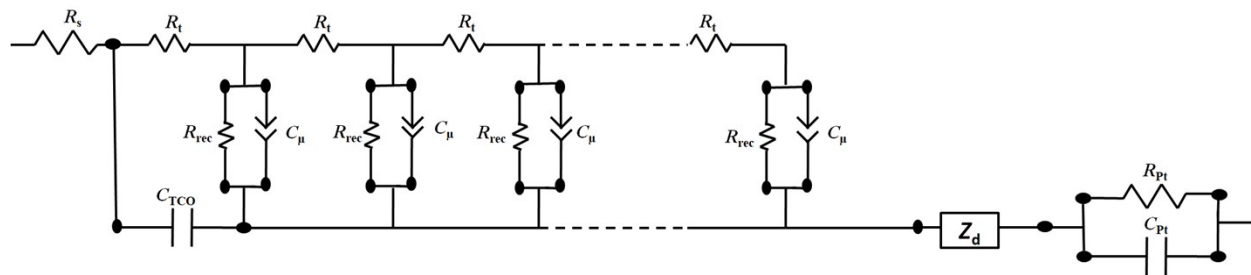


Figure S5. Equivalent circuit for EIS fitting.

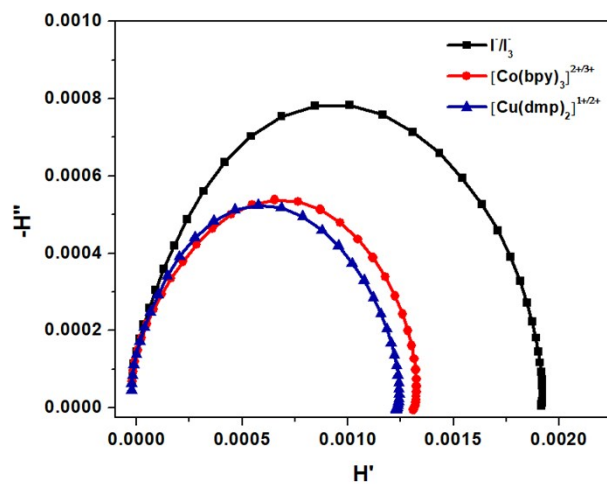


Figure S6. Nyquist plot for I/I_3^- , $[Co(bpy)_3]^{2+/3+}$ and $[Cu(dmp)_2]^{1+/2+}$ electrolytes obtained from IMPS measurement.

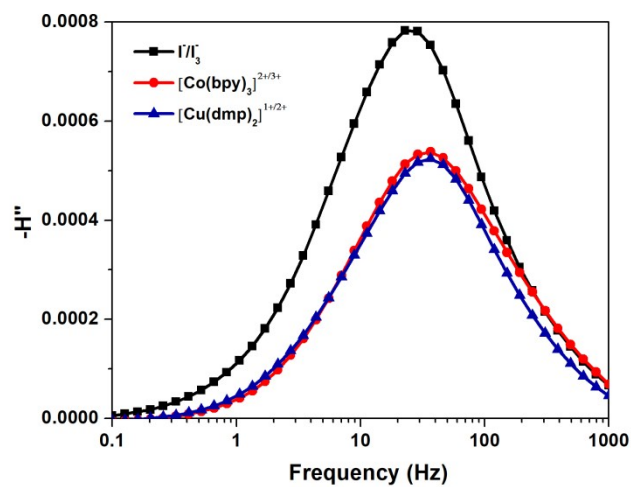


Figure S7. Bode plot of I/I_3^- , $[Co(bpy)_3]^{2+/3+}$ and $[Cu(dmp)_2]^{1+/2+}$ electrolytes obtained from IMPS measurement.

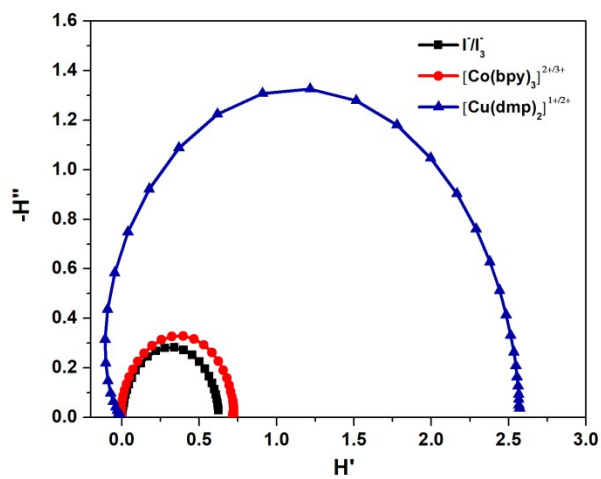


Figure S8. Nyquist plot of I/I_3^- , $[Co(bpy)_3]^{2+/3+}$ and $[Cu(dmp)_2]^{1+/2+}$ electrolytes obtained from IMVS measurement.

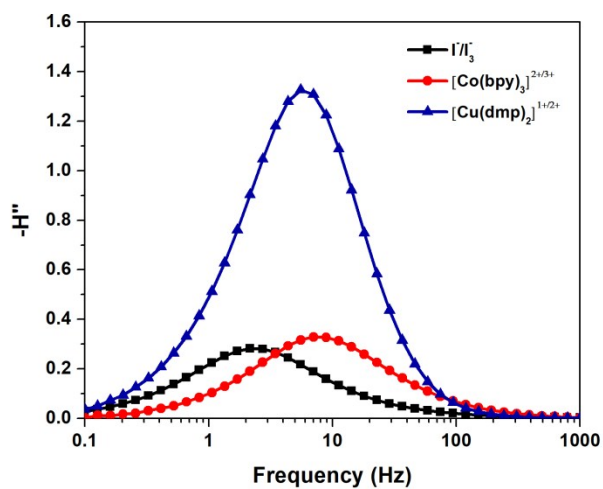


Figure S9. Bode plot of I^-/I_3^- , $[Co(bpy)_3]^{2+/3+}$ and $[Cu(dmp)_2]^{1+/2+}$ electrolytes obtained from IMVS measurement.

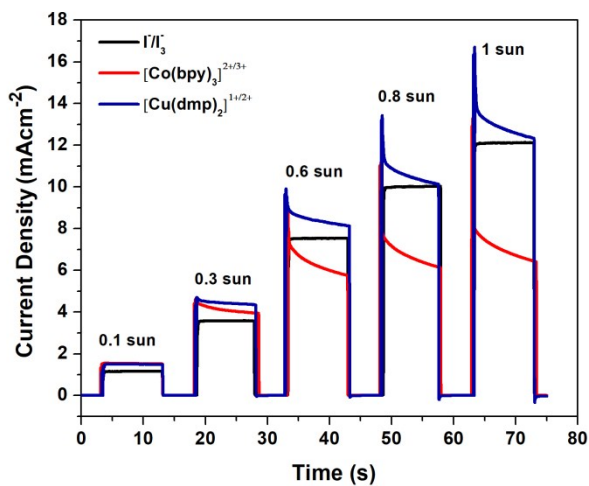


Figure S10. Current Transients of I^-/I_3^- , $[Co(bpy)_3]^{2+/3+}$ and $[Cu(dmp)_2]^{1+/2+}$ electrolytes at various light intensities.



Cite this: DOI: 10.1039/d1tc05803g

Probing photovoltaic performance in copper electrolyte dye-sensitized solar cells of variable TiO₂ particle size using comprehensive interfacial analysis†

Sourava Chandra Pradhan,^{ab} Jayadev Velore,^{ab} Anders Hagfeldt ^{*c} and Suraj Soman ^{*ab}

Copper-based metal complex redox mediators proved to be an efficient, futuristic electrolyte for dye-sensitized solar cell (DSC) applications addressing many critical issues of conventional iodide/triiodide electrolytes. However, copper redox mediators being bulkier than conventional iodine electrolytes impose movement restrictions contributing to unfavourable charge transfer processes. In the present manuscript, we analyzed the impact of TiO₂ particle size (20 nm and 30 nm) on the photovoltaic parameters of DSCs using an organic D35 dye and an alternate copper redox mediator, Cu[(tmbpy)₂]^{2+/1+}. DSC photoanodes with 20 nm TiO₂ particles realized a lower power conversion efficiency (PCE) of 6.32 ± 0.07% in comparison to 7.36 ± 0.12% efficiency achieved using DSCs made with 30 nm TiO₂ particles. The improved PCE using 30 nm TiO₂ particles is associated with the enhancement in short circuit current density (J_{sc}), open-circuit potential (V_{oc}) and the fill factor (FF). Furthermore, comprehensive analysis of various charge transfer processes at discrete interfaces in these devices reveals collective enhancement in light-harvesting, dye regeneration and charge collection efficiency that ultimately contributed to achieving 16% improvement in PCE using 30 nm TiO₂ particles.

Received 3rd December 2021,
Accepted 7th February 2022

DOI: 10.1039/d1tc05803g

rsc.li/materials-c

Introduction

Third-generation solar cells have garnered tremendous attention in recent years as a potential light-harvesting option, mainly due to their capability to work under diffused/artificial light conditions.^{1–7} Among the various types of third-generation photovoltaic (PV) technologies, dye-sensitized solar cells (DSCs) are considered as one of the most promising cost-effective PV technology. They have fascinated researchers since their invention by Brian O' Regan and Michael Grätzel due to their lower production cost, ease of fabrication, transparency, flexibility, and aesthetics.^{8–13} Promising power conversion efficiencies (PCE) above 14% have already been reported for DSCs under one sun illumination (100 mW cm⁻²).^{14,15} In recent times, DSCs have emerged as one of the most brilliant photovoltaic technologies for indoor photovoltaics (IPV), even surpassing GaAs solar cells with

power conversion efficiencies >30% under artificial light illumination (1000 lux, CFL).^{16–18}

In DSCs, dye absorbs light, and correspondingly electron-hole pairs are created. The excited electrons are then injected into the semiconductor (TiO₂) and collected through the working electrode. Meanwhile, the oxidized dye is reduced by the electron-rich species present in the electrolyte. The cycle completes as the oxidized species in the electrolyte gets re-reduced at the counter electrode. The output current primarily depends upon the light-harvesting capability of the sensitizer and the voltage constitutes the Fermi energy difference between TiO₂ and the redox potential of the electrolyte. Since the Fermi level of TiO₂ offers fewer opportunities for modification, V_{oc} of DSCs can be increased more readily by employing electrolytes with positive redox potentials. Unfortunately, conventional I⁻/I₃⁻ redox electrolyte offers minimal flexibility to tune the redox potential (0.4 V vs. NHE), limiting DSC's open-circuit potential.¹⁹ One of the redox complexes that successfully fulfilled the shortcomings of the I⁻/I₃⁻ redox shuttle was cobalt-based metal complex redox mediators (Co³⁺/Co²⁺).²⁰ Unlike I⁻/I₃⁻, Co³⁺/Co²⁺ offers modulation of redox potential through structural changes carried out on the peripheral organic ligands attaining a voltage close to 1 V.²¹ However, the reorganization energy is relatively high for cobalt redox

^a Photosciences and Photonics Section, Chemical Sciences and Technology Division, CSIR-National Institute for Interdisciplinary Science and Technology (CSIR-NIIST), Thiruvananthapuram 695019, India. E-mail: suraj@niist.res.in

^b Academy of Scientific and Innovative Research (AcSIR), Ghaziabad-201002, India

^c Department of Chemistry – Ångström Laboratory, Uppsala University Box 523, SE-75120 Uppsala, Sweden

† Electronic supplementary information (ESI) available: Additional data analysis. See DOI: 10.1039/d1tc05803g

mediators since Co(III) has a high spin state, and Co(II) has a low spin state necessitating a minimum driving force of 400–500 meV for efficient dye regeneration, limiting further improvement in V_{oc} .^{21,22} A significant advancement in voltage gain was achieved recently with the introduction of copper electrolytes where merely 100 mV driving force was sufficient enough for efficient dye regeneration leading to $V_{oc} > 1$ V from a single junction device.^{23–27} Recently, using $Cu[(tmby)_2]^{2+/1+}$ Hagfeldt and co-workers achieved an outstanding V_{oc} of 1.24 V from a single junction device leading to a power conversion efficiency of 13.5%.¹⁸ Fabrication of efficient copper-based DSCs requires an entirely new set of innovative materials and optimized device architectures. One such critical device engineering parameter involves the use of mesoporous titanium dioxide particles with variable particle sizes. In standard I^-/I_3^- electrolyte based DSCs, mesoporous TiO_2 with an average particle size of 20 nm is commonly used as an active layer, which provides a balance between dye uptake and charge transport. However, in copper electrolyte DSCs, mesoporous TiO_2 with an average particle size of 30 nm is primarily preferred over 20 nm. Ferdowsi *et al.* used TiO_2 particle sizes of 20 nm and 30 nm with the $[Cu(tmby)_2]^{2+/1+}$ electrolyte and newly synthesized sensitizers L156 and L224, which showed improvement in efficiency.²⁸ Cao *et al.* also observed an improvement in PCE by replacing 20 nm TiO_2 particles with 30 nm TiO_2 particles under one sun illumination using the copper electrolyte.¹⁷ Though the difference between 20 nm and 30 nm TiO_2 particles is minimal, it critically alters the surface area and porosity, which further influences the charge transfer process at the TiO_2 /electrolyte interface.²⁹ For instance, larger size TiO_2 particles are considered to be favourable for charge transport supported by higher recombination resistance and longer diffusion length using an N719 dye and an I^-/I_3^- electrolyte.³⁰ Similarly, better porosity for 30 nm particles facilitates easy movement of alternative bulky electrolytes.³¹ Unlike I^-/I_3^- redox mediators, Cu^{2+}/Cu^{1+} ions are bulky with a higher tendency for interfacial recombination. Thus a slight change in porosity or surface area may substantially influence photovoltaic parameters. Moreover, a detailed investigation on the gain in PCE

using mesoporous TiO_2 of variable particle sizes is not explored in detail for DSCs using copper electrolytes. In the present study, we carried out a comprehensive interfacial analysis of DSCs fabricated using 20 nm and 30 nm TiO_2 particles along with the organic D35 sensitizer and $Cu[(tmby)_2]^{2+/1+}$ redox mediator. Chart 1 shows the molecular structure of the D35 dye and $Cu[(tmby)_2]^{2+/1+}$ electrolyte and the energy level diagram of TiO_2 , dye and electrolyte.

Results and discussion

Photovoltaic performance

Current density–voltage (J – V) characterization was carried out under one sun illumination (AM 1.5G, 100 $mW\ cm^{-2}$). Fig. 1 shows the J – V and IPCE plots for DSCs fabricated using 20 nm and 30 nm TiO_2 particles and the resultant photovoltaic parameters are summarized in Table 1 employing a D35 sensitizer and $[Cu(tmby)_2]^{2+/1+}$ electrolyte. DSCs with 20 nm particles delivered an open-circuit voltage (V_{oc}) of 928 ± 2 mV, a short circuit current density (J_{sc}) of 9.95 ± 0.09 $mA\ cm^{-2}$ and a fill factor (FF) of 0.68 ± 0.01 , leading to a power conversion efficiency (η) of $6.32 \pm 0.07\%$. Under similar conditions, DSCs with 30 nm particles exhibited a V_{oc} of 948 ± 3 mV and J_{sc} of 10.96 ± 0.10 $mA\ cm^{-2}$ and FF of 0.71 ± 0.01 realizing an improved η of $7.36 \pm 0.12\%$. DSCs with 30 nm TiO_2 particles showed 16% improvement in PCE with respect to devices fabricated using 20 nm TiO_2 particles. This enhancement in PCE is mainly attributed to the 10% improvement in current density and minor gains in V_{oc} and FF. The improvement in efficiency was also observed for photovoltaic measurements carried out under indoor 1000 lux warm white CFL illumination (Fig. S1 and Table S1, ESI†). IPCE onset for both the devices extended up to a wavelength of 640 nm with IPCE_{max} at 470 nm. The J_{sc} obtained by integrating IPCE was found to be 9.22 $mA\ cm^{-2}$ for 20 nm and 10.05 $mA\ cm^{-2}$ for 30 nm TiO_2 particles. The improvement in J_{sc} was also reflected in the IPCE spectra, where DSCs using 30 nm TiO_2 particles showed a higher

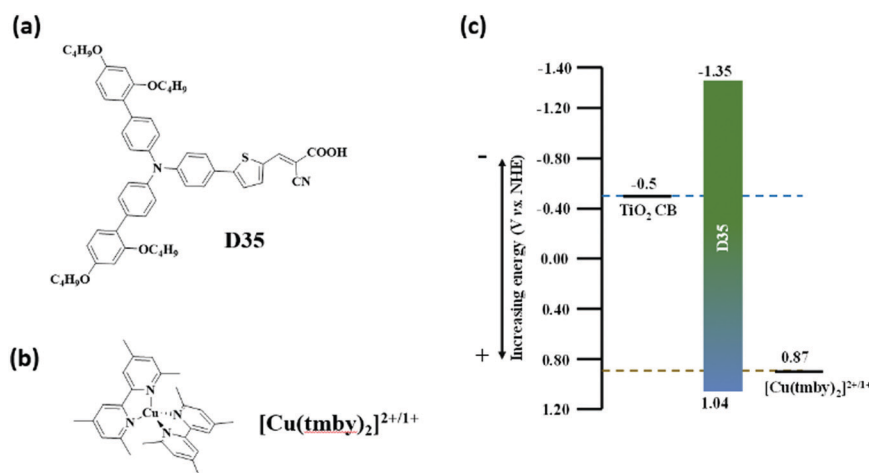


Chart 1 (a) Molecular structure of a D35 dye (b) copper complex $[Cu(tmby)_2]^{2+/1+}$, and (c) energy level diagram of TiO_2 , dye and electrolyte.

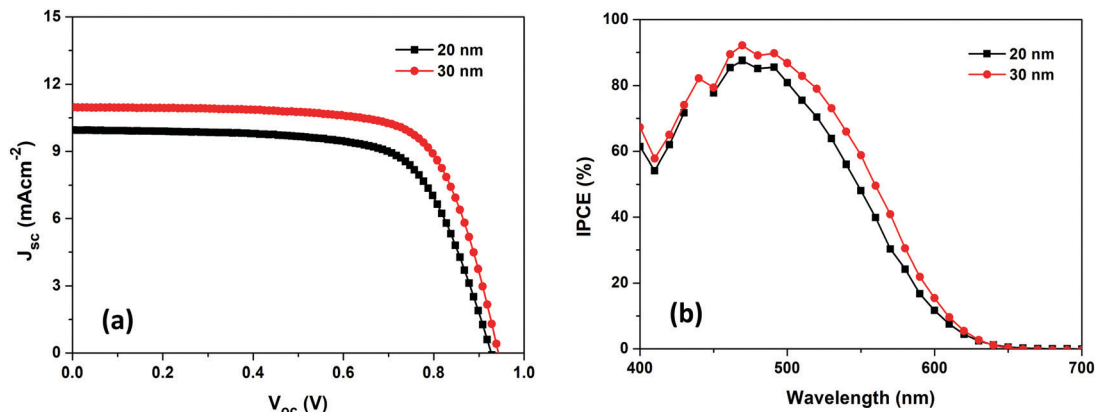


Fig. 1 (a) Current density–voltage (J - V) and (b) incident photon current conversion efficiency (IPCE) plot of DSCs fabricated with 20 nm and 30 nm TiO_2 particles employing a D35 sensitizer and $[\text{Cu}(\text{tmbpy})_2]^{2+/1+}$ redox mediator.

Table 1 J - V parameters of DSCs fabricated using 20 nm and 30 nm TiO_2 particles using a D35 sensitizer and $[\text{Cu}(\text{tmbpy})_2]^{2+/1+}$ electrolyte

Device	V_{oc} (mV)	J_{sc} (mA cm^{-2})	FF	η (%)
20 nm	928 ± 2	9.95 ± 0.09	0.68 ± 0.01	6.32 ± 0.07
30 nm	948 ± 3	10.96 ± 0.10	0.71 ± 0.01	7.36 ± 0.12

absorption profile in the visible region with a relatively more improvement from 500 nm to 600 nm. IPCE is given by the relation,^{32–34}

$$\text{IPCE} = \eta_{\text{LHE}} \times \eta_{\text{inj}} \times \eta_{\text{reg}} \times \eta_{\text{cc}} \quad (1)$$

where η_{LHE} is the light-harvesting efficiency, η_{inj} , η_{reg} and η_{cc} denote injection, regeneration and charge collection efficiency. A more detailed analysis of each of these parameters is discussed in the following sections.

Probing light harvesting efficiency

Light-harvesting efficiency (LHE) demonstrates the capability of the device to absorb light and is the first step in the photon to electrical energy conversion process. During this process, light is absorbed, and electron-hole pairs are created. In DSCs, the sensitizer/dye serves the role of a light harvester; thus, the absorption capability and molar extinction coefficient of dyes primarily determine the light-harvesting capability.

Light-harvesting efficiency is given by eqn (2)^{35,36}

$$\text{LHE} = 1 - 10^{-\text{abs}} \quad (2)$$

where abs is the absorbance. Fig. 2 shows the LHE of dye soaked TiO_2 electrodes using 20 nm and 30 nm TiO_2 particles as a function of wavelength. The LHE of the dye-soaked electrodes with 30 nm TiO_2 particles marginally red-shifted. The redshift in LHE particularly at higher wavelengths (> 500 nm) can be attributed to better light scattering induced by the higher particle size and roughness provided by 30 nm particles. Fig. S2, ESI† shows the surface profile AFM images for 20 nm and 30 nm TiO_2 particles. From the AFM image, the roughness was found to be 129 nm for TiO_2 films with 20 nm

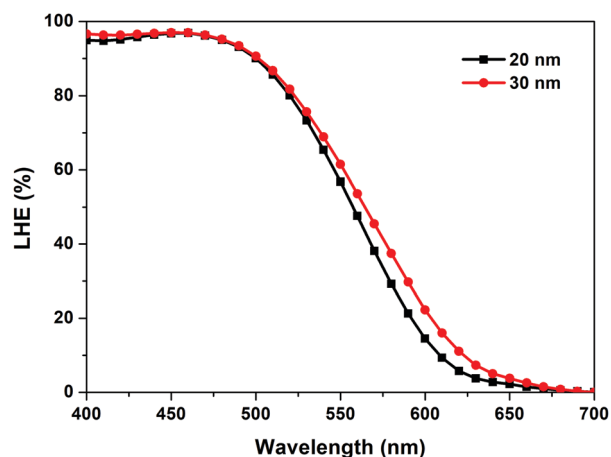


Fig. 2 LHE of dye soaked TiO_2 electrodes with 20 nm and 30 nm TiO_2 particles as a function of wavelength. The thickness of the TiO_2 layer is 4 μm .

particles, whereas the roughness value for 30 nm TiO_2 films was found to be 339 nm. Larger roughness contributed towards higher dye loading for 30 nm TiO_2 particles (1.3×10^{-7} mol cm^{-2} for 30 nm and 1.2×10^{-7} mol cm^{-2} for 20 nm). Thus the larger-sized particles with higher roughness improved the scattering and dye intake thereby contributing towards better LHE for devices fabricated using 30 nm TiO_2 particles, particularly in the red region.^{37,38}

Probing recombination

The most critical process that determines the performance of DSCs is the back electron transfer/recombination at the TiO_2 /electrolyte interface. At this interface, the injected electrons in the conduction band (CB) and sub-bandgap states of TiO_2 recombines with the oxidised species/holes present in the electrolyte. Recombination is more prominent in copper electrolyte-based devices since the redox potentials of $\text{Cu}^{\text{I}}/\text{Cu}^{\text{II}}$ systems are more positively placed than the conventional iodide electrolyte, resulting in larger driving force for

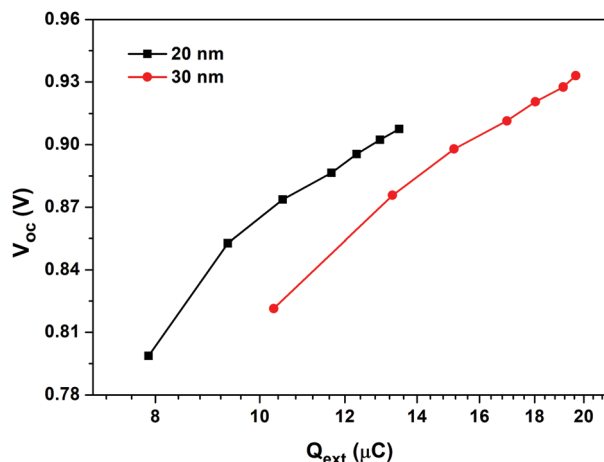


Fig. 3 V_{oc} as a function of extracted charge for DSCs with 20 nm and 30 nm TiO_2 particles.

recombination. Thus minor alterations at a TiO_2 /electrolyte interface remarkably impacts the rate of recombination in copper electrolyte based DSCs. We first analyzed the location of CB in both 20 nm and 30 nm devices using charge extraction measurement. Fig. 3 shows V_{oc} as a function of extracted charge for DSCs with 20 nm and 30 nm TiO_2 particles, respectively. As apparent from Fig. 3, at analogous charge density, V_{oc} for a 30 nm device is lower than that for a 20 nm one, which indicates that the CB of TiO_2 using 30 nm TiO_2 particles shifted towards more positive potentials compared to 20 nm. After locating the CB of TiO_2 , the recombination at the TiO_2 /electrolyte interface using transient photovoltage decay and open-circuit voltage decay (OCVD) were measured (Fig. 4). Employing these two perturbation techniques, we estimated the lifetime, which provides the information on recombination. Both measurements revealed that devices fabricated using 30 nm TiO_2 particles achieved higher lifetime than devices fabricated using 20 nm TiO_2 particles. Similar results were also obtained from electrochemical impedance spectroscopy (EIS) measurement (Fig. S3, ESI[†]). 30 nm particles possess relatively higher dye loading than 20 nm particles, which blocks the TiO_2 surface more effectively from the oxidized $Cu(II)$ species, leading to reduced interfacial charge recombinations. Nevertheless, the CB of TiO_2 in 30 nm devices are also placed at lower potentials than 20 nm, which aids in reducing recombinations as a result of a lower recombination driving force. Owing to the improved lifetime, DSCs fabricated using 30 nm TiO_2 particles showed higher V_{oc} and fill factor than the devices fabricated using 20 nm TiO_2 particles.

Recombination from the sub-bandgap states of TiO_2 also cannot be ignored for devices using the $[Cu(tmby)_2]^{2+/1+}$ electrolyte with a positive redox potential of 0.87 V vs. *NHE* that leads to non-ideality.^{39,40} We estimated the ideality factor from the V_{oc} vs. light intensity plot (Fig. 5) using the relation,⁴¹

$$\frac{dV_{oc}}{d \log I} = \frac{2.30 m k_B T}{q} \quad (3)$$

where I is input light intensity, m is the ideality factor, k_B is Boltzmann's constant and T is the temperature. Using eqn (3),

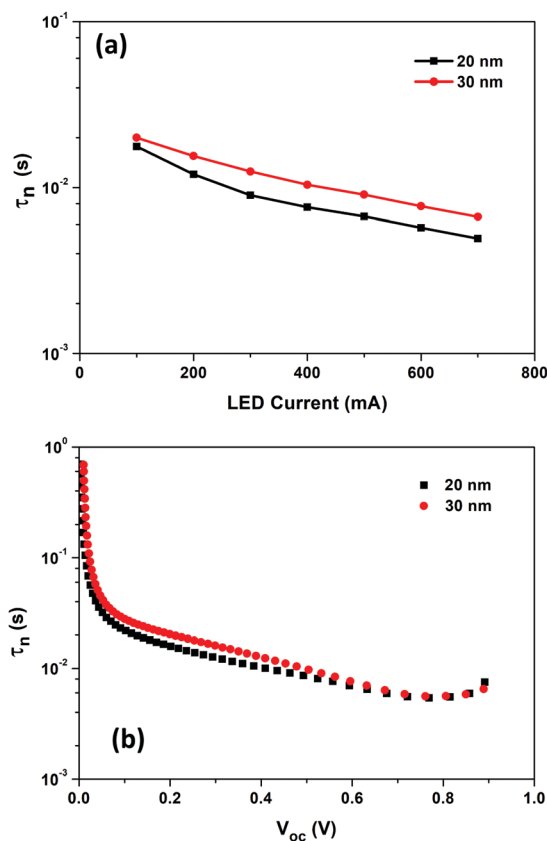


Fig. 4 Lifetime (τ_n) measurements using (a) transient photovoltage decay and (b) OCVD for DSCs with 20 nm and 30 nm TiO_2 particles.

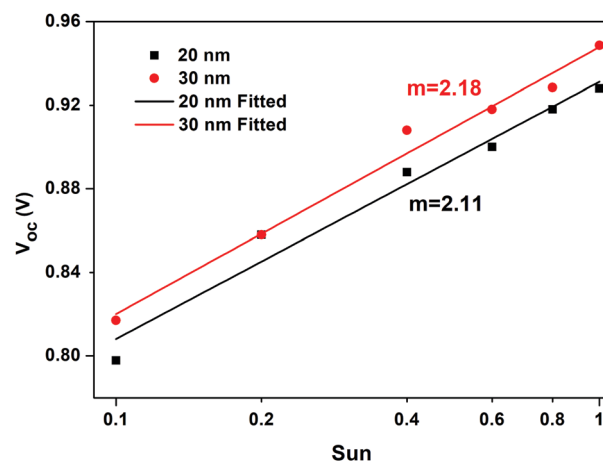


Fig. 5 V_{oc} as a function of light intensity for DSCs with 20 nm and 30 nm TiO_2 particles.

m was found to be 2.11 and 2.18 for devices fabricated using 20 nm and 30 nm TiO_2 particles. It is to be noted that the ideal value of m is 1. The non-ideal value in both cases indicates recombination from sub-bandgap states. The extent of non-ideality is nearly similar; thus, the recombination from sub-bandgap states is likely to be identical for both 20 nm and 30 nm TiO_2 particles.

Probing injection, regeneration and mass transport

The injection and regeneration studies were carried out using photo induced absorption measurements (PIA). Fig. 6 shows the PIA spectra of dye-soaked electrodes and copper electrolyte filled devices. For dye-soaked electrodes, the ground state bleaching was detected at around 580 nm; meanwhile, the absorption of the oxidised D35 dye was observed beyond 800 nm wavelength, showing effective injection of electrons to TiO₂ dye excited state.^{35,42,43} The PIA spectrum of devices fabricated with both the 20 nm and 30 nm TiO₂ particles overlap with each other, indicating similar injection. The absorption spectra of the oxidised D35 dye were quenched by the addition of the electrolyte, suggesting effective regeneration of oxidized dye ground state.⁶ Moreover, faster regeneration can be anticipated qualitatively for devices using 30 nm TiO₂ particles with respect to devices using 20 nm TiO₂ particles, as the extent of absorption quenching is more in the former case.

Dye regeneration can also be influenced by the slower diffusion of ions present in the electrolyte, particularly in DSCs employing alternative redox electrolytes due to the molecular bulkiness of the transition metal complexes.^{44–46} We carried out intensity-dependent J_{sc} measurement and current transient measurements to explore the mass transport limitation in these devices. Fig. 7(a) shows J_{sc} as a function of light intensity. Current density is related to the irradiation intensity by the relation, $J_{sc} \propto I^\alpha$ where α is a constant. $\alpha = 1$ suggests ideal relationship between J_{sc} and input light intensity. Using 20 nm and 30 nm TiO₂ particle, α was found to be unity which suggest that both the devices are free from mass transport limitation irrespective of the difference in the size of the TiO₂ particles being used in respective devices. This is applicable to devices using dyes of similar architecture as D35. This may not hold the same using bulky dyes or while employing co-sensitized approach. Fig. 7(b) displays the current transient measurement for DSCs fabricated using photoanodes having 20 nm and 30 nm TiO₂ particles. Current transient measurements were carried out under one sun illumination (100 mW cm⁻², AM 1.5G). Once the light is irradiated, the current response of the device reached a

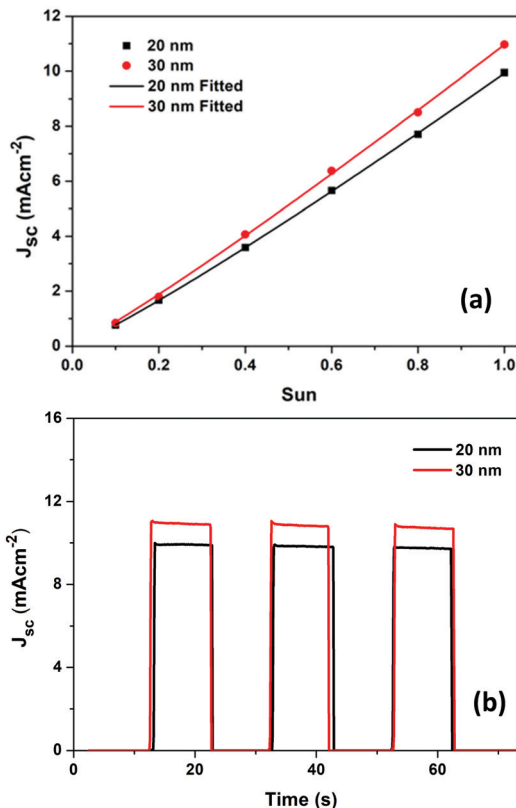


Fig. 7 (a) Light intensity dependence on the J_{sc} for DSC with TiO₂ particles of 20 nm and 30 nm (b) current transient plot measured under AM 1.5G simulated light for DSCs fabricated using 20 nm and 30 nm TiO₂ particles.

maximum current (J_{max}) followed by a decay reaching to a saturation (J_{sat}) current over the passage of a few seconds. As apparent from Fig. 7(b) J_{max} and J_{sat} are nearly equal using the present dye–electrolyte combination (D35-[Cu(tmby)₂]^{2+/1+}), which further confirms that devices fabricated with both 20 nm and 30 nm TiO₂ particles are free from mass transport limitations.

Probing charge collection

Once electrons are injected, they must be collected at the respective electrodes to generate current. The ratio of the number of electrons injected to the number of electrons collected determines the charge collection efficiency (η_{cc}).^{47,48} For efficient charge collection, diffusion length (L_n) must be longer than the thickness of TiO₂.^{49,50} Fig. 8 shows diffusion length (L_n) and charge collection efficiency (η_{cc}) as a function of LED current. Diffusion length (L_n) and charge collection efficiency (η_{cc}) were estimated from eqn (4) and (5),^{47,51,52}

$$L_n = L \sqrt{\frac{\tau_d}{\tau_n}} \quad (4)$$

$$\eta_{cc} = 1 / \left(1 + \frac{\tau_d}{\tau_n} \right) \times 100 \quad (5)$$

where L is the thickness of TiO₂, τ_d is the transport time and τ_n is the lifetime. The lifetime and transport time were

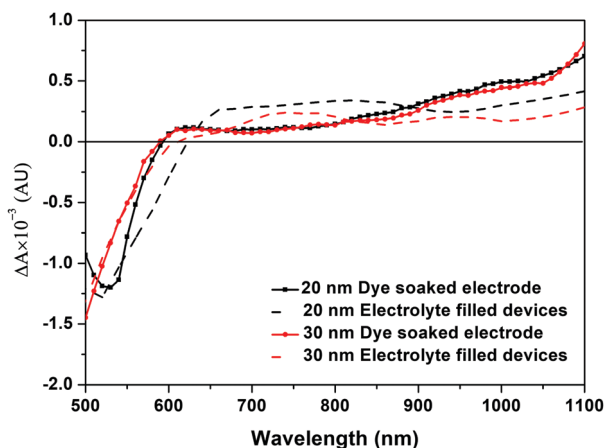


Fig. 6 PIA spectra for DSCs with TiO₂ electrodes with 20 nm and 30 nm TiO₂ particles.

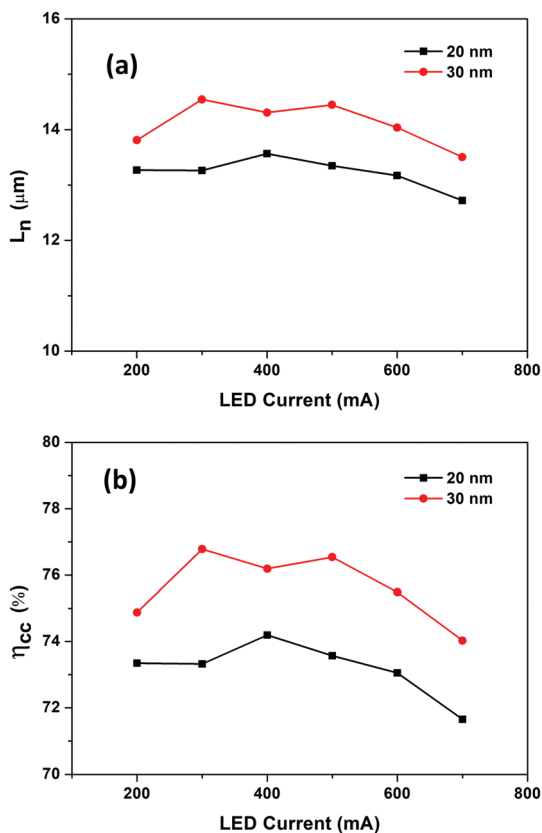


Fig. 8 (a) Diffusion length (L_n) and (b) charge collection efficiency (η_{cc}) as a function of LED current for DSCs using 20 nm and 30 nm TiO_2 particles.

determined from transient photovoltage decay and transient photo current decay measurements. Transient photo current decay is given in Fig. S4, ESI.†

As shown in Fig. 8(a), for devices fabricated using 20 nm and 30 nm TiO_2 particles, the diffusion length is three times longer than the thickness of the TiO_2 film ($\sim 4 \mu\text{m}$ irrespective of the particle size), which is large enough for efficient charge collection. L_n remains approximately constant irrespective of light intensity while DSCs with 30 nm TiO_2 particles showcased a longer diffusion length than DSCs fabricated using 20 nm TiO_2 particles. Longer diffusion length in 30 nm TiO_2 particles can be attributed to the improved lifetime which resulted in comparatively better charge collection efficiency for 30 nm TiO_2 particle based devices (Fig. 8(b)).

Conclusions

We systematically studied the effect of a photoanode comprising of 20 nm and 30 nm TiO_2 particles, respectively, employing $\text{Cu}[(\text{tmby})_2]^{2+/1+}$ as the redox mediator with an organic D35 sensitizer. The device fabricated using 30 nm TiO_2 particles showed an improvement in PCE compared to the device fabricated with 20 nm TiO_2 particles under full sun and indoor illumination. The improvement in PCE is attributed to the enhancement of the current density (J_{sc}), open-circuit potential (V_{oc}) and fill factor (FF). The gain in V_{oc} and FF is mainly

attributed to the improved lifetime. The diode quality factor (m) was found to be non-ideal for DSCs using both 20 nm and 30 nm TiO_2 particles, indicating the possibility of recombination from surface states. To provide a more detailed justification on enhancement in J_{sc} , we analysed parameters such as η_{LHE} , η_{inj} , η_{reg} and η_{cc} . LHE was marginally improved at higher wavelengths for photoanodes using 30 nm TiO_2 particles as a result of higher roughness, better dye loading and improved scattering. The PIA result suggests better regeneration for devices fabricated using 30 nm TiO_2 particles. Furthermore, devices fabricated using 20 nm and 30 nm TiO_2 particles were free from mass transport with an ideal α value of 1. Devices fabricated using 30 nm TiO_2 particles realized longer lifetime and diffusion length contributing to a better charge collection efficiency. In a nutshell, the collective enhancement in LHE, dye regeneration, and charge collection efficiency assisted in bringing higher J_{sc} , V_{oc} , FF and improved PCE for devices fabricated using 30 nm TiO_2 particles employing the D35 sensitizer and $\text{Cu}[(\text{tmby})_2]^{2+/1+}$ as the redox mediator.

Experimental

General methods

The solvents and materials used for device fabrication were of HPLC grade purchased from Sigma-Aldrich, Merck, GreatCell Solar and used without further purification. D35 organic dye and $[\text{Cu}(\text{tmby})_2]^{2+/1+}$ copper complexes were obtained from Dyenamo AB (Stockholm, Sweden). 20 nm 18 NRT TiO_2 paste was obtained from GreatCell Solar and 30 nm TiO_2 paste was obtained from Dyenamo AB.

Solar cell fabrication

Working electrode preparation starts with cutting of FTO glasses (TEC15, GreatcellSolar) into $1.5 \times 1.5 \text{ cm}^2$ pieces. Thereupon FTO glasses were sonicated in a detergent for 30 minutes followed by gentle scrubbing in water and again sonication in deionized (DI) water for 30 minutes, followed by sonication in IPA and acetone for 15 minutes each. To further remove any other organics, processed FTOs were annealed at $500 \text{ }^\circ\text{C}$ for 15 minutes in a muffle furnace followed by UV-ozone cleaning. A compact TiO_2 blocking layer was created over FTO using TiCl_4 treatment followed by annealing at $500 \text{ }^\circ\text{C}$ for 30 minutes. TiCl_4 treatment includes dipping cleaned FTO in 53 mM TiCl_4 bath for 30 min at $70 \text{ }^\circ\text{C}$ followed by rinsing of FTO using DI water and ethanol. Following this, either a 20 nm TiO_2 particle layer (18NRT, GreatcellSolar) or 30 nm (Dyenamo, Sweden) was deposited by screen printing with a total thickness of $4 \mu\text{m}$. Further TiO_2 coated substrates were annealed at $325 \text{ }^\circ\text{C}$ for 5 minutes, $375 \text{ }^\circ\text{C}$ for 5 minutes, $400 \text{ }^\circ\text{C}$ for 5 minutes and $500 \text{ }^\circ\text{C}$ for 15 minutes. Again, TiCl_4 treatment was performed on electrodes followed by annealing at $500 \text{ }^\circ\text{C}$ for 30 minutes to create a compact TiO_2 post-blocking layer over mesoporous TiO_2 . The electrodes were then kept inside the dye bath overnight. The dye solution consists of 0.2 mM D35 (Dyenamo, Sweden) in 1:1 acetonitrile and *tert*-butanol. For counter

electrodes, predrilled $1.5 \times 1.5 \text{ cm}^2$ FTO glasses (TEC8, Great-Cell Solar) were sonicated in detergent, DI water, and ethanol for 45 minutes and consequently annealed at $500 \text{ }^\circ\text{C}$ for 15 minutes. Prior to PEDOT [poly(3,4-ethylene dioxythiophene)] deposition, electrodes were treated using UV- O_3 for 15 min. Preparation of the PEDOT counter electrode involves electropolymerisation of 3,4-ethylene dioxythiophene (EDOT) from a micellar aqueous solution of 0.1 M sodium dodecyl sulfate (SDS) and 0.01 M EDOT.^{53,54} The electrodes were assembled using a $30 \text{ }\mu\text{m}$ Surlyn spacer and heat pressing at $110 \text{ }^\circ\text{C}$. $[\text{Cu}(\text{tmbpy})_2]^{2+/1+}$ electrolyte, which consists of 0.20 M Cu(I), 0.04 M Cu(II), 0.1 M LiTFSI, and 0.6 M 4-*tert*-butylpyridine in acetonitrile, was injected through the predrilled holes and the holes were subsequently sealed using a cover glass.

Solar cell characterization

Photocurrent voltage (J - V) characteristics were determined using an Oriol Class-AAA solar simulator (Model PVIV-94043A) equipped with a Keithley 2440 power source. The intensity of irradiation was measured using a certified calibrated Si solar cell. The photovoltaic results reported are from the data obtained from 8 devices, and the error was estimated using the standard deviation method. Indoor light measurement was carried out inside a dark box with warm white CFL as the illumination source. The indoor J - V responses were recorded using a Dyanamo potentiostat (DN-AE05). The intensity of light was measured using a radiometrically calibrated Ocean optics Jaz spectrometer. A circular black mask of areas 0.1256 cm^2 (smaller than the active area) was used during the J - V measurements to minimize the contribution of light falling outside the active area. The incident photon-to-current conversion efficiency (IPCE) of devices was determined under the DC mode using a 300 W Xenon lamp integrated with a Newport monochromator and power meter, controlled using Oriol software. Both current transient and open-circuit voltage decay (OCVD) measurements were carried out under AM 1.5G illumination. For current transient measurements, the lamp was sequentially switched on and switched off at intervals of 10 seconds, and the photocurrent response was recorded using an Autolab PGSTAT302N by applying 0 V across the device. In OCVD measurement, the device was illuminated for 30 seconds, and then the light was switched off, and the photovoltage decay was recorded. Furthermore, from the photovoltage the decay lifetime was calculated.^{55,56} Photo induced absorption spectroscopy (PIA) was performed using a Dyanamo DN-AE02. It uses a 1 W blue light-emitting LED ($\lambda = 470 \text{ nm}$) as a pump and a 20 W tungsten halogen lamp as a probe. The transmitted light through the sample falls on the monochromator and is detected using a UV enhanced Si detector connected to a lock-in amplifier (SR830) via a current amplifier. The PIA spectra of the devices were recorded using excitation from a LED, which has a square wave with a modulation frequency of 9.3 Hz. For PIA measurement the TiO_2 thickness of devices was $4 \text{ }\mu\text{m}$. Transient photovoltage decay, transient photocurrent decay, and charge extraction were measured using a Dyanamo Toolbox set-up (DN-AE01). It generates light using a white LED, and current or voltages response is

recorded using a digital acquisition board. For transient photovoltage and photocurrent decay, small amplitude square wave perturbations involving different light intensities are given to the device, and the response is recorded at open circuit and short circuit respectively. In charge extraction measurements, the device is illuminated to attain V_{oc} , simultaneously the light is switched off and the device is short-circuited, and the current response is recorded. Electrochemical Impedance Spectroscopy (EIS) of DSCs were carried out under dark conditions with perturbation of amplitude 10 mV, frequency ranging from 100 mHz to 100 kHz using an Autolab (PGSTAT302N). For the LHE study, absorption of dye soaked electrodes were carried out using an Ocean Optics Jaz spectrometer. For dye loading study dye desorption was performed using 0.1 M NaOH in ethanol and absorption of desorbed dye solutions were recorded using an Ocean Optics Jaz spectrometer.

Author contributions

The manuscript was written through contributions of all authors. All authors have given approval to the final version of the manuscript.

Conflicts of interest

There are no conflicts to declare.

Acknowledgements

S. S. gratefully acknowledges financial support from the SERB CRG project (CRG/2020/001406) and CSIR-FIRST project (MLP65). S. C. P. thanks CSIR, Government of India, for providing Senior Research Fellowship and J. V. thanks DST-SERB (DST/SERB/F/481) for research fellowships.

References

- 1 M. Kokkonen, P. Talebi, J. Zhou, S. Asgari, S. Ahmed Soomro, F. Elsehrawy, J. Halme, S. Ahmad, A. Hagfeldt and S. Ghufuran Hashmi, *J. Mater. Chem. A*, 2021, **9**, 10527–10545.
- 2 P. R. Nitha, S. Soman and J. John, *Mater. Adv.*, 2021, **2**, 6136–6168.
- 3 G. Gokul, S. C. Pradhan and S. Soman, *Advances in Solar Energy Research*, Springer, Singapore, 2019, pp. 281–316.
- 4 A. Aslam, U. Mehmood, M. H. Arshad, A. Ishfaq, J. Zaheer, A. Ul Haq Khan and M. Sufyan, *Sol. Energy*, 2020, **207**, 874–892.
- 5 Q. Huaulmé, V. M. Mwalukuku, D. Joly, J. Liotier, Y. Kervella, P. Maldivi, S. Narbey, F. Ostwald, A. J. Riquelme, J. A. Anta and R. Demadrille, *Nat. Energy*, 2020, **5**, 468–477.
- 6 E. Tanaka, H. Michaels, M. Freitag and N. Robertson, *J. Mater. Chem. A*, 2020, **8**, 1279–1287.
- 7 H. Michaels, I. Benesperi and M. Freitag, *Chem. Sci.*, 2021, **12**, 5002–5015.
- 8 B. O'Regan and M. Grätzel, *Nature*, 1991, **353**, 737–740.
- 9 M. K. Nazeeruddin, E. Baranoff and M. Grätzel, *Sol. Energy*, 2011, **85**, 1172–1178.

- 10 E. Tanaka, M. S. Mikhailov, N. S. Gudim, E. A. Knyazeva, L. V. Mikhalechenko, N. Robertson and O. A. Rakitin, *Mol. Syst. Des. Eng.*, 2021, **6**, 730–738.
- 11 J. M. dos Santos, E. Tanaka, A. A. Wiles, G. Cooke and N. Robertson, *Mol. Syst. Des. Eng.*, 2021, **6**, 381–389.
- 12 E. Tanaka and N. Robertson, *J. Mater. Chem. A*, 2020, **8**, 19991–19999.
- 13 A. B. Muñoz-García, I. Benesperi, G. Boschloo, J. J. Concepcion, J. H. Delcamp, E. A. Gibson, G. J. Meyer, M. Pavone, H. Pettersson, A. Hagfeldt and M. Freitag, *Chem. Soc. Rev.*, 2021, **50**, 12450.
- 14 K. Kakiage, Y. Aoyama, T. Yano, K. Oya, J. I. Fujisawa and M. Hanaya, *Chem. Commun.*, 2015, **51**, 15894–15897.
- 15 Y. K. Eom, S. H. Kang, I. T. Choi, Y. Yoo, J. Kim and H. K. Kim, *J. Mater. Chem. A*, 2017, **5**, 2297–2308.
- 16 M. Freitag, J. Teuscher, Y. Saygili, X. Zhang, F. Giordano, P. Liska, J. Hua, S. M. Zakeeruddin, J. E. Moser, M. Grätzel and A. Hagfeldt, *Nat. Photonics*, 2017, **11**, 372–378.
- 17 Y. Cao, Y. Liu, S. M. Zakeeruddin, A. Hagfeldt and M. Grätzel, *Joule*, 2018, **2**, 1108–1117.
- 18 D. Zhang, M. Stojanovic, Y. Ren, Y. Cao, F. T. Eickemeyer, E. Socie, N. Vlachopoulos, J. E. Moser, S. M. Zakeeruddin, A. Hagfeldt and M. Grätzel, *Nat. Commun.*, 2021, **12**, 1–10.
- 19 T. W. Hamann, *Dalton Trans.*, 2012, **41**, 3111–3115.
- 20 M. Yoosuf, S. C. Pradhan, M. M. Sruthi, S. Soman and K. R. Gopidas, *Sol. Energy*, 2021, **216**, 151–163.
- 21 S. M. Feldt, E. A. Gibson, E. Gabrielsson, L. Sun, G. Boschloo and A. Hagfeldt, *J. Am. Chem. Soc.*, 2010, **132**, 16714–16724.
- 22 Y. Hao, W. Yang, L. Zhang, R. Jiang, E. Mijangos, Y. Saygili, L. Hammarström, A. Hagfeldt and G. Boschloo, *Nat. Commun.*, 2016, **7**, 1–8.
- 23 Y. Saygili, M. Söderberg, N. Pellet, F. Giordano, Y. Cao, A. B. Muñoz-García, S. M. Zakeeruddin, N. Vlachopoulos, M. Pavone, G. Boschloo, L. Kavan, J. E. Moser, M. Grätzel, A. Hagfeldt and M. Freitag, *J. Am. Chem. Soc.*, 2016, **138**, 15087–15096.
- 24 M. Freitag, F. Giordano, W. Yang, M. Pazoki, Y. Hao, B. Zietz, M. Grätzel, A. Hagfeldt and G. Boschloo, *J. Phys. Chem. C*, 2016, **120**, 9595–9603.
- 25 S. Hattori, Y. Wada, S. Yanagida and S. Fukuzumi, *J. Am. Chem. Soc.*, 2005, **127**, 9648–9654.
- 26 W. Zhang, Y. Wu, H. W. Bahng, Y. Cao, C. Yi, Y. Saygili, J. Luo, Y. Liu, L. Kavan, J. E. Moser, A. Hagfeldt, H. Tian, S. M. Zakeeruddin, W. H. Zhu and M. Grätzel, *Energy Environ. Sci.*, 2018, **11**, 1779–1787.
- 27 P. S. Gangadhar, A. Jagadeesh, A. S. George, G. Reddy, S. Prasanthkumar, S. Soman and L. Giribabu, *Mol. Syst. Des. Eng.*, 2021, **6**, 779–789.
- 28 P. Ferdowsi, Y. Saygili, F. Jazaeri, T. Edvinsson, J. Mokhtari, S. M. Zakeeruddin, Y. Liu, M. Grätzel and A. Hagfeldt, *ChemSusChem*, 2020, **13**, 212–220.
- 29 Y. J. Son, J. S. Kang, J. Yoon, J. Kim, J. Jeong, J. Kang, M. J. Lee, H. S. Park and Y.-E. Sung, *J. Phys. Chem. C*, 2018, **122**, 7051–7060.
- 30 K. Park, Q. Zhang, D. Myers and G. Cao, *ACS Appl. Mater. Interfaces*, 2013, **5**, 1044–1052.
- 31 H. S. Kim, S. B. Ko, I. H. Jang and N. G. Park, *Chem. Commun.*, 2011, **47**, 12637–12639.
- 32 M. Hu, J. Shen, Z. Yu, R.-Z. Liao, G. G. Gurzadyan, X. Yang, A. Hagfeldt, M. Wang and L. Sun, *ACS Appl. Mater. Interfaces*, 2018, **10**, 30409–30416.
- 33 M. Yoosuf, S. C. Pradhan, S. Soman and K. R. Gopidas, *Sol. Energy*, 2019, **188**, 55–65.
- 34 J. Halme, G. Boschloo, A. Hagfeldt and P. Lund, *J. Phys. Chem. C*, 2008, **112**, 5623–5637.
- 35 M. Pazoki, U. B. Cappel, E. M. J. Johansson, A. Hagfeldt and G. Boschloo, *Energy Environ. Sci.*, 2017, **10**, 672–709.
- 36 Q. Wu, J. Hou, H. Zhao, Z. Liu, X. Yue, S. Peng and H. Cao, *Dalton Trans.*, 2018, **47**, 2214–2221.
- 37 S. Sasidharan, S. C. Pradhan, A. Jagadeesh, B. N. Nair, A. A. P. Mohamed, K. N. Narayanan Unni, S. Soman and U. N. S. Hareesh, *ACS Appl. Energy Mater.*, 2020, **3**, 12584–12595.
- 38 K. Zhu, N. Kopidakis, N. R. Neale, J. Van De Lagemaat and A. J. Frank, *J. Phys. Chem. B*, 2006, **110**, 25174–25180.
- 39 J. Halme, P. Vahermaa, K. Miettunen and P. Lund, *Adv. Mater.*, 2010, **22**, 210–234.
- 40 J. Bisquert, A. Zaban and P. Salvador, *J. Phys. Chem. B*, 2002, **106**, 8774–8782.
- 41 P. Salvador, M. G. Hidalgo, A. Zaban and J. Bisquert, *J. Phys. Chem. B*, 2005, **109**, 15915–15926.
- 42 M. Freitag, J. Teuscher, Y. Saygili, X. Zhang, F. Giordano, P. Liska, J. Hua, S. M. Zakeeruddin, J.-E. Moser, M. Grätzel and A. Hagfeldt, *Nat. Photonics*, 2017, **11**, 372–378.
- 43 R. Haridas, J. Jayadev, S. C. Pradhan, V. Asarikal, Y. Karuvath, S. Soman, K. N. Narayanan Unni and A. Ajayaghosh, *Mater. Adv.*, 2021, **2**, 7773.
- 44 T. W. Hamann and J. W. Ondersma, *Energy Environ. Sci.*, 2011, **4**, 370–381.
- 45 B. M. Klahr and T. W. Hamann, *J. Phys. Chem. C*, 2009, **113**, 14040–14045.
- 46 S. C. Pradhan, A. Hagfeldt and S. Soman, *J. Mater. Chem. A*, 2018, **6**, 22204–22214.
- 47 K. Zhu, S. R. Jang and A. J. Frank, *J. Phys. Chem. Lett.*, 2011, **2**, 1070–1076.
- 48 K. Zhu, N. R. Neale, A. Miedaner and A. J. Frank, *Nano Lett.*, 2006, **7**, 69–74.
- 49 J. Ondersma and T. Hamann, *J. Phys. Chem. C*, 2010, **114**, 638–645.
- 50 F. Fabregat-Santiago, J. Bisquert, G. Garcia-Belmonte, G. Boschloo and A. Hagfeldt, *Sol. Energy Mater. Sol. Cells*, 2005, **87**, 117–131.
- 51 M. Adachi, M. Sakamoto, J. Jiu, Y. Ogata and S. Isoda, *J. Phys. Chem. B*, 2006, **110**, 13872–13880.
- 52 J. Van De Lagemaat, N. G. Park and A. J. Frank, *J. Phys. Chem. B*, 2000, **104**, 2044–2052.
- 53 H. Ellis, N. Vlachopoulos, L. Häggman, C. Perruchot, M. Jouini, G. Boschloo and A. Hagfeldt, *Electrochim. Acta*, 2013, **107**, 45–51.
- 54 S. Soman, S. C. Pradhan, M. Yoosuf, M. V. Vinayak, S. Lingamoorthy and K. R. Gopidas, *J. Phys. Chem. C*, 2018, **122**, 14113–14127.
- 55 S. Sasidharan, S. Soman, S. C. Pradhan, K. N. N. Unni, A. A. P. Mohamed, B. N. Nair and H. U. N. Saraswathy, *New J. Chem.*, 2017, **41**, 1007–1016.
- 56 J. Bisquert, A. Zaban, M. Greenshtein and I. Mora-Seró, *J. Am. Chem. Soc.*, 2004, **126**, 13550–13559.

Supporting Information

Probing Photovoltaic Performance in Copper Electrolyte Dye-Sensitized Solar Cells of Variable TiO₂ Particle Size Using Comprehensive Interfacial Analysis

Sourava Chandra Pradhan,^{ab} Jayadev Velore^{ab}, Anders Hagfeldt^{*c} and Suraj Soman^{*ab}

^aPhotosciences and Photonics Section, Chemical Sciences and Technology Division, CSIR-National Institute for Interdisciplinary Science and Technology (CSIR-NIIST), Thiruvananthapuram-695019, India. ^bAcademy of Scientific and Innovative Research (AcSIR), Ghaziabad-201002, India. ^cDepartment of Chemistry – Ångström Laboratory, Uppsala University Box 523, SE-75120 Uppsala, Sweden.

Email: suraj@niist.res.in

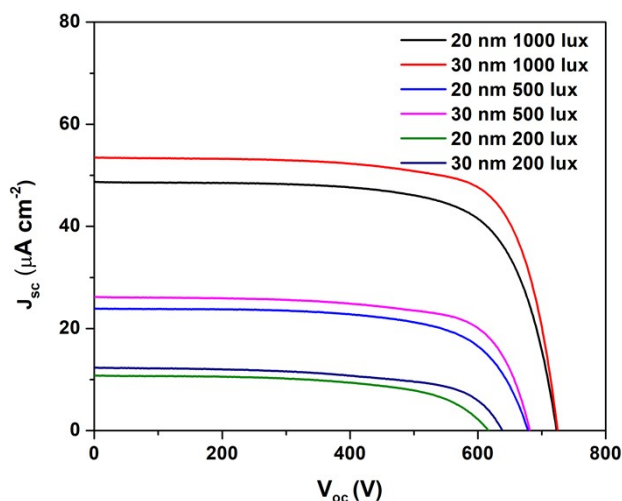


Figure S1. Current density - voltage (J - V) of DSCs fabricated with 20 nm and 30 nm TiO₂ particles employing D35 sensitizer and [Cu(tmby)₂]^{2+/1+} redox mediator under cfl light.

Table S1. Indoor photovoltaic parameter of DSCs fabricated with 20 nm and 30 nm TiO₂ particles employing D35 sensitizer and [Cu(tmby)₂]^{2+/1+} redox mediator under cfl light.

Device	Input power lux ($\mu\text{W}/\text{cm}^2$)	V_{oc} (mV)	J_{sc} ($\mu\text{A}/\text{cm}^2$):	FF	P_{max} ($\mu\text{W}/\text{cm}^2$)	PCE (%)
20 nm	1000 (283)	722 ± 1	48.68 ± 0.26	71.08 ± 0.33	25.01 ± 0.31	8.83 ± 0.11
	500 (143)	679 ± 4	23.92 ± 0.23	66.97 ± 0.37	10.88 ± 0.23	7.61 ± 0.16
	200 (59)	617 ± 2	10.79 ± 0.22	59.71 ± 0.25	3.98 ± 0.27	6.74 ± 0.14
30 nm	1000 (283)	727 ± 3	53.74 ± 0.22	75.14 ± 0.45	$29.36 \pm .74$	10.37 ± 0.26
	500 (143)	687 ± 3	26.54 ± 0.20	73.95 ± 0.80	13.49 ± 0.20	9.43 ± 0.14
	200 (59)	639 ± 2	12.33 ± 0.10	61.43 ± 0.55	4.84 ± 0.33	8.21 ± 0.22

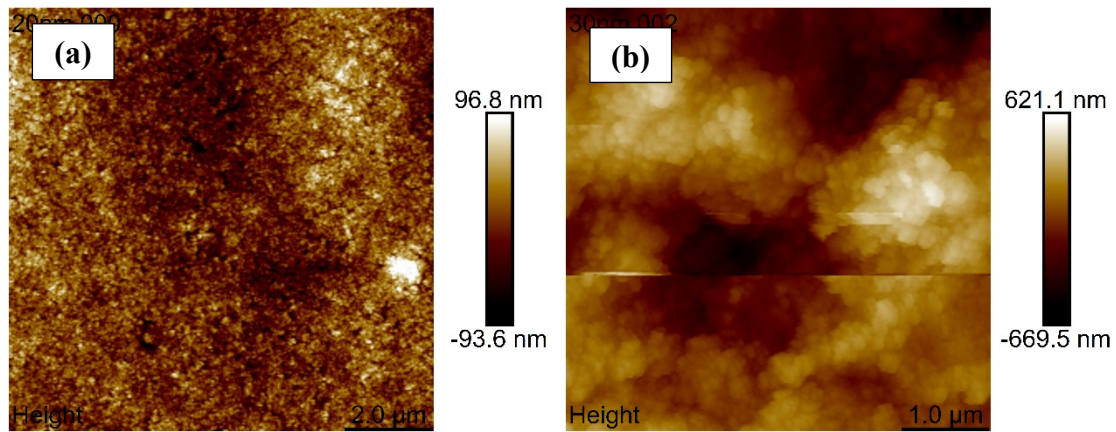


Figure S2. AMF image of TiO₂ film with (a) 20 nm (b) 30 nm diameter.

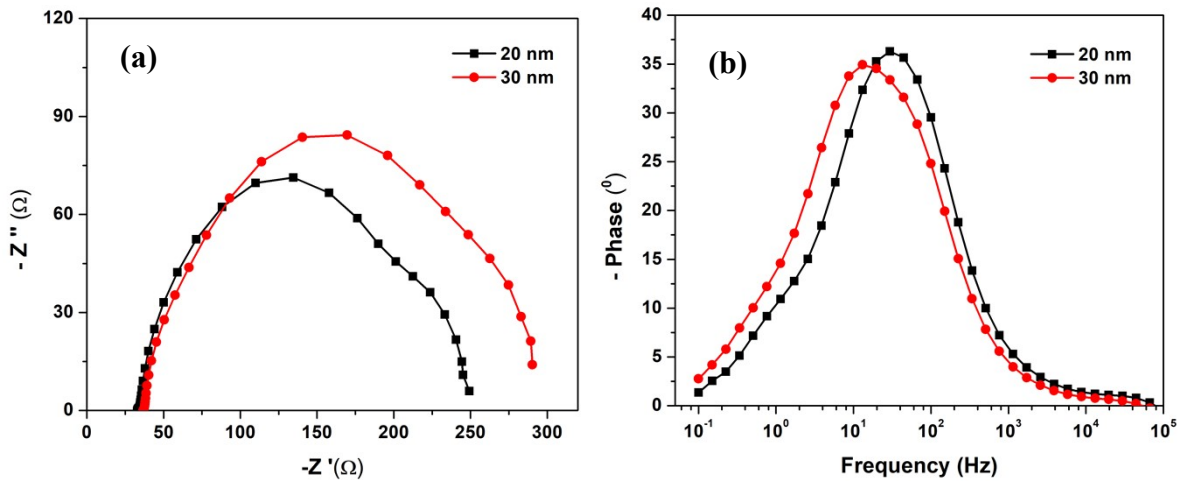


Figure S3. (a) Nyquist plot and (b) Bode plot of DSCs fabricated with 20 nm and 30 nm TiO₂ particles

EIS was measured at open circuit potential for both DSC with TiO₂ particle 20 nm and 30 nm. Figure S2 (a) and (b) displays Nyquist plot and bode plot. The Nyquist plot consists of three distinguished semicircle, the semicircle at high frequency region corresponds to charge transfer at counter electrode electrolyte interface, second semicircle corresponds to charge transfer at TiO₂/electrolyte interface and the third semicircle corresponds to diffusion of ions on electrolyte. As seen in Figure S2 (a) the radius of second semicircle of 30 nm device is larger than 20 nm device which shows higher recombination resistance in 30 nm device than 20 nm device. We calculated lifetime (τ_n) from Bode plot using the relation, $\tau_n = 1/2\pi f_{max}$ where f_{max} is frequency at highest phase value. 30 nm device showed lifetime of 5.3 ms while 20 nm device showed 12.1 ms.

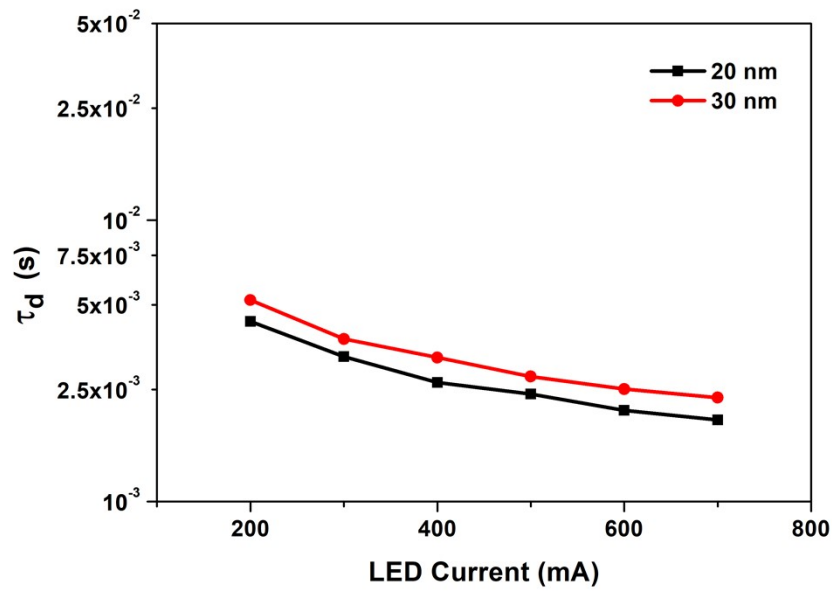


Figure S4. Transport time (τ_d) measurements using transient photocurrent decay for DSCs with 20 nm and 30 nm TiO_2 particles.